Calcium Based Metallic Glasses: Ductile by Design; Embrittlement by Environment

---

A Dissertation

Presented to

the faculty of the School of Engineering and Applied Science

University of Virginia

---

in partial fulfillment

of the requirements for the degree

Doctor of Philosophy

by

Andrew M. Cheung

August

2018

APPROVAL SHEET

The dissertation

is submitted in partial fulfillment of the requirements

for the degree of

Doctor of Philosophy

_____
AUTHOR

The dissertation has been read and approved by the examining committee:

Gary J. Shiflet
_____
Advisor

James M. Fitz-Gerald, Chair
_____

S. Joseph Poon
_____

William C. Johnson
_____

James M. Howe
_____

Elizabeth J. Opila
_____

Accepted for the School of Engineering and Applied Science:

Craig H. Benson, Dean, School of Engineering and Applied Science

August
2018

Abstract

Metallic glasses made predominately from calcium were, for a short time, of interest for use within the transportation and aerospace industries. This was because of their low density, favorable strength to density ratio, and relatively low materials cost. When the other constituent elements of the Ca glasses are also biodegradable, e.g., Ca-Mg-Zn, then there is interest for their use in the biomedical industry.

For these applications, the glasses need to be strong and ductile, or at least less brittle. Most metallic glasses have a high tensile strength, when compared to their crystalline counterparts, but low ductility, and therefore low toughness. From a previous study at UVa, one way for increasing the toughness in Fe-based glass was to employ an alloying strategy where the addition of solute elements would tune the electron structure of the glass composition in a direction that leads to more metallic behavior of the host element, in this case iron. A similar electronic structure manipulation strategy model was proposed and used here to determine which calcium-based glass compositions might improve toughness. From this work it was determined that Ca-Mg was the most ductile system, while Ca-Al and Ca-Cu systems were very brittle. The binary system with Mg was more ductile than the Al or Cu systems because when alloyed, the lowest amount of charge was transferred away from Ca, the solvent metallic element.

Adjusting the compositions, $Ca_{72}Mg_{28}$ was determined to be the most ductile. Unfortunately, this predicted and experimentally verified ductile composition rapidly embrittled in ambient lab conditions, once removed from a vacuum. The time for embrittlement was on the order of minutes. Based on these results, a research project was established to determine, as clearly as possible, the atomic/electronic mechanism for this embrittlement. The goal was that if the process could be understood, then it might be possible to mitigate the deleterious effects. The research proposed was to isolate the atmospheric component(s) responsible for the embrittlement and then to follow the chemical reactions within the bulk of the Ca-glass in a detailed fashion. Further, the hypothesis to be tested is whether this atmospheric component is responsible for any charge transferred away from calcium, thus decreasing the metallic bonds present and in the process embrittling the Ca glass. This would be an independent test of the strategy applied for the Fe-based amorphous steels and demonstrate that it is applicable across alloy systems.

To study this process the alloy $Ca_{75}Mg_{15}Al_{10}$ was selected. It was less ductile than $Ca_{72}Mg_{28}$ but its duration until becoming brittle was nearly 30 minutes long. Melt-spun ribbons of $Ca_{75}Mg_{15}Al_{10}$ about 20 microns thick were tested. Ductility was monitored through a bend-over-mandrel critical failure test that was performed on these ribbons, after they were exposed to various ambient lab conditions and individual high purity components of the atmosphere. Following these tests it was determined that the condition leading to embrittlement was a reaction of the calcium ribbon surface with humidity, or water vapor, in the lab air.

Following the identification of the atmospheric component leading to rapid deterioration of the metallic glass ribbons, reactions of H_2O with the ribbon were more closely examined. Here it was determined that the humidity dissociates into hydrogen as a byproduct of the reaction between H_2O and Ca to produce $Ca(OH)_2$. This is the initial reaction responsible for the embrittlement mechanism. The free hydrogen penetrates the Ca glass rapidly to bond with metal Ca in the ribbon bulk to form CaH_2, a strong ionic salt. The ionic bonds replace the metallic Ca bonds leading to charge transfer, thus embrittling the calcium glass.

To verify this process, measurements of various calcium compound formation and determining the location of hydrogen over time was done using x-ray photoelectron spectroscopy (XPS) and secondary ion mass spectrometry (SIMS). Their results plus the growth kinetics of the $Ca(OH)_2$ layer, that was grown in a 75% relative humidity (RH) environment, measured using scanning electron microscope (SEM), established that hydrogen is causing the embrittlement though electron transfer from calcium. Further, it is water vapor from the atmosphere that initiates the process.

Acknowledgements

In the spirit of the Latin phrase '*nanos gigantum humeris insidentes*' there are many folks whom I would like to acknowledge and thank.

First and foremost, I would like to express my sincerest gratitude to Professor Shiflet for his advice and support of my research without whom this work would not be possible. His guidance has helped shape me into an independent researcher.

I would also like to thank Professors Poon, Howe, Opila, Fitz-Gerald, Scully, Reinke, Agnew and Zhigilei for their valuable input and help. Without them this thesis would not be so thorough.

My journey at UVa has been a long one. I did not foresee this path when I sent in my undergraduate application back in the fall of '98. The UVa community, who have trained, guided, and supported me along the way has been wonderful. Many thanks to the staff, machinist, research scientists, and faculty from MSE, Physics, and Astronomy. Too many to name, but all are appreciated. Without their constant support, the outcome would have surely been different. Specifically, I would like to thank Richard White and Cathy Dukes. Without their guidance and training I would not have been able to perform all the characterizations necessary for this thesis.

This marathon was made easier due to all the kind and supportive words from former Shiflet lab students. Thanks to, the second to last, Aleks Ontman for all his help. For keeping me sane, I'd like to thank the F. D. C. Willards and George P. Burdells of the world and all my wonderful friends.

A special thanks to Kim Fitzhugh and Professor Bill Johnson who help me through a particular rough patch, without them this process would have been infinitely harder.

I want to also thank my relatives, my in-laws for helping raise my daughter, and my mom and pop, Linda and Chi-wing Cheung. Without my parents' constant support, this would not have been possible.

Finally, I must save my most significant thank you for my wife Jirakan 'Dear' Nunkaew, for her constant encouragement and support. I know it has not been easy for her with our two-continent two-body problem and it has not gotten any easier as that two body problem has morphed into a two and a half body problem. I take great joy in sharing this achievement with Dear and my daughter Charlotte, for they bring me constant happiness and motivation.

Table of Contents

Table of Contents

Table of Contents

List of Figures

Table of Contents

Table of Contents

Table of Contents

Table of Contents

List of Tables

List of Symbols

B	Parabolic Rate Constant
B/A	Linear Rate Constant
BM	Metals from Periodic Table Groups IIIB-IVB
BMG	Bulk Metallic Glass
BSE	Backscatter Electron SEM Image Mode
CMA	Cylindrical Mirror Electron Energy Analyzer
COHP	Crystal Orbital Hamilton Population
D	Diffusion Coefficient
DSC	Differential Scanning Calorimeter
$\Delta \bar{H}_H^\infty$	Relative Partial Molar Enthalpy at Infinite Dilution
e	Elementary Charge
$\bar{E}$	Effective Modulus of the Composition
E_A	Activation Energy
E_i	Modulus of the *i*-th Element
EDS	Energy-Dispersive (X-ray) Spectroscopy
ETM	Early Transition Metals
FWHM	Full Width Half Maximum
G	Shear Modulus
GFA	Glass Form-Ability
HRXPS	High Resolution X-ray Photoelectron Spectra
K	Bulk Modulus
k_s	Reaction-Rate Coefficient at the Interface Surface
Ln	Lanthanide Metals
LTM	Late Transition Metals
M	Metal
M	# of Hydroxidant Molecules Interacted per Unit Vol. of Hydroxide Grown
MS	Melt Spun (Spinning)
N_s	Concentration of Water Molecules at the Surface of the Hydroxide
v	Poisson Ratio
PDF	Pair Density Function
PPZ	Plastic Processing Zone
Q_{Ca}	Fraction of Charge Transferred from Calcium
R	Gas Constant
R_c	Critical Cooling Rate
RH	Relative Humidity
RQ	Rapid Quenching
ρ	Density
$\rho(E_f)$	Electronic Density of States at the Fermi energy
S(Q)	Structure Function

List of Symbols

SE	Secondary Electron SEM Image Mode
SEM	Scanning Electron Microscope (Microscopy)
SIMS	Secondary Ion Mass Spectrometer (Spectroscopy)
SQ	Slow Quenching
σ_y	Yield Strength
t	Time
T	Temperature
T_b	Absolute Boiling Temperature of a Liquid at 1 atm.
TEM	Transmission Electron Microscope (Microscopy)
T_g	Glass Transition Temperature
T_l	Liquidus Temperature
T_m	Melting (Solidus) Temperature
T_x	Onset Crystallization Temperature
UHV	Ultra-high Vacuum
v_i	Volume Fraction
x	Hydroxide Thickness
XPS	X-ray Photoelectron Spectrometer (Spectroscopy)
XRD	X-ray Diffraction

Chapter 1 - Introduction

1.1 Metallic Glasses

Metallic glasses are amorphous solids. These amorphous metals are engineered alloys. In nature, non native metals are extracted from ores. Commercial alloy systems usually contain two or three principal elements and are crystalline. At the atomic level these structures are arranged in translational periodic lattices. Cooling of a liquid metal almost always results in a crystal lattice forming.

In the middle of the 20th century, it was discovered that if this rate of cooling was dramatically increased, a new disordered structure could be formed. This new frozen liquid structure, when compared to conventional metal materials, was found to have unique properties due to compositional homogeneity and an absence of atomic translational periodicity.

An amorphous solid is defined as a non-crystalline solid that lacks long range order. Amorphous solids lack a global periodic structure. They are known to exhibit short to medium range order. This order is in the local bonding between atoms and bonding of nearest neighbors. Glasses can be made with different types of atomic bonds. There are glasses with ionic, covalent, hydrogen, metallic, or van der Waals bonds.

Another characteristic of glass is that it exhibits a glass transition on cooling. The use of the term amorphous alloy originated from the fact that most metallic glasses were first formed from two or more components with a solvent metal. While most metallic glasses are alloys, there have been a few monatomic metallic glasses [1,2].

Metallic glasses can be formed by processing material from the gas, liquid, or solid state. The processing techniques in these categories include electrodeposition, vapor condensation, sputtering, ion implantation, electron beam evaporation, chemical vapor deposition, melt spinning, suction casting, injection casting, splat cooling, squeeze casting, mechanical alloying, irradiation processing, thin film diffusion, cold rolling thin foils, hydrogen induced, and pressure induced amorphization.

Within this document the terms amorphous metal, amorphous alloy or metallic glass are used interchangeably to describe a liquid metal melt that has been quenched sufficiently rapidly

to form a non-crystalline solid.

It has not been determined whether all alloy compositions can be glass formers, though through conventional rapid quench techniques the alloy space accessible is limited. Given the proper processing conditions, select alloy compositions can make metallic glasses with excellent corrosion resistance, soft magnetic behavior, high fracture strength, superior wear resistant, and other technological intriguing applicable properties. These improvements are a direct result of the amorphous atomic structure. The lack of crystalline structures means there are no grain boundaries or dislocations, thus, traditional modes of failure are not present.

1.2 Brief History of Metallic Glasses

The first metallic glass structure was directly observed in 1930 by Brill [3]. He used x-ray diffraction to examine thin films of nickel sulfur created by electrolytic deposition. These x-ray diffraction patterns were observed to be like that of liquids. There was sporadic work with metallic glass from the 1930s to 1950s [4-7]. The metallic glasses where prepared by electrodeposition and vapor quenching. They were not expressly made to be amorphous, but were the byproducts of other experiments.

The formation of the first metallic glass produced from a rapidly quenched metal melt of $Au_{75}Si_{25}$ was reported in 1960 by Duwez, Willens and Klement [8]. These amorphous foils were created by splat-quenching the binary Au-Si alloy. The foils ranged from 1 μm to 500 μm in thickness. The initial purpose of this experiment had been to obtain solid solutions from binary alloys of Cu and Ag [9]. They developed a rapid quenching technique for chilling metallic liquids at very high rates of $10^5 - 10^6$ K/s. The significance of this work was that it demonstrated a method for yielding large amounts of a metallic glass compared to other methods like electrochemical and vapor condensation. It showed for the first time that the growth of a crystalline phase could be kinetically bypassed in select alloy melts if significant cooling rates are achieved. This cooling resulted in a frozen liquid configuration. With this technique of splat cooling on a heat conductive metal cylinder [10], large amounts of amorphous foils could readily be made.

Over the following decade other metallic glasses systems were synthesized, but their sizes are limited by necessary high cooling rates. In 1969, Chen and Turnbull created ternaries of

Pd-M-Si (M = Ag, Cu, or Au) by using a ceramic tube which guided the melt during splat cooling [11]. The substitution of ceramic instead of steel tubes to guide the melt allowed for the melt to reach higher temperatures. These glasses require lower cooling rates, around 100 K/s to form glasses with thickness up to 1 mm thick.

With an increase in complexity of alloy systems, the cooling rates required for quenching decreased and allowed for the creation of thicker amorphous solids. The techniques of melt quenching were further developed and extended to produce a wide variety of metallic glasses.
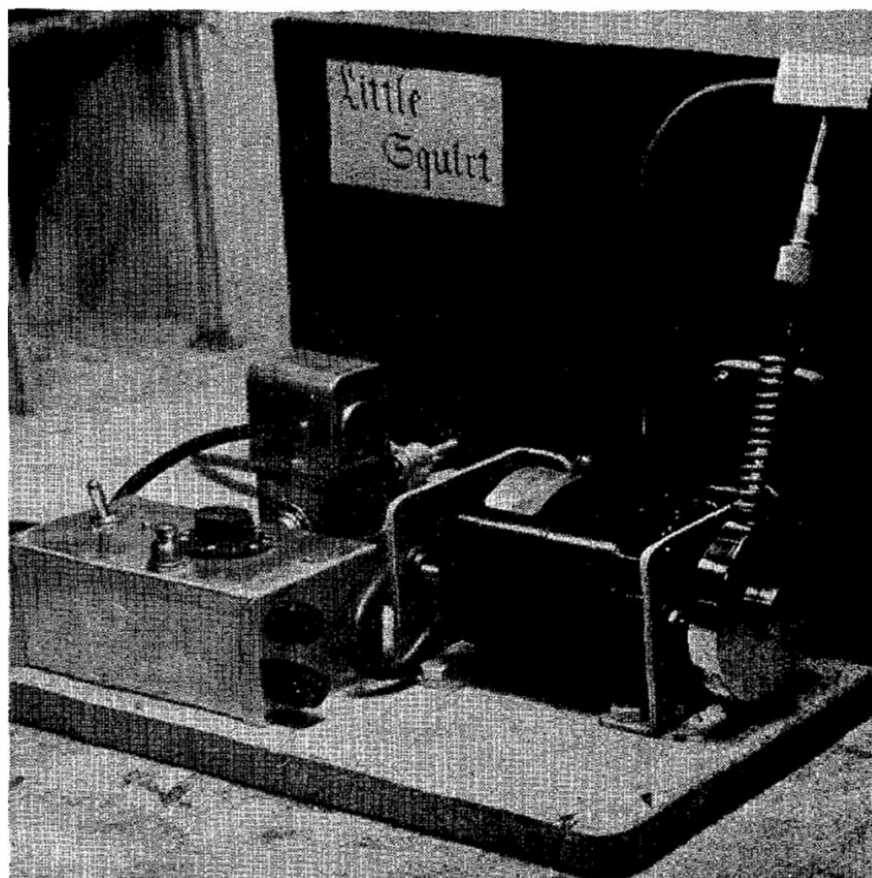
Figure 1.1. *Picture of the first ever melt spinner 'Little Squirt' created by Liebermann and Graham in 1976 [12].*

The next major step with metallic glasses was facilitated by Liebermann and Graham in 1976 with the invention of the melt spinner as seen in Figure 1.1. The device consisted of a liquid metal melt being injected on, and rapidly cooled by, a high rotational velocity spinning metal wheel.

From this point forward the field of metallic glasses expanded quickly. From the 1980s to early 1990s many groups, particularly ones headed by Inoue at Tohoku University and Johnson at Caltech, discovered multi-component La-, Mg-, Zr-, Pd-, Fe-, Cu-, and Ti-based alloys with cooling rates in the range of 1 K/s to 100 K/s [13-21]. The sizes of metallic glasses increased to 1 cm and greater. These larger glasses are bulk metallic glasses (BMG). By the late 1990s, selected BMG systems were being created up to 72 mm [20] in casting thickness. Work since then has focused on increasing the size of BMGs and understanding where in elemental parameter space these multi-component alloys lie.

1.3 General Criteria for Glass Creation

For making rapidly quenched metallic glasses, there has yet to be an all encompassing scientific law that predicts whether a particular alloy chemistry will result in forming a metallic glass. Guidelines [22-28], models [29-33], and empirical rules [34-36] for glass formation ability (GFA) have all been proposed.
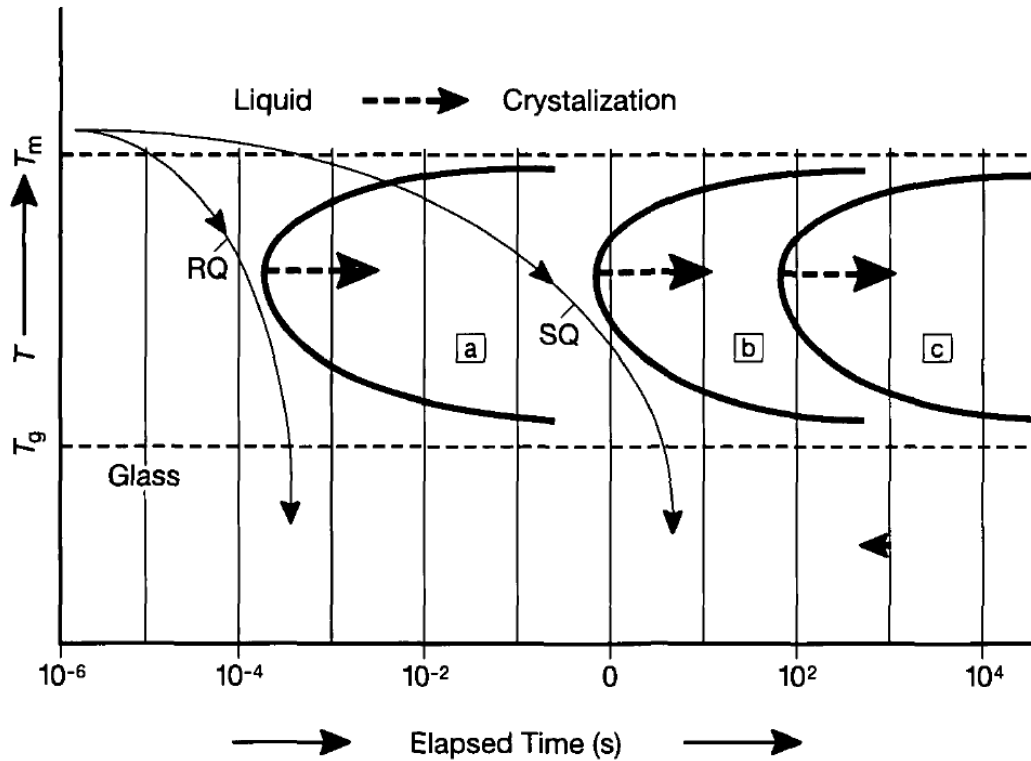
Figure 1.2. *Schematic drawing from Johnson* [37] *of a time-temperature-transformation diagram comparing the different crystallization kinetics of different quenched alloys. Curve (a) is a rapidly quenched alloy like a glass ribbon. Curve (b) is a slower quenched alloy like a splat cooled foil. And Curve (c) is a bulk-glass-forming alloy. The rapid quenching (RQ) at 10^6 K/s and relatively slow quenching (SQ) at 10^2 K/s curves are the cooling histories of these two quench rates.*

Kauzmann [22] noted that glass formation ability (GFA) improved with an increase in the glass transition temperature to melt temperature (T_g/T_m) ratio, where T_g is the glass transition temperature and T_m is the alloy melting temperature. Turnbull and Cohen [24] noted that the condition for GFA required that the ratio of T_b/T_m to be close to 2, where T_b is the absolute boiling temperature of the liquid at 1 atm. And according to Turnbull, if the ratio between $T_g/T_m=.67$ there is a range where a liquid melt can be sufficiently undercooled at a low enough cooling rate to form an amorphous state [26]. Figure 1.2, shows a schematic TTT diagram for crystallization of undercooled liquids. Nagel and Tauc [31] showed that a stable glass composition corresponds to a certain electron concentration to atomic size ratio of 1.7. Egami and Waseda [34] found that glasses form near eutectic compositions and that the minimum solute

concentration needed for a stable amorphous phase is inversely related to the atomic size mismatch. Inoue has postulated that there are three empirical rules [35] for bulk metallic glass formability: (1) multi-component alloy systems with three or more elements, (2) significant atomic size mismatch above 12% among at least the three main constituent elements, and (3) suitable negative heats of mixing among the main constituent elements. Figure 1.3 shows a proposed BMG classification system of groups based on the constituent elements outlined by Inoue. The different groups of BMG compositions are labeled I-VII. They are characterized by having constituent elements that fall into five groups on the periodic table. The five groups from the periodic table are alkaline metals (IIA), early transition metals (ETM), lanthanide metals (Ln), late transition metals (LTM), and metals from IIIB-IVB (BM). The BMG compositions are grouped by which combination of the five periodic table groups their constituent elements belong to.
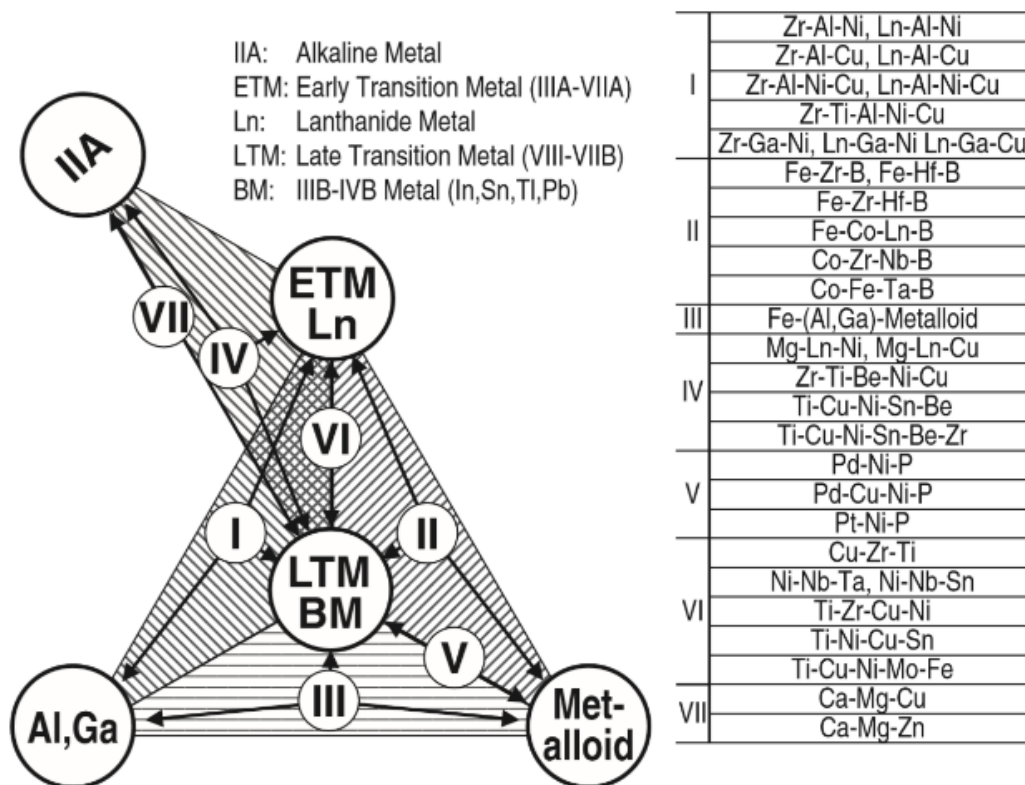
Figure 1.3. *BMG classification scheme from Takeuchi and Inoue* [38]. *There are seven groupings labeled I-VII of different BMG compositions. They are grouped on the diagram by which constituting elements they share between five different groupings, listed on the diagram, of periodic table groups.*

These guidelines, models, and rules describe most existing glasses. There are exceptions. For instance, the Pd-based BMG systems of Pd-Cu-Ni-P and Pd-Ni-P do not satisfy the empirical rules of Inoue. The heats of mixing for Pd-Cu and Pd-Ni are near zero and the atomic size ratio between the two pairs is less than 10%.

There is possibly no limit to which metallic alloys can be made into a glass. A metal could be made into a glass as long as the cooling rate is quicker than the crystallization rate. The limits would be on the size and thermal stability of the glass produced. With an ultra quick quench rate of 10^{14} K/s, observed on a high resolution transmission electron microscope, even pure nanowires of tantalum can be made into a monatomic metallic glass [2].

Increasing the known compositional space through trial and error adds to the understanding of metallic glasses. Many glass systems have been explored. Figure 1.3 shows the different BMG systems explored. It is better to understand the fundamentals of a metallic glass system and use that knowledge to predict where property specific alloys in compositional space will lie.

Numerous groups have focused on understanding the fundamentals of metallic glasses. Primarily this knowledge has been applied to understanding and predicting GFA [29, 34, 39-44]. Only recently has this knowledge been utilized to attempt to make glasses with predicted physical properties for specific applications.

1.4 Calcium Glasses

The calcium glasses that will be studied herein are not BMGs but rather ribbon foils. They are formed from melt spinning. The composition space that they occupy is vast. They are only limited by the main constituent elements for formation needing to be near a deep eutectic composition. The applied purpose for studying calcium metallic glasses is to create the lightest structural alloy.

There are several reasons for using calcium as a base for this metallic glass system. First, calcium is used abundantly in nature as a building block for structural materials. Calcium is a component necessary for all living things. It is an essential element in nature and appears frequently as a structural material in skeletons, teeth, shells, corals and stalactites.

Secondly, calcium is the fifth lightest metal with a density of 1.55 g/cc only denser than

lithium, potassium, sodium, and rubidium. While there are many Al- and Fe- based amorphous alloy systems, these are all denser than any Ca- based alloy. Al- or Mg- based amorphous alloy systems are light, but using Ca will ensure the creation of a lower density glassy alloy. For select compositions of calcium metallic glasses, its strength to density ratio is superior to Al and Mg alloys. With fracture strengths around 300-430 MPa they are in the same range as commercial Mg alloys which are at 200–400 MPa [45]. Figure 1.4 is a plot of elastic limit (yield strength, σ_y) vs. Young's modulus and shows how calcium metallic glasses relate to other materials.
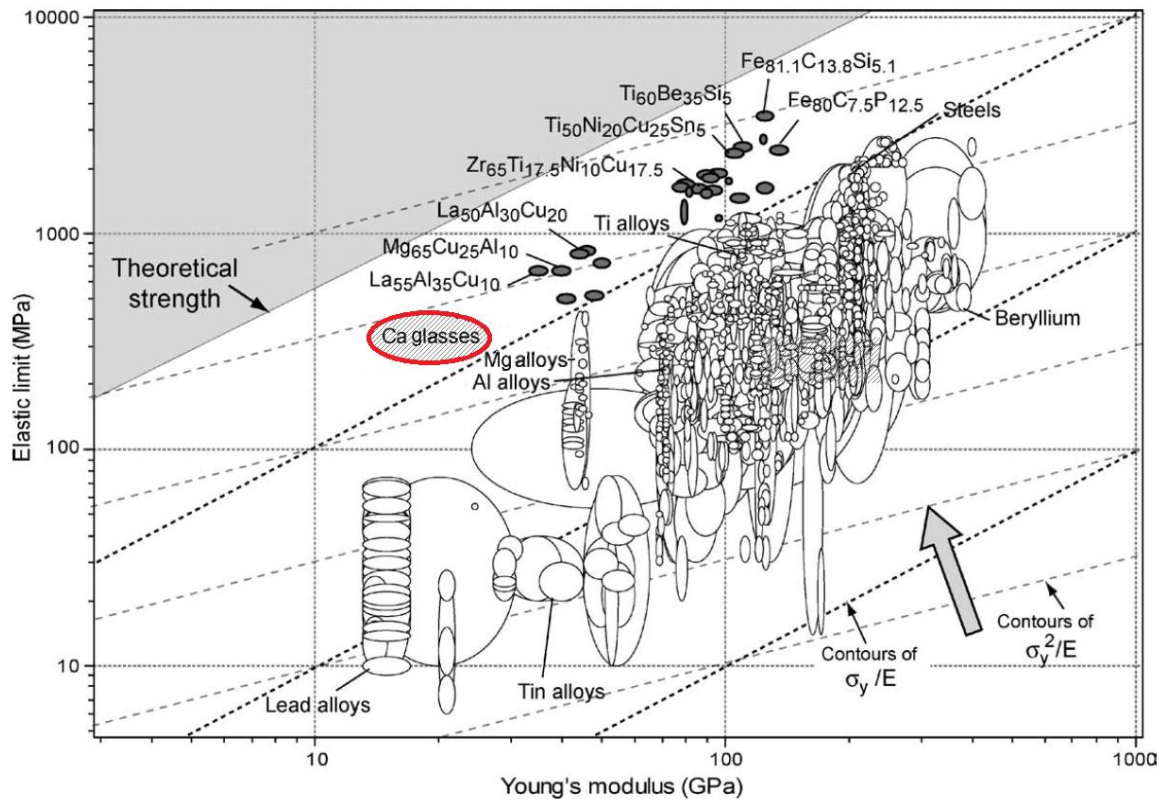
Figure 1.4. *Plot of the elastic limit (yield strength) from Ashby and Greer* [46]. *Their initial plot contains the data from 1507 metals, alloys, metal matrix composites and metallic glasses. Superimposed on the figure are data* [47] *from calcium glasses estimated to be bounded in the red oval shaded with slant lines.*

Thirdly, calcium is the fifth most common element in the earth crust at 3.6% of the weight and the third most abundant metal after aluminum at 8.1%, and iron at 5.0% wt. [48]. Calcium is not found in its pure element form in nature. Terrestrial calcium predominantly exists as limestone ($CaCO_3$), gypsum ($CaSO_4 \cdot 2H_2O$) and fluorite (CaF_2). Fortunately, calcium

compounds are readily available and can be cost effectively reduced to produce the metallic form through thermal reduction [49].

Calcium is an ideal light weight metallic glass candidate solvent constituent since it is abundant, inexpensive, and has a low density. This light weight glass would be useful in the aerospace industry or where the composition must be nontoxic for use in the human body for biodegradable structures. For these purposes, understanding and controlling the ductility of calcium glass is necessary. Most importantly, controlling alloy reaction with the environment is necessary.

1.5 Calcium Glass History

Calcium glasses were only first discovered 40 years ago. The first metallic glasses made predominantly from calcium were created in 1978 by Amand and Giessen [50]. They were able to produce several amorphous binary compositions through the rapid quenching melt-spinning technique. Calcium was alloyed with Cu, Ag, Mg, Zn or Al. The authors reported the preparation and thermal properties of these binaries.

Over the past several decades there has been periodic work on calcium metallic glasses. Through the 1980s, further work was done characterizing the electronic structure, transport and thermopower properties of the previously discovered binary systems [51-70]. The latter half of the 1980s and the 1990s consisted of further studies of the electronic properties but with ternary systems of Ca-Al-Ga, Ca-Mg-Al and Ca-Mg-Cu [70-74].

While the 1990s were a decade full of discoveries of various compositions of bulk metallic glasses, little was published on calcium metallic glass. This drought of calcium metallic glass related work ended in the 2000s when several groups turned their attention to the composition space that used calcium. With that came a flurry of publications [32, 75-90] of calcium bulk metallic glasses. The first calcium bulk metallic was the quaternary Ca-Mg-Ag-Cu reported by Amiya and Inoue in 2001 [89]. The only binary calcium bulk metallic glass, Ca-Al was reported by Gou et al. in 2004 [91].

The first corrosion work was done in 2006 by Morrison et al [92]. Their results showed that the corrosion of $Ca_{55}Mg_{18}Zn_{11}Cu_{16}$ and $Ca_{50}Mg_{20}Cu_{30}$ BMG alloys are comparable to some Fe-based bulk metallic glasses and Mg-based crystalline alloys. Other corrosion works have

followed [92-102].

Over the last decade with many calcium glass systems identified, work has turned to further explore their structure and physical properties [47, 103-115], improving fabrication processing [112, 115-119] and novel applications [115, 120-121] of calcium metallic glasses. One novel application is the delivery mechanism of Ag from the dealloying of a Ca-Ag metallic glass for use as a catalyst or sensor [121]. Another novel application is to examine calcium glasses as a hydrogen storage medium. In particular, the $Ca_{72}Mg_{28}$ glass has been studied and found to store up to 0.96 wt. % hydrogen, but it does not release hydrogen well during desorption [115].

Recently, there is a burgeoning interest in using calcium glasses as a bioresorbable material. This was based on the alloys derived from the Mg-Ca-Zn system [122]. Studies on this reabsorption have monitored the corrosion [92, 94-102] and attempt to control it [120, 123].

The research conducted on calcium glasses has thus focused on finding glassy compositions and atomic structure. Only four papers [82, 104, 106, 109] out of almost eighty papers on calcium metallic glasses have examined the elastic properties of calcium glasses. Those four papers dealt with only measuring the elastic properties of specific calcium glass compositions. No work prior to this document and a paper published with collaborators [47] has addressed predicting ductile Ca metallic glass compositions.

1.6 Ductility in Metallic Glass

Increasing the ductility of calcium glass will increase its resistance to shear failure and make it a better structural material. There is prior work on ductility in metallic glass, but the present work is the first to examine ductility applied to the calcium based metallic glasses system.

Ductility is the measure of the strain required to cause fracture. The classical shape of the stress-strain curve for a tensile tested material reveals whether a material is ductile or brittle. Ductile materials endure strain longer than brittle materials. Ductility is traditionally measured as the percent reduction in area or the percent elongation [124] measured subsequent to fracture failure. There is also the less common bend ductility test. The sample is bent over a radius of curvature. The minimum radius at which the sample can be bent without fracturing defines bend

ductility [125]. As the ratio of the radius of curvature to thickness of the glass sample increases the ductility decreases [126].

Ductility depends on the nature of the situation. In crystalline systems, ductility is dependent on low lattice resistance and multiple-slip systems from high symmetry in crystalline structures for dislocation motion. A material can transition from ductile to brittle by different mechanics. As the temperature of a metal is lowered it can become less ductile. The ductility of crystalline metal alloys is also dependent on its atomic structure and chemical bonding. The brittleness of a material can be related to the ratio of the elastic shear modulus G to the bulk modulus B. When a critical value of G/B is passed then the material is brittle.

Within this document the term ductility will be limited to bending ductility. Several variants of the bend tests [127-130] have been conducted on metallic glasses. First, there was a bend test over the edge of a razor [128]. Then there was a bent loop pinched between the platens of a micrometer [127]. Similarly, a bent loop was placed in a toolmaker vise and it was turned until the glass failed [130]. There were also the V-bend and the L-bend testing rigs built by Suto [129]. A test conducted by Sapeapen [131] consisted of the glass sample being bent over successively smaller radii of curvature until failure.

Metallic glasses lack the failure mechanisms (primarily dislocations) that allow crystalline metals to be ductile. For metallic glasses, brittleness is more common than ductility. Still there have been a number of studies [127-172] carried out on the ductile nature of select metallic glass systems.

There are several things that are thought to affect ductility. First, controlling the shear band lengths and their rate of formation has been proposed as a way of tuning ductility [172-174]. Shear bands in the metallic glass are the carriers of plastic deformation. They initiate strain softening and the glasses with limited global plasticity fail. There have been enhancements of ductility by the addition of nanocrystals which help control shear banding in select metallic glasses [171-179]. Second, replacing the elements that create ionic and covalent bonds with those that favor metallic cohesion improves ductility [163]. Third, It has been shown that the toughness of metallic glasses is related to the ratio between the shear and bulk moduli [142, 145]. The Poisson ratio $v = (3K - 2G)/(6K + 2G)$ is also a function of the shear (G) and bulk (K) modulus. Ductile metallic glasses were found to be where $G/K < 0.41$ to 0.43, and then Poisson's ratio is $v > 0.31$ to 0.32 [163]. Fourth, there is temperature induced brittle to ductile

transitions [134, 147-159]. Fifth, slight changes in composition can lead to embrittlement or ductility in metallic glasses [104, 160-165]. And sixth, changes in processing parameters like cooling rate or annealing for structural relaxation lead to changes in ductility [143-147, 180].

These mechanisms show that ductility is intrinsically related to the chemical and physical properties of metallic glass component elements. The properties of the constituent atoms matter in determining ductility. While there are ductile-to-brittle transitions with a change in temperature; for calcium glasses there is also an environmental chemical reaction induced ductile to brittle transition. It will be shown, in Section 4.2, that this is not a result of thermal relaxation, but it is indeed environmentally dependant.

1.7 Interactions Between Metals and Gas

To determine the cause for embrittlement, the interactions of the most common gases in the environment and a calcium metallic glass are examined. The most common gases are N_2, O_2, Ar, and CO_2. These four represent 99.99% of the volume of atmospheric gas. Common in the 0.01% trace are also H_2 and He. In a standard dry air composition, at 15 °C, the molar percentage of the four most common gasses are 78.09 g of N_2, 20.95 g of O_2, 0.93 g of Ar, and 0.03 g of CO_2 [181]. In addition to gases there is also water vapor. The amount of water vapor changes with relative humidity (RH) in the air. For an RH=75% at 15 °C there 0.007 pounds of water vapor per pound of dry air.

In general, there are two possible types of interactions at a metal-gas interface, either absorption or adsorption. Absorption is defined as the assimilation of molecular species throughout the bulk of a solid. Adsorption is defined as the accumulation of the molecular species at the surface rather than in the bulk of a solid. The physical process of the reaction between a metal and a gas separates into two steps, the adsorption step and then the solution step. Adsorption has two forms. One is physical adsorption and the other is chemical adsorption also known as chemisorption. Physical adsorption occurs when molecules are attached to the surface of an adsorbent by secondary valence of van der Waals forces like dipole and multipole moments. The process of physical adsorption is reversible.

1.7.1 Theory of Chemisorption

Chemisorption is the process of binding of atoms or molecules to the surface of a metal through the exchange of or the sharing of electrons between the metal and molecule. Hence, chemisorption can either be ionic type binding, covalent type binding or a mixture of both types. The process of chemisorption is often less reversible and has a high heat of adsorption.

Chemisorption precedes solution. The physics underlying physical or chemical adsorption derives from the Lennard-Jones potential energy changes occurring during the adsorption of a molecule on a metal surface. In Figure 1.5, such a potential energy curve is sketched for hydrogen and a metal.
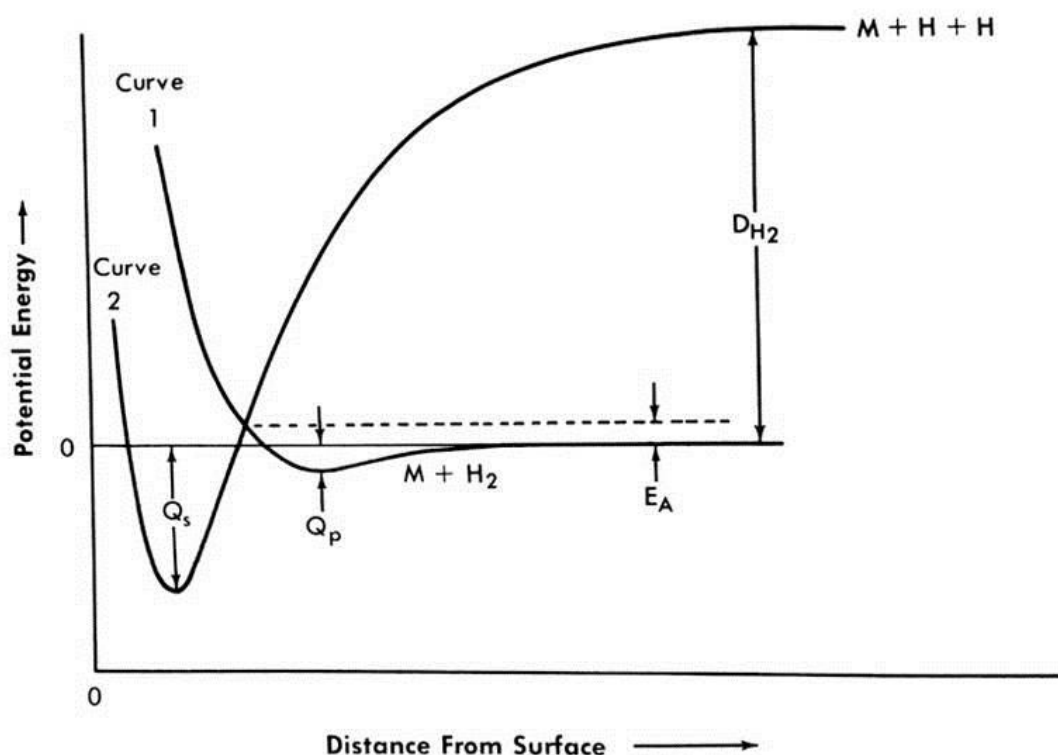
Figure 1.5. *Plotted are the potential energy curves during physical adsorption (Curve 1) and chemisorption (Curve 2) of a metal with hydrogen gas. Q_S is the heat of chemisorption. Q_P is the heat of physical adsorption. E_A is the activation energy for chemisorption. D_{H_2} is the dissociation energy of hydrogen gas. This is a diagram* [182] *which is an adaptation of the original Lennard-Jones diagram* [183].

The minimum for the physical adsorption curve (Curve 1) for hydrogen is located at 0.2 to 0.3 nm (2-3 A) [182]. This is the distance of the hydrogen molecule from the metal surface. The depth of this minimum is the heat of physical adsorption, which is 8.4 kJ, at most, for hydrogen [182]. The minimum for the chemisorption curve (Curve 2) for hydrogen is located at 0.05 to 0.1 nm (0.5-1 A) [182]. The depth of this minimum is the heat of chemisorption adsorption, which is 104.6 to 209.2 kJ for hydrogen [182]. For a hydrogen molecule to be chemisorbed it must have energy greater than the activation energy. The hydrogen molecule moves up Curve 1 towards the surface, until it shifts over to Curve 2 at the intersection. It then dissociates into monatomic hydrogen and is chemisorbed at the distance corresponding to the heat of chemisorption minimum. However, if its kinetic energy is lower than the heat of physical adsorption, then it is physically adsorbed and remains at a distance from the surface of the metal corresponding to the minimum of Curve 1.

1.7.2 Chemisorption of gases on Ca

The initial velocity of chemisorption is broken down into three categories; non-activated, activated and no adsorption below 273 K [184]. All three categories are defined in relation to the presence of chemisorption below 273 K. Fast, or non-activated, is above 77 K and below 90 K. Slow, or activated, occurs above 90 K to 273 K [184].

Trapnell determined the chemisorption activations of various gases in different metals [185]. Trapnell determined that gases of N_2, H_2 and O_2 can be chemisorbed by calcium. The activation energy of H_2 and N_2 respectively chemisorbed on Ca is 1.7-4.0 kcal/mol and 1.5-3.8 kcal/mol [185]. Calcium is initially a fast chemisorber of O_2 and a slow chemisorber of H_2 and N_2 [185]. As with most metals, after several layers of O_2 adsorption on the surface of calcium the chemisorption to a slow chemisorption rate.

For chemisorption to occur, a surface must be clean and unsaturated [184]. The melt spun metallic glass ribbons have been created in a vacuum thus providing an initial unsaturated surface.

1.7.3 Hydrogen absorbed in metals

In crystalline metals, small amounts of hydrogen can be accommodated in the host metal lattice before a structural phase change is induced [182]. Any change upon accommodation of the hydrogen must take into account the possible occurrence of a new structure or changes in the metal lattice [186].

For amorphous materials, their semi-random arrangements often create voids, where as the ordered packing of crystalline metallic alloys is denser and more efficient than disordered packing. Hydrogen has more space to ingress and to interact in the amorphous material than its crystal counterpart.

Hydrogen has a significant mobility in metals. At room temperature and below, its mobility is many orders of magnitude larger than other types of interstitially dissolved atoms [187]. High diffusivity is a consequence of the low activation energy for hydrogen diffusion. Comparing the activation of H_2 in several light metals, Ca is around an order of magnitude lower at 6.41×10^{-21} J [184] than Mg at 5.61×10^{-20} J [188] and Al at 7.53×10^{-20} J [189].

1.7.4 Hydrogen gas absorbed into calcium

Of particular interest here is the interaction of hydrogen with the calcium alloys. There is an affinity to attract hydrogen into the calcium metallic lattice [190]. The solubility of hydrogen is known to be high in unfilled d-band metals. But an unfilled d-band is not necessary for hydrogen to have a high solubility. The alkaline earth metals have the highest hydrogen affinity [190]. Figure 1.6, demonstrates that hydrogen absorption takes place in calcium. $\Delta \bar{H}_H^\infty$, the relative partial molar enthalpy at infinite dilution, is an index of the ability of the metal to absorb hydrogen freed of the complications due to hydride formation, since at a given concentration level the entropy of solution of hydrogen is relatively the same for all metals. Thus the effects of hydride formation can be neglected with respect to the solubility of hydrogen in metals.
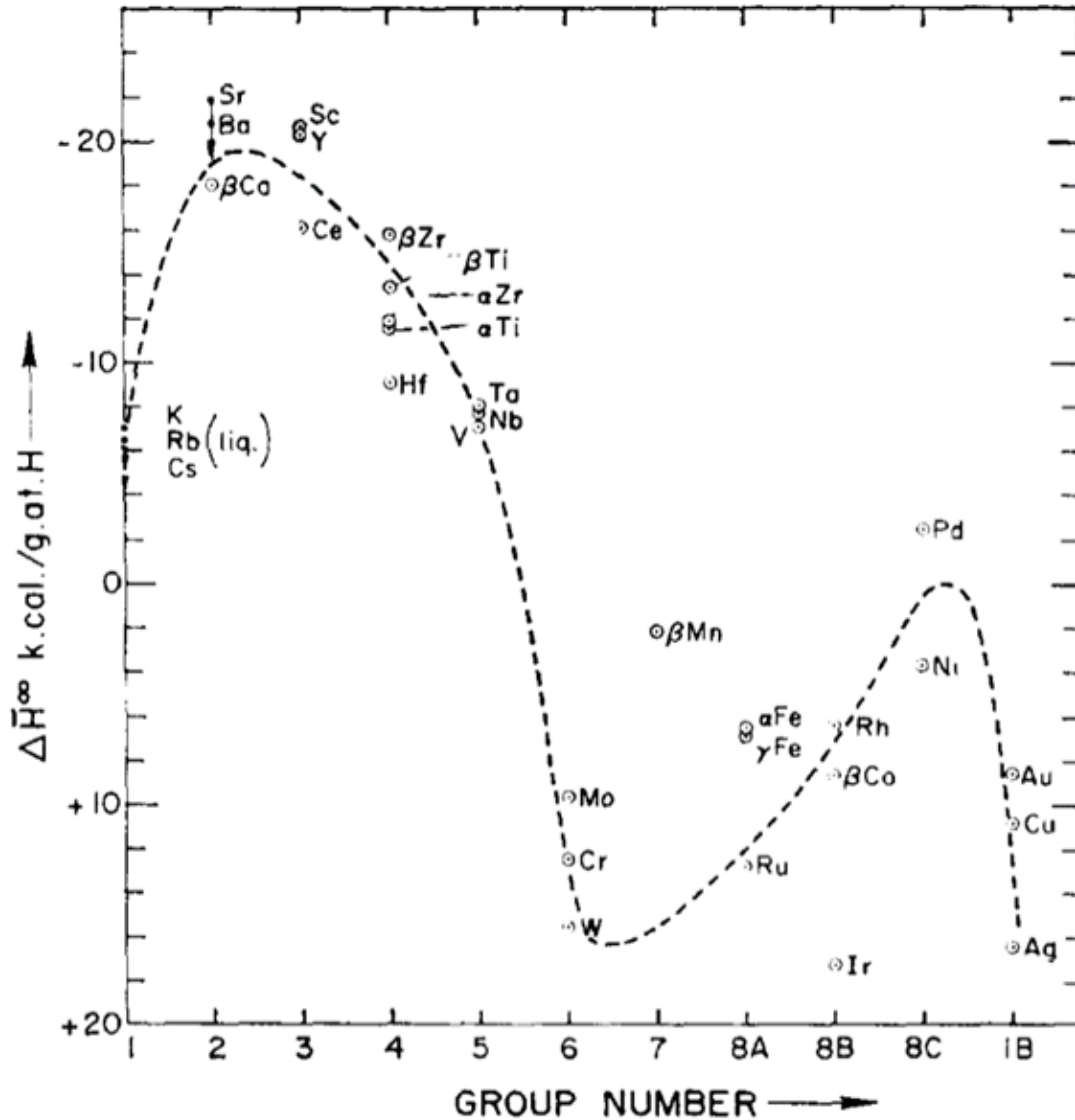
Figure 1.6. *The relative partial molar enthalpy at infinite dilution, $\Delta \bar{H}_H^\infty$, plotted with the position of the solvent metal on the periodic table. The figure is of data on the solubility of hydrogen compiled and plotted by McLellan and Oates* [190].

1.7.5 Interactions with calcium

The rate of dissociation of hydrogen in calcium is small at room temperature. The temperature needs to be at 400 °C for the process to occur rapidly in calcium [191]. It is required for H_2 to dissociate prior to reacting with Ca at room temperature. Either a significant thermal excitation or a chemical reaction would help breach this interaction barrier.

As for other interactions with calcium, there are over 100 known different calcium

inorganic and organic compounds [192]. Of these compounds only six are of interest for this study. And of the six pertinent reactions listed below, the first four are the most crucial and further elaborated on below.

1. $Ca(s) + 2H(g) < -> CaH_2(s)$
2. $Ca(s) + 2H_2O(v,l) < -> Ca(OH)_2(s) + 2H(g)$
3. $CaH_2(s) + 2H_2O(v,l) < -> Ca(OH)_2(s) + 2H_2(g)$
4. $Ca(OH)_2(s) + CO_2(g) < -> CaCO_3(s) + H_2O(l)$
5. $2Ca(s) + O_2(g) < -> 2CaO(s)$
6. $CaO(s) + H_2O(v,l) < -> Ca(OH)_2(s)$

Calcium hydride, CaH_2, is an ionic salt. It is prepared by heating calcium and hydrogen gas together. Metallic calcium that is exposed to standard lab conditions does not appreciably react with hydrogen. Calcium placed in a vacuum with purified hydrogen gas reacts slowly, but the reaction is not favored. A study in 1939 by Johnson et al. [193], shows that in a vacuum it takes days to form CaH_2 at room temperatures but if the system is heated to 250 °C it takes hours for full conversion.

Similarly, a reaction is not favored when calcium is exposed to an oxygen-rich gas environment unless the system is thermally encouraged [194]. The product of this heated reaction is calcium oxide, CaO, also known as quicklime. Though CaO is typically produced from the thermal decomposition of calcium carbonate. Calcium hydroxide, $Ca(OH)_2$, is commonly known as slaked lime. There are several ways to form it. It can be formed from the interactions of water with metallic calcium, calcium hydride, or calcium oxide.

Calcium carbonate, $CaCO_3$, also known as limestone is the natural equilibrium product of calcium. Carbonatation is the term used to describe the interaction of calcium hydroxide and carbon dioxide in the earth's environment to form calcium carbonate. It has three naturally occurring mineral forms and their space groups are: aragonite ($Pmcn$), vaterite ($P6_3/mmc$), and calcite ($R\bar{3}c$).

The calcium compounds CaO, $Ca(OH)_2$, CaH_2, and $CaCO_3$ are all ionic compounds.

1.8 Research Objectives

      The thesis research here seeks to address two separate topics that are fundamentally linked by understanding the nature of atomic bonding and its role on the ductility of the material. The first is the prediction of the ductile to brittle transitions in alloy compositions. The second is the rapid embrittlement of the ductile calcium glasses.

      This work was initiated due to the design of a calcium BMG, $Ca_{60}Mg_{15}Zn_{15}Al_5Cu_5$, that possessed good mechanical properties, had a metallic luster, and an alloy density of 2.12 g/cc. The alloy was developed for satellite applications. While this impressive glass former had good and useful properties, it was brittle.

      Only several studies have examined the elastic properties of calcium metallic glasses, but none have tried to predict these properties. To determine which calcium glass compositions are ductile, an experimental study presented in Chapter 3 was conducted concurrently with a first-principles simulation at Carnegie Mellon University. This study consists of revisiting the first produced Ca-based binary systems [50] to identify the characteristics of ductile composition systems. Once the ductile glasses were discovered, these results helped tune the molecular dynamic simulations which then predicted further alloys to be tested. This modeling approach was designed to show the parameters which create a ductile calcium metallic glass.

      Although successful, the experimental verification of ductility in the calcium metallic glass ribbons could only be measured over a short time frame. The ductility is short lived. The ductile glasses rapidly embrittle in lab conditions. It is noted that if the calcium glass is left in the melt spinner it would stay ductile longer.

      The compositional ductile study led to the second study on the embrittlement of the initially ductile glasses. This thesis is a study to unravel what led to the dramatic deterioration of properties. Only with some knowledge of what factors are responsible can a possible mitigation of the deterioration culprits be attempted.

      The hypothesis proposed is that one of the components of the atmosphere leads to the embrittlement of the calcium glass ribbon. An element of the atmosphere is proposed to be increasing the charge transferred away from calcium. For Fe-based metallic glasses substituting certain elements resulted in more metallic bond. The change in electron structure by the addition of P resulted in more metallic bonds creating a ductile metallic ribbon [163-164]. A similar path

is proposed here except that instead of substituting an element to increase ductility, an element is added from the environment that decreases ductility.

This hypothesis is also based on the ductile composition study presented in Chapter 3, showing that when the charge transfer of calcium is low, the Poisson's ratio of the alloy is high. An increase in Poisson's ratio is associated with an increase in ductility. Therefore, the lack of transferring of electrons from calcium ensures that those metallic glass alloys are ductile. and when the calcium transfers its charge the glasses are brittle.

Chapter 2 - Experimental Data Collection Procedures

2.1 Sample Preparation

The various calcium metallic glass alloys studied were prepared in a similar fashion. Elements with purities greater than 99.5% were used. Depending on the constituent elements of the alloy being fabricated, an arc melter, an induction melter, or both were employed to create the master ingot. Induction melting was used only if a low melting element with a low vaporization temperature, such as Li, Mg or Zn were a component in the alloy.

Calcium reacts readily with water vapor and must be stored in a low humidity environment. The calcium is stored in a closed container with the opening lined with Teflon tape. This container is located in a second container that is filled with a desiccant, calcium sulfate. These containers are placed in a glove box filled with Ar (99.995%). Calcium that is kept in these conditions can last for years. If the calcium is kept in only the closed container in lab conditions, it will last less than a week. If it is stored in a glove box without calcium sulfate, it will be useful for a few months.

The expiration of calcium means that when Ca is arc melted it will smoke and expel a fine layer of residue on the crucible radially from the melted ingot. Also when the master Ca alloy ingot is placed in a quartz tube and induction melted for melt spinning, the ingot will adhere readily to the quartz tube instead of collecting as a melt pool at the base of the quartz tube.

The alloy elements are weighed out to the thousandths place. The weight scale measured mass lost, was typically 0.01 g from the final master ingot, during the alloy making process which is less than 0.5% of the initial sum of the mass of the individual component pure elements used to make a 2.0g ingot.
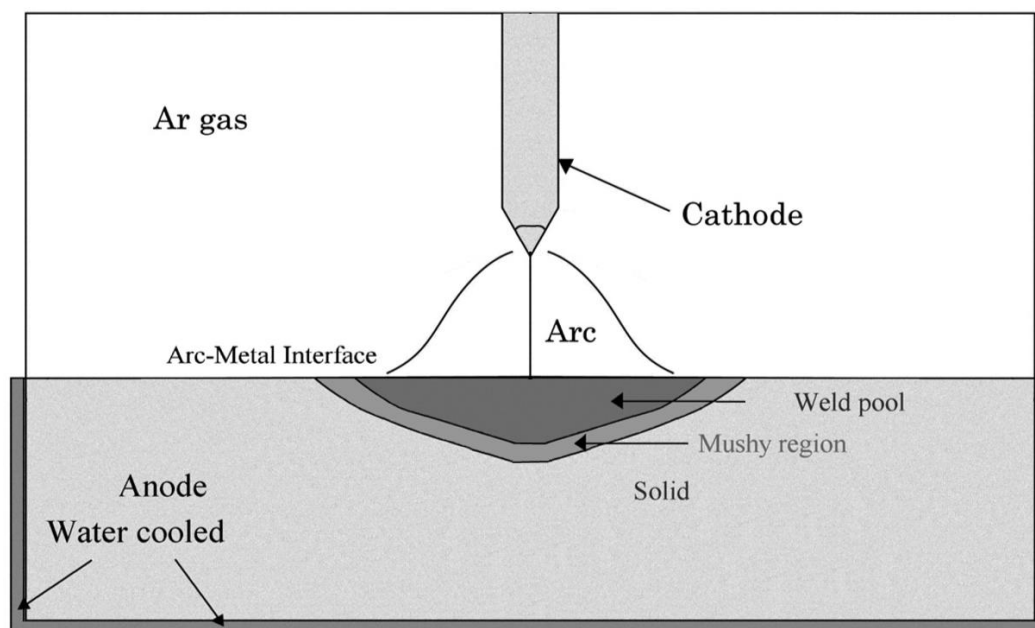
Figure 2.1. *Schematic illustration of the arc melting technique. The melt region is diagramed between the cathode and the anode. The illustration is adapted from a figure by Nishiyama [195].*

To make a ternary alloy of Ca-Mg-Al, Al and Ca are first melted in an arc melter. Figure 2.1 is a diagram of a sample being arc melted. The sample elements are placed in a water cooled copper anode crucible, in an atmosphere with in a 15 psi vacuum that has been back filled to this level with Ar gas, and then melted using a thoriated tungsten cathode. Ca and Al are alloyed first, separately from Mg. This is due to Mg having a low vaporization point. If Mg was arc melted, the loss of Mg mass would be great and uncontrollable. After the Ca and Al are homogeneously arc melted, slag from the surface of the solid button ingot is removed using a fine wire brush grinding polishing wheel. The polished button is then placed under a piece of Mg in a graphite crucible. The crucible has been coated with a boron nitride paste. The boron nitride paste acts as a barrier preventing the alloy from interacting with the graphite crucible at high temperatures. The crucible is placed in an -15 psi Ar gas environment in a radio frequency coupled induction melter and heated to approximately 800 °C.

The homogenous master ingot is then cleaned again with the wire brush. The ingots were weighed before and after each cleaning. Each cleaning resulted in no more than a 0.2% loss in mass. The material removed from the surface is a combination of oxides and solidified boron

nitride paste. These compounds all have high melting temperatures in excess of 1000 °C, thus they are not incorporated into the ingot but instead remain on the surface of the ingot.

Small pieces of the master ingot, 0.5 cm in maximum dimension, are sectioned off. Any remaining surface that was part of the outside of the master ingot is removed. This external surface layer of less than 1mm is removed to ensure that the sectioned pieces will not adhere to the quartz tube during induction melting. The pieces are loaded into a quartz tube that has been funneled at one end with an exit hole diameter of 0.5-0.8 mm. This exit hole diameter is roughly one third of the final ribbon size. The melt spinning chamber is back filled with Ar to -5 psi. The master ingot pieces are heated to approximately 500 °C. The pieces of the ingot melt at a low temperature. They do not glow. They remain metallic in appearance but they flow as a liquid.

The liquid melt is then injected with Ar pressurized at 5 psi onto a 10 cm copper wheel spinning at a minimum of 3500 rpm. This radial velocity converts to a transverse velocity of 35 m/s and this translates to a cooling rate on the order of 1000 K/s. This melt spinning process is displayed in Figure 2.2.
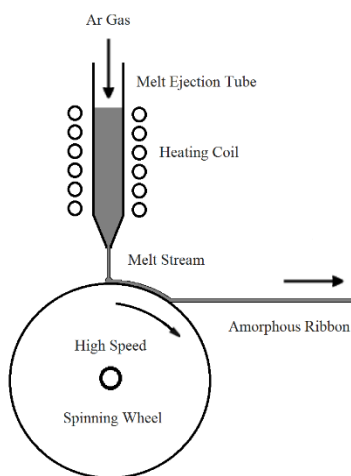
Figure 2.2. Schematic illustration of the melting spinning technique for amorphous ribbon creation.

The finished ribbons were either immediately tested or sealed in Pyrex tubes and pumped to a vacuum of 0.20 Torr. The time for processing and transferring to the vacuum is approximately 5 min.

2.2 Amorphous Nature Verification

Two methods for verifying the amorphous nature of a metallic glass are powder x-ray diffraction (XRD) and transmission electron microscopy (TEM). XRD scans are quick, but the technique has a size limitation. Samples composed of or containing nanocrystals cannot be distinguished from fully amorphous samples using this technique. To determine if a sample is fully amorphous the sample must be viewed on a TEM. A selected area diffraction pattern is needed to verify the amorphous nature.

For XRD preparation, the metallic ribbons were cut into 1 cm strips and placed on a zero diffraction plate made of optical grade SiO_2 within a 1 cm^2 area. They were adhered using double sided tape. The powder XRD patterns are collected on a Philips X'pert with a Cu K-alpha 0.154 nm source. 2θ scans were taken from 20-120° with a step size of 0.017°. The calcium alloy samples were determined to be XRD amorphous if their XRD pattern had no peaks but only a broad hump of approximately 10° in width near 2θ=30°.

To determine if the sample was truly amorphous, a diffraction pattern taken on a TEM is required. The amorphous nature would be present as a large diffuse ring in the diffraction pattern. To prepare a sample for TEM, 3 mm long pieces of ribbon were mounted on a 3 mm copper annulus with a 2 mm inner diameter using super glue. The glue was used due to the time sensitive nature of these calcium alloy ribbons. Other glues and epoxies would take too long to cure at room temperature. The heat required to cure mounting epoxies or melt wax would be enough to crystallize these ribbons. Once mounted the samples are ion milled using a Gatan 691 precision ion polishing system. The liquid nitrogen cooling finger is used to keep the sample from crystallizing during ion milling. The ribbon foil is ion milled with 5 keV Ar gas.

To ensure a clean sample void of hydrocarbons, the TEM sample holder with specimen is plasma cleaned using Ar and O plasma in the PC-2000 plasma cleaner from South Bay Technologies. The TEM work was conducted on the field emission gun FEI 80-300 Titan at 300 kV. The diffraction patterns taken in the 2000FX are taken with a camera length of 25 cm. The diffraction patterns taken in the Titan are taken with a camera length of 770 mm. Combined, the

XRD and TEM amorphous verification are required to establish whether the alloy being tested is actually a true amorphous material.

Calorimetry is also preformed to verify the amorphous nature of the calcium glasses. The glass transition temperature (T_g) and crystallization temperatures (T_x) were determined for the calcium ribbons. The ribbons were placed in Al sample pans. After being loaded with 10-15 mg of ribbon and sealed with an Al lid, the samples were placed in a Perkin Elmer DSC 7 Differential Scanning Calorimeter (DSC). The sample was held at 50 °C and then heated to 450 °C at 20 K/s. The samples were then cooled to 50°C and a second baseline scan was run. The difference in the scans produced a plot from where the T_g and T_x temperatures are extracted. The temperature results were determined using Pyris 4.0 software supplied with the DSC. An example of a calcium glass DSC curve is plotted in Figure 2.3. The T_g is measured following the ASTM E1356 [196] standard and using the inflection temperature as the T_g.
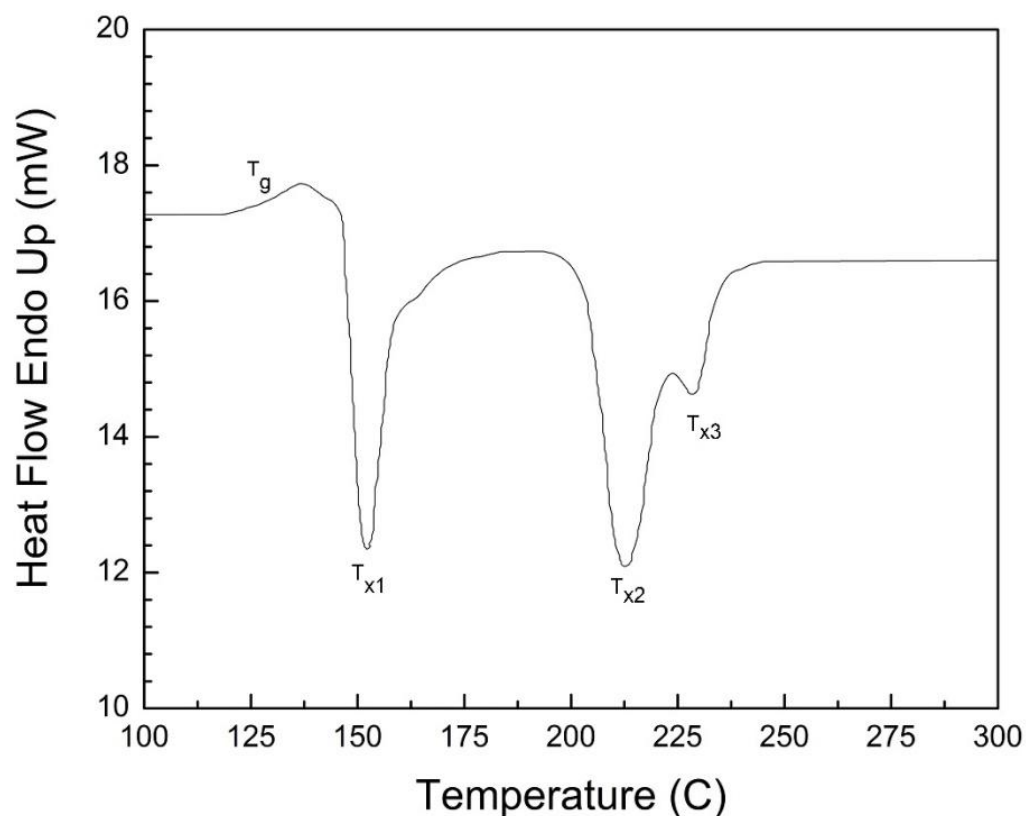
Figure 2.3. *DSC plot of metallic glass $Ca_{75}Mg_{15}Al_{10}$ ribbon tested immediately after melt spinning, with thermal events labeled. There is the one endothermic glass transition temperature T_g. and there are three exothermic crystallization temperatures, T_{xi} with i=1,2,3.*

2.3 Mechanical Testing

2.3.1 Intrinsic Ductility

Many different alloys of calcium glass, Table 3.2, were tested to determine which compositions had the best bend ductility. The ductility of the ribbons is tested immediately as they are initially exposed to lab conditions. They are handled with gloves since they are sensitive to moisture. The ribbons are taken out of the melt spinner and qualitative ductility is tested using a simple pinch test. The pinch test is illustrated in Figure 2.4. The ribbons are first bent into a loop. Then the loop is pinched. Then the ribbon is pulled taunt. If the ribbons fail during the bending of the loop they are classified as very brittle. If they fail during pinch they are labeled brittle. If they fail while being pulled taunt, they are marginally ductile. If they do not fail, then they are classified as ductile.
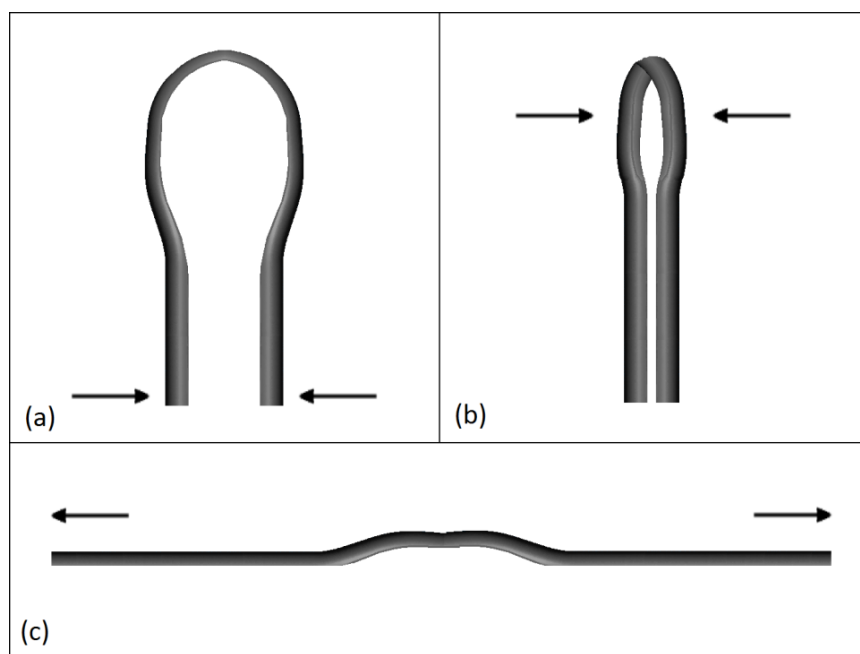
Figure 2.4. Illustration of the pinch test for determining ductility rating. When the ribbon fails during the bend in (a), then it is rated very brittle. When the ribbon fails during the pinch (b), it is rated brittle. If the ribbon fails during being pulled taunt (c) it is rated marginally ductile. When the ribbon can be pulled taunt without breaking, then it is rated ductile.

There are quantitative tests for ductility, however since this property for calcium glass is fleeting, a quick test is required. A quantitative test would take too much time to setup and prolonged exposure to lab conditions will result in the ribbons becoming brittle.

2.3.2 Extrinsic Embrittlement:

The Ca amorphous alloy ribbons which pass the bend ductility qualitative test will fail the same test after a short period of time in lab conditions. The mechanism for failure must either be gases in the atmosphere, thermal relaxation, or humidity. The relative humidity (RH) of the lab was monitored and recorded using a Traceable 4093 hygrometer with resolution of 1% and accuracy of $\pm 3.5\%$ RH. For the embrittlement of ductile alloy studies, the amorphous alloy composition $Ca_{75}Mg_{15}Al_{10}$ was chosen. It was selected due to its initial bend ductility and its ability to retain its ductility longer than binary $Ca_{72}Mg_{28}$. The binary alloy of Ca and Mg was the most bend ductile calcium glass tested, but the duration of this property was fleeting. $Ca_{72}Mg_{28}$ would remain ductile for less than a minute in average lab conditions. Adding Al decreased the relative bend ductility, but it increased the duration of that ductility to the order of tens of minutes.

To determine which condition caused the rapid failure of the ribbons, the ribbons were placed in a vacuum chamber and then back filled with +5 psi of each gas individually. The major constituents of gas listed in Section 1.7 were tested. The following gases with their listed purities were used: Ar (99.995%), CO_2 (99.9%), H (99.95%), O (99.5%), N (99.995%), and He (99.995%).

For each gas a new batch of ribbons was melt spun. Half the ribbons were placed in the pressurized gas chamber. The other half were exposed to lab conditions and tested immediately. This set of ribbons tested immediately after melt spinning created a control set that acted as a baseline for each set of ribbons that were exposed to different conditions. The test consisted of taking a 2 cm piece of ribbon and bending it over a mandrel with diameters listed below. The ribbons were tested in even intervals of time. When the ribbon broke on the mandrel the interval between testing was increased. The rate of increase depended on the time it took to fail the preceding mandrel. For instance, the first mandrel of 0.6 mm would be tested every 5 minutes. If

the ribbons were not breaking quickly, the next interval would be every 15 minutes and the following interval would be every 45 minutes etc.

After a certain time exposed to lab conditions the ribbon would become brittle and fail while being bent over the mandrel. For each test point, four pieces of ribbon were tested. Each mandrel test used a new piece of ribbon that had not been previously tested. When two of the four pieces broke, the time of failure was noted and then the next greater size mandrel was tested. The ribbons were tested over rods ranging from 0.6 to 2.48 mm. The rods used had diameters of 0.6, 0.8, 1.0, 1.13, 1.24, 1.30, 1.60, 1.66, 1.80, 1.85, 2.05, 2.34, 2.40, and 2.48 mm.

The other half of the batch of ribbons was kept in pure pressurized gas for the amount of time it took the control batch to fail two mandrel sizes. After the control batch had failed two mandrel sizes, the individual pure gas exposed ribbons were then placed in the lab environment. The ribbons were then tested in the same manner as the control batch. For their plots, the initial time recorded for these pure gas exposed ribbons was when they were first exposed to lab conditions after being removed from the gas pressurized vessel.

Two other tests were conducted. One to test for thermal relaxation and another to test for embrittlement due to humidity. The test to show if thermal relaxation caused the ribbon to become brittle was the same as the gas tests. There was one slight difference, instead of placing the ribbons in a pressurized chamber they were placed in a vacuum of 0.020 Torr with no backfilling gas employed. The baseline test is conducted in the same manner as the gas test. The test to determine if humidity causes the decay was done the same as the others except that the ribbons were held in controlled humidity environment, as illustrated in Figure 2.5.

2.3.3 Measuring Plastic Processing Zones:

As the calcium glass ribbons embrittle with exposure to lab or humidity controlled environments, there is a change in yield strength, σ. The estimate of yield strength comes from the size of the plastic processing zones (PPZ) formed on the fracture surface of tensile pulled samples.

The calcium ribbons sealed in Pyrex tubes under vacuum with Ar gas were used. Each sample is tested individually. After removal from the sealed vial, ribbon samples are mounted with super glue across the split between two aluminum test blocks. The two blocks are fixed on a

guided track. They are separated using a turn mechanism until the ribbon fractures. The section of the ribbon with the fracture surface is then mounted with super glue, normal to the surface, of a copper mount. The FEI Quanta 650 Scanning Electron Microscope (SEM) was used with beam energy of 2 kV, spot size 2, and in the secondary electron (SE) image mode. The average size of the PPZ was measured from the SE images using the linear density method used for finding the average crystal grain size.

2.4 Chemical Analysis

2.4.1 Growing and Measuring the $Ca(OH)_2$ Layer

One consequence of exposing the calcium ribbons to humidity is that different surface layers of calcium compounds grow. $Ca_{75}Mg_{15}Al_{10}$ ribbons which sat in lab air for six years had layers of $CaCO_3$ and $Ca(OH)_2$. The growth kinetics of these layers will provide insight into the embrittlement of calcium glasses. Of the two layers, the focus is on the $Ca(OH)_2$ layer and not the $CaCO_3$ layer because embrittlement will be shown to be related to the more rapidly advancing $Ca(OH)_2$. To study its growth, the ribbon samples are placed in an air tight container that has little to no input of CO_2. The isolation from CO_2 hinders the formation of $CaCO_3$. Following the ASTM E104-02 [197] standard, a relative humidity environment was created in an air tight chamber with a volume of 0.375 m^3. A 100 g water saturated $NaCl_2$ salt solution was placed in an Al pan in the sealed chamber. The chamber was allowed to come to equilibrium over the course of 24 hours. The equilibrium humidity was 75% RH at temperature of 24 °C. Figure 2.5, is sketch of this humidity test chamber.
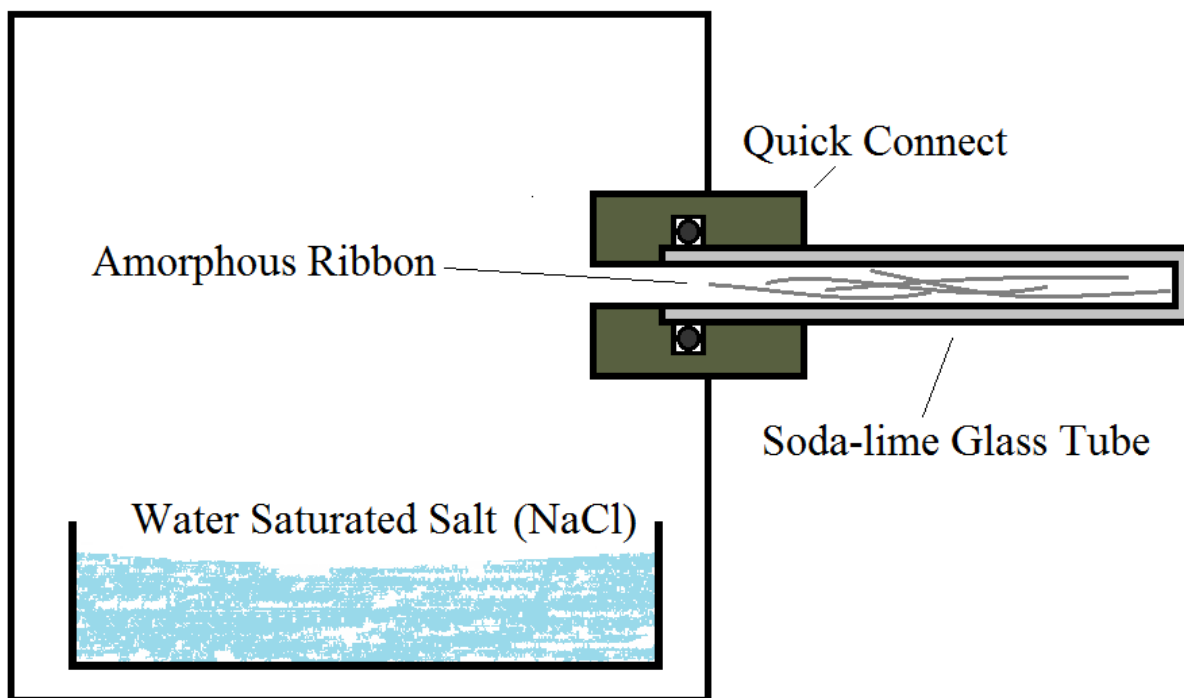
Figure 2.5. *Schematic illustration of the humidity test chamber used to expose calcium ribbons to a controlled uniform humidity before testing for the affects of this exposure. The NaCl which is saturated with water sets the level of humidity at 75% RH in the chamber by an equilibrium process between the balance of water in the solution and water in the air.*

Sealed tubes with ribbons were unsealed and then attached to the controlled humidity chamber using the quick connect feed through. The ribbons were exposed for various durations from 3 hours to 4 months. After each exposure the ribbons were sealed in Pyrex tubes under 0.020 Torr vacuum pressure. These ribbons were later examined in the SEM to measure the Ca compound layer thickness as a function of time.

Sample preparation for the SEM entailed opening the sealed tubes, and sectioning the ribbons perpendicular to their length into 5 mm long pieces on a glass slide. A new razor blade was used for each batch as the sectioning tool. The freshly cut sections were adhered with super glue to a vertical surface on the center of a copper mount instead of aluminum. An aluminum mount would have added a spurious aluminum signal to the Al Energy-dispersive X-ray spectroscopy (EDS) collection of the studied alloy containing aluminum.

The FEI Quanta 650 Scanning Electron Microscope was used with beam energy of 8 kV, spot size 6, and in the backscatter electron (BSE) mode. This corresponds with values for FEI of a beam current of 7.81 nA and a spot size of 14.5 nm. EDS spectra were taken using the Oxford Instruments X-Man^N instrument and were analyzed using Oxford AZtec software. The cut surface of the ribbon was aligned with the EDS detector. Line scans and elemental maps were taken of Al Kα (1.487 keV), Ca Kα$_{1,2}$ (3.690 keV), Mg Kα (1.254 keV), C Kα (0.277 keV), and O Kα (0.523 keV). EDS has limits. It cannot detect lighter elements like the hydrogen in $Ca(OH)_2$. Since hydrogen cannot be detected, differentiating $Ca(OH)_2$ from CaO must be accomplished with another technique. A technique that distinguishes the two by using the difference in the calcium binding energies of the compounds must be employed.

2.4.2 Hydrogen Detection

A combined X-ray Photoemission spectroscopy (XPS) and Secondary ion mass spectroscopy (SIMS) was employed since EDS cannot detect hydrogen. An illustration of this system is given in Figure 2.6. SIMS can detect the ions of all elements, including hydrogen. Elemental hydrogen analysis was conducted using dynamic SIMS. SIMS is a sensitive surface analysis technique that returns ion counts from the surface layer of atoms that are being removed by a focused Ar ion beam etching process. Dynamic SIMS was used here for obtaining compositional information as a function of depth below the surface.
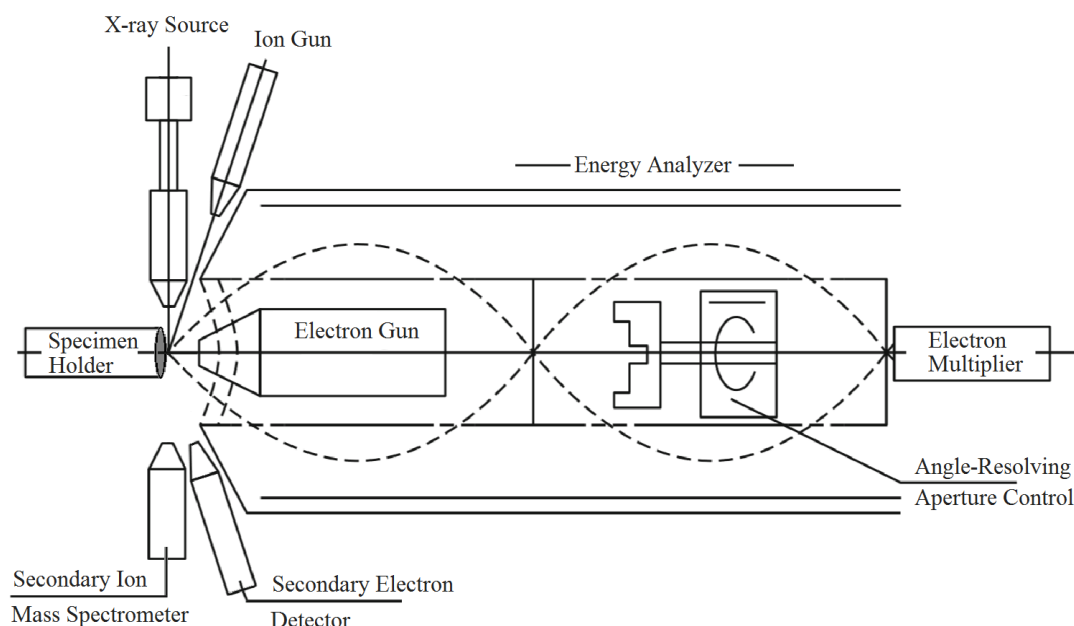
Figure 2.6. *Adapted schematic illustration* [198] *of a multi-technique surface analysis system possessing XPS, SEM, and SIMS functionality. A sample is placed on a specimen holder and positioned to be exposed directly to either x-ray radiation or ions. (1) For XPS, the sample is bombarded with x-rays, the emitted photo electrons passing through the energy analyzer are angularly resolved, and then are captured in the electron multiplier. (2) For SEM, the electron gun probes the samples surface and detector collects secondary electrons from samples surface. (3) For SIMS, Ar ions from the ion gun etch the sample. The etched ions are detected by a secondary ion mass spectrometer.*

       The SIMS ion yield is extremely sensitive to the local electronic structure of the sputtered species at the time of sputtering. Due to the effect of electronic structure from the matrix of the sample, ion yield is very difficult to quantify even with standards. This technique is used to determine the location of the hydrogen. It is also used to detect the relative amount of various elements as a function of depth. To find the relative amounts, ratios of the various ions detected were taken. Taking the ratios removed the effects of instrumental biases.

       XPS is also a surface sensitive technique providing quantitative information of the first 3-5 nm of surface composition. Chemical analysis of the $Ca_{75}Mg_{15}Al_{10}$ ribbon sample was done via XPS. XPS cannot directly detect hydrogen. It can however indirectly detect hydrogen by observing shifts in binding energy of other elements due to their bonding with hydrogen.

An XPS electron energy spectrum is acquired by collecting the electrons emitted from the sample surface. They are ejected after the interaction of impacting x-rays with the atoms of the sample. The x-rays are emitted from the Al source with energy of 1486.6 eV. The x-rays that collide with atomic core electrons knock them from their orbit and transfers energy. The emitted photoelectrons leave the surface. Their detected kinetic energy is equal to the energy of the x-ray less the binding energy of the core electron with respect to the Fermi level minus the work function of the electron spectrometer. The XPS spectra are typically plotted as counts of collected electrons versus binding energy. The spectra have a continuous background that increases with increasing binding energy. The photoelectron and Auger electron peaks are superimposed on this background. The XPS spectra were normalized with respect to the C 1s peak at 284.8 eV.

The sample preparation for XPS and SIMS involved removing the sample from the sealed quartz vial in a glove bag filled with nitrogen gas. The relative humidity in the glove bag was 23%. The sample is fitted to a 64 mm^2 area on a Cu sample holder using carbon tape. The sample holder is then placed into the XPS and SIMS system. The chamber vacuum is maintained at a pressure of 10^{-9} Torr to minimize adsorption of contaminants on the sample surface during the analysis. It is pumped with a 200 L/s ion pump and assisted by a small sublimation pump. These pumps allow the vacuum chamber to remain virtually free of hydrocarbon contamination.

The XPS collection system used, at the University of Virginia, is a Physical Electronics 560, equipped with a double-pass cylindrical mirror electron energy analyzer (CMA). The CMA is operated in constant pass energy mode during data collection. Survey spectra were measured from 0-1350 eV. High resolution spectra were collected of the Ca 2p doublet, C 1s, and O 1s peaks. The survey spectra were taken with pass energy of 200 eV. The detailed spectra were taken with pass energy of 40 eV. The corresponding energy resolutions of the two types of scan are 1.0 eV and 0.2 eV. Survey spectra took approximately half an hour to accumulate, while the high resolution spectra needs 3 hours to acquire reasonable statistics. Trial high resolution scans for Al 2s and Mg 2s were taken, but to get a significant signal to noise ratio for these spectra would increase the collection time by a minimum of threefold and thus was not feasible for this experiment.

The dynamic SIMS measurements were collected, at the University of Virginia, with a Hiden EQS 300/HAL 4 quadrupole mass spectrometer attached to a port off of the Physical Electronics 560. Ar+ ions at 4 keV were employed as incident ions to perform the sputter of the surface. The ions remove negative, positive and neutral species from the surface. This system did not allow for simultaneous collection of all species, hence the spectrometer has to be biased to collect either positive or negative ions. The SIMS spectra were collected simultaneously as the sample surface was sputtered with Ar+ ions.

Survey scan of XPS were taken after sputtering. SIMS data were acquired during sputtering. The SIMS and XPS scans were taken in alternating sequential scans. Two different collection scans were used for positive SIMS. Initially, for the powder samples, a range of masses from 0.1 amu to 75 amu was scanned. Each scan takes 2.5 min[1] and the step size is 0.1 amu. The SIMS spectra have a low flat background. There is little signal other than where on the mass spectrum the ions are recorded. To maximize relevant signal collection a second scan method was employed for the $Ca_{75}Mg_{15}Al_{10}$ ribbon sample. Windows of 0.1 amu selected around each ion of interest. The mass spectrometer dwelled for 1s at each window and took 0.1 s to pivot to the next window.

---

[1] Note on Non SI Units : Certain units used herein (min, h, d, and °) in plots and text are outside the International System of Units. But given their importance and wide use the National institute of standards(NIST) and the Committee for Weights and Measures (CIPM, Comité International des Poids et Mesures) recommends that these are accepted for use with SI units [199].

Chapter 3 - Ductile Calcium Glasses

3.1 Alloy Synthesis Data and Modeled Prediction Criteria

Calcium-based amorphous alloys can be easily produced through rapid quenching. The difficulty is determining in the myriad of systems which system will produce low density ductile metallic glass ribbons. As described in Section 1.6, a high Poisson's ratio (v) is linked to ductile materials.

Alloy compositions were selected with densities below 2 g/cc. The density was estimated assuming the specific volume of the individual species does not change. The calculated density is the sum of the contributions from the atomic percent of each element in the alloy. Table 3.1 lists compositions of amorphous ribbons verified using powder XRD analysis. However, as noted in Section 2.2.1 nanocrystals may still be present and undetected by X-rays. These ribbons were quenched using a wheel spin rate equal to or greater than 35 m/s. Additionally, DSC data taken at 20 K/s is presented for glass transition temperatures and crystallization temperatures.

Composition	ρ(gcc)	T_g(C)	T_{x1}(C)	T_{x2}(C)	T_{x3}(C)	T_{x4}(C)
$Ca_{75}Ag_{25}$	2.60	90.73	140.14	---	---	---
$Ca_{75}Al_{25}$	1.68	204.58	210.33	---	---	---
$Ca_{75}Cu_{25}$	2.17	128.69	143.29	236.30	239.48	---
$Ca_{73}Mg_{27}$	1.58	103.73	134.83	203.75	---	---
$Ca_{72}Mg_{28}$	1.58	99.43	128.27	190.22	---	---
$Ca_{60}Mg_{40}$	1.60	101.40	134.12	165.79	197.71	230.15
$Ca_{72}Zn_{28}$	2.23	109.00	128.54	---	---	---
$Ca_{75}Al_{20}Cu_5$	1.78	---	---	---	---	---
$Ca_{80}Mg_{15}Al_5$	1.59	115.4	133.42	216.86	---	---
$Ca_{80}Mg_{10}Al_{10}$	1.61	114.4	130.71	207.78	217.75	---
$Ca_{75}Mg_{22}Al_3$	1.59	109.0	133.71	236.50	---	---
$Ca_{75}Mg_{20}Al_5$	1.60	111.4	137.60	235.30	---	---
$Ca_{75}Mg_{15}Al_{10}$	1.62	134.74	152.53	211.76	229.34	---
$Ca_{75}Mg_{10}Al_{15}$	1.64	147.07	167.53	211.25	---	---
$Ca_{72}Mg_{27}Al_1$	1.59	100.07	137.75	225.47	---	---
$Ca_{70}Mg_{27}Al_3$	1.60	112.40	144.63	201.34	252.71	301.34
$Ca_{70}Mg_{20}Al_{10}$	1.63	144.40	157.57	230.04	241.27	---
$Ca_{67}Mg_{30}Al_3$	1.60	116.73	152.75	206.66	213.89	262.05
$Ca_{75}Mg_{20}Cu_5$	1.69	---	---	---	---	---
$Ca_{75}Mg_{15}Cu_{10}$	1.80	---	---	---	---	---
$Ca_{72}Mg_{27}Si_1$	1.58	104.07	137.19	154.87	182.19	216.69
$Ca_{72}Mg_{27}Y_1$	1.61	95.74	137.77	206.86	---	---
$Ca_{70}Mg_{27}Cu_3$	1.65	104.07	130.66	186.82	---	---
$Ca_{70}Mg_{26}In_4$	1.74	115.00	154.99	206.35	268.03	---
$Ca_{67}Mg_{30}Zn_3$	1.66	103.67	139.98	203.51	---	---
$[Ca_{75}Mg_{22}Al_3]_{99.7}Si_{0.3}$	1.59	110.07	135.39	240.38	---	---
$[Ca_{75}Mg_{20}Al_5]_{99.7}Si_{0.3}$	1.60	120.00	139.19	240.56	---	---
$Ca_{70.5}Mg_{27.5}Al_2Si_{0.5}$	1.59	112.07	143.02	194.00	240.43	253.1
$Ca_{69}Mg_{27}Al_2Cu_2$	1.64	110.74	138.46	199.12	---	---
$Ca_{69}Mg_{27}Al_2Zn_2$	1.64	109.07	140.08	200.54	---	---
$Ca_{60}Mg_{15}Zn_{15}Al_5Cu_5$	2.12	123.07	162.72	---	---	---

Table 3.1. *List of amorphous alloy compositions with calculated densities and experimentally measured, immediately after melt spinning, glass transition temperatures (T_g) and crystallization temperatures (T_x).*

A ductility rating for these same alloy ribbons was done using the bend pinch test. Also, estimates of effective elastic moduli were calculated using the Voigt [200] and Reuss [201] models. They are weighted means used to predict various properties. The Voigt model is for axial loading while the Reuss model is for transverse loading. These models are used to provide upper and lower boundaries for properties. It was shown that isotropic elastic moduli are bound by Voigt and Reuss models [202]. From an empirical basis these estimates are a power law average of the constituent elements, $\overline{E} = v_i E_i^{\alpha}$. The effective modulus of the composition is $\overline{E}$. The modulus of the i-th element is E_i. The volume fraction is v_i. The Voigt method applies when α=1, is an estimate of an upper bound for elastic moduli, and assumes that strain everywhere is uniform. The Reuss method is where α=-1, it is an estimate of a lower bound for elastic moduli and it assumes that stress everywhere is uniform.

Poisson's ratio was calculated from $v = (3K - 2G)/(6K + 2G)$, using the shear and bulk moduli estimates. The ductility rating and elastic moduli estimates are displayed in Table 3.2. The initial limits for ductility testing were Poisson's ratio $v > 0.31$ and density $\rho < 2.0$ g/cc. With these limits, trends from Table 3.1 and Table 3.2 are not clear. It appears that for the compositions listed, those with a lower T_g (lower T_x's) are more likely to be ductile.

Composition	Voigt				Reuss				Ductility Rating (Pinch Test)
	K (GPa)	G (GPa)	E (GPa)	v	K (GPa)	G (GPa)	E (GPa)	v	
$Ca_{75}Ag_{25}$	26.7	10.0	27.4	0.333	18.8	8.1	22.0	0.312	Very Brittle
$Ca_{75}Al_{25}$	23.7	9.5	25.7	0.323	18.7	8.1	21.8	0.311	Very Brittle
$Ca_{75}Cu_{25}$	27.3	10.8	29.2	0.325	18.4	8.0	21.5	0.310	Very Brittle
$Ca_{73}Mg_{27}$	21.7	9.0	24.2	0.318	19.0	8.2	22.0	0.312	Ductile
$Ca_{72}Mg_{28}$	21.9	9.1	24.3	0.318	19.1	8.2	22.1	0.312	Ductile
$Ca_{60}Mg_{40}$	24.4	9.9	26.6	0.321	20.4	8.7	23.5	0.313	Brittle
$Ca_{72}Zn_{28}$	23.4	11.7	30.7	0.286	18.7	8.2	22.2	0.308	Ductile
$Ca_{75}Al_{20}Cu_5$	24.4	9.8	26.4	0.324	18.6	8.0	21.7	0.311	Very Brittle
$Ca_{80}Mg_{15}Al_5$	20.8	8.7	23.3	0.317	18.3	7.9	21.4	0.311	Marginal
$Ca_{80}Mg_{10}Al_{10}$	21.2	8.8	23.7	0.318	18.3	7.9	21.4	0.311	Brittle
$Ca_{75}Mg_{22}Al_3$	21.6	8.9	24.0	0.318	18.8	8.1	21.8	0.311	Ductile
$Ca_{75}Mg_{20}Al_5$	21.8	9.0	24.2	0.318	18.8	8.1	21.8	0.311	Marginal
$Ca_{75}Mg_{15}Al_{10}$	22.2	9.1	24.6	0.320	18.7	8.1	21.8	0.311	Marginal
$Ca_{75}Mg_{10}Al_{15}$	22.7	9.3	24.9	0.321	18.7	8.1	21.8	0.311	Brittle
$Ca_{72}Mg_{27}Al_1$	22.0	9.1	24.4	0.318	19.1	8.2	22.1	0.312	Ductile
$Ca_{70}Mg_{27}Al_3$	22.6	9.3	24.9	0.319	19.2	8.3	22.3	0.312	Marginal
$Ca_{70}Mg_{20}Al_{10}$	23.3	9.5	25.5	0.321	19.2	8.3	22.3	0.312	Marginal
$Ca_{67}Mg_{30}Al_3$	23.2	9.5	25.5	0.320	19.5	8.4	22.6	0.312	Brittle
$Ca_{75}Mg_{20}Cu_5$	22.4	9.2	24.8	0.319	18.7	8.1	21.8	0.311	Marginal
$Ca_{75}Mg_{15}Cu_{10}$	23.6	9.6	25.9	0.321	18.6	8.0	21.7	0.311	Brittle
$Ca_{72}Mg_{27}Si_1$	22.1	9.4	24.3	0.314	19.1	8.2	22.1	0.312	Marginal
$Ca_{72}Mg_{27}Y_1$	21.9	9.2	24.6	0.316	19.1	8.2	22.2	0.311	Brittle
$Ca_{70}Mg_{27}Cu_3$	23.0	9.4	25.3	0.319	19.2	8.3	22.3	0.312	Brittle
$Ca_{70}Mg_{26}In_4$	22.1	8.9	23.8	0.323	19.2	8.0	21.4	0.318	Brittle
$Ca_{67}Mg_{30}Zn_3$	23.1	9.7	25.9	0.316	19.5	8.4	22.7	0.312	Marginal
$(Ca_{75}Mg_{22}Al_3)_{99.7}Si_{0.3}$	21.7	9.1	24.1	0.317	18.8	8.1	21.9	0.311	Ductile
$(Ca_{75}Mg_{20}Al_5)_{99.7}Si_{0.3}$	21.9	9.1	24.2	0.317	18.8	8.1	21.9	0.311	Marginal
$Ca_{70.5}Mg_{27}Al_2Si_{0.5}$	22.5	9.4	24.8	0.317	19.2	8.3	22.3	0.312	Ductile
$Ca_{69}Mg_{27}Al_2Cu_2$	23.1	9.5	25.5	0.320	19.3	8.3	22.4	0.312	Brittle
$Ca_{69}Mg_{27}Al_2Zn_2$	22.8	9.5	25.5	0.317	19.3	8.3	22.4	0.312	Marginal
$Ca_{60}Mg_{15}Zn_{15}Al_5Cu_5$	27.3	12.1	32.0	0.307	20.1	8.7	23.5	0.311	Brittle

Table 3.2. *List of amorphous alloy compositions with elastic properties. The Bulk (K), Shear (G) and Young's elastic moduli are calculated using the Voigt or Reuss method. The ductility rating listed was experimentally determined immediately after melt spinning.*

Estimates of elastic moduli from Voigt and Reuss methods indicate an average range bounded from roughly 18.5 - 22.5GPa for bulk moduli, 8 - 9.5 GPa for shear moduli, and 22 - 25 GPa for elastic moduli. The estimated moduli compared to the ductility ratings show no clear indicators of trends with ductility. A better model for calculating moduli is needed. One that takes into account the interactions of constituent elements. The ductility rating tests conducted here were used to help validate a simulated model of certain calcium glasses by Michael Widom's group at the Department of Physics at Carnegie Mellon University. This model accounted for the local atomic bonding in the simulated calcium glasses.

3.2 Molecular Dynamic Simulations of Calcium Glasses

The Widom model is a molecular dynamic simulation that uses the Vienna Ab initio Simulation Package (VASP) [203] to determine the solution to the many-body Schrödinger equation. VASP uses the Kohn-Sham method [204] for solving this system of equations. The Kohn–Sham method maps a system of one electron interacting particles onto a fictitious system of non-interacting particles. The non-interacting particles move in a local external pseudo potential. This potential is the sum of the external potential acting on the interacting system, a Coulomb term, and the exchange-correlation potential. The projector augmented wave potentials [205] and the generalized-gradient approximation to the exchange-correlation potential [206] are used for the simulation wave function. Using this electronic density functional theory, forces and energies are calculated that can be used to calculate elastic moduli.

The exact simulation parameters [47] included creating a system of 200 atoms confined to a cubic cell with dimensions on the order of 20 Å. After annealing the sample at 2000 K it is reduced to an equilibration temperature approximately 200 degrees above liquidus temperature, T_l. Then the sample is quenched at 1 K/fs from the equilibration temperature to 300 K and relaxed until the average forces were below 10^{-2} eV/A.

The solution of the Kohn–Sham equations for this simulation yields energies and forces for the simulated glasses. Using these results, elastic properties, charge transferred away from Ca (Q_{Ca}), electronic density of states at the Fermi energy $\rho(E_f)$, crystal orbital Hamilton population (COHP), partial pair correlation functions, charge densities, and other properties can be

calculated. Further details of the model are found in a collaborative paper [47] published with Widom. Table 3.3 contains published properties of certain modeled calcium metallic glasses like the calcium alloys presented in Tables 3.2 and 3.1. Listed in the table are the computed bulk modulus, shear modulus, Poisson's ratio, charge transfer of calcium, density of state, and the crystal orbital Hamilton population (COHP).

Composition	K (GPa)	G (GPa)	v	$\rho(E_f)$	Q_{Ca}	COHP
Ca$_3$Ag	22.4	8.2	0.34	0.88	0.071	0.68
Ca$_3$Al (Brittle)	22.7	9.5	0.32	0.90	0.102	0.88
Ca$_3$Cu	22.1	9.3	0.32	0.89	0.080	0.57
Ca$_3$Mg (Ductile)	19.7	5.7	0.37	1.07	0.054	0.56
Ca$_3$Zn	21.5	6.3	0.37	1.03	0.065	0.54
Ca$_{12}$Al$_3$Li	20.8	7.9	0.33	0.96	0.099	---
Ca$_{12}$Mg$_3$Al	20.2	6.0	0.37	1.03	0.066	---
Ca$_{12}$Mg$_3$La	19.5	5.6	0.37	1.19	0.062	---
Ca$_{12}$Mg$_3$Zn	19.9	5.4	0.38	1.07	0.057	---

Table 3.3. *Table of simulated data with bulk modulus (K) in GPa, shear modulus (G) in GPa, Poisson's ratio (v) unitless, density of states (ρ) in states/eV/atom, charge transfer (Q$_{Ca}$) in fractions of e, and the crystal orbital Hamilton population (COHP) in eV* [47].

The bulk and shear modulus contribute to the calculation of the Poisson's ratio, which correlates with ductility. The charge transfer measures ionicity and the COHP measures the covalency of the interatomic bonds. From Table 3.3, the values for COHP increase from 0.56 eV for the ductile Ca$_3$Mg system to 0.88 eV for Ca$_3$Al the brittle. COHP solely is not a good indicators since Ca$_3$Cu is 0.57 eV and it is a very brittle glass. The density of states at the Fermi energy, $\rho(E_f)$, reveals characteristics of binding. If a high density of states, then it is metallic bonding. If a low density of states, then it is covalent or ionic bonding. In Fe-based metallic glasses, density of state has been correlated with ductility [163, 207]. From Table 3.3, the trends of relating the density of states to ductility hold better than for COHP. For the ductile Ca$_3$Mg and Ca$_3$Zn alloys their values are close to each other while the brittle systems of Ca$_3$Ag, Ca$_3$Al, and Ca$_3$Cu are significantly lower.

The brittle alloys here have lower densities of states than the ductile ones. From Table 3.3, the Q_{Ca} value for the most ductile glass Ca$_3$Mg is half the value of the very brittle glass Ca$_3$Al. The Q_{Ca} trackes the ductility well, with low values associated with ductile systems and

higher values associated with brittle systems. The simulated Poisson's ratio for the ductile alloys is higher than brittle ones. A plot, Figure 3.1, of the simulated charge transfer from Ca vs. Poisson's ratio colored with ductility rating shows the clear trend. The calcium metallic glasses with higher Poisson's ratios and a low charge transferred away from calcium are more ductile, while lower Poisson's ration and high charge transfer are more brittle. Since Ca is able to keep its electrons it maintains a ductile nature due to the metallic charge distribution surrounding it.
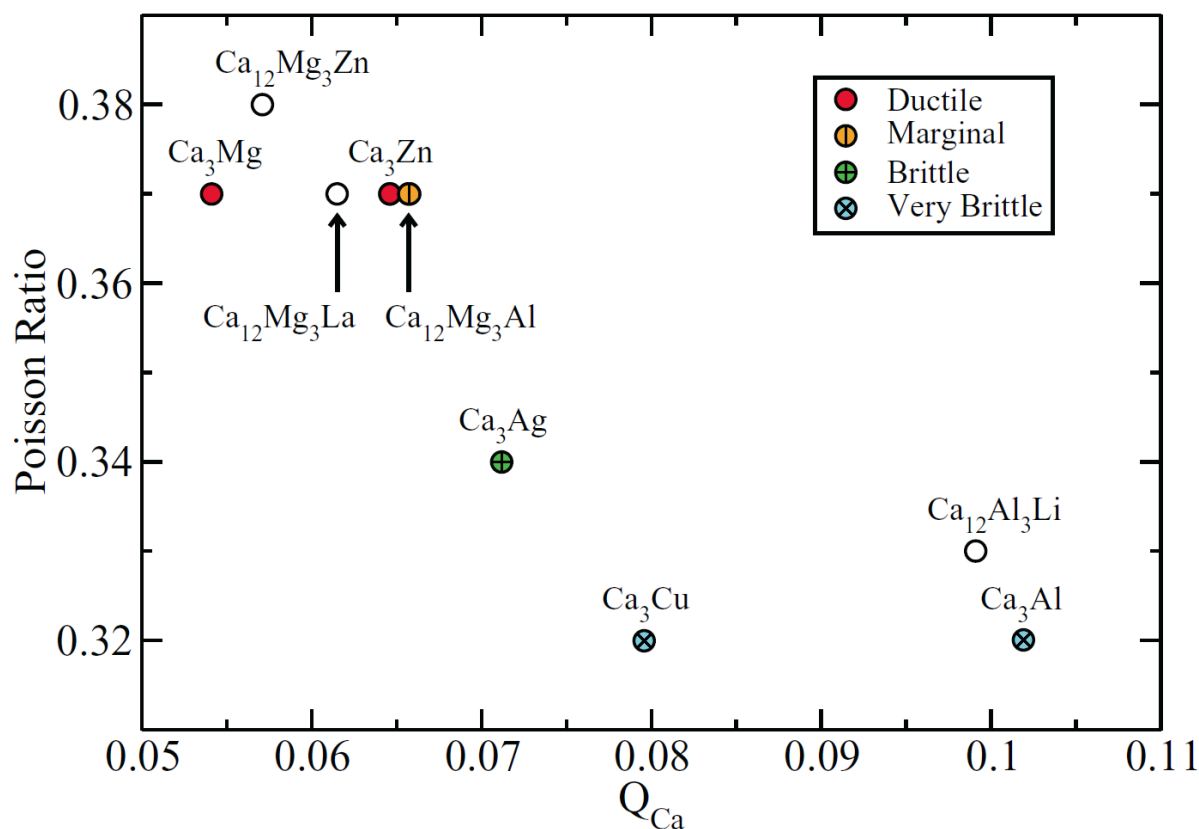
Figure 3.1. *Plot of the calculated Poisson ratios (v) as a function of charge transfer from Ca (Q_{Ca}). The experimentally tested, immediately after melt spinning, compounds are color coded from most ductile (red) to most brittle (blue)* [47].

A comparison of the Voigt and Reuss estimates of bulk and shear moduli from Table 3.2 with the Widom molecular dynamic model is presented in Figure 3.2. The bulk moduli fall within the Voigt estimate (upper bound) and Reuss estimate (lower bound). The shear values are bounded well for the brittle alloys, while for the ductile alloys the shear is over estimated by both the Voigt and Reuss methods. Difference between bulk and shear could be due to what bulk and

shear measure. Bulk moduli are a compression of atoms while shear is tangential resistance to separation. The bonding of local atoms would resist a shear force. The Voigt and Reuss methods do not account for bonding. The molecular dynamic simulations do, however, account for local bonding.
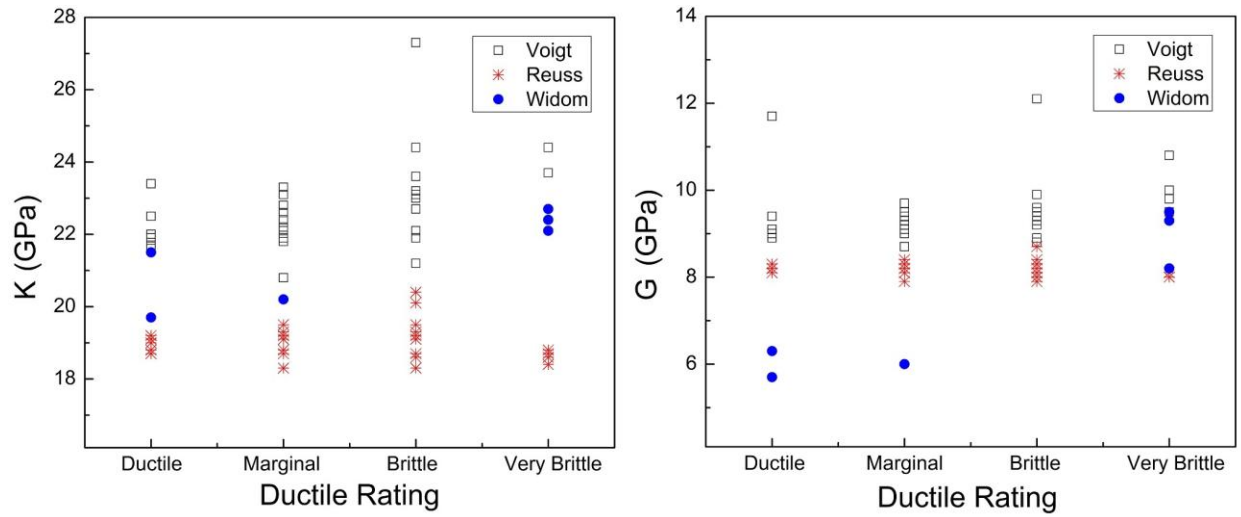
Figure 3.2. Moduli for various amorphous calcium alloy compositions are plotted against the ductility rating from their pinch test results. The plotted moduli are the bulk moduli (K) and shear moduli (G) calculated from the Voigt and Reuss estimates plotted with moduli calculated from the Widom molecular dynamic model.

Another quantity calculated from the model is formation enthalpy. The formation enthalpy is indicative of interatomic bond strength. The more negative the formation enthalpy, the stronger the bond formed. The stronger the bond between calcium and other elements the more brittle the calcium glass is. In Figure 3.3, the Ca-Al and Ca-Cu alloy systems have bond enthalpies more negative than the Ca-Mg alloy system. The amorphous structures follow this same trend. Amorphous Ca_3Mg has a positive formation enthalpy, while Ca_3Cu, and Ca_3Al have negative formation enthalpies. This further supports the link between bond strength and ductility.
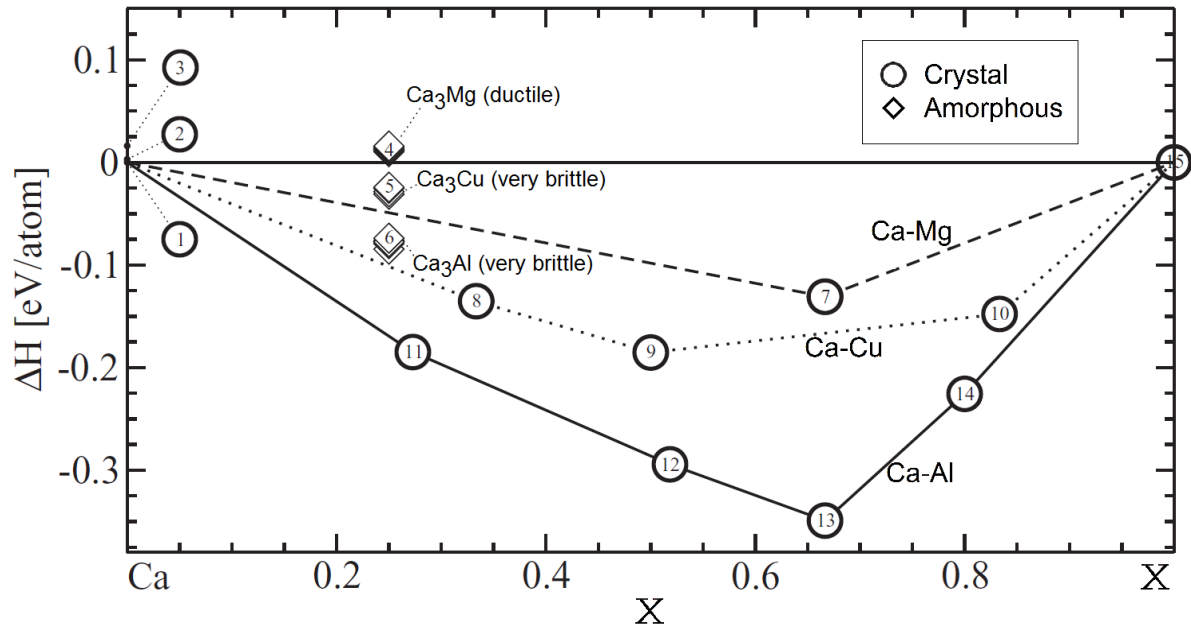
Figure 3.3. *Plots of formation enthalpies of Ca-Al (solid lines), Ca-Cu (dotted lines), and Ca-Mg (dashed lines) relative to tie-lines joining pure elements. 'X' in the plot stands for the atomic percent of Al, Cu, or Mg. The amorphous structures are plotted as open diamonds, ◇, and the crystal structures are plotted as open circles, ○. The structures types are identified by Pearson notation. The structures labeled 1–3 are elemental Ca (cF4, hP2, and cI2); 4–6 are amorphous structures (Ca$_3$Mg, Ca$_3$Cu, and Ca$_3$Al); 7 is CaMg$_2$ (hP12); 8 is Ca$_2$Cu (oP12); 9 is CaCu (mP20/oP40); 10 is CaCu$_5$ (hP6); 11 is Ca$_8$Al$_3$ (aP22); 12 is Ca$_{13}$Al$_{14}$ (mC54); 13 is CaAl$_2$ (cF24); 14 is CaAl$_4$ (tI10); 15 is elemental Mg (hP2), Cu (cF4), and Al (cF4)[47].*

Figure 3.3 is a plot of convex hull lines. The plotted lines bound all the convex sets containing the enthalpies of formation for a given alloy system. Known crystal structures of each alloy family were fully relaxed and their derived enthalpies were then plotted as a function of the composition [208].

The boundary of the convex hall is lined with stable crystal structures. The enthalpies of formation for amorphous alloys are indicated with diamond shapes. They lie above the convex hall since they are metastable states. The enthalpies of formation of Ca$_3$Al and Ca$_3$Cu are stronger than that of Ca$_3$Mg. Hence ductile Ca$_3$Mg is relatively less strongly bonded than the brittle Ca$_3$Al and Ca$_3$Cu systems.

3.3 Experimental Validation of Simulations

There were several experimental validations of this model. The first are the ductility rating results, listed in Table 3.2, from the pinch test described in Section 2.3.1. These correlate with the Poisson's ratio, density of state and charge transfers found in Table 3.3. The ductile systems have high Poisson's ratios, high density of state, and low charge transfers.

A second confirmation is of plastic processing zone (PPZ) size. PPZ are the zones created when metal ribbons are pulled apart in the tensile direction. These zone are created by the intersections of river and vein like features on the fracture surface. The average size of PPZ has been used to characterize ductile behavior [209]. The change in size and structure of the PPZ is comparable with trends noted in Fe-based calcium glasses [164, 210]. Secondary electron images of the fracture surface of $Ca_{72}Mg_{28}$, Ca_3Al, and $Ca_{12}Mg_3Al$ taken on a JEOL JSM-6700F SEM show the trend in PPZ size. From Figure 3.4, the average PPZ sizes are extracted by a semi-automated as described next in Section 4.4. The PPZ were 1.6 µm for $Ca_{72}Mg_{28}$, 0.8 µm for $Ca_{12}Mg_3Al$, and 0.2 µm for Ca_3Al. The ductility rating decreases as the PPZ decreases.
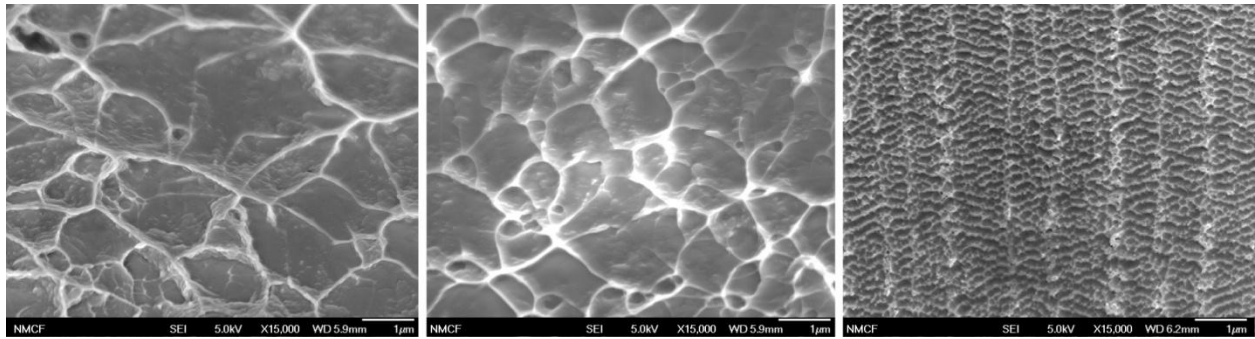
Figure 3.4. *SE SEM images of fracture surfaces from left to right of Ca₃Mg, Ca₁₂Mg₃Al, and Ca₃Al tested immediately after melt spinning* [47].

A third experimental validation of the model was conducted locally with assistance from the group of Despina Louca at the UVa Physics department. Samples of the three binary alloy ribbons Ca_3Mg, Ca_3Cu and Ca_3Al were taken to the Advanced Photon Source of the Argonne National Laboratory. X-ray diffraction data were collected on the 11-ID B beam line using a wavelength of 0.2127 Å. Louca's group processed data extracting structure functions (*S(Q)*).

Fourier transformations of the $S(Q)$ yielded the pair distribution functions (PDF). The PDF ($g_{\alpha\beta}(r)$) describe the distance between pairs of elements in a given volume. Where α and β are either Al, Ca, Cu or Mg. The results are plotted in Figure 3.5 along with the simulated PDFs from the model. For the two samples which the PDFs were created, the simulated and experimental PDFs are in agreement.
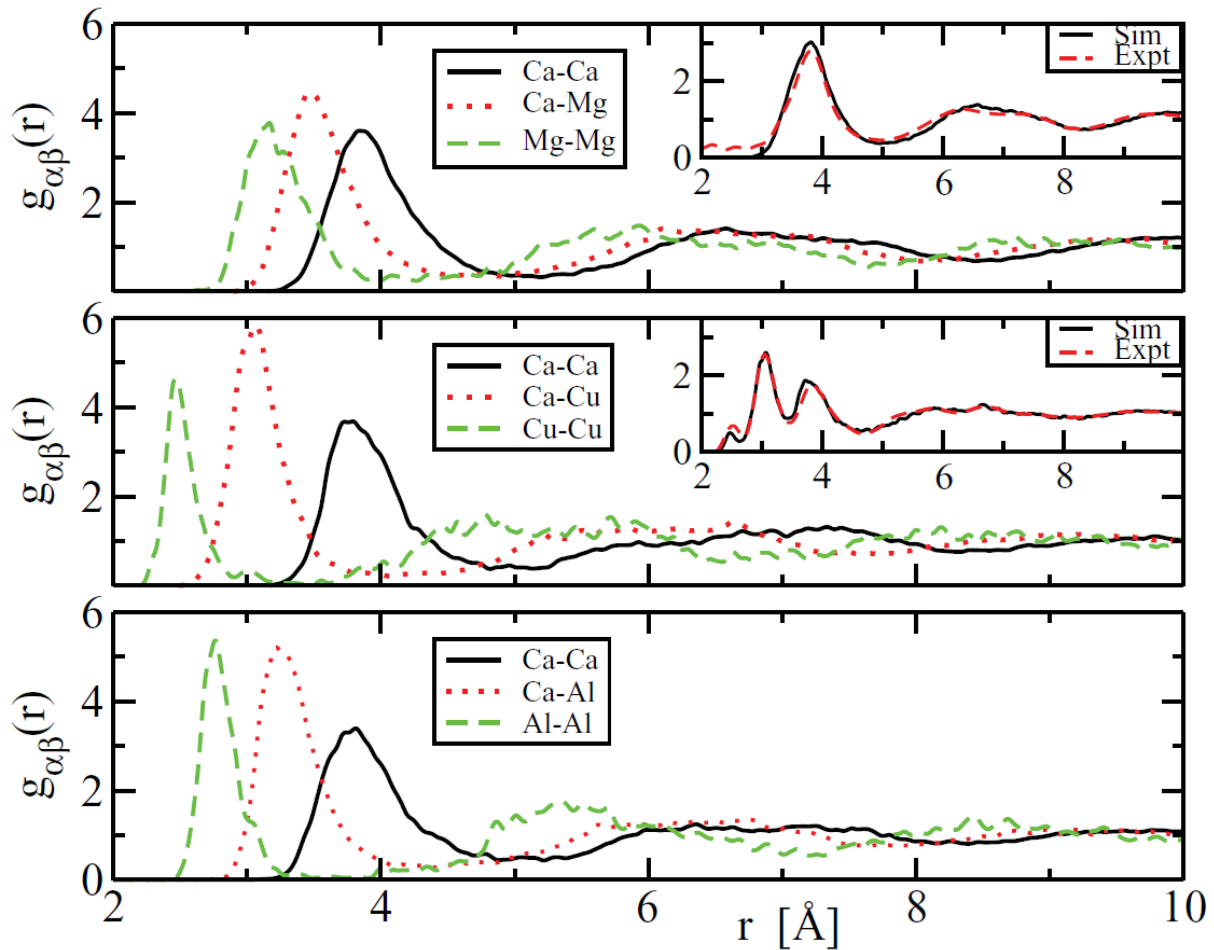
Figure 3.5. *The partial pair correlation functions from top to bottom of ductile Ca₃Mg, very brittle Ca₃Cu, and very brittle Ca₃Al glasses. These as spun ribbons were placed immediately in quartz vials before being sent for measuring. The insets for Ca₃Mg and Ca₃Cu compare the experimental RDF with the x-ray weighted sum of simulated partial pair correlation functions [47].*

Comparing the ductile Ca-Mg system to the brittle Ca-Cu system, there are less Ca-Ca bonds for Ca-Cu than for the Ca-Mg system. As expected from the modeling work, in the brittle Ca-Cu system more of the charge of the calcium is transferred.

3.4 Ductile Ribbon Embrittled

The results of the simulations tie the atomic bonding to the brittle or ductile nature of calcium metallic glass. Metallic bonds are good for ductility. Iconic and covalent bonded calcium glasses are brittle. During the pinch test conducted for assigning ductility rating, several ribbon compositions would turn from initially ductile to brittle results in the course of minutes. In particular, the ductile Ca-Mg binaries made around the $Ca_{72}Mg_{28}$ eutectic point would become marginal ductile in under a minute after being removed from the vacuum on the melt spinner.

The calcium glass ribbons do not last in the ductile state. To study this brittle to ductile transition, a composition that can maintain its ductility longer than $Ca_{72}Mg_{28}$ is needed. Adding Al to the Ca-Mg binary extend the ductile lifetime, but does increase the brittleness. Figure 3.6, shows the qualitative ductility pinch test results for several alloys tested in the Ca-Mg-Al ternary system.
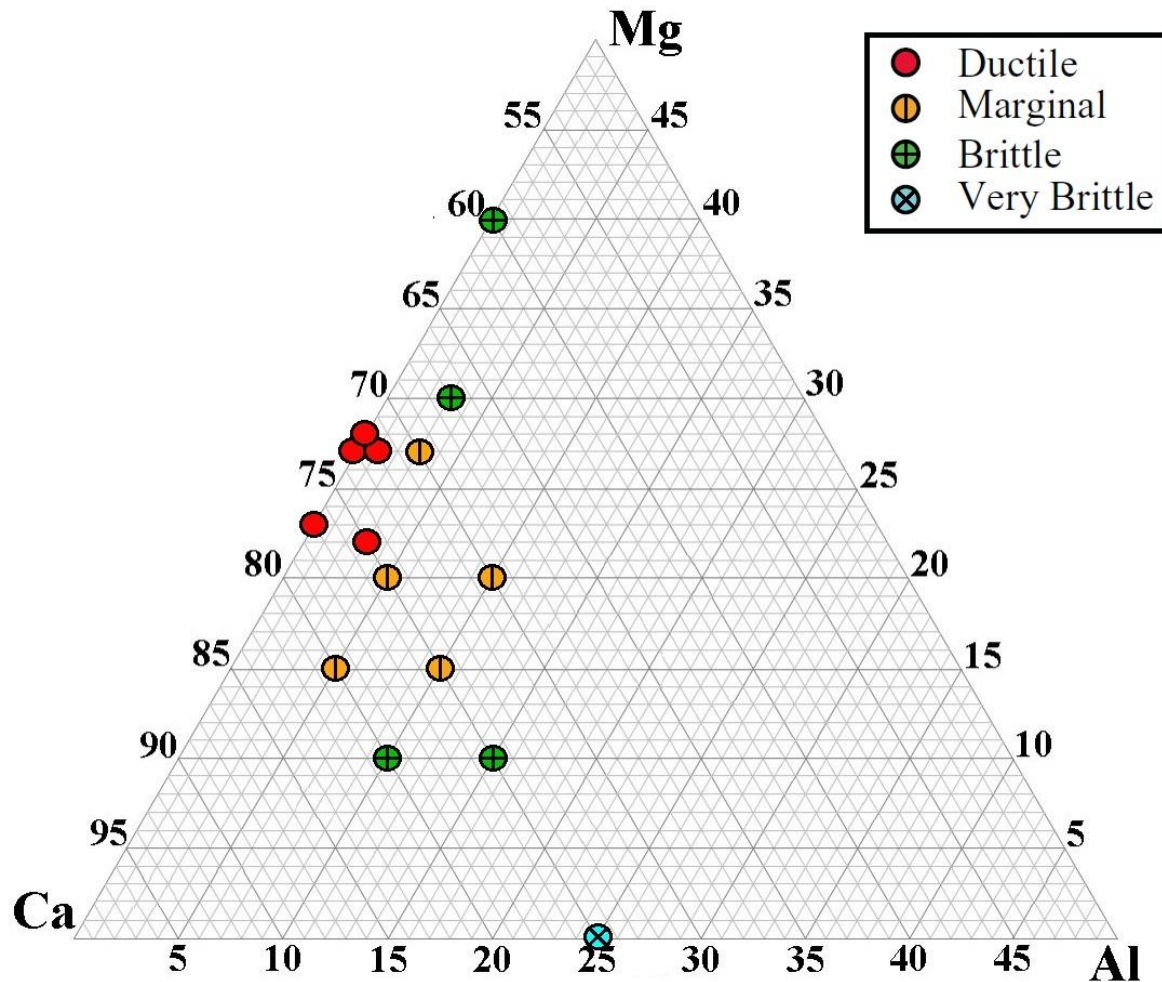
Figure 3.6. Ternary diagram of the Ca-Mg-Al system indicating amorphous compositions tested for ductility using the pinch test immediately after melt spinning. The alloy $Ca_{75}Mg_{15}Al_{10}$ was selected for further study. This composition is only marginally ductile, in that it failed the pulling taunt stage of the pinch test. However, it held this property for at least half an hour. The next part of the thesis uses this alloy to determine the mechanism that causes the embrittlement of ductile calcium metallic glasses.

The results from this chapter lay the ground work for the remaining thesis research. Similar to the strategy that that led to the composition optimization for ductile amorphous steel [164, 207], a combination of computational and experimental research resulted in ductile Ca amorphous alloys. The difficulty is the ductility is short lived. To explore the reason for this property degradation the Ca $Ca_{75}Mg_{15}Al_{10}$ is selected, based on the previous results and discussion.

Chapter 4 - Embrittlement of Calcium Glasses and Data Processing Procedures

4.1 Observations of Embrittlement

Amorphous ribbons which passed the initial pinched test became brittle within minutes. To determine the embrittlement mechanism, ribbons which had been left in ambient lab conditions for an extended period of time were examined. Ambient conditions for temperature in the lab were centered at 20.5 ± 2.0 °C; humidity in the lab initially would range from 20 to as high as 70% RH with a variance of $\pm10\%$ RH over a typical 24 hour period.

The specific alloy studied is $Ca_{75}Mg_{15}Al_{10}$. It was selected for reasons given in Section 3.4. This alloy was verified to be amorphous, Figure 4.1. The criteria demonstrating amorphicity include a diffuse ring in the selected area diffraction pattern (Figure 4.1a); a uniform TEM image; endothermic glass transition temperature (Figure 4.1c) from DSC; and a broad x-ray hump void of ancillary sharp spikes (Figure 4.1d). Over time these ribbons transform from metallic ribbons to powder.

A batch of amorphous $Ca_{75}Mg_{15}Al_{10}$ ribbons was left in an envelope, in ambient lab conditions for six years transformed from initially shiny ductile ribbons to a mixture of dull metallic brittle ribbon shards, a grey powder, and a white powder. Figure 4.2 is an optical image of these products.
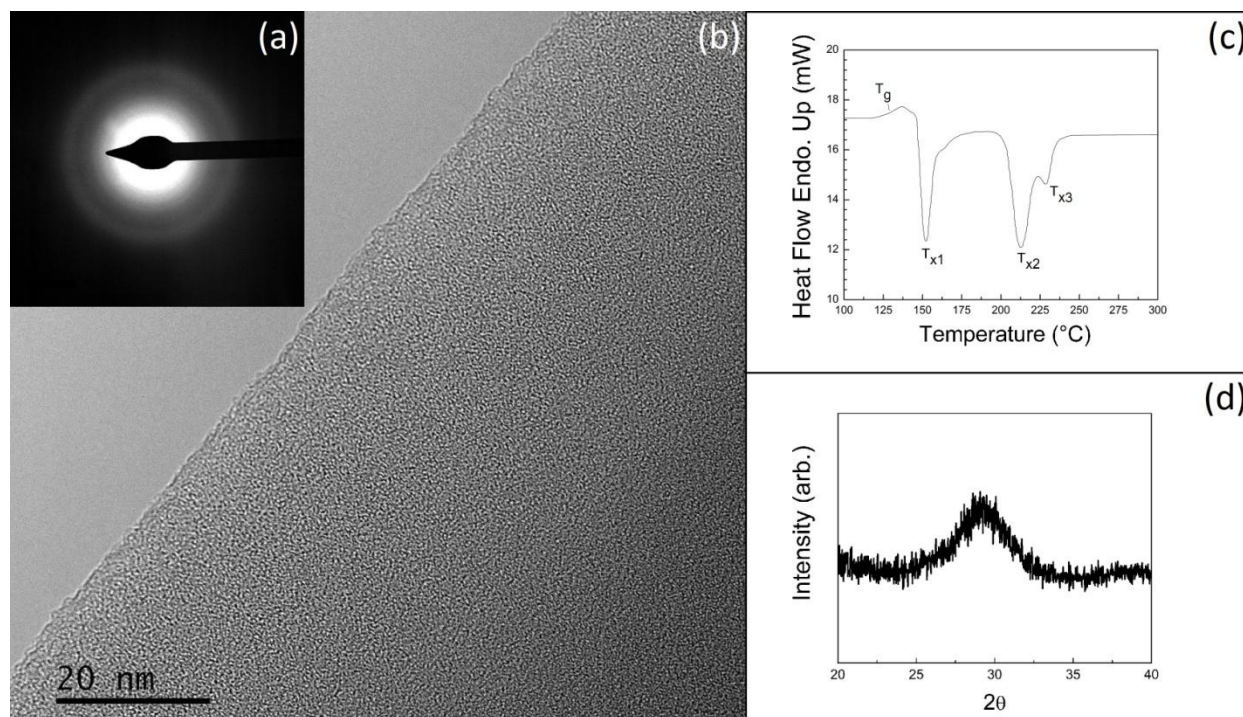
Figure 4.1. *Steps to demonstrate the $Ca_{75}Mg_{15}Al_{10}$ melt spun ribbon are fully amorphous. (a) electron diffraction pattern with circular halo and no diffraction spots; (b) bright-field TEM image, slightly under focused illustrating the mottled uniform, microstructure and no crystalline features; (c) DSC signature illustrating a T_g glass transition event and three crystallization exothermic peaks; and (d) a powder x-ray scan revealing a broad peak, similar to (a) for electron diffusion, and no sharp spikes.*
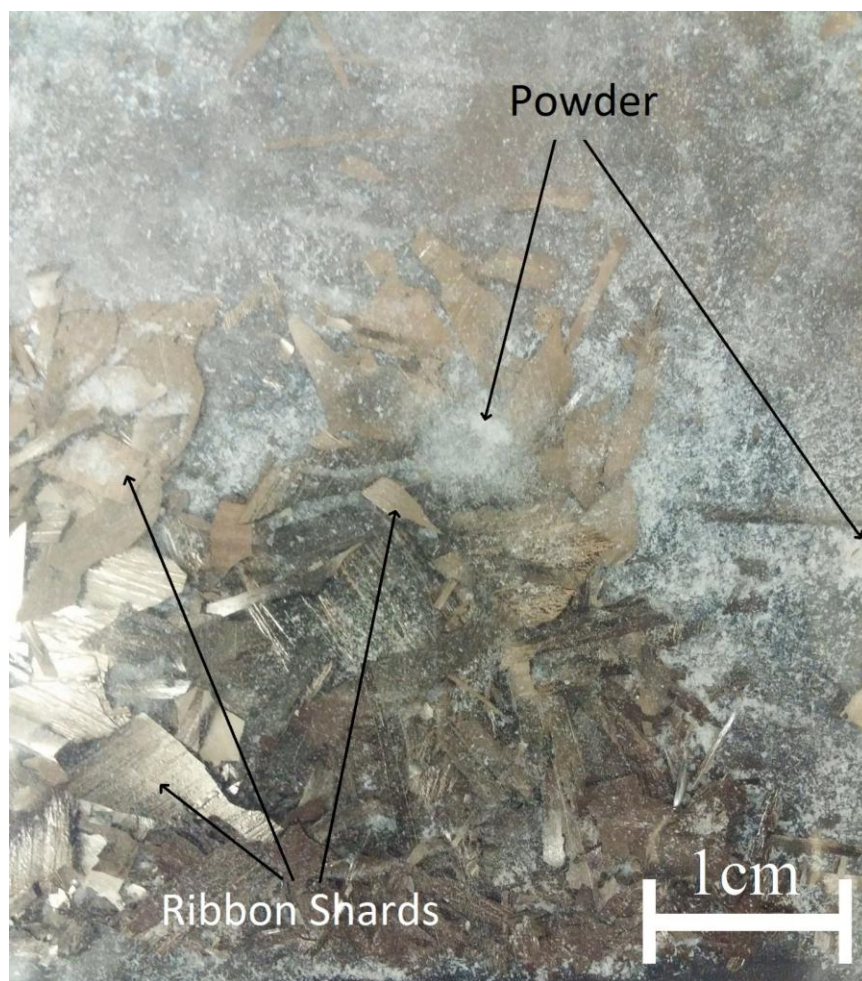
Figure 4.2. *Optical image aged ribbon exposed to 6 years of ambient lab conditions (20.5±2.0 °C, 20-70±10% RH). Here metallic ribbon shards and white powder are intermingled on top of a black background to highlight the white powder. The lower left hand corner contains a higher concentration of shards while the upper right corner has a higher concentration of powder present.*

Samples of the metallic ribbon shards and the powders were analyzed using XRD, Figure 4.3. The XRD scan of the powders exhibited peaks from calcium hydroxide and also three variants of calcium carbonate structures: calcite, aragonite, and vaterite. The XRD of the dulled metallic ribbon shards had the characteristic amorphous hump and also peaks from calcium hydroxide. Also displayed in the XRD plot for comparisons are as spun ribbons, as well as ribbons exposed to ambient lab conditions for 21 and 54 days. In XRD the as spun and the 21 day ribbons are amorphous. The ribbons for 54 days are starting to show a slight hump near $2\theta=35°$ where the main peak of $Ca(OH)_2$ is located.
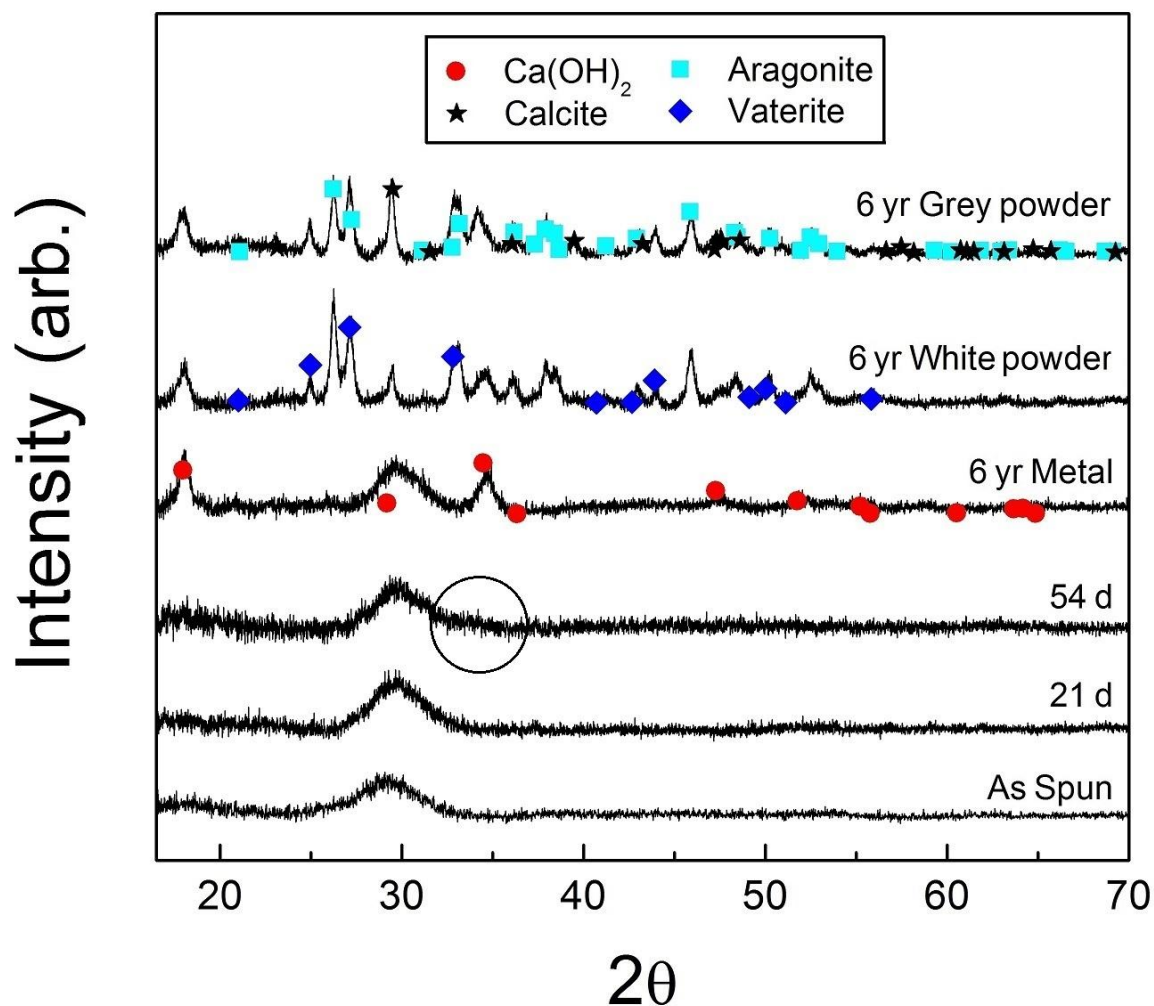
Figure 4.3. *XRD of a Ca$_{75}$Mg$_{15}$Al$_{10}$ ribbons after being exposed to ambient lab conditions for various times. The products of the interaction of the ribbons with ambient lab conditions are labeled. Aragonite, Vaterite, and Calcite are different forms of CaCO$_3$. XRD of as spun ribbons and ribbons exposed to exposed of ambient lab conditions (20.5±2.0 °C, 20-70±10% RH) for, 21 d, 54 d and 6 years. The 6 year exposed ribbons were in three products, metal ribbon shards, a grey powder, and a white powder. The circle at 2θ=35° for 54 d indicates the beginning of a peak for Ca(OH)$_2$.*

An SEM image Figure 4.4, is for a 6 year old ribbon shard exposed to ambient conditions. The shard is in cross section. The aged metallic ribbon has a metallic core between two thick oxygen rich layers, best seen in the figure with oxygen mapped in red. There is also a carbon rich layer on the surface. It will be shown from current results that the metal ribbons are growing hydroxide layers and then the hydroxide is converting to calcium carbonate. Spallation is associated with this carbonate layer. Spallation then exposes a new layer of Ca(OH)$_2$ for

conversion to $CaCO_3$. From SEM and XRD data it will be demonstrated that the ribbons in long term ambient lab conditions are converting to various forms of carbonate. The process is not yet at equilibrium since the metal cores and hydroxide layers are still in the process of being converted to calcium carbonate, even after 6 years.
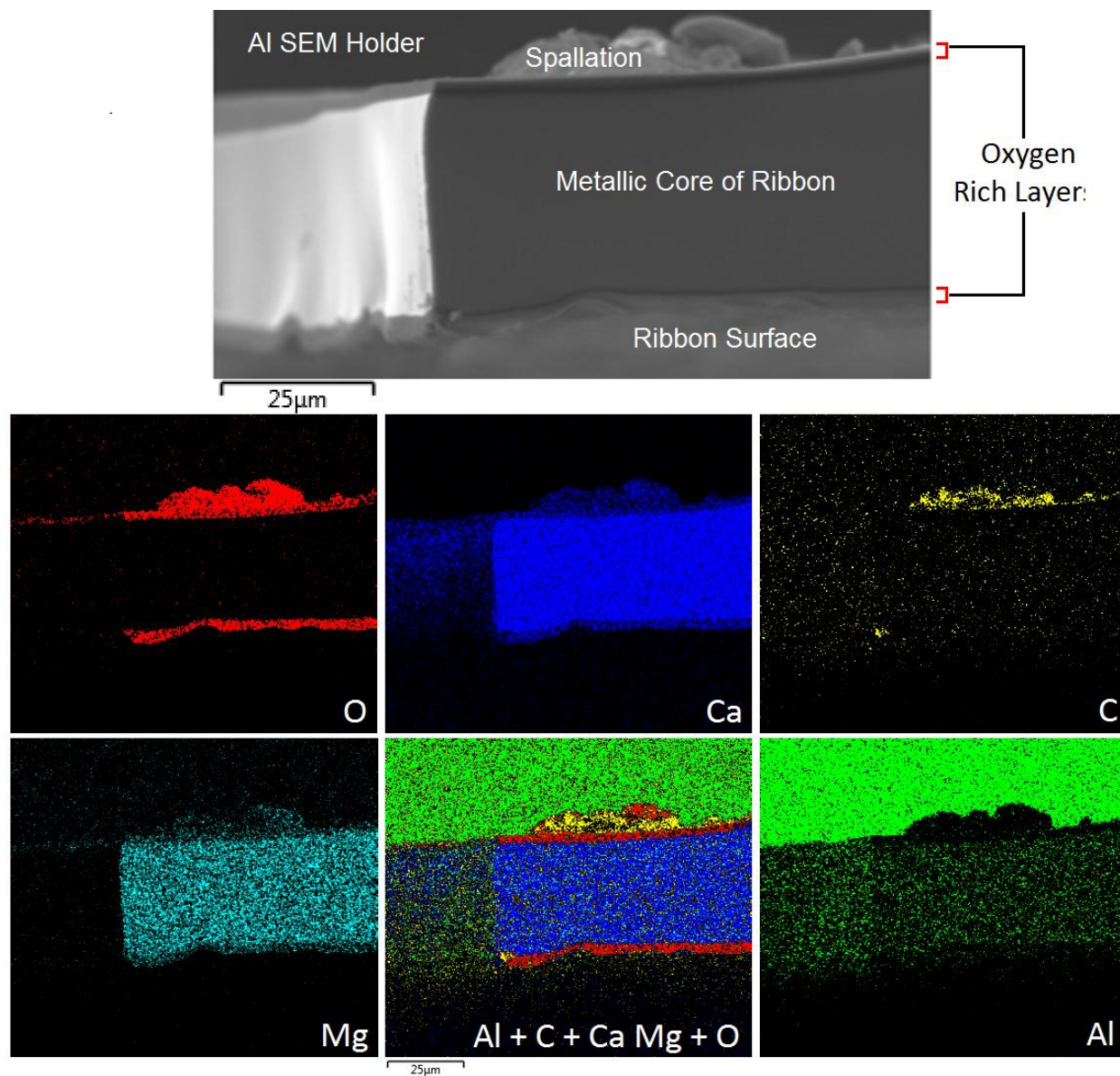
Figure 4.4. *Cross section of ribbon exposed to 6 years of ambient lab conditions (20.5±2.0 °C, 20-70±10% RH) is mounted and fixed to an Al SEM sample holder. Displayed are a BSE labeled image, an elemental EDS composite map, and individual elemental EDS maps of Ca, Mg, C, Al and O. The Al holder contributes a strong Al signal seen in the combined and Al EDS elemental maps.*

Exposure to ambient lab conditions is resulting in significant changes to the ribbons, and the exact embrittlement mechanism will be determined, analyzed, and discussed in greater detail in Chapter 5.

4.2 Testing Individual Ambient Conditions to Determine Embrittlement Condition

Since the embrittlement is occurring in ambient lab conditions, different aspects of the lab environment were isolated and examined. These included various atmospheric gasses and ambient temperature. To determine whether ambient lab conditions were affecting the ribbons the following protocol was initiated. Immediately after melt spinning, a batch of ribbons was split into two or three sets. A batch of ribbons is defined as the ribbons produced by melt spinning an initial 0.5 mg of master alloy. The sets from a batch include a control set and up to two test sets. The test sets are isolated in a quartz tube enclosure and held in either a vacuum or at a positive pressure in one of the high purity gases to be examined. The control set is tested immediately in ambient lab conditions over mandrel rods as described in Section 2.3.2. To ensure adequate testing material for the duration of each experiment, the testing intervals were increased after each mandrel size failure. The series of test before failing the mandrel can be noted in the control set data in Figure 4.5a.

The testing method is to perform bending experiments over mandrel diameters until the lab exposed ribbons (control set) failed over two different diameters. Then the vacuum set, exposed to a pure gas, would be removed from its environment and tested in a similar fashion. The time the encapsulated set spent exposed to a pure gas was about 1.5 hours before the whole set is removed from the gas and placed into lab conditions. The mandrel bending experiments were repeated. The time 'offset' between the labs exposed set and the set held in an encapsulated state is marked in Figure 4.5a where the x-axis is 'Lab Time'. The staggered start shows whether the isolated ambient condition is related to the embrittlement of the $Ca_{75}Mg_{15}Al_{10}$ glass ribbons. Holding the test condition set for the duration of two control set mandrel failures ensures that the ribbons have experienced ambient lab conditions long enough for significant measured embrittlement to occur. When the test set and the control set are compared, the spacing between failures over the mandrels would be the same if the isolated ambient condition is not a factor in

embrittlement. If the isolated ambient condition is related to embrittlement, then the initial test will show failure over multiple mandrel sizes initially.

4.2.1 Thermal Relaxation

Given this testing methodology, the first batch of ribbons is tested to show if thermal relaxation due an ambient temperature in lab environment occurred. One set of the batch was held in a vacuum of 0.01 Torr, and the control set was placed in ambient lab conditions. Holding one set in vacuum while testing the other in lab air allowed for both to experience the same thermal history.

The mandrel diameters are plotted versus the points in time when ribbons fail. For all subsequent plots testing various isolated ambient conditions, the horizontal axis is in units of square root of time. This will be useful later when linking to the hydroxide growth kinetics. Additionally, the plots of the ribbon sets held in various conditions have a time offset removed. Lab time, Figure 4.5a, is the time the ribbons exist after being removed from the melt spinner regardless of being placed in a controlled test environment or held in the lab environment. The offset between the control set and the test set is equal to the time it takes for the control set of ribbons to fail the second smallest mandrel. The difference between the lab time and offset corrected time is seen when comparing the two plots in Figure 4.5.
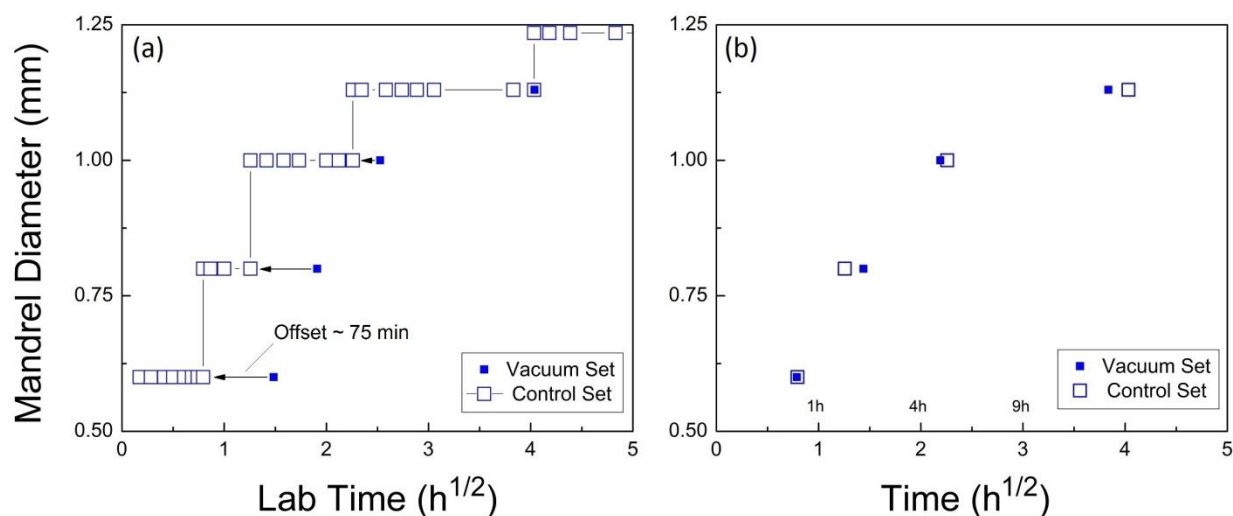
Figure 4.5. (a) Plots of the size of mandrel diameter when a ribbon break when bent over the mandrel versus total lab time. The control set is tested immediately after melt spinning is shown with open squares, □. The plot consists of a control set that only experiences ambient lab conditions and a vacuum set that is first held in a vacuum of 0.010 Torr to test for effects of thermal relaxation. The vacuum test set is shown as solid squares, ▪. This set is held in vacuum until the ribbons in the control set break when tested over the 0.8 mm mandrel. (b) The plot of the same control set data but the vacuum offset time is removed. Note the two sets now overlap.

From Figure 4.5b, the control and vacuum-held sets are seen to fail at similar rates beginning at the same time. Additional thermal information is found from a DSC scan of an as spun $Ca_{75}Mg_{15}Al_{10}$ ribbon. From Figures 2.3 & 4.1c, the DSC scan taken at 20 K/s has a glass transition at $T_g=134.74$ °C and there are three crystallization events higher than 150 °C, see Table 3.1. This T_g is typical of calcium glasses. Even though the T_g can fall in a range of temperatures dependent on the DSC scan rate, this range is well above the lab temperature of 23 °C. The thermal relaxation of calcium glass ribbons studied here is not likely to occur at lab temperature.

4.2.2 High Purity Gasses

All the gas tests were conducted similar to the thermal relaxation test. The only exception is the Ar and He tests which had the same control set, i.e., the batch used for Ar and He was divided into three sets. The Ar and He sets were encapsulated in separate containers. The control set is the third set and is shared by both gases. The other gases tested N_2, O_2, H_2, and CO_2 each have a control set which is held in ambient lab conditions and a set held in the various gases.

The gas test set was held in the high purity testing gas until the lab set ribbons failed over the second smallest mandrel test rod of 0.8 mm. The humidity in the lab (uncontrollable, but recorded) was different during each of the gas tests. The initial humidity is noted in the inset in Figure 4.9a and the would range by ± 10% over a day. Hence a different control set is needed for each gas test. The size of the mandrel that the gas sets and their control sets fail were plotted versus their total amount of time exposed to ambient lab conditions; that is, the time spent encapsulated in a test gas is not included. Only after the ribbons are released does the time start. The plots in Figure 4.6 are for all the gases tested (Ar, He, N_2, O_2, H_2, and CO_2) and they reveal that the rates of failure and start times follow the control sets once the offset time is removed.
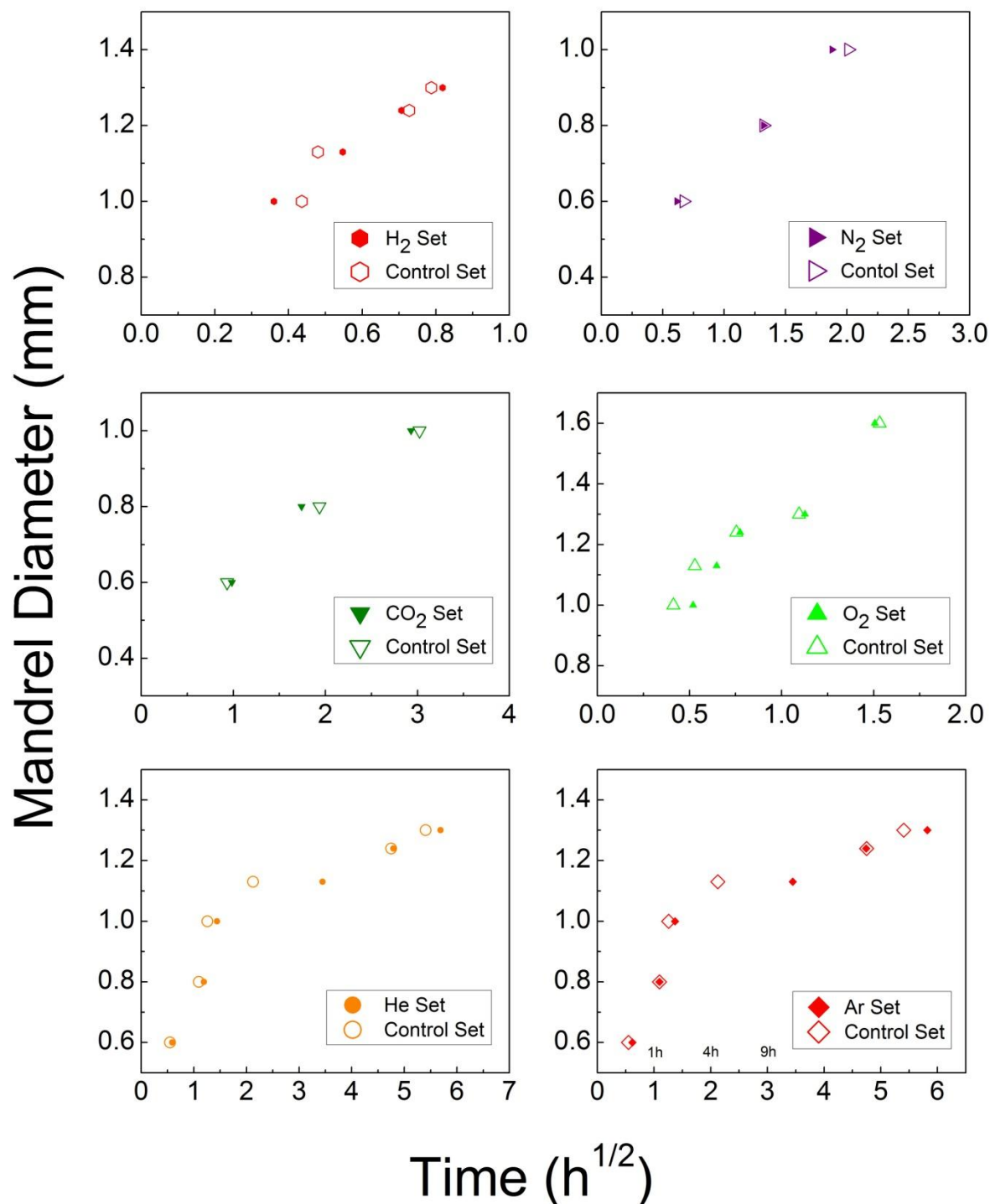
Figure 4.6. *Mandrel diameter size that a ribbon fails when being bent over the mandrel is plotted as a function of time exposed to* ambient *lab conditions for $Ca_{75}Mg_{15}Al_{10}$ ribbons. Each plot consists of a control set that experiences* ambient *lab conditions only and a test condition set that is first exposed to a gas. The test condition set is exposed to the ultra-pure gas for the time that it takes the control set to fail the first two mandrel diameter sizes. The offsets for each plot due to time the ribbons spent in a test gas are removed (see Figure 4.5).*

When the data for Figure 4.6 were collected the RH was also measured. The initial lab humidity affects the rate of failure when comparing across the various gas test control sets, as in Figure 4.9a. The starting humidity is noted for each control set. The higher the starting humidity the quicker the samples from the set fail. Figure 4.9a takes the data from Figures 4.6 & 4.8 for only the control sets along with the RH at the time of testing and replotted the data. The role of high RH and earlier ribbon failure (embrittlement) is apparent. For instance, when comparing the H_2 control test with an initial humidity of 62% to the CO_2 control test with an initial humidity of 29%, the higher initial humidity increases the higher the mandrel diameter failed at a given time and decreased exposure time to fail the same sized mandrel.

4.2.3 Humidity

      Given the results from the control sets of the gas test sets, a further experiment testing humidity was conducted. It used water saturated NaCl to create a controlled RH environment of 75%. Using a humidity monitor, the RH in the box was tested for loading and unloading a sample. The attached tube had a volume 0.1% of the volume of the chamber. The tube was attached and then disconnected using a quick-connect feed through. The variation caused by the addition of the tube was at most RH=1%, and took approximately 10 min to return to equilibrium humidity, as seen in Figure 4.7.
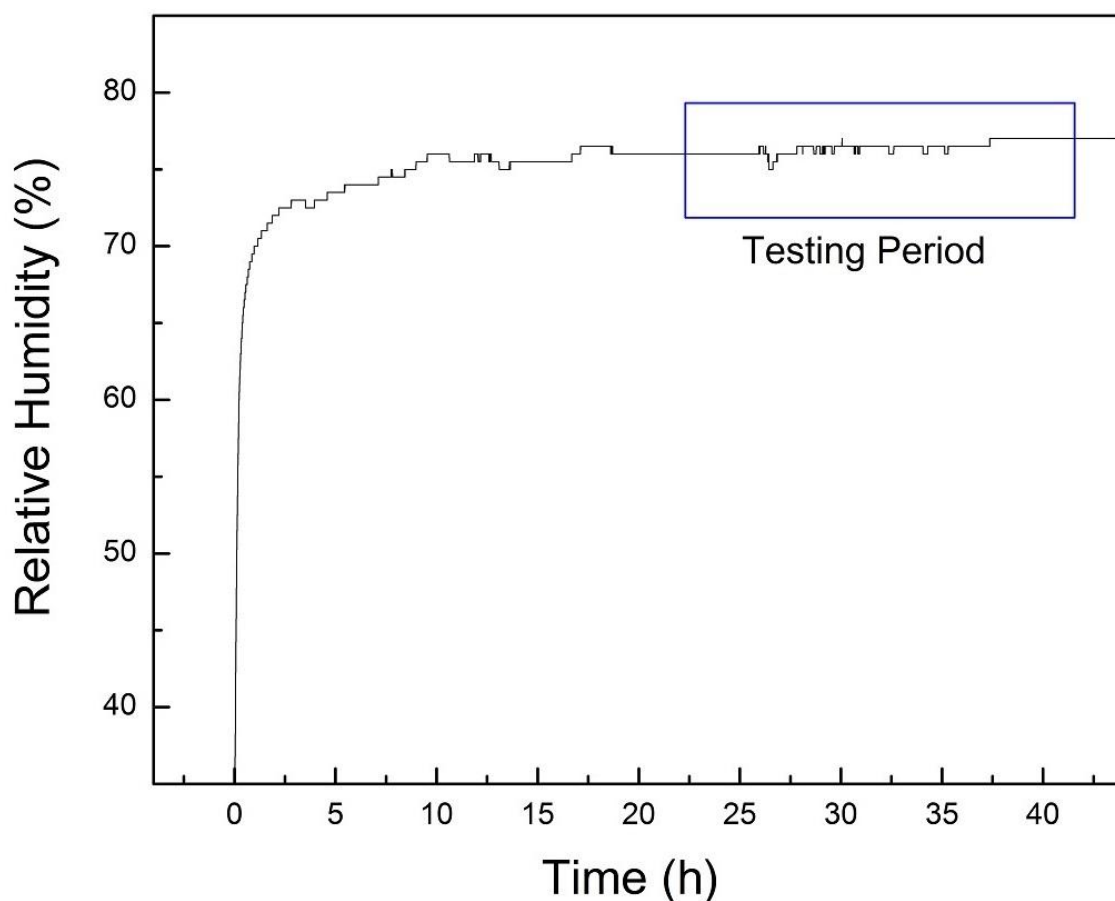
Figure 4.7. *Plot of the humidity measured in the salt chamber device used to control humidity at 75% RH as a function of time from when the water saturated salt is first added to the test chamber to the time when samples are loaded and unloaded for testing. The sample testing period is highlighted to show the relatively small variance in humidity during testing.*
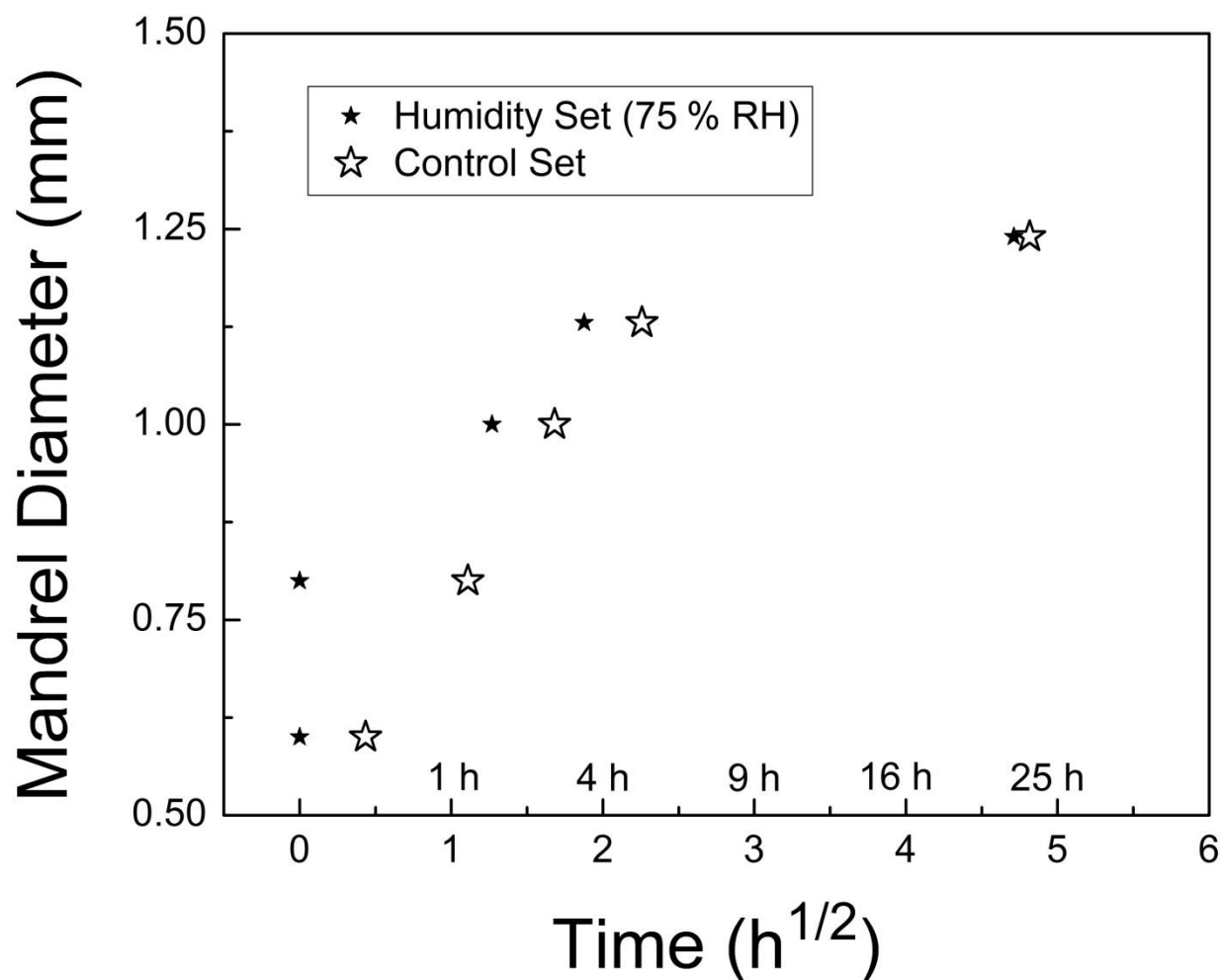
Figure 4.8. *Mandrel diameter of ribbon failure plotted as a function of time exposed to 75% RH for $Ca_{75}Mg_{15}Al_{10}$ ribbons. The rod shaped mandrel diameter where the sets fail is plotted as a function of time exposed to* ambient *conditions. The plot consists of a control set that experiences* ambient *lab conditions only and a test condition set that is first exposed to 75% RH for about one hour.*

The 75% RH plot in Figure 4.8, shows that when the set is removed from the controlled humidity chamber, the first two mandrel sizes fail immediately. The rate of failure of the humidity set then follows that of the lab control set.
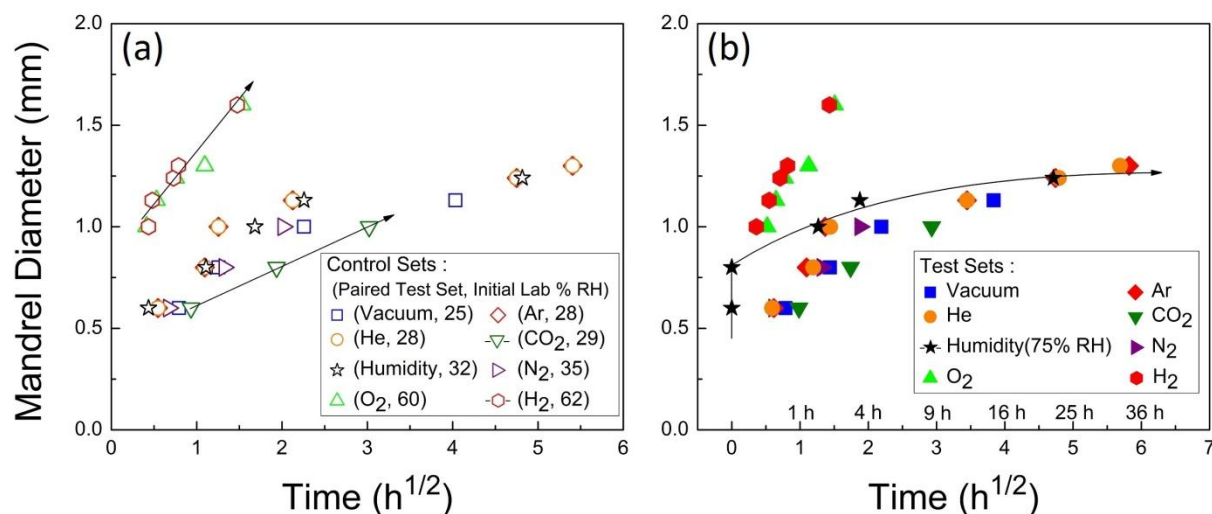
Figure 4.9. *(a) The combined plot of mandrel diameter ribbon failure as a function of time exposed to* ambient *lab conditions control sets[2] and the RH that each control set experienced in the lab. The inset shows the control set associated with the gas tested. The H_2 and CO_2 test sets are trace to show a contrast between a set that experienced high initial humidity with one that experienced low initially humidity. (b) The combined plot of mandrel diameter ribbon failure as a function of time exposed to* ambient *lab conditions after being exposed to a gas, a humidity or a thermal relaxation test. The inset shows the condition that was tested in the test set. The RH 75% test set is highlighted to show its deviation from the other test sets.*

The plots in Figure 4.9 summarize the results of the isolated ambient condition tests. Figure 4.9a shows all the control sets and Figure 4.9b shows the gas, thermal relaxation and controlled humidity test sets. The only outlier in all the plotted data in Figure 4.9 is the 75% RH test set. Specifically, the first two mandrel rod sizes fail when tested immediately out of the control box. This indicates that humidity is enabling the embrittlement.

---

[2] A reminder: Control sets are the sets that have been immediately exposed to ambient lab conditions following being melt spun. Test sets are the sets that were immediately exposed to a gas, a humidity level, or a vacuum following being melt spun.

4.3 Measuring Ca(OH)$_2$ Growth Layer

      Since humidity is observed to be related to embrittlement interaction with the calcium glass, it is examined in detail. This is a rapid embrittlement process where a ribbon can lose ductility in less than half an hour. First, the growth kinetics of the Ca(OH)$_2$ layer is examined. Ca is known from literature to form Ca(OH)$_2$ in the presence of water vapor [211-212]. Since the calcium glass ribbons react quickly, they have to be prepared and mounted rapidly. To get a clean surface for cross sectional elemental analysis, samples were cut using an unused razor blade. The ribbons were sliced with the wheel contact side facing down on a glass slide. After cutting, the section of ribbon was then mounted on the side of a copper block using quick setting adhesive. There are more stable ways to mount samples, but the calcium glass ribbons must be attached in this fashion. Other methods do not capture, or would interfere with, the current state of the sample. They either take too long to prepare and the sample has excessive time to interact with the lab environment or the mounting procedure would alter the sample. Hot mounting procedures would crystallize this calcium glass. In the time required for traditional cold mountings to set, the cross sectional surface would have a new surface layer growth.
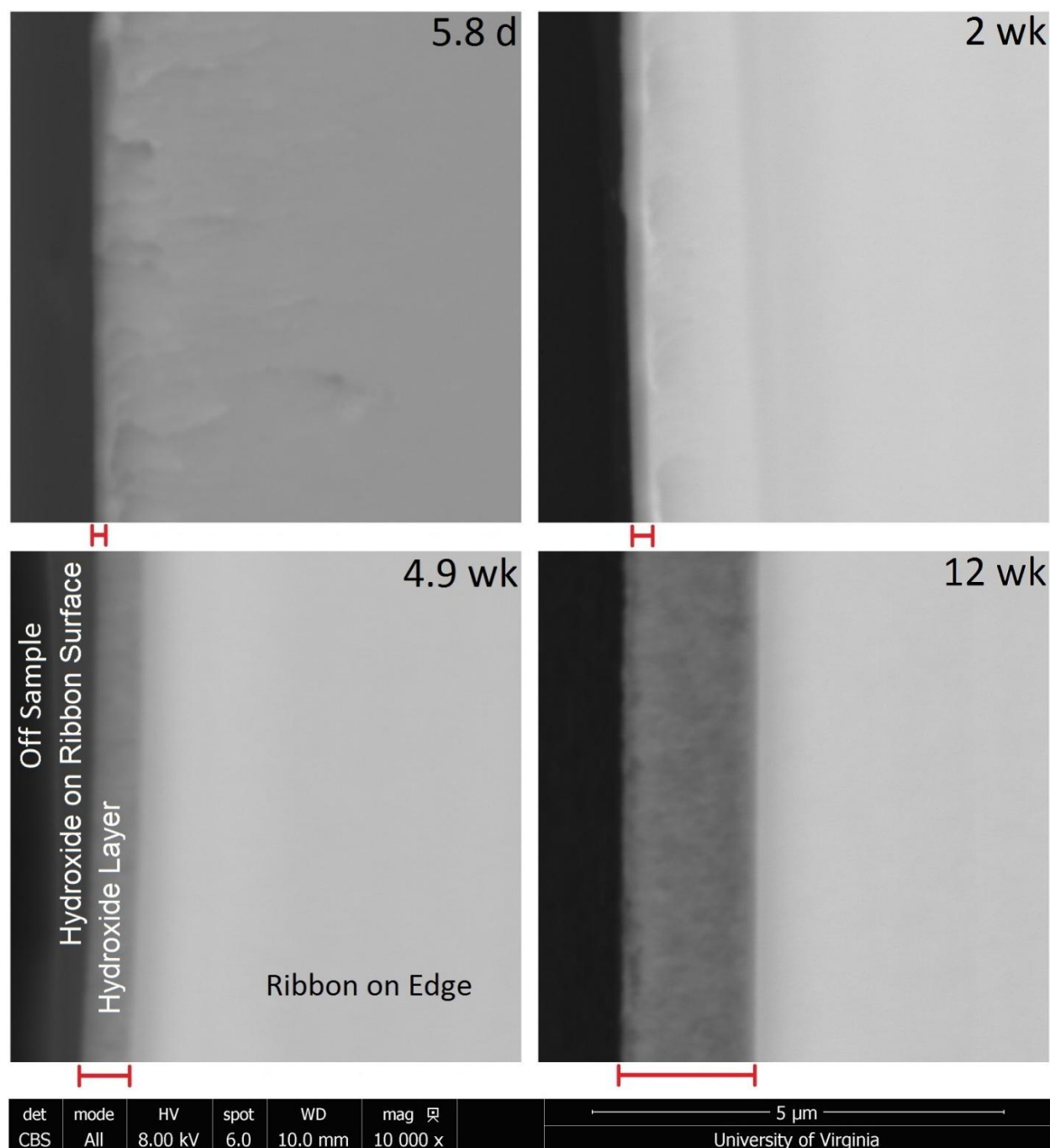
Figure 4.10. BSE images taken on the SEM of the edge of cross sections of Ca₇₅Mg₁₅Al₁₀ ribbons exposed to 75% RH. *Below each image the hydroxide layer is identified with the red bars.* The humidity exposure duration are 5.8 d (500 ks), 2 wk (1200 ks), 4.9 wk (2900 ks), and 12 wk (7300 ks). The dark area to the left of each image is the receding out of focus hydroxide on the melt side surface of the ribbons. The beginning of the depth of each cross section is marked by the bar below each image. The width of this bar corresponds with the thickness of the hydroxide layer. The area to the right of the hydroxide indicating bar is the near edge part of the cross section of the on average 20 μm thick ribbons.

The cross section surface is examined using backscattered electrons on a SEM. Figure 4.10 shows the edge of the cross section of different ribbons exposed to different durations of 75% RH. The hydroxide layer is the middle region present between the dark left-hand off sample side and the right most light bulk of the sample region. The samples are all shown at the same scale for easy qualitative comparison. In Figure 4.10, the increase in thickness of the hydroxide layer is indicated by the bar length. The 5.8 d (500 ks) image has a thin layer barely visible between the dark edge and light rough cross sectional surface. The 2 weeks sample has a visible sub-micron layer between the dark edge and bright ridge line on the cross section surface. The 4.9 weeks cross section has a light grey layer roughly greater than 0.5 µm that is visible. On this sample it is between a smooth cross section surface and a layer that is the out of focus ribbon surface next to the dark of sample region. The ribbons surface is not perfectly flat. They have hills and valleys locked-in from liquid flow during quenching. The 12 weeks sample has a defined 1.5 µm image of the hydroxide layer.

A line scan of the 4.9 weeks sample, as seen in Figure 4.11, shows where the hydroxide layer is present in the BSE image. The right side of the image is the surface which is facing the EDS detector. The plot of different elemental line scans shows hydroxide layers on either side of the ribbon. While the hydroxide layer can be imaged using a backscattered electron detector, an elemental oxygen map, or oxygen line scan, shows the thickness of $Ca(OH)_2$ growth layer more clearly.
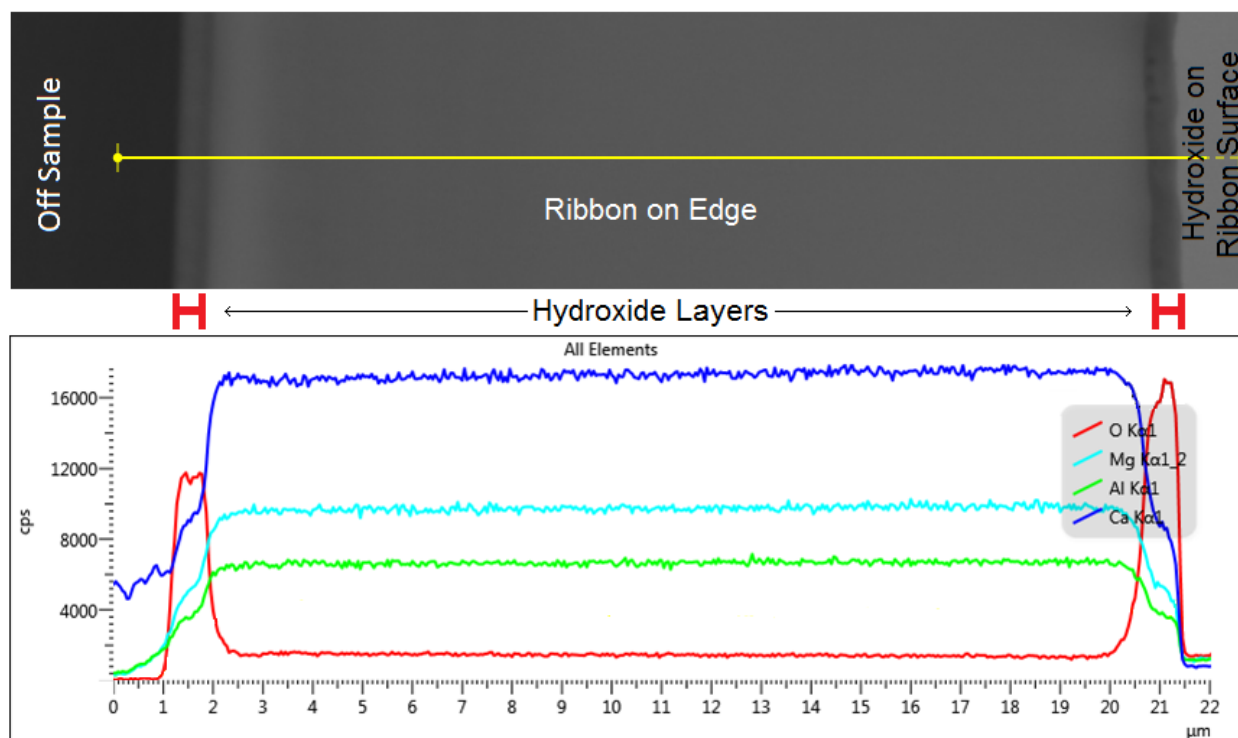
Figure 4.11. *A cross section of a $Ca_{75}Mg_{15}Al_{10}$ ribbon that has been held in 75% RH for 4.9 weeks. The BSE image is of the area where the line scan was collected. The yellow trace is the line scan. The hydroxide layers and their thicknesses are indicated with the red bars below the BSE image. The bottom plot is of the elemental line scans of the O $K_{\alpha 1}$, Mg $K_{\alpha 12}$, Al $K_{\alpha 1}$ and Ca $K_{\alpha 1}$ emission lines. There are four types regions of the cross section of ribbon labeled in the top BSE image. The order from left to right is first an off the sample region, then an layer of hydroxide, then the ribbon on edge with bulk composition, then a second hydroxide layer, and then there is the top surface of the last hydroxide layer on the outside surface of the ribbon. This final region is due to the ribbon being tilted toward the EDS detector and not the BSE detector.*

To take elemental maps and do line scans, a compromise had to be made in mounting of the samples. To obtain the best image, the sample has to be on the plane perpendicular to normal of the electron detector. For optimal EDS maps and lines scans, the face of the sample has to be pointed 45° from azimuth of the loading door plane and 45° from normal. To have the cross section face point in both directions during a SEM session is possible only if the SEM has access to all three Euler angles of rotation. The Quanta 650 only has two of the three angles of rotation.
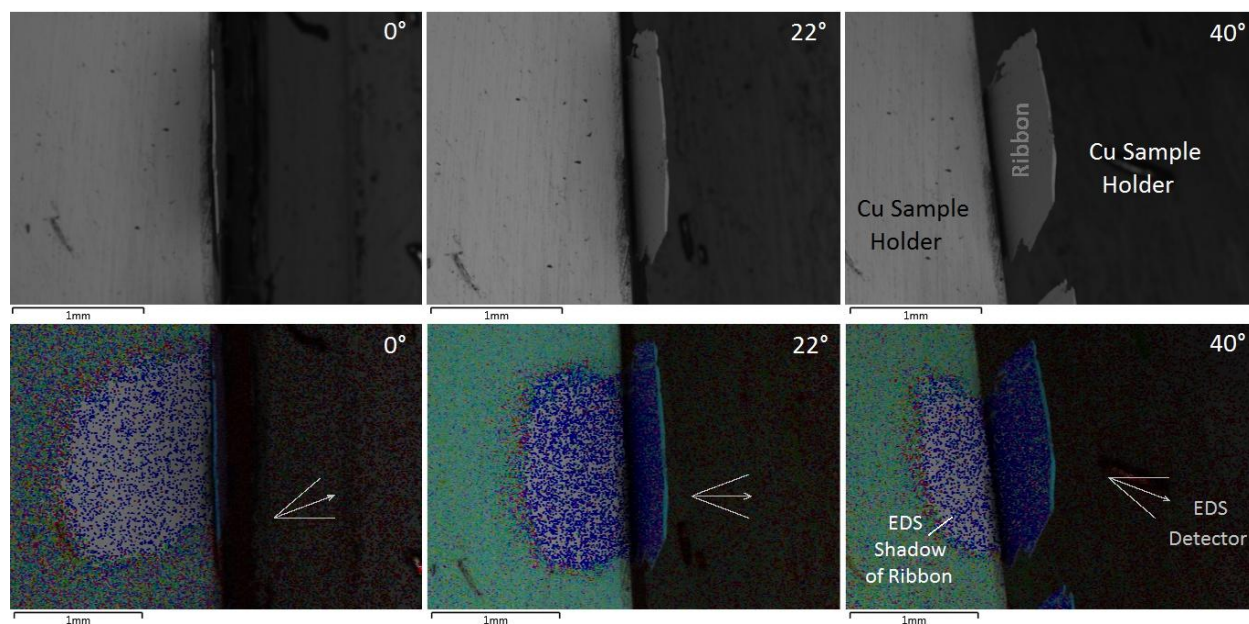
Figure 4.12. *Pairs of BSE images (top row) and composite EDS maps (bottom row) with the ribbon tilted at 0°, 22°, and 40°. The direction to the EDS detector is highlighted on the EDS maps. This corresponds with the tilt of the EDS shadow cast by the ribbon. The EDS elemental map is a combination O (red), C (yellow), Ca (blue), Al (green), and Mg (light blue).*

Low magnitude images, Figure 4.12, show the shadow of the ribbons sticking over the edge of the copper mount. Face on imaging is best at 0° tilt. EDS is best near 22° tilt. Tilting further through angles past 40° demonstrates that the EDS becomes less optimal. The 40° condition is similar to that at 0°.
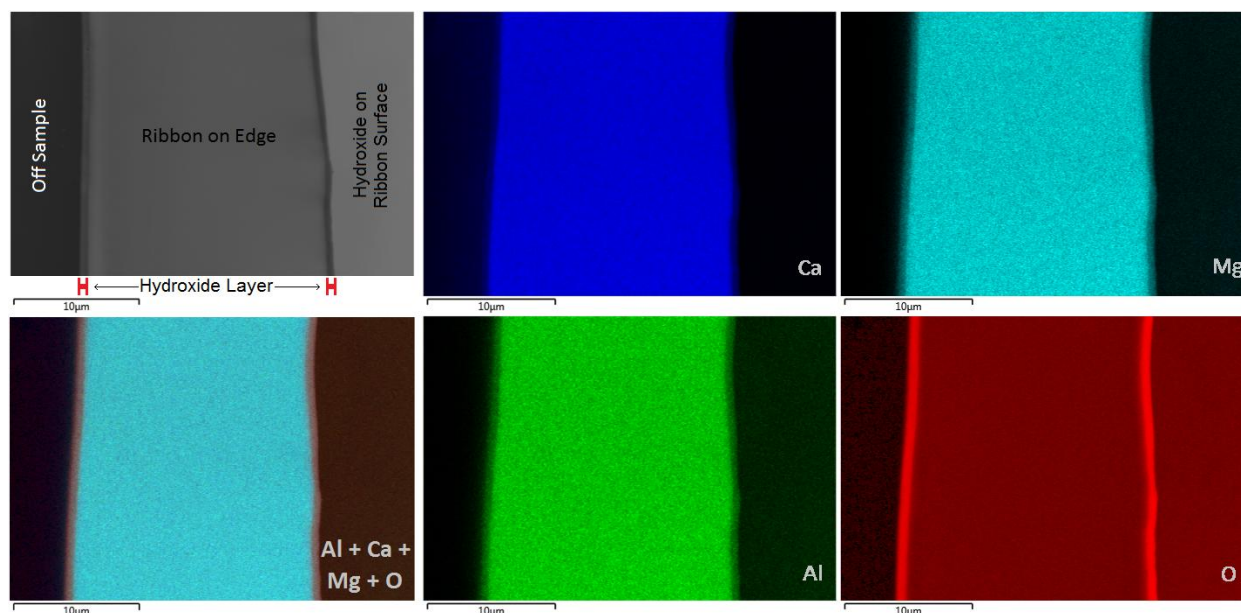
Figure 4.13. *SEM BSE image, a composite EDS map, and elemental EDS maps of Ca, Mg, Al, and O of a cross section of a Ca$_{75}$Mg$_{15}$Al$_{10}$ ribbon* exposed to 75% RH for 4.9 weeks. *The hydroxide layers and their thicknesses are indicated with the red bars below the BSE image.*

      The hydroxide layer can be measured from the EDS of the map or the line scan data. In Figure 4.13, we can see the thickness of the hydroxide in the 75% RH 4.9 weeks exposed sample. Also noticeable is that the Mg and Al maps have lower intensity levels compared to the center of the ribbons. This lower intensity corresponding to where the hydroxide is in the oxygen map. Figure 4.14 shows the growth of the hydroxide layer of different exposure times from 3 h (11 ks), 1.2 d (100 ks), 2 wk (1200 ks), and 4.9 wk (2900 ks). For easy qualitative comparison, images of 3 h, 1.2 d, and 2 weeks were adjusted to be on the same scale as the 4.9 weeks image and the 3 h and 1.2 d were aligned so that the cross section runs vertical, like the 2 and 4.9 weeks images. The EDS detector is to the right side of the images. For the 3 h and 1.2 d images, the dark area on the left is the cross section surface and the brighter area on the right is the ribbon surface. For the 2 and 4.9 weeks images, the dark far left side in off sample, the bright lines are the hydroxide layers bounding the cross section, and the right most side is the ribbon surface.
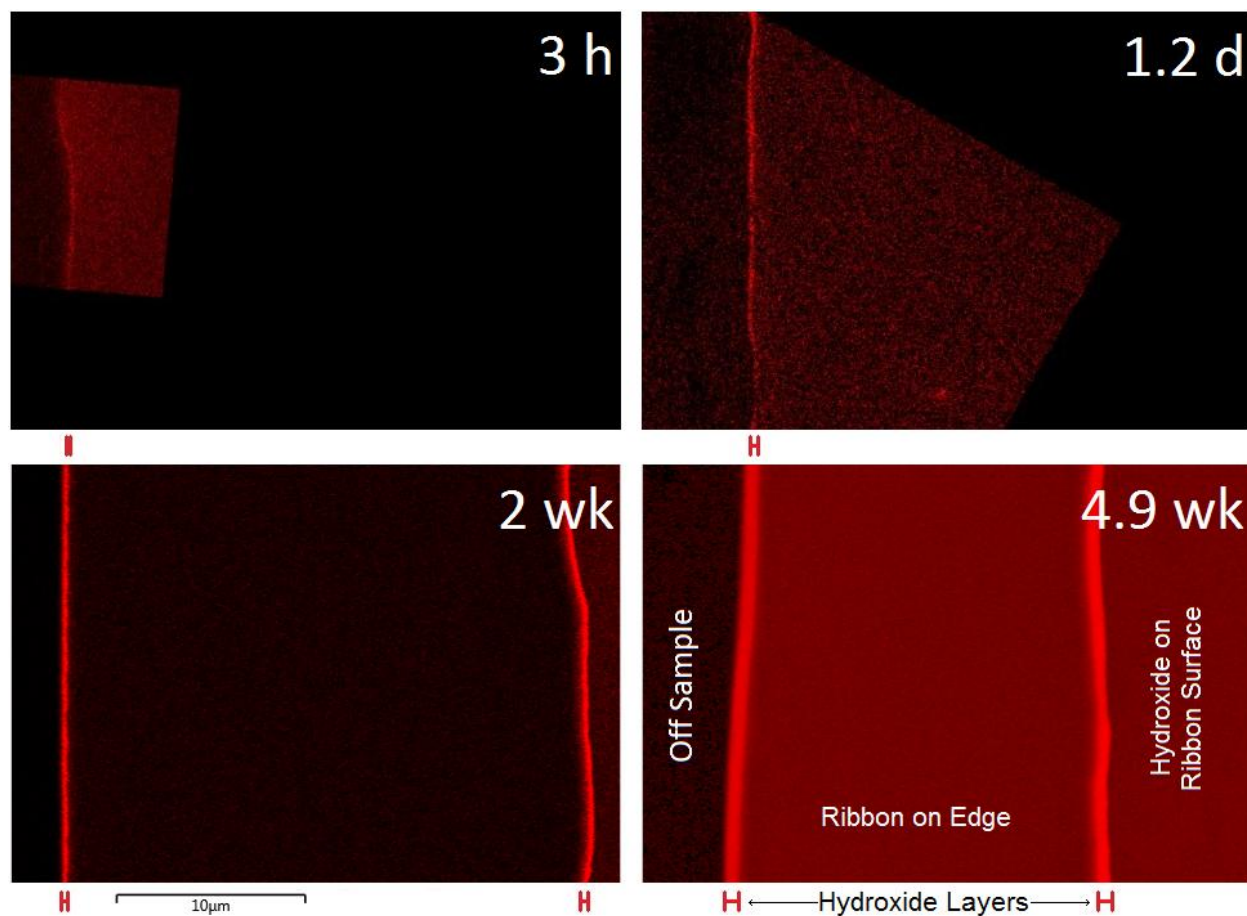
Figure 4.14. *EDS oxygen maps of the cross section views of $Ca_{75}Mg_{15}Al_{10}$ ribbons exposed to 75% RH for 3 h (11 ks), 1.2 d (100 ks), 2 wk (1200 ks), and 4.9 wk (2900 ks). The hydroxide layers and their thicknesses are indicated with the red bars below the BSE image.*

For lower exposure times, the thickness measurements for EDS maps overestimate the thickness of the hydroxide layer. The diffuse interior edge has a low signal, making it difficult to determine the exact edge. If the EDS maps detection time were to increase, the sample would drift due to the mounting limitations. Line scans are used to create a standard means of measuring the hydroxide thickness. Elemental maps provide rapid survey results to select region on the sample to take the line scans.
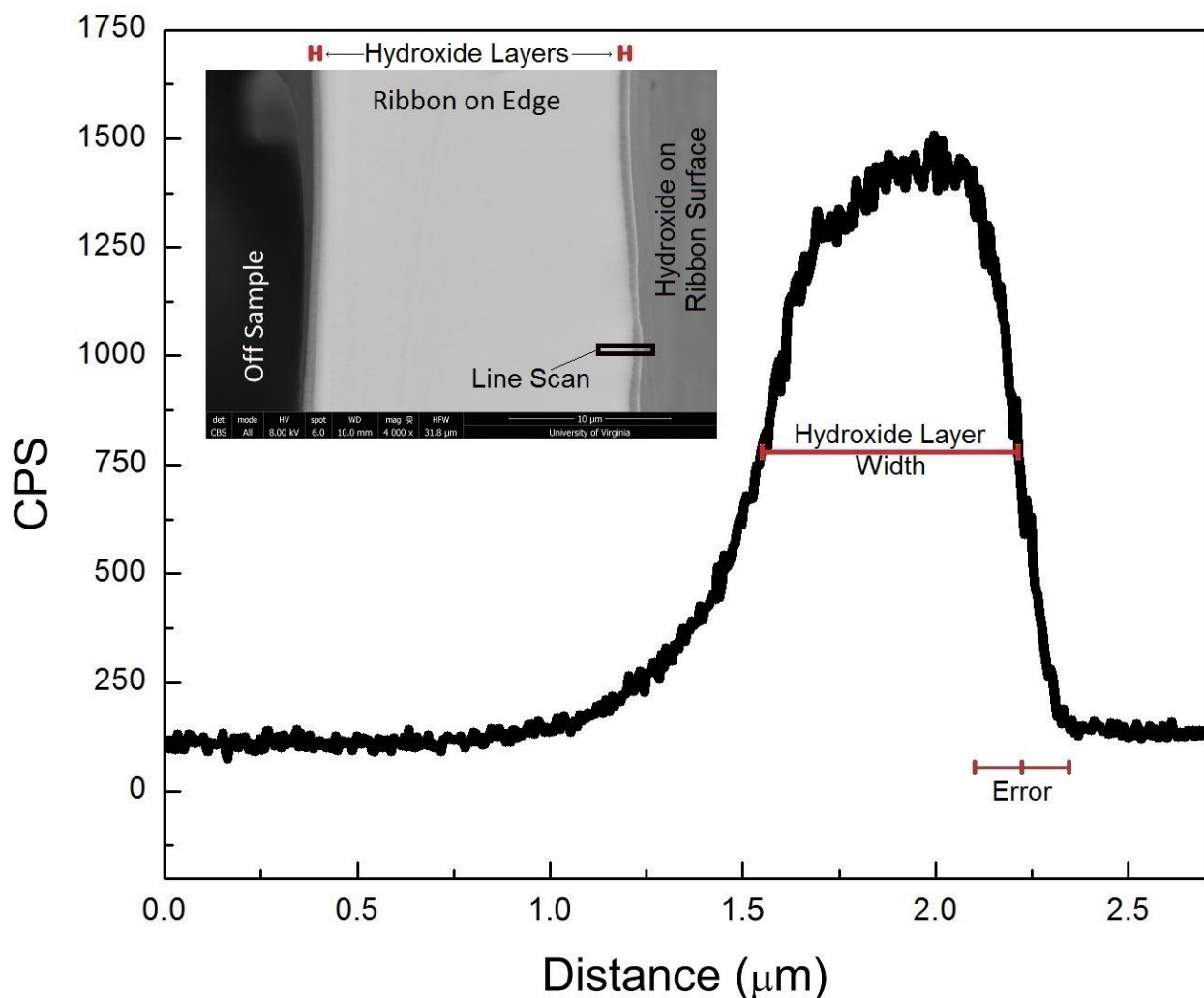
Figure 4.15. *This is a sample SEM EDS oxygen line scan taken on a ribbon of $Ca_{75}Mg_{15}Al_{10}$ that has been exposed to 75% RH for 4.9 weeks. A black box is drawn around region from the BSE image that the line scan was extracted. The BSE image is in the upper left corner. The BSE image is of the edge profile of the cross section of the ribbon. The FWHM that was used as the thickness of the hydroxide layer, and an error used, are labeled on the line scan as the hydroxide layer width and error.*

For each ribbon, multiple line scans were taken at several regions along the edge closest to the detector. An example of one of these oxygen line scans and location on a BSE image is shown in Figure 4.15. These oxygen line scans have different level backgrounds depending on which side of cross section is closest to the detector. A standardized way of measuring the hydroxide thickness was created. To get a bottom standard starting point for measuring the width of the hydroxide layer an average background level was established by determining the point half

way between the oxygen background level in the bulk and the value at exterior face. The full width half maximum level was measured and used as a thickness of the hydroxide layer.

Using the full width half maximum (FWHM) here gives a standardized measurement that takes into account the variances introduced by the slight differences in alignment of the curvy sample edge and cross section face angle relative to EDS detector across the various samples measured. The hydroxide measurement can be stated as being the thickness where the hydroxide is a majority of the composition. The average result of the 15-20 line scans per sample and error is reported in Table 4.1. One error measurement is the distance between the distance coordinate of the line scan where the FWHM starts, to the point where the background level on the ribbon surface side is. This distance used as an error is identified in Figure 4.15. This was comparable to a calibration standard of Au, evenly spaced and deposited on Si. The standard was scanned at the same conditions to determine the line scan resolution. A calcium standard is not easy to make or procure. For the Au on Si standard the error is 0.03 μm. This is comparable to the prior described error measurements made on the calcium ribbon line scans. A second source of error is the standard deviation of the average of samples. Due to the large sample set and homogeneousness of the measurements, this error is not the largest limiting error. A third error for the larger hydroxide thickness was probe site spacing. Scanning too slowly or too close in spacing for the larger thicknesses resulted in damage to the hydroxide layer. The largest of the three errors was used as the error to associate with the thickness measurement.

Time (s) x 10^5	Hydroxide Thickness (µm)
0.1 (3 h)	0.119 ± 0.03
0.5 (13.9 h)	0.143 ± 0.05
1.0 (1.2 d)	0.224 ± 0.05
5.0 (5.8 d)	0.260 ± 0.07
9.3 (10.8 d)	0.304 ± 0.07
12.2 (2 wk)	0.308 ± 0.10
29.3 (4.9 wk)	0.631 ± 0.12
41.5 (6.8 wk)	0.864 ± 0.08
52.7 (8.7 wk)	1.302 ± 0.12
72.6 (12 wk)	1.547 ± 0.15

Table 4.1. *Table of averaged measured Ca(OH)$_2$ thickness layers grown on ribbons of Ca$_{75}$Mg$_{15}$Al$_{10}$ and the times that the ribbons were exposed to 75% RH. Plotted in Figure 5.6.*

4.4 Measuring PPZ Size

To see how the sample exposure to humidity affects their ductility, the samples were tested in a tensile test. Their cross section surfaces were examined under the SEM using secondary electron imaging. Samples of different exposure to 75% RH durations: 0.5 h, 3 h, 13.9 h, 1.2 d, 5.8 d, 10.8 d, 2 wk, 4.9 wk and 6.8 wk were imaged, Figure 4.16. The plastic processing zone (PPZ) can be related to the ductility of a sample. The PPZ are the closed areas created by the intersection of river and vein patterns. These patterns are on the fracture surface of tensile tested metallic glass ribbons. As PPZs become smaller the metallic ribbons trend toward being more relatively brittle.

The change in size of the PPZ is noted in Figure 4.16. All the images are on the same magnification scale. Several visual groupings can be made of these PPZ images. The 0.5 h, 3 h and 13.9 h have large irregular shaped PPZ. The 1.2 d and 5.8 d images have a mixture of regular spaced smaller PPZ, and a few larger size ones. The 10.8 d, 2 wk and 4.9 wk images all show fine, regular spaced PPZ. And at 6.8 weeks the PPZ are small enough that visually they are difficult to differentiate, but line profiles do show small PPZ are present. It is noted that the 3 h, 2 wk, and 4.9 wk images are taken near the outer surface of the ribbon. The larger PPZ on the halves further from the edge are representative of the average size of the PPZ present over the

fracture surface on these tensile pulled ribbons. The PPZ decrease in size as the hydroxide layer is approached. This may indicate a gradient of brittleness from the edge of the hydroxide layer extending into the ribbon, with the near surface layer being more brittle than the interior. For the analysis, the edge PPZ will be ignored. The relation sought is the link between average PPZ size of the interior core and the duration of exposure to 75% RH to reveal a general trend between the decreases in PPZ size to the embrittlement of the ribbons. It is also noted that these gradients are not seen in other whole ribbon scans of metallic glasses which unlike these Ca-based glasses are stable in ambient lab conditions [148, 153, 157, 167].

det	mode	HV	spot	WD	mag ⊡	HFW	2 µm
ETD	SE	2.00 kV	2.0	4.3 mm	20 000 x	6.35 µm	University of Virginia

det	mode	HV	spot	WD	mag ⊡	HFW	2 µm
ETD	SE	2.00 kV	2.0	2.7 mm	20 000 x	6.35 µm	University of Virginia
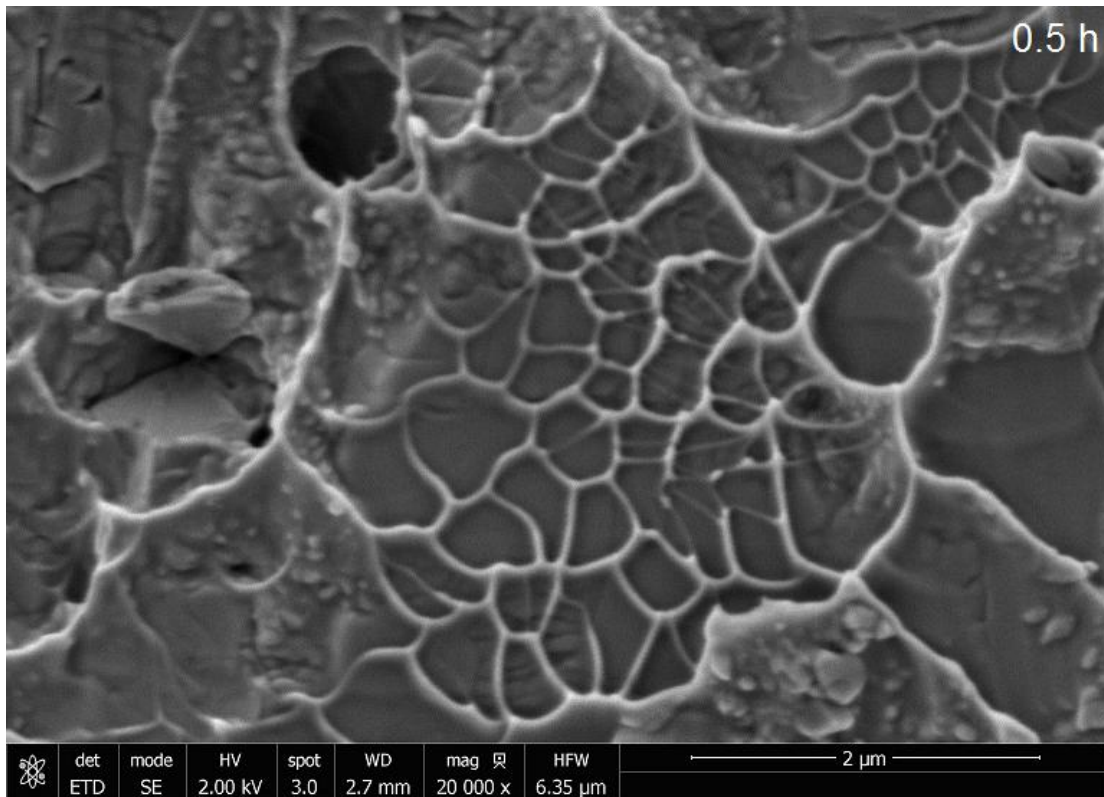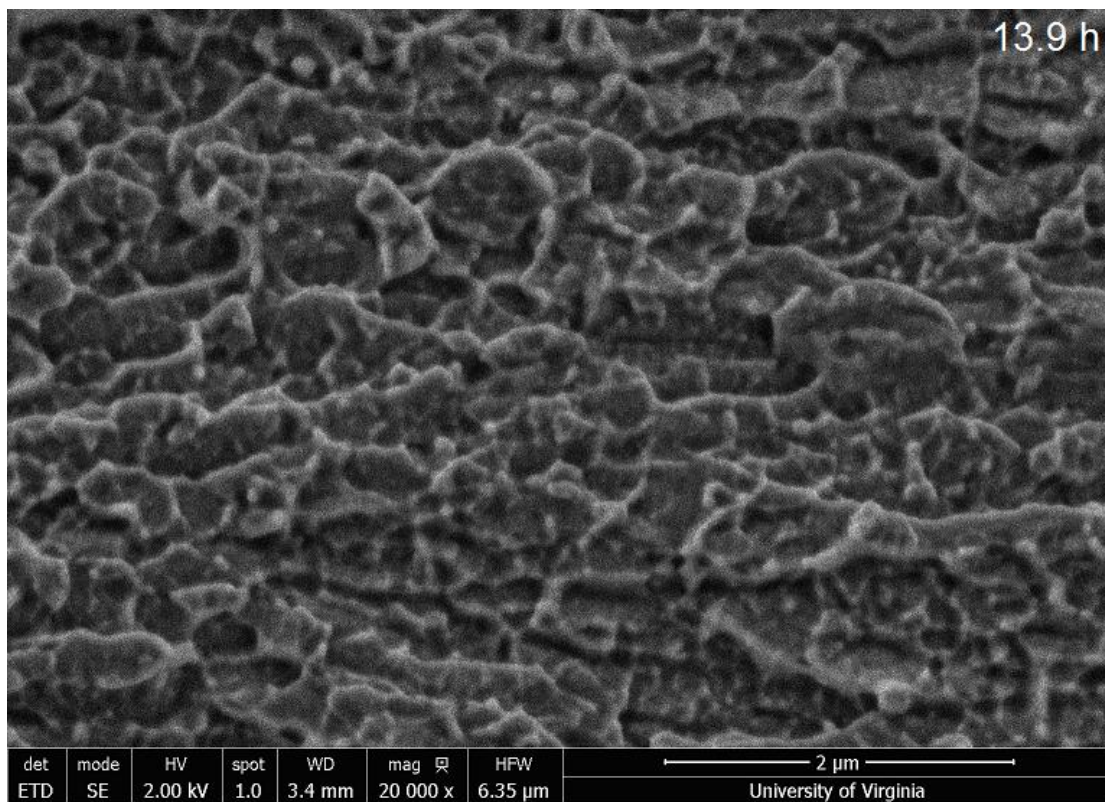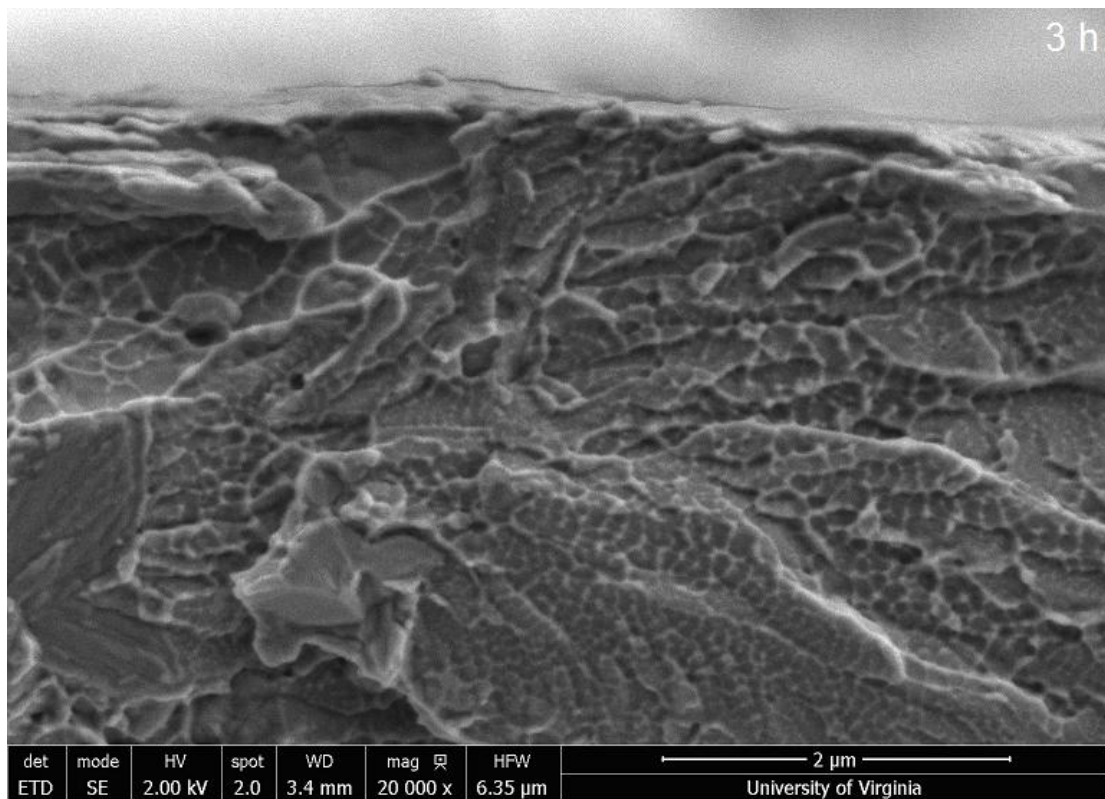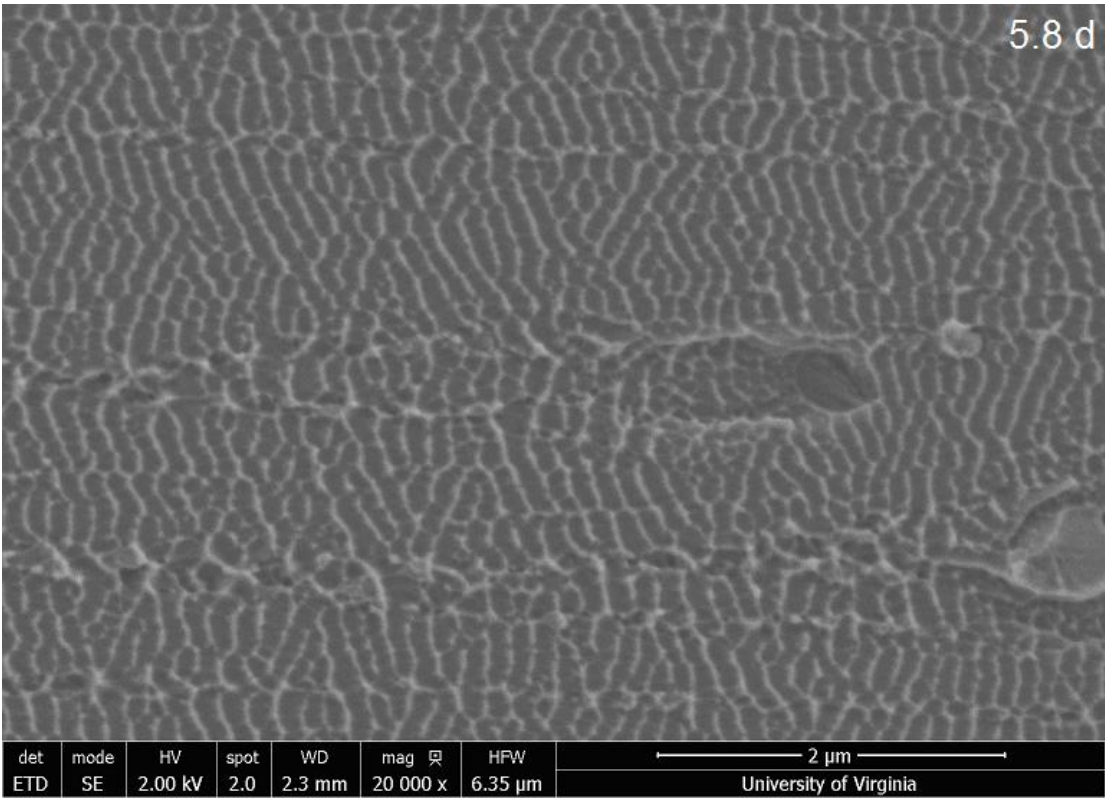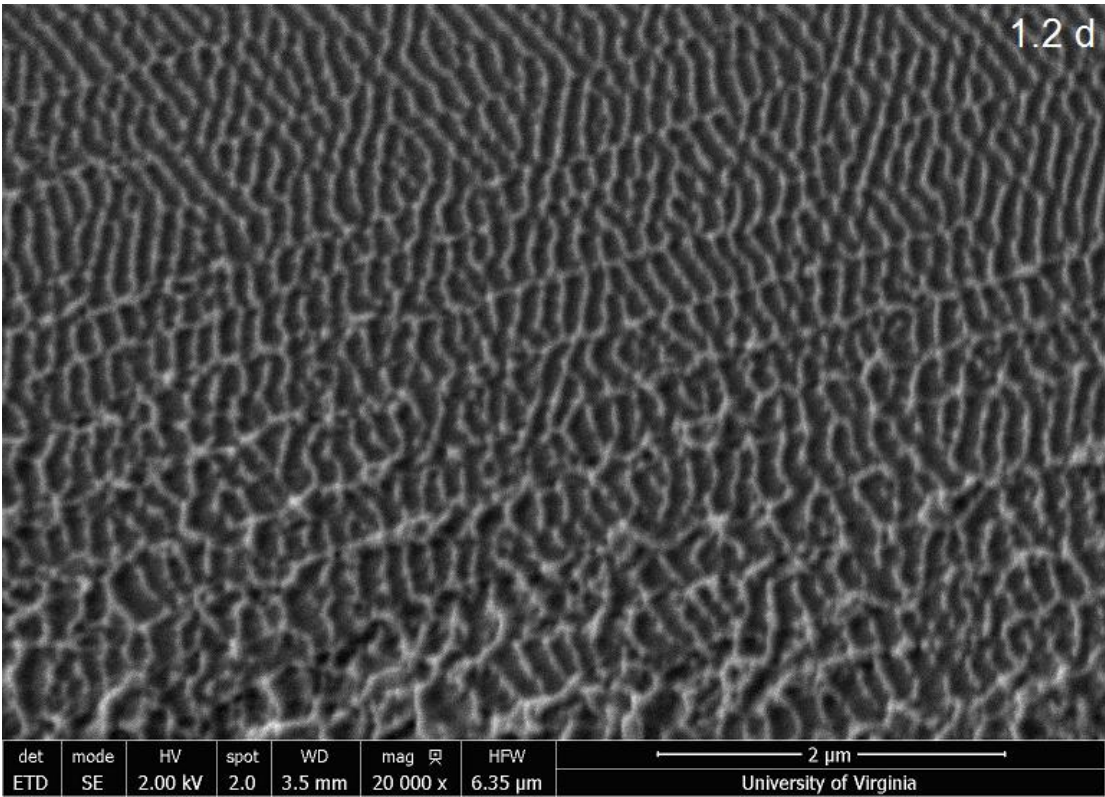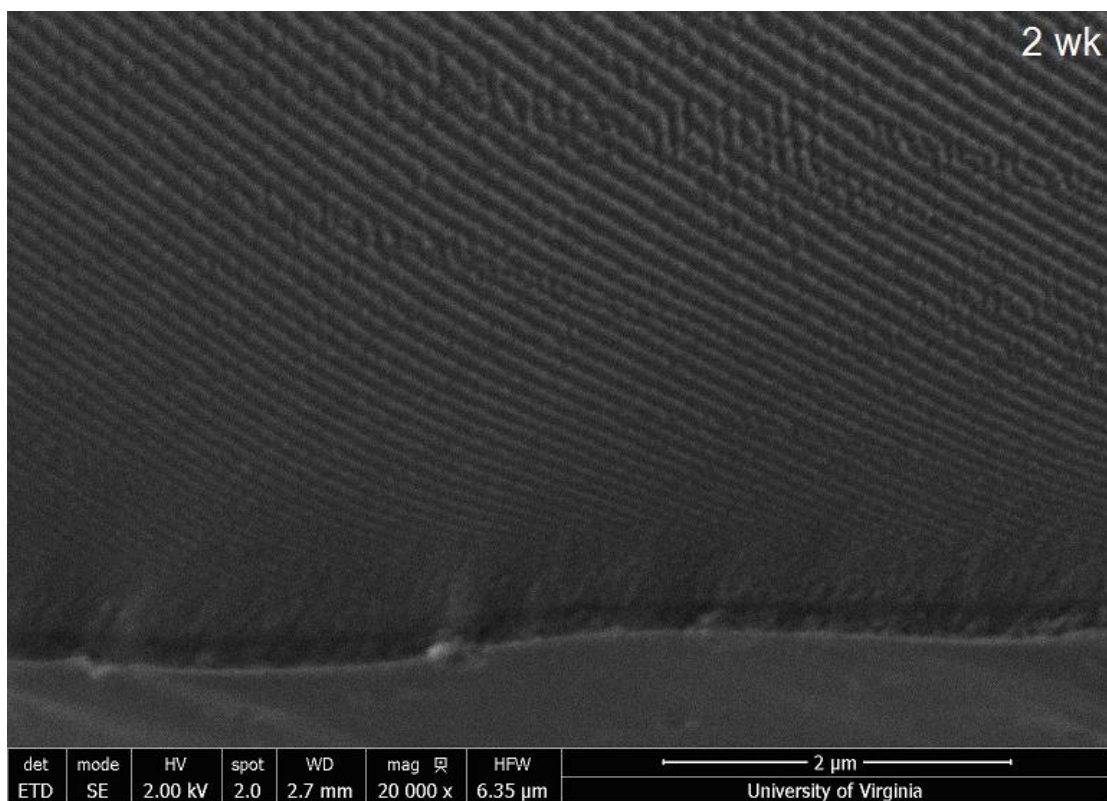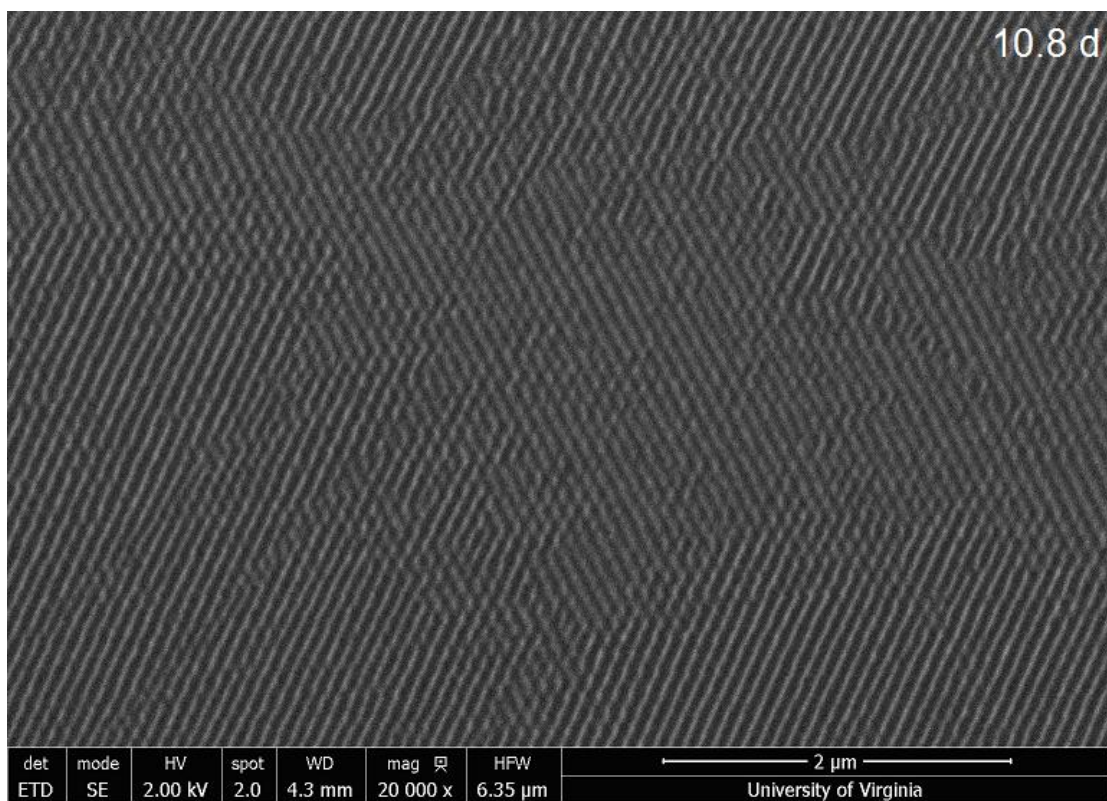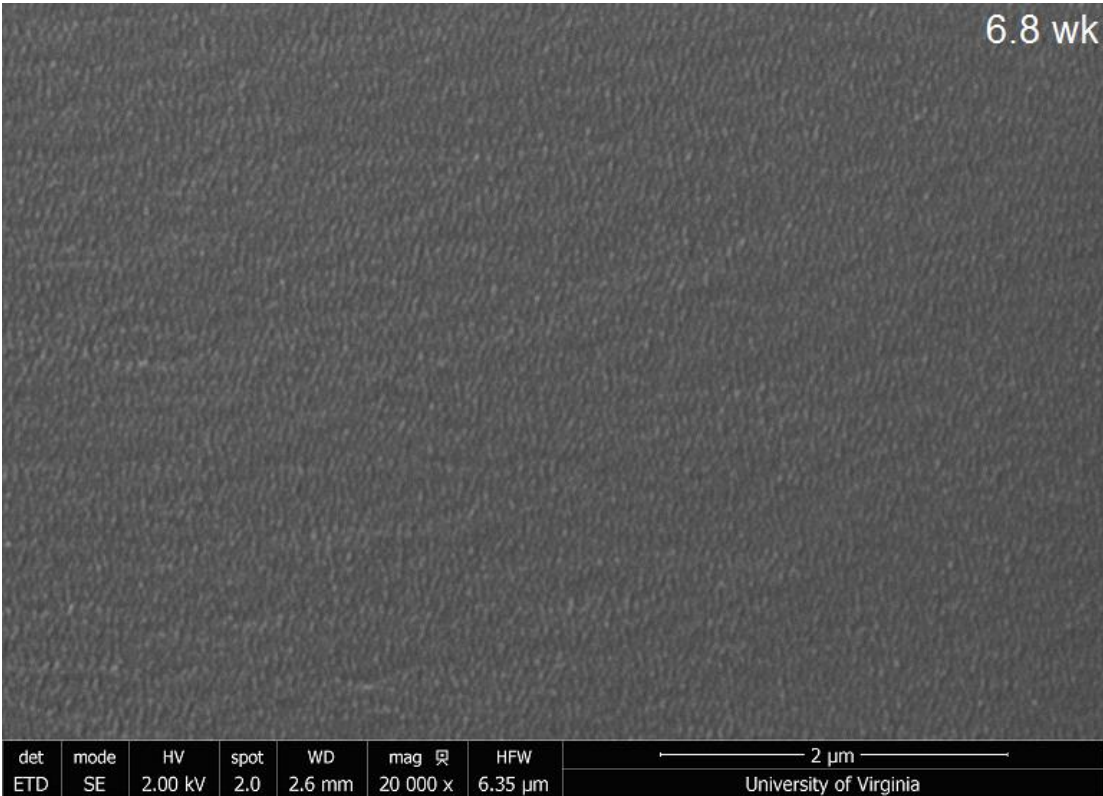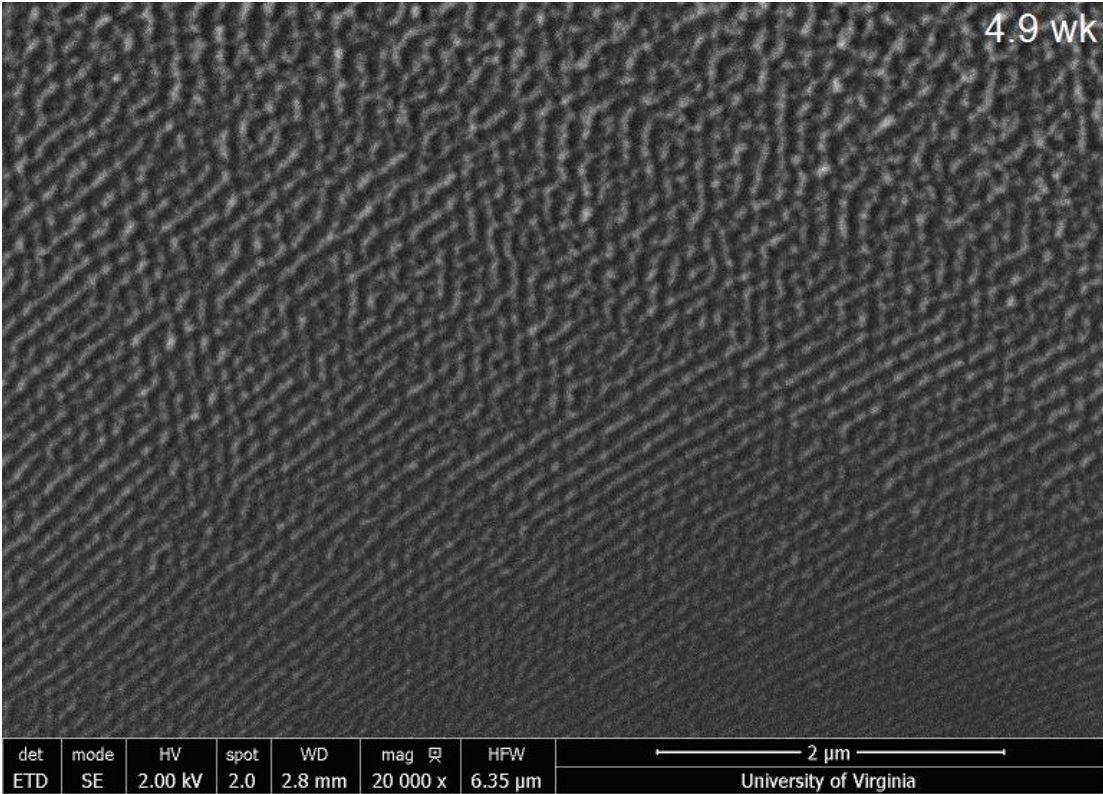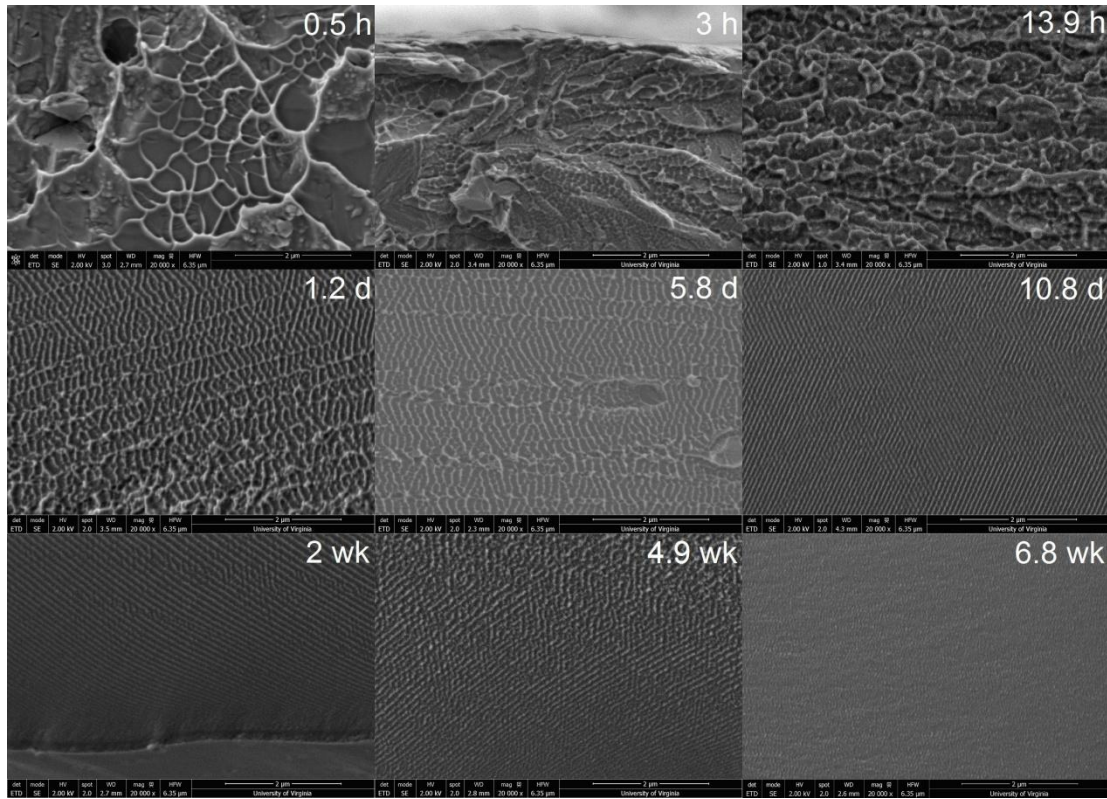
Figure 4.16. *Postage stamp sized image of fracture surface of ribbons of $Ca_{75}Mg_{15}Al_{10}$ that are tensile tested after being exposed to an 75% RH for 0.5 h (1.8 ks), 3 h (11 ks), 13.9 h (50 ks), 1.2 d (100 ks), 5.8 d (500 ks), 10.8 d (1000 ks), 2 wk (1200 ks), 4.9 wk (2400 ks) and 6.8 wk(3600 ks). Images were taken from regions of the ribbon representative of the samples average PPZ sizes. Preceding the postage stamp summary image are enlargements of each image.*

To create a standard technique for measuring the PPZ, each of the different samples was counted using a semi-automated linear density method. Like the traditional grain boundary counting method, the number of boundary intercepts is divided by the length of draw line to get the average size of the PPZ. In the Digital Micrograph software, evenly spaced line profiles of 10 pixel width were taken across the image in a grid like pattern.
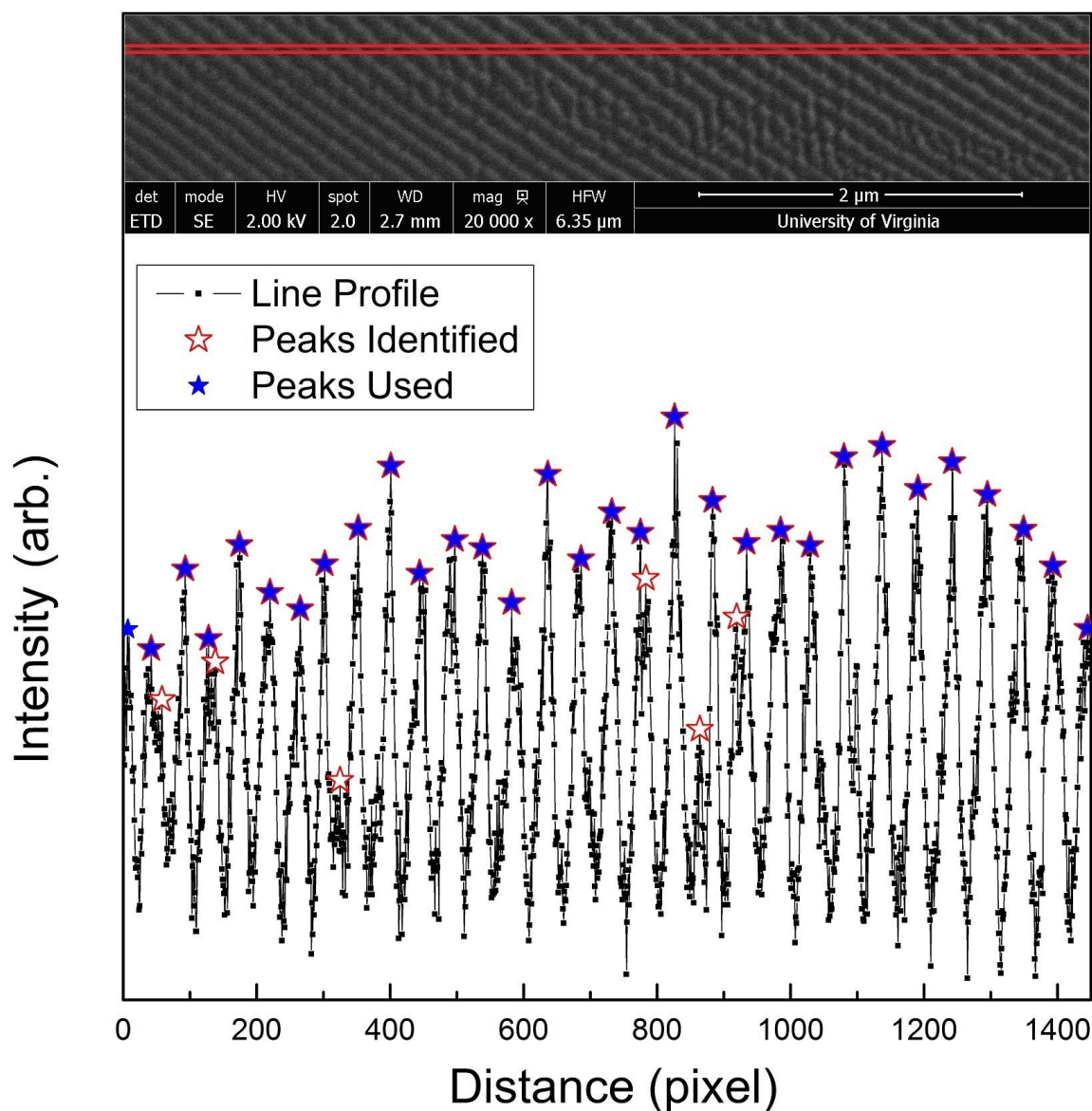
Figure 4.17. *Example of the results from the peak finder algorithm used on ribbon of Ca$_{75}$Mg$_{15}$Al$_{10}$ exposed to 75% RH for 2 weeks. The SE SEM image with the region when the 10 pixel width line profile was extracted is displayed. The plot is of the line profile with the points the peak finder found plotted as red stars ☆. The peaks that were kept and used for the PPZ measurement are plotted as solid blue stars ★.*

The peaks in these line profiles correspond to the intercepts of the PPZ boundaries. A peak finding algorithm was created using Microsoft Excel (2007) macros which tested for local maxima over 30 pixel ranges. For Figure 4.17 the conversion from pixel to unit length was 0.0041 μm/pixel. The pixel conversion for all images used was on a similar order of magnitude.

The macros were able to identify all the peaks plus a few erroneous ones. The over counting of peaks was due to ~5% of the peaks appearing to be split, but they were actually broader PPZ boundaries. Also, there were low level peaks that were identified that did not correspond to PPZ boundaries in the image. The identified peaks were plotted with the line profiles. The broad boundary and low level peaks that were not associated with PPZ were manually identified and removed. An example of this processing is seen in Figure 4.17. The final average PPZs and errors are listed in Table 4.2. One source of error for this was the calibration of the magnification scale bar. This error was determined to be on average 0.040 µm error per 5.0 µm using a calibration standard at the various working distances, spot sizes, beam energies and magnifications employed. The major source of error for the PPZ measurements came from the standard deviation of the sample measurements. For the shorter times there was a larger spread due to greater variance in sample PPZ sizes. The PPZ became more homogeneous the longer the samples were exposed to 75% RH.

Time (s) x 10^5	PPZ Thickness (µm)
0.02 (0.5 h)	0.33 ± 0.10
0.10 (3 h)	0.20 ± 0.07
0.5 (13.9 h)	0.19 ± 0.07
1.0 (1.2 d)	0.17 ± 0.05
5.0 (5.8 d)	0.16 ± 0.05
9.3 (10.8 d)	0.14 ± 0.02
12.2 (2 wk)	0.14 ± 0.06
29.3 (4.9 wk)	0.11 ± 0.03
41.5 (6.8 wk)	0.05 ± 0.02

Table 4.2. *Table of measured average sizes of the PPZs on the fracture surface of $Ca_{75}Mg_{15}Al_{10}$ ribbons that were tensile tested after different exposure times to 75% RH. Plotted in Figure 5.16 and plotted with the $Ca(OH)_2$ thickness growth in Figure 5.17.*

4.5 XPS measurements

4.5.1 Low and High Resolution XPS Spectra

XPS was used to determine information about the relative location of calcium compounds from the surface to the bulk. Also, the ratio of calcium to elements other than hydrogen can be determined. Full spectra survey scans of calcium glass ribbons where taken from 0-1400 eV binding energy.
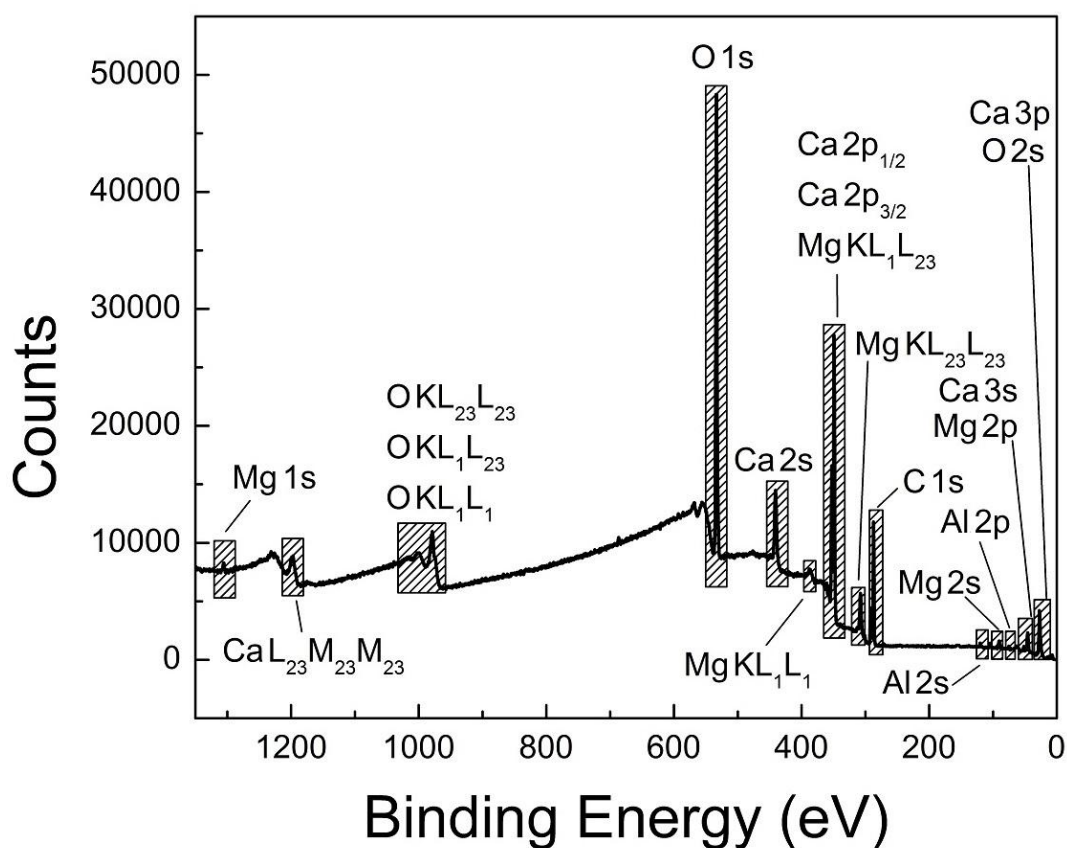
Figure 4.18. *XPS scan on binding energy from 0-1400 eV of a ribbon of $Ca_{75}Mg_{15}Al_{10}$ exposed to ambient lab conditions for 20mins. The different XPS transitions lines are labeled.*

Figure 4.18 is an example of a full spectra of a $Ca_{75}Mg_{15}Al_{10}$ metallic glass alloy. The peaks are identified and labeled. The known binding energy values [213] are listed in Table 4.3.

Element	Transition	Binding Energy (eV)
O	2s	23
Ca	2p	26
Ca	3s	45
Mg	2p	50
Al	2p	73
Mg	2s	89
Al	2s	118
C	1s	285
Mg	$KL_{23}L_{23}$	301
Ca	$2p_{3/2}$	347
Mg	KL_1L_{23}	347
Ca	$2p_{1/2}$	351
Mg	KL_1L_1	381
Ca	2s	440
O	1s	531
O	$KL_{23}L_{23}$	978
O	KL_1L_{23}	999
O	KL_1L_1	1013
Ca	$L_{23}M_{23}M_{23}$	1197
C	KVV	1223
Mg	1s	1303
Al	$L_{23}M_1M_{23}$	1419

Table 4.3. *Table of known binding energies* [213] *of transitions for the elements in a ribbon of* $Ca_{75}Mg_{15}Al_{10}$.

In addition to full low resolution XPS spectra, high resolution X-ray photoelectron spectra (HRXPS) were taken. The full spectra have information about which elements are present and their relative amounts. The HRXPS spectra of Ca 2p are used to compare the different calcium compounds present. A comparison of the Ca 2p peaks collected from the selected rage of the full spectra as compared to the HRXPS spectra, as seen in Figure 4.19, shows why the full spectra cannot be used for calcium compound information, as the Ca 2p doublet is not resolved.
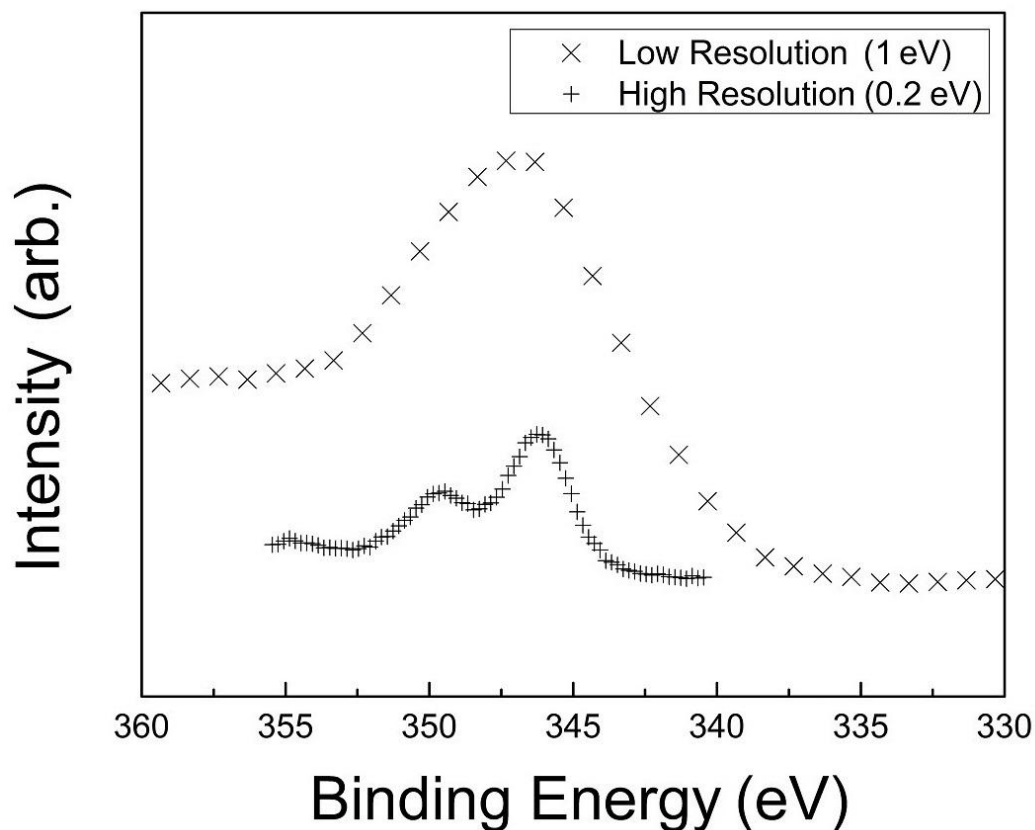
Figure 4.19. *Comparison of the Ca 2p doublet using a high resolution scan with a 0.2 eV step size and a low resolution scan using a 1 eV step size.*

HRXPS spectra are taken with a smaller scan step size of 0.2 eV versus the 1 eV step size of the full spectra. The XPS lines that were examined in HRXPS were the O 1s, Ca 2p and C 1s. Initially Al 2s and Mg 2s were also examined, but their collection did not yield usable peaks in allowable collection time. As shown later, this sample is sensitive, and reacts, to the humidity present even in a vacuum of 10^{-10} Torr. The O 1s and C 1s were used for processing of the Ca 2p peaks.

The Ca 2p peaks were chosen due to abundant literature values at this peak for various calcium compounds. They are listed in Table 4.4. The range and overlap in literature values could be attributed to the measurements being taken on different experimental setups. The differences between calcium compounds are relatively small. In general, the most metallic behavior is toward the lower binding energies and as the binding energies increase the compounds behave more like insulators. The literature studies for $Ca(OH)_2$ and CaH_2 were taken

with different XPS equipment. Having the same value for the two different compounds, CaH_2 and $Ca(OH)_2$ is suspect, especially since CaH_2 readily oxidizes forming $Ca(OH)_2$.

Compound	Binding Energy (eV)	Normalized with C 1s = 284.8 eV (eV)	Calibration Standard		Reference
			Line	Energy (eV)	
Ca	344.7	344.5	C 1s	285.0	Sosulnikov [214]
Ca	345.7	345.7	Au 4f$_{7/2}$	83.8	VanDoveren [215]
Ca	345.7	345.7	Au 4f$_{7/2}$	83.8	VanDoveren [215]
Ca	345.9	345.9	C 1s	284.8	VanDoveren [215]
CaCO$_3$	346.5	347	C 1s	284.3	Christie [216]
CaCO$_3$	346.6	346.8	C 1s,	284.6	Demri [217]
CaCO$_3$	346.7	346.5	Au 4f$_{7/2}$	84.0	Briggs [218]
CaCO$_3$	346.9	346.9	Au 4f$_{7/2}$	83.8	Moulder [213]
CaCO$_3$	347	347.2	C 1s	284.6	Barr [219]
CaCO$_3$	347.3	347.1	C 1s	285.0	Sosulnikov [214]
CaH$_2$	346.7	346.5	Au 4f$_{7/2}$	84.0	Franzen [220]
CaO	345.9	345.9	Au 4f$_{7/2}$	83.80	Seyama [221]
CaO	346	345.8	C 1s	285.0	Sosulnikov [214]
CaO	346.3	346.1	C 1s	285.0	Inoue [222]
CaO	346.5	346.7	C 1s	284.6	Barr [219]
CaO	346.6	346.8	C 1s	284.6	Demri [217]
CaO	347.1	347.1	Au 4f$_{7/2}$	83.80	VanDoveren [215]
CaO	347.3	347.3	C 1s	284.8	VanDoveren [215]
Ca(OH)$_2$	346.7	346.5	C 1s	285.0	Sugama [223]

Table 4.4. *List of calcium compounds, their known binding energies for the 2p$_{3/2}$ spectral line, their known normalized binding energy with respect to the C 1s peak defined at 284.8 eV, the standard used to calibrate the data and literature source of the data, respectively.*

4.5.2 Procedure for Extracting XPS Spectra

Full spectra XPS scans were taken after each Ar ion etching for SIMS collection. A full spectra was taken every 5 min to 120 min, every 10 min up to 200 min and then every 20 min till 240 min. HRXPS spectra were taken after etching at 0, 5, 10, 30, 35, 50, 80, and 240 min. All the XPS processing was done using CasaXPS software [224].

First, all the XPS spectra need to be aligned. This is done by using a standard like Au 4f$_{7/2}$ (83.8 eV), Cu 2p$_{3/2}$ (932.4 eV), Si 2s (153.4 eV), or C 1s adventitious carbon (284.8 eV). In this work, the ever present adventitious carbon is used. The background is fitted using a Shirley fit [225]. A Shirley fit is used to remove the asymmetric backgrounds. The extrinsic background in XPS spectra is due to inelastic scattering of electrons beneath the surface. After background removal, the remaining symmetric peaks are fitted using a multiplicative combination of a Gaussian and a Lorentzian functions. The shape of the photoelectron lines are a convolution of the core level line shapes and instrumental broadening. The analyzer broadening is Gaussian, the primary X-ray radiation is Lorentzian, and the core level is Lorentzian in nature [226].

The photoelectron lines are fitted with multiple Gaussian-Lorentzian peaks. There are several constraints for the fitting with the XPS system used here. The FWHM's of the Gaussian-Lorentzian are constrained. For the HRXPS scans with step size 0.2 eV, the FWHM was constrained between 2.2 eV to 2.6 eV. For the low resolution XPS scans with step size 1 eV, the FWHM was constrained between 6 eV and 10 eV. And, depending on the number of compounds present, the number of peaks fitted would change.

The C 1s and O 1s lines are fitted with single peaks for each compound present. The Ca 2p is a doublet peak. The Ca 2p line has a two spin states, 2p$_{1/2}$ and 2p$_{3/2}$. This is due to the spin orbital splitting. The ratio of the areas of the two peaks is 1:2. The ratio is dictated by the degeneracy of the two states. Additionally, the two peaks in the doublet are intrinsically separated by 3.6 eV. These Gaussian-Lorentzian peaks are then fit by a Levenberg–Marquardt algorithm [227-228]. The algorithm is also known as the damped least- squares method. Once the peaks have been fitted, information like binding energy peak position, ratio of elements and ratio of compounds can be extracted.

4.5.3 Full Spectrum XPS Spectra for Determining Bulk Composition

The full survey spectra were used to determine when the etching of the sample had reached the bulk alloy. Figure 4.20 displays the ratio of Al to Ca to Mg data from the full spectra surveys. The Al 2s, Ca 2s and Mg 2s lines were used. They are each isolated lines without other elemental lines overlapping. The background of each peak was removed using a Shirley fit. Then

area of each peak was measured using a Gaussian-Lorentzian fit. These data were then normalized using the sensitivity factors known for an Al source on a Physical Electronics (Perkin Elmer) 550 spectrometer [229]. Then for each survey scan these data are used to determine the relative amounts between Ca, Mg and Al. As seen in Figure 4.20, the bulk alloy composition of $Ca_{75}Mg_{15}Al_{10}$ is reached near 80 min of etching.
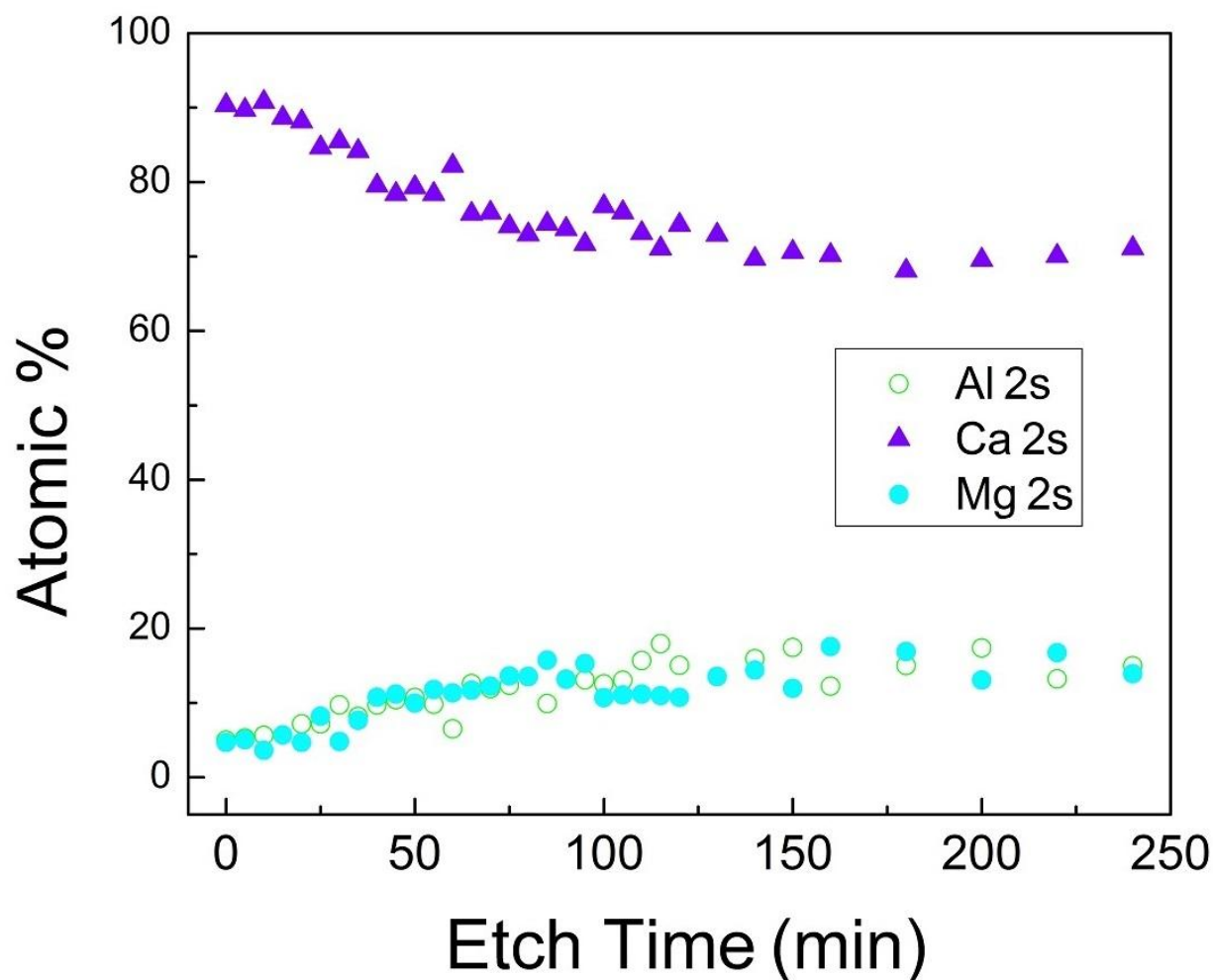
Figure 4.20. *Plot of the relative amounts of Al 2s to Ca 2s to Mg 2s peak areas extracted from XPS full spectrum scans of a $Ca_{75}Mg_{15}Al_{10}$ ribbon, exposed to ambient lab conditions (23% RH, 21.5 °C) for 25 minutes, at different depths after SIMS collection at various Ar etched time depths.*

4.5.4 Standards[3]

To find a depth relation of each calcium compound present in the $Ca_{75}Mg_{15}Al_{10}$ metallic glass, the positions of the Ca 2p peaks must be known for these compounds. The literature spread needs to be narrowed. The way to do this is to measure the different calcium compounds on the same instrument. First, standards of CaH_2 and $Ca(OH)_2$ were fitted to determine the positions of the $CaCO_3$, CaO, $Ca(OH)_2$ and CaH_2 2p peaks.

It is possible to measure the four compounds from these two standards. Traces of CaO remain from the production of $Ca(OH)_2$ and CaH_2. $CaCO_3$ is present in $Ca(OH)_2$ due to its reaction with carbon dioxide. $CaCO_3$ and $Ca(OH)_2$ are present in CaH_2 due to its reaction with humidity and carbon dioxide.
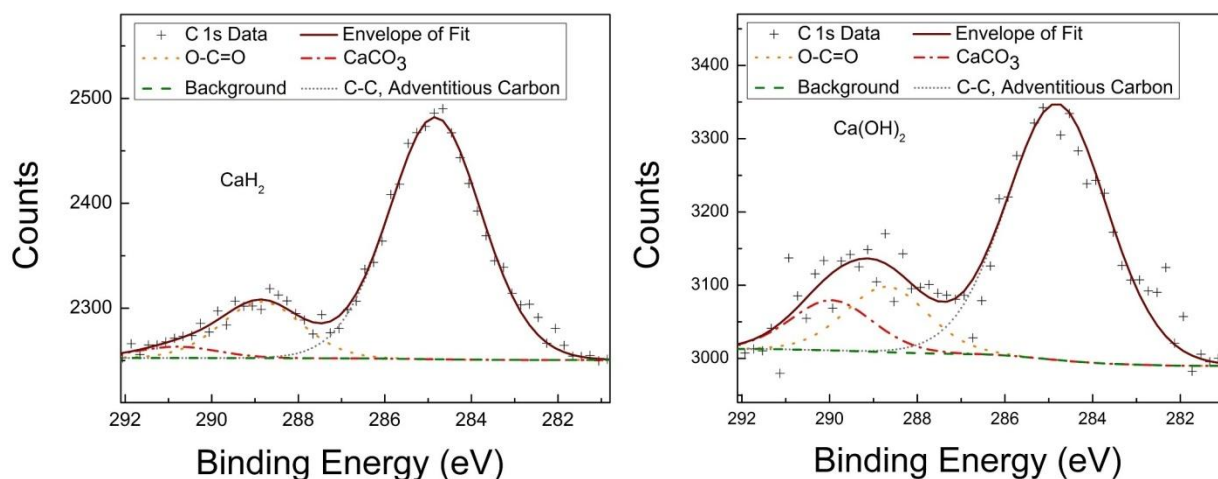
Figure 4.21. *HRXPS scans of the C 1s peak from powder samples of CaH_2 (left) and $Ca(OH)_2$ (right). The O-C=O, $CaCO_3$, and C-C lines are fitted. The C 1s HRXPS data is plotted with black '+' signs. The background is plotted with dark green dashes and the envelope which is the summed fit of all the peaks is plotted with a solid maroon line. The C 1s peaks of O-C=O (yellow dots), $CaCO_3$ (red dash dot dash), and adventitious carbon (C-C) (grey dots) are fitted. The legend is ordered in decreasing value, with respect to the total area under the fitted curves, is C 1s, envelope fit, C-C, O-C=O, $CaCO_3$, and then background.*

---

[3] Note for this section: Figure 5.7 may be helpful in keeping track of the calcium compounds and reactions at room temperature.

To extract the Ca 2p peaks from XPS data, first the samples have to be aligned. All samples have adventitious carbon bonds. As seen in the Ca(OH)$_2$ spectra Figure 4.21, the C 1s line is fitted with three curves. The three peaks correspond with: (1) C-C adventitious carbon to carbon surface bonds, (2) O-C=O adventitious carbon to oxygen bonds, and (3) calcium carbon bond from CaCO$_3$. The envelope fit that traces the data is a combined fit of the three fitted separate peaks. Using the position of the fitted adventitious carbon peak, the C 1s spectra and the other HRXPS spectra are adjusted according to the peak set to 284.8 eV.
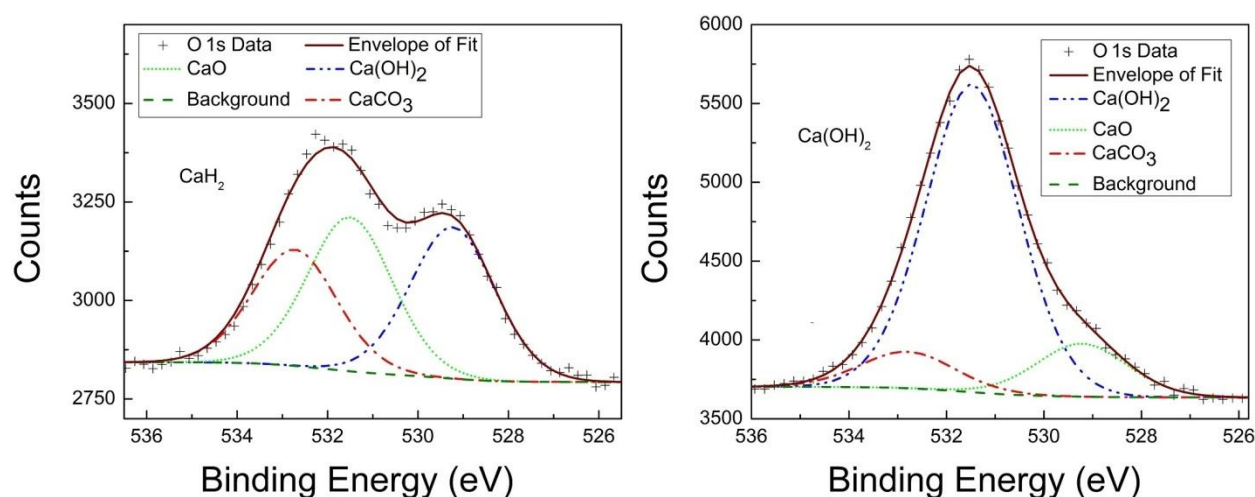
Figure 4.22. HRXPS scans of the O 1s peak from powder samples of CaH$_2$ (left) and Ca(OH)$_2$ (right). The O 1s HRXPS data is plotted with black '+' signs. The background is plotted with dark green dashes and the envelope which is the summed fit of all the peaks is plotted with a solid maroon line. The O 1s peaks of CaO (green dots), CaCO$_3$ (red dash dot dash), and Ca(OH)$_2$ (blue dash dot dot dash) are fitted. The legend is ordered in decreasing values with respect to the total area under the fitted curves.

Once the spectra of the standards are aligned the O 1s line can be fitted. The Figures 4.22 the CaH) spectra, three Gaussian-Lorentzian curves are used to fit the O 1s peak. These peaks are CaO, Ca(OH)$_2$, and CaCO$_3$. The O 1s and C 1s peak show that the two powder standards of CaH$_2$ and Ca(OH)$_2$ have CaO and CaCO$_3$ contaminants present.

Using the ratios of calcium to oxygen in each compound and the area under the three fitted peaks for each of the O 1s lines of $Ca(OH)_2$ or CaH_2, the relative amounts of CaO to $Ca(OH)_2$ to $CaCO_3$ can be determined.
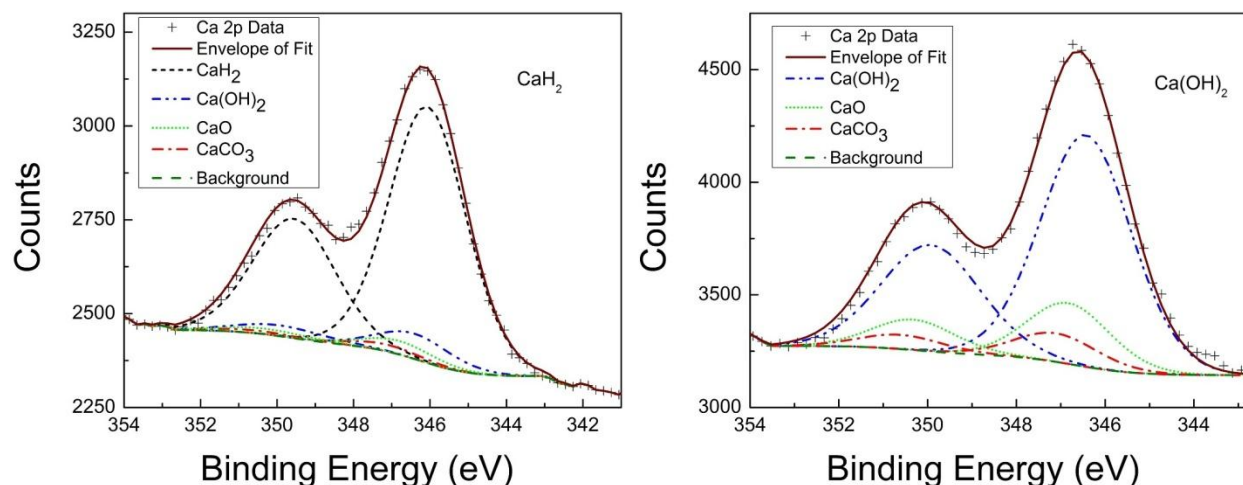
Figure 4.23. *HRXPS scans of the Ca 2p doublet line from powder samples of CaH₂ (left) and Ca(OH)₂ (right). The Ca 2p HRXPS data is plotted with black '+' signs. The background is plotted with dark green dashes and the envelope which is the summed fit of all the peaks is plotted with a solid maroon line. The doublet peaks CaO (green short dots), CaCO₃ (red dash dots), CaH₂ (black short dashes), and Ca(OH)₂ (blue dash dot dots) are fitted. The legend is ordered in decreasing values with respect to the total area under the fitted curves.*

The Ca 2p line of the $Ca(OH)_2$ compound is fitted first in the $Ca(OH)_2$ plot of Figure 4.23. The $Ca(OH)_2$ spectrum does not have CaH_2, but CaH_2 does contain $Ca(OH)_2$. Since in storage conditions, CaO and $CaCO_3$ are possible products from $Ca(OH)_2$ but not CaH_2. CaH_2 reacts readily with water to form $Ca(OH)_2$. The $Ca(OH)_2$ reacts with CO_2 to from $CaCO_3$. Unreacted CaO can be left from the combination of it with water to form $Ca(OH)_2$. Based on energetics, there is no mechanism at room temperature to form CaH_2 from $Ca(OH)_2$. For the $Ca(OH)_2$ spectra, the positions of the CaO, $CaCO_3$ and $Ca(OH)_2$ are determined by using the relative ratios of each determined from the O 1s line and the doublet fitting described earlier.

These now known relative positions of CaO, $CaCO_3$ and $Ca(OH)_2$ can be used to remove their contributions from the CaH_2 spectra of the CaH_2 plot in Figure 4.23. Taking the three Ca 2p positions, combined with their area ratios from the O 1s line of the CaH_2 spectra, and adding a

fourth pair of unconstrained peaks to the Ca 2p line of CaH_2 gives the area and position of the CaH_2 doublet peaks. The summary of all the peak fitting for the C 1s, O 1s and Ca 2p peaks are given in Table 4.5.

Sample	Component	Peak	Position (eV)	Area (eV^2)	% Total Area
CaH_2	CaH_2	Ca 2p $_{3/2}$	346.05	1746.9	66.67
		Ca 2p $_{1/2}$	349.65	873.4	33.33
	$Ca(OH)_2$	Ca 2p $_{3/2}$	346.45	159.7	6.09
		Ca 2p $_{1/2}$	350.05	79.9	3.05
	CaO	Ca 2p $_{3/2}$	346.83	81.7	3.12
		Ca 2p $_{1/2}$	350.43	40.8	1.56
	$CaCO_3$	Ca 2p $_{3/2}$	347.20	41.4	1.58
		Ca 2p $_{1/2}$	350.80	20.7	0.79
	CaO	O 1s	529.23	912.7	35.72
	$Ca(OH)_2$	O 1s	531.50	933.7	36.54
	$CaCO_3$	O 1s	532.73	709.0	27.75
	C-C	C 1s	284.84	630.5	80.32
	O-C=O	C 1s	288.85	129.0	16.43
	$CaCO_3$	C 1s	290.78	25.5	3.25
$Ca(OH)_2$	$Ca(OH)_2$	Ca 2p $_{3/2}$	346.43	2693.3	49.31
		Ca 2p $_{1/2}$	350.03	1346.6	24.65
	CaO	Ca 2p $_{3/2}$	346.80	645.3	11.81
		Ca 2p $_{1/2}$	350.41	322.7	5.91
	$CaCO_3$	Ca 2p $_{3/2}$	347.10	302.8	5.54
		Ca 2p $_{1/2}$	350.70	151.4	2.77
	CaO	O 1s	529.22	803.8	13.09
	$Ca(OH)_2$	O 1s	531.47	4767.3	77.61
	$CaCO_3$	O 1s	532.80	571.4	9.30
	C-C	C 1s	284.81	816.0	72.39
	O-C=O	C 1s	288.74	190.0	16.85
	$CaCO_3$	C 1s	290.10	121.3	10.76

Table 4.5. *List of the of measured compound peak locations from binding energies of the peaks from Ca 2p, O 1s, and C 1s XPS lines. The data was taken using HRXPS scan resolution of powder samples of CaH$_2$ and Ca(OH)$_2$.*

For the Ca 2p fits of $Ca_{75}Mg_{15}Al_{10}$, an additional Mg KL_1L_1 peak had to be fitted. Survey spectra of MgO were used. The MgO standard provided a ratio between the Mg 2s or Mg 1s line

to the Mg KL_1L_1 line. The size of the Mg KL_1L_1 contribution to the Ca 2p is found by measuring the Mg 2s and Mg 1s line data from the $Ca_{75}Mg_{15}Al_{10}$ survey scans. The relative amount of Mg changes as layers of the sample milled away. From the size of the Mg 2s or Mg 1s line at each layer the contribution of Mg KL_1L_1 is inferred from the known ratio of the lines. With the compound positions and Mg KL_1L_1 positions known, the relative concentrations of the calcium compounds in various etch depth times can be extracted from the $Ca_{75}Mg_{15}Al_{10}$ HRXPS Ca 2p data. Table 4.6 list these extracted values.

Etch Time (min)	Percent of Ca 2p Peak				
	Ca	$CaCO_3$	CaH_2	CaO	$Ca(OH)_2$
0	4.76	57.77	27.35	10.01	0.11
5	3.69	0.34	89.2	0.83	5.94
10	10.27	0	87.62	1.55	0.56
30	23.14	0	76.33	0	0.54
35	23.41	0	75.6	0.04	0.94
50	25.78	0	74.22	0	0
80	36.1	0	63.76	0	0.14
240	60.91	0	39.09	0	0

Table 4.6. *List of the percent area of the HRXPS scanned Ca 2p doublet that Ca, CaO, CaCO₃, CaH₂, and Ca(OH)₂ doublets have as a function of depth of Ar etching of a ribbon of Ca₇₅Mg₁₅Al₁₀ exposed to ambient lab conditions (23% RH, 21.5 °C) for 25 minutes.*

4.6 SIMS Measurements

SIMS was collected between XPS measurements. The SIMS data are used to determine the relative ratios between different collected ions. The ions collected are etched from the surface of the calcium ribbons through Ar ion milling. SIMS has the advantage over other characterization techniques since it can detect H ions. The SIMS setup used can detect positive or negative ions.

4.6.1 Standards

First, SIMS standards of CaH_2 and $Ca(OH)_2$ were taken to determine if SIMS could be used to differentiate the two. Also the standards were used to determine whether positive or negative ions were better suited for studying the calcium metallic glasses. Powder samples of $Ca(OH)_2$ and CaH_2 were employed. Scans of 0.1 to 65 amu were taken for either negative ions or positive ions.
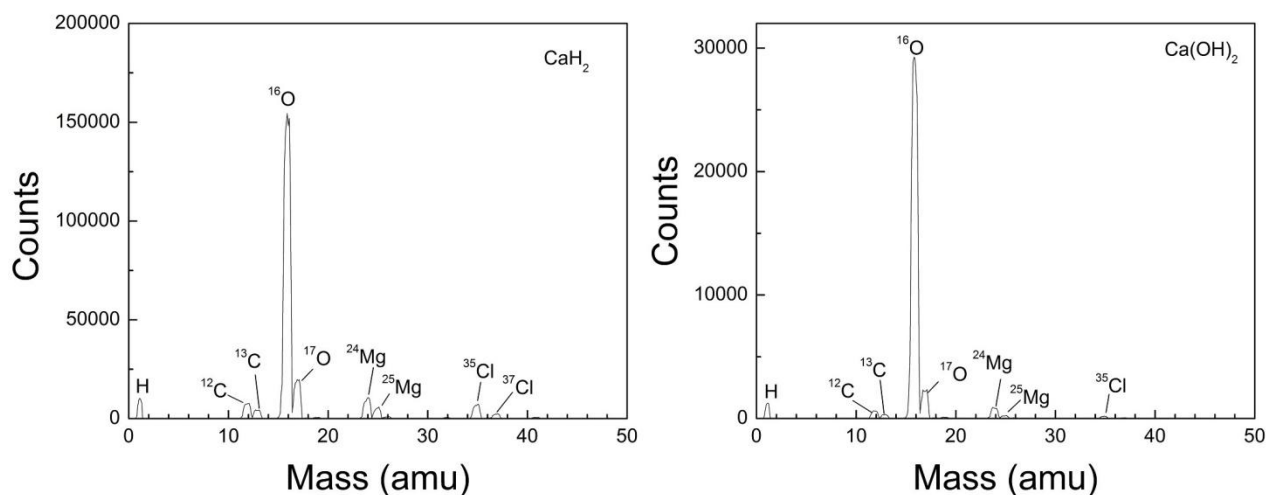
Figure 4.24. *Plots of negative ion SIMS from powder samples of CaH₂ (left) and Ca(OH)₂ (right).*
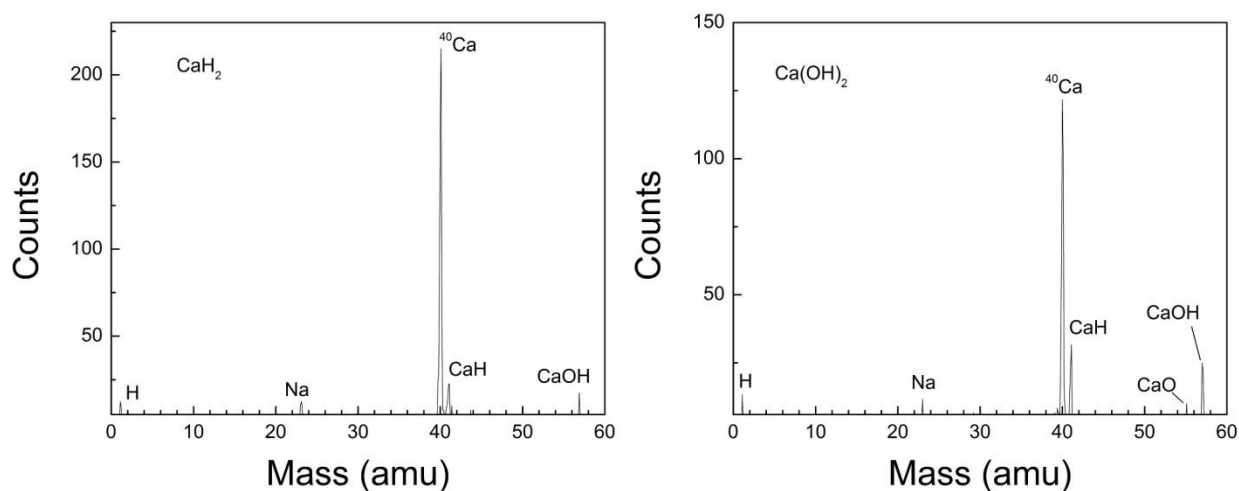
Figure 4.25. *Plots of positive ion SIMS from powder samples of CaH₂ (left) and Ca(OH)₂ (right).*

Figure 4.24 shows the negative ions that are collected from the two standards and Figure 4.25 shows the positive ions. The negative ions collected were H, ^{12}C, ^{13}C, ^{16}O, ^{17}O, ^{24}Mg, ^{25}Mg, ^{35}Cl, and ^{37}Cl. The positive ions collected were H, Na, ^{40}Ca, CaH, CaO and CaOH. The ions of H, CaH, O, and CaOH are present from the powder compounds. C is always present in any surface science experiment. Traces of contaminants of Mg, Na and Cl are known to be present from the assays of calcium compounds.
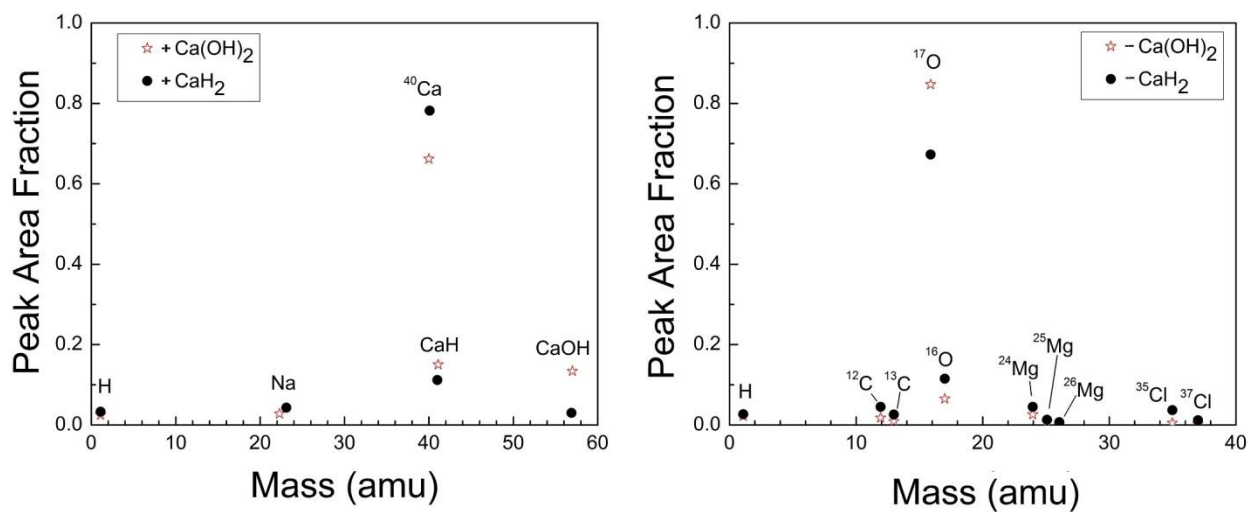
Figure 4.26. *Comparison of the fraction of total area to individual peaks of the positive ion and negative ion SIMS spectra from powder samples of CaH$_2$ (left) and Ca(OH)$_2$ (right) as a function of atomic mass.*

An effective way to compare the four plots in Figures 4.24 & 4.25 is by comparing the peak area fraction of the compounds in positive SIMS and negative SIMS. The derived plots in Figure 4.26 show that for the positive ions both standards have the same ions present, but Ca(OH)$_2$ has more CaOH as expected. CaH$_2$ has CaOH ions since CaH$_2$ reacts readily with humidity to form Ca(OH)$_2$ and SIMS is a surface sensitive technique. Figure 4.26 shows that the biggest difference between negative ions from the two standards is that Ca(OH)$_2$, as expected, has more O negative ions. CaH$_2$ also has an O peak. This is due to CaH$_2$ reacting readily with moisture in the air to form Ca(OH)$_2$.

The results show that hydrogen can be detected using either positive or negative ion collection, though positive ion collection is of greater use for the calcium glass system since it detects the Ca, CaH and CaOH ions additionally. For positive or negative SIMS collection, the spectra of pure CaH$_2$ and Ca(OH)$_2$ can be distinguished. If a sample had an unknown ratio of the

two, it is harder to differentiate the two. Positive SIMS is more useful for this experiment. It will show where the H, Ca, CaH or CaOH ions are present, and XPS of the same layer will determine the quantitative amounts of the calcium compounds.

4.6.2 Data Collection Optimization
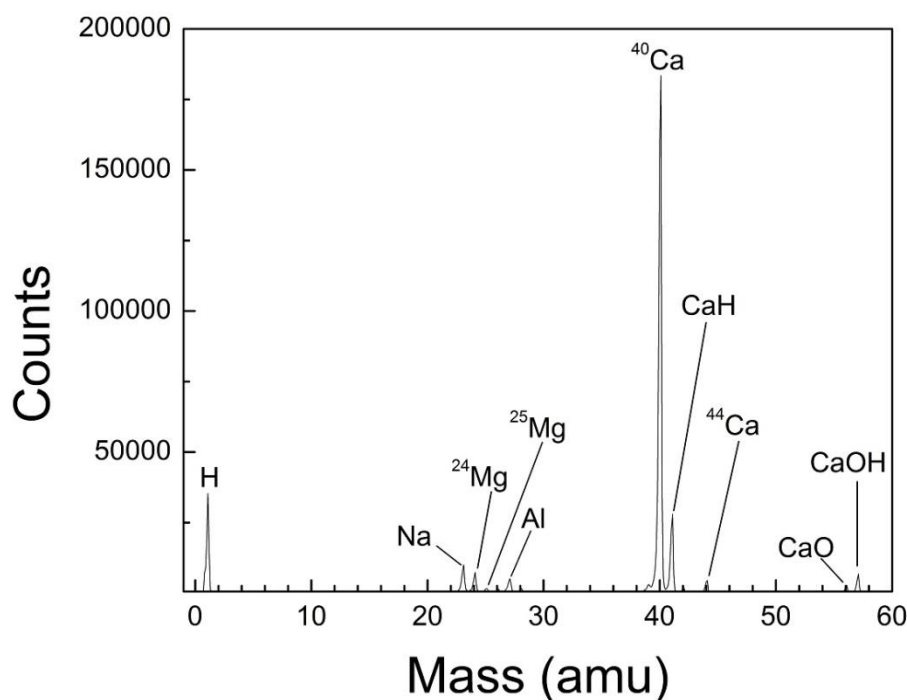
Figure 4.27. *Positive SIMS from a $Ca_{75}Mg_{15}Al_{10}$ metallic glass ribbon exposed to ambient lab conditions (23% RH, 21.5 °C) for 25 minutes.*

Figure 4.27 has a SIMS spectra of a $Ca_{75}Mg_{15}Al_{10}$ metallic glass ribbon. The positive SIMS scan contains all the expected Ca ions. Additionally there is Na, which is present in the same relative amount as in the CaH_2 and $Ca(OH)_2$ standards. In addition to the assays, this gives further credence that the presence of Na is a contaminant associated with calcium compounds.

The positive SIMS spectrum of the Ca75Mg15Al10 ribbon also has Mg and Al positive ions. This spectrum allows for the comparisons of ^{40}Ca, Al, ^{24}Mg, CaOH, CaH and H ions. It was

collected with parameters of a scan range of 0.4 to 75 amu with a step size of 0.1 amu and a dwell time of 200 ms.

To increase the amount of non-trivial SIMS data collected, the parameters were changed to scan ranges of 0.1 amu windows around several peaks of interest with dwell times of 500 ms. The peaks collected were a back ground signal (22 amu), H (1.1 amu), ^{24}Mg (24.1 amu), Al (27 amu), ^{40}Ca (40.05 amu), CaH (41.05 amu), and CaOH (57.05 amu). For the pertinent peaks, these adjustments increased by close to forty fold the data collected.
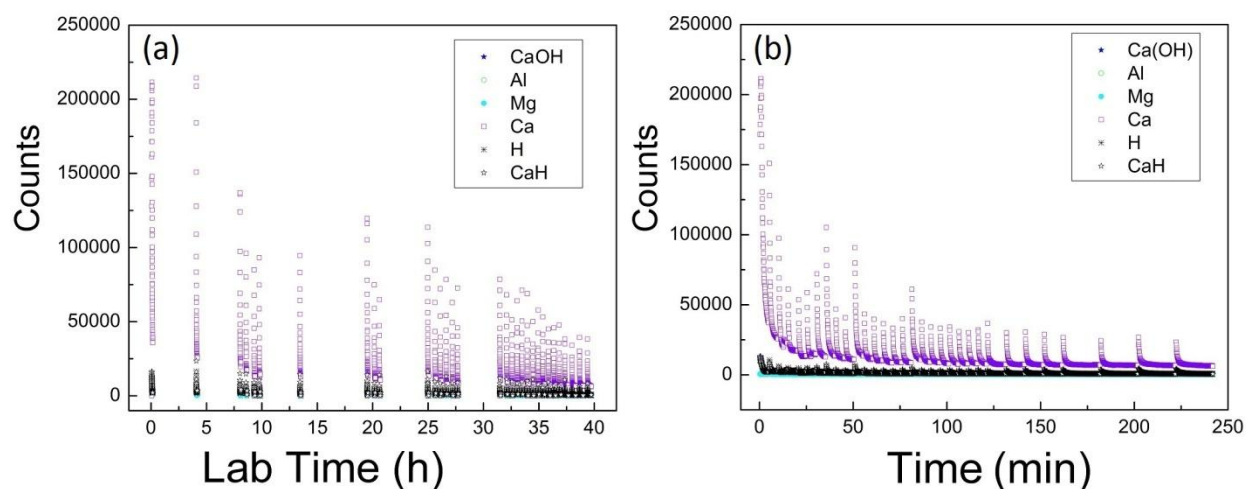
Figure 4.28. *Two plots of SIMS scan data from a ribbon of Ca$_{75}$Mg$_{15}$Al$_{10}$ exposed to ambient lab conditions (23% RH, 21.5 °C) for 25 minutes. (a) is the lot of SIMS scans as a function of continuous collection time or lab time in hours. (b) is a plot of SIMS scans plotted as a function of Ar etching time in minutes. The data are compressed with the understanding that individual compounds are difficult to resolve. These will be more clearly displayed in later plots. Here the point is to highlight the spacing between data sets in (a) and in (b) the total collection time with the gaps in (a) removed.*

A plot of the raw SIMS data, as collected as a function of real lab time, is displayed in the plot, Figure 4.28a. The horizontal spaces between the data points are due to XPS collection. Larger spaces are HRXPS while smaller spaces are full spectra survey XPS data collections. When data are compressed to remove the XPS gaps it is seen in the time plot of Figure 4.28b that the total Ar etch time is approximately 240 min. The next chapter will show that this effect does not hinder data analysis.

The observation is that the signal in Figure 4.28b starts out strong and then diminishes with time. This is due to the instrumentation setup. Given that the composition is constantly changing as the surface is etched away, the collection parameters were first optimized on the initial surface of the sample. The signal is initially higher since the system is optimized for collection of data at the starting surface which is more of an insulator in characteristics. As the sample is milled away from the initial surface layer, it becomes more metallic and the collection is not as optimized as it was before. If the detector is changed to optimize at each new layer, the baseline for comparing each layer to the next will be lost.

It is apparent from these data that as the sampled is milled there are upwards tails that occur at the start of each new mill session. These tails on the first half of each SIMS collection show a more insulating nature. They can be removed to give a clearer picture of what is occurring in the material. Later in Chapter 5, the nature of these tails and why they can be removed will be explained.
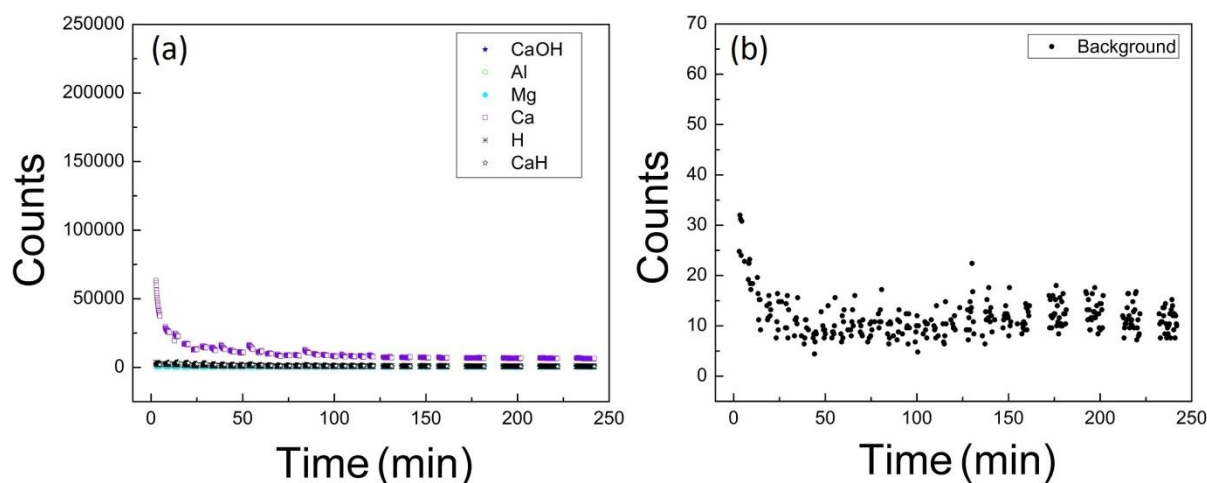
Figure 4.29. Two plots of SIMS scan data, from a ribbon of $Ca_{75}Mg_{15}Al_{10}$ exposed to ambient lab conditions (23% RH, 21.5 °C) for 25 minutes, plotted as a function of Ar etching time. (a) is a plot of the second half of all the positive ion SIMS data scans. (b) is a plot of the second half of each background signal (22 amu) SIMS data scan.

The truncated data appear in Figure 4.29a. To extrapolate the signal further, the data are processed by averaging every 5 points. The plot of the signal divided by (normalized) the background signal, plot in Figure 4.29b, illustrates that the signal starts out optimized then

decreases for the first 30 minutes of etching. It then remains constant for the rest of the SIMS experiment. The other data collected normalized by the background data, as seen in Figure 4.30, shows each ion without the influence of the detector.
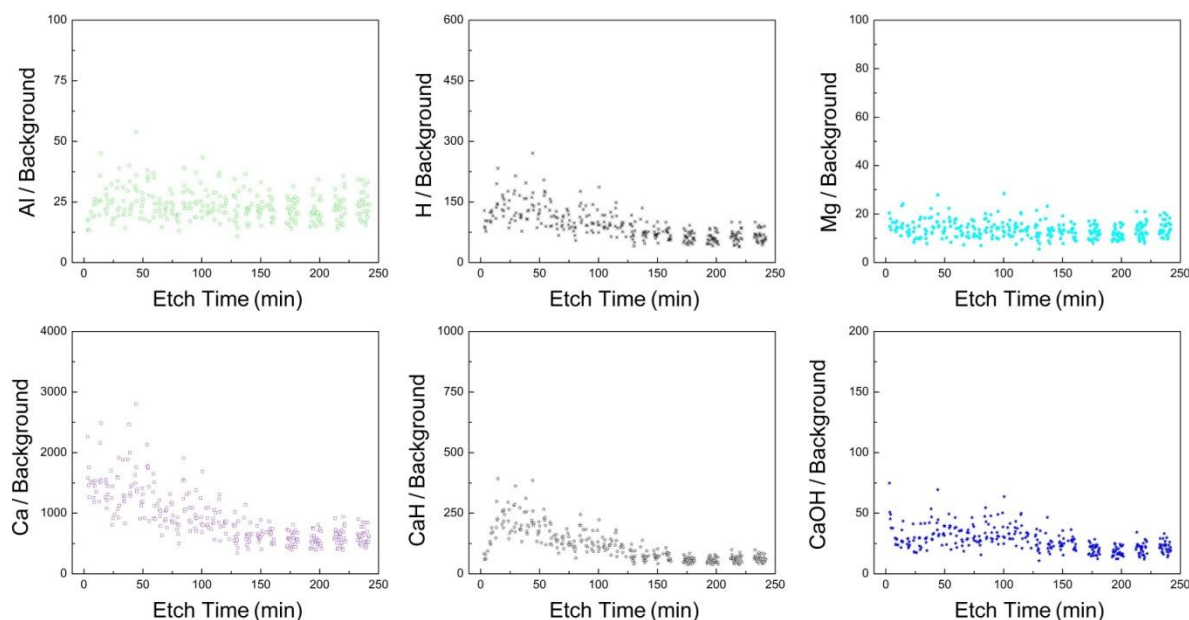
Figure 4.30. *Individual positive ion SIMS data plots, from a ribbon of $Ca_{75}Mg_{15}Al_{10}$ exposed to ambient lab conditions (23% RH, 21.5 °C) for 25 minutes, normalized by the background signal taken at 22 amu.*

4.6.3 SIMS Ratios

An important point about SIMS is that the intensities do not correspond directly to quantitative amounts. Standards are needed to turn the data into quantitative data. SIMS standards are not easy to do particularly for Ca-based alloys as noted below. Hence all SIMS plots here are plotted as a function of etching time.

To have quantitative SIMS with an analytical accuracy of better than ±20% requires the use of standards. SIMS ion yields can vary by several orders of magnitude [230]. This variation is known as the SIMS matrix effect. For quantitative SIMS, these standards are necessary since

secondary ion yields are dependent on the impurity species and its surrounding matrix. Different chemical environments will change the sputtered ion yields. The local bonding can significantly affect the ion yield. To remove this effect, standard samples must contain the impurity species in a known chemical matrix. For the case here, first the milling rate of pure calcium using Ar must be known. Then the mill rate can be compared to a sample with a known ratio of $Ca(OH)_2$ to metal calcium and similar for other calcium compounds. These sample would be difficult if not impossible to create given how quickly calcium and its compounds can react with humidity in the environment.

While quantitative SIMS will not work here, the relative ratios will. The ratios do not require standards since they are directly comparing ions originating from the same conditions in the matrix. The one requirement is that the settings of the detectors are not changed. Thus if the SIMS detector is optimized for the surface composition that is different from an interior composition, the strength of the signal will change as the matrix changes.
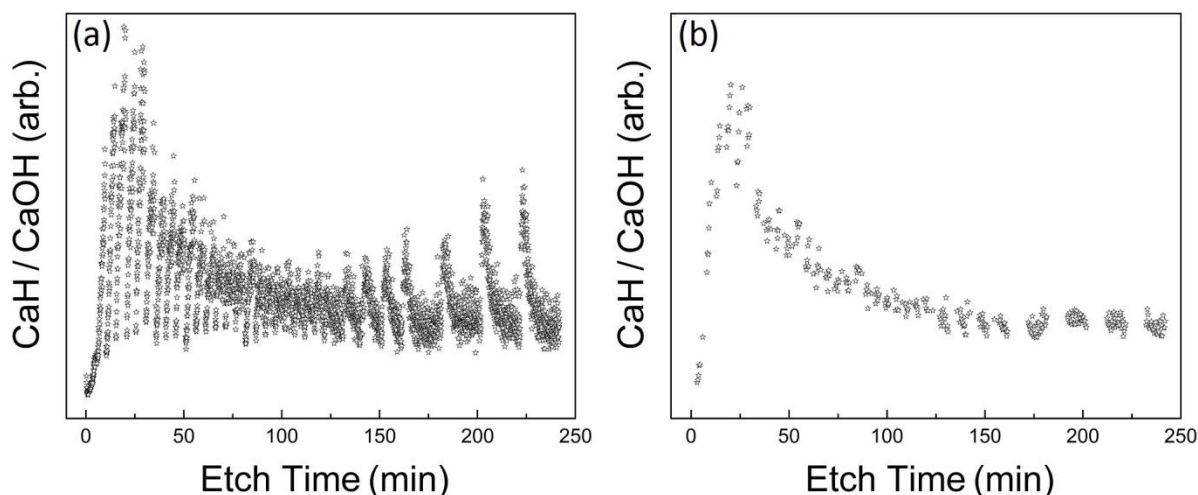
Figure 4.31. *Full SIMS data plot, from a ribbon of $Ca_{75}Mg_{15}Al_{10}$ exposed to ambient lab conditions (23% RH, 21.5 °C) for 25 minutes, of (a) the ratio of CaH to CaOH ions compared to (b) only the second half of each SIMS data scan of the ratio of CaH to CaOH ions.*

Taking the relative ratios, of the individual ions from Figure 4.29a, like CaH to CaOH with all the data or the truncated SIMS data yields the two plots in Figure 4.31. The truncated data plot Figure 4.31b shows the trend between the two ions as a plot with etch time, while that same trend is buried in the full data plot with all the tails.

4.6.4 Validity of SIMS Measurements

There are two checks for the validity of the SIMS data. The first is of a ribbon of $Ca_{75}Mg_{15}Al_{10}$ that had been scanned using 0.4-75 amu length spectra. The ratios of the area under the ^{40}Ca and the ^{44}Ca peaks for all the spectra taken yields the plot in Figure 4.32.

Figure 4.32. *SIMS data plot, from a ribbon of $Ca_{75}Mg_{15}Al_{10}$ exposed to ambient lab conditions (23% RH, 21.5 °C) for 25 minutes, of the relative ratio of ^{44}Ca to ^{40}Ca ions compared with the empirical known ratio.* These SIMS data, as expected, are centered on the empirically known ^{44}Ca to ^{40}Ca isotope ratio of 0.022 [192].

The second check is plotting the SIMS data from the 0.1 amu window scans with XPS survey scan data of the Mg 2s and Al 2s lines. The data in the bulk of the material from 150 minutes on are then tied to the known ratio value of Mg to Ca (0.2) and Al to Ca (0.133) from

SEM EDS data. This yields Figure 4.33. Here it is seen that the XPS, SIMS and SEM data are self-consistent for the bulk alloy composition made from pure elements.
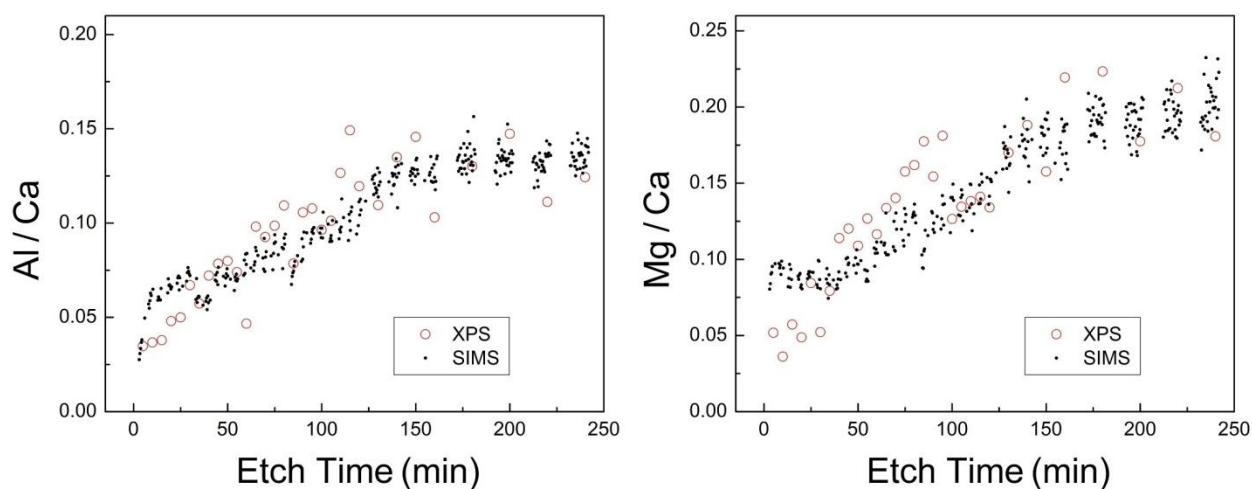
Figure 4.33. *SIMS and XPS data of the Al to Ca ion ratio (left) and the Mg to Ca ratio (right) normalized with SEM EDS data from an as spun ribbon of Ca$_{75}$Mg$_{15}$Al$_{10}$ exposed to ambient lab conditions (23% RH, 21.5 °C) for 25 minutes.*

The checks are useful as a sanity check since all the SIMS data will be relative ratios. The y-axis of the ratio intensity will be without a scale since the number will not have a quantitative meaning due to the difficulty of obtaining standards in a Ca system. In conjunction with HRXPS data, the SIMS data will explain how the surface reaction is enabling the embrittlement of the calcium metallic glass ribbons.

Chapter 5 - Summary and Discussion of Experimental Results

5.1 Experimental Humidity Test Mandrel Failures and PPZ Size Ductility Relationship

Chapter 4 presented all the methodology in the collection, selection, and reduction of data. This chapter uses these methods presenting an analysis of the reason for embrittlement. The data from Table 3.3 and Figure 3.1 show that calcium glasses are ductile when calcium does not transfer electrons, maintaining a metallic electron configuration around the calcium atoms. When calcium transfers electrons to surrounding atoms the result is a brittle glass. Current experiments show an initially ductile glass exposed to the atmosphere would rapidly deteriorate, becoming brittle. To test for the individual atmosphere components, originally ductile ribbons were divided into sets. One set was exposed to ambient lab conditions as a control set[4] and another set was exposed to isolated high purity gases, plus a set exposed to high humidity. These experiments were able to isolate the embrittling component of the environment, i.e., humidity. What remains to be investigated is whether there is causational relationship between electron transfer and the role of humidity with the mechanism causing embrittlement of the once ductile calcium amorphous ribbons. Figure 5.1 shows the effect of high lab humidity on the embrittlement process of marginally ductile $Ca_{75}Mg_{15}Al_{10}$ metallic glass ribbons.

---

[4] A reminder: Control sets are the sets that have been immediately exposed to ambient lab conditions following being melt spun. Test sets are the sets that were immediately exposed to a gas, a humidity level, or a vacuum following being melt spun.
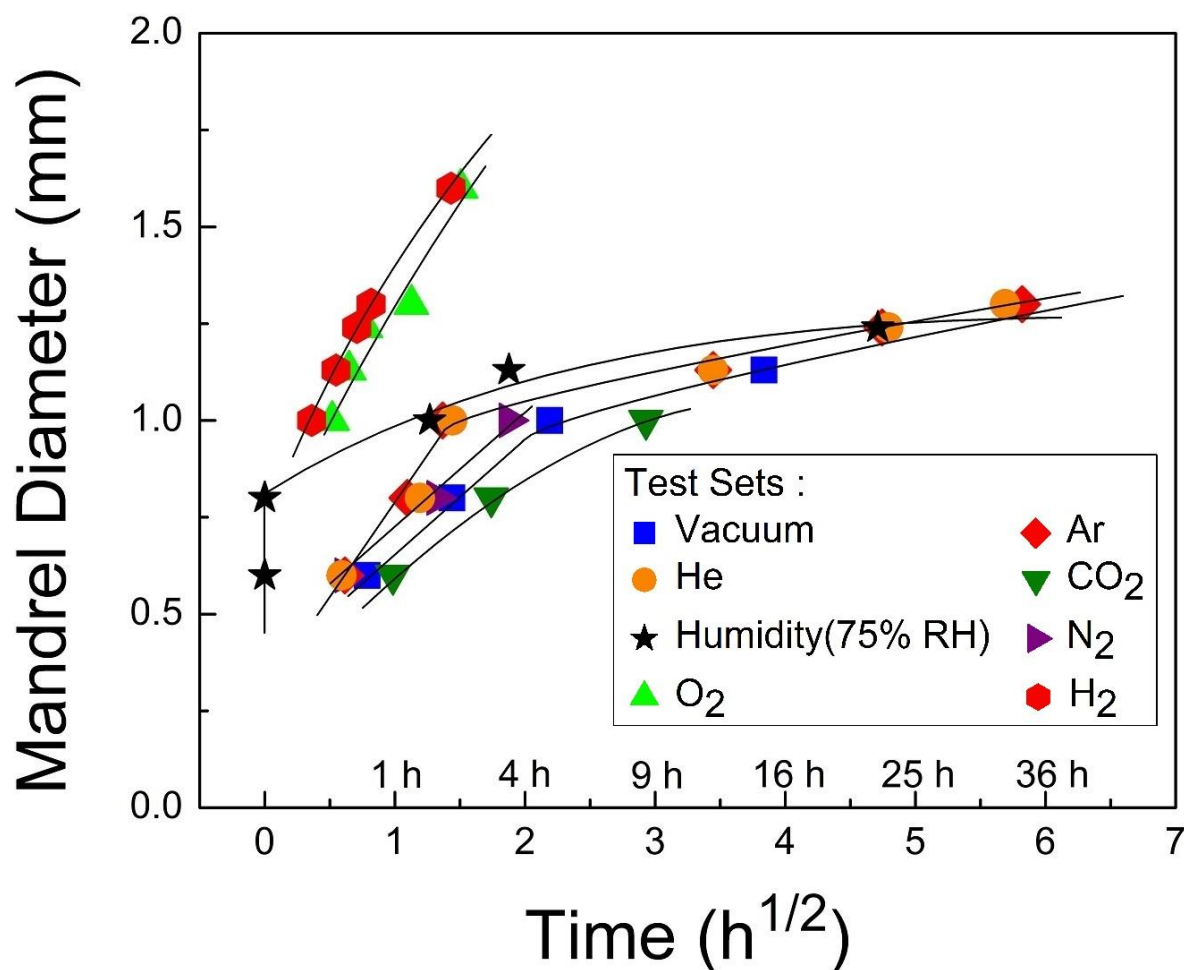
Figure 5.1. *Combined plot of mandrel diameter failures of $Ca_{75}Mg_{15}Al_{10}$ ribbons as a function of time. Each test set was exposed to an individual ambient lab condition test. Same as Figure 4.9b but with tracer lines added to all the test sets to act as a guides to group the data points.*

The control sets are combined in one plot, Figure 4.9a. The ribbons exposed to lower initial lab humidity (25% RH) take longer to fail than those exposed to high initial humidity (60% RH). Also, for the case of low initial humidity, they fail at one rate for the first 1-2 hours; then the rate changes to a slower one. This dual failure rate is also noted when comparing data from two thermal relaxation sets, Figure 5.2. It is assumed that the second slow rate would show up on the other sets if the experiment had been carried out for longer times.
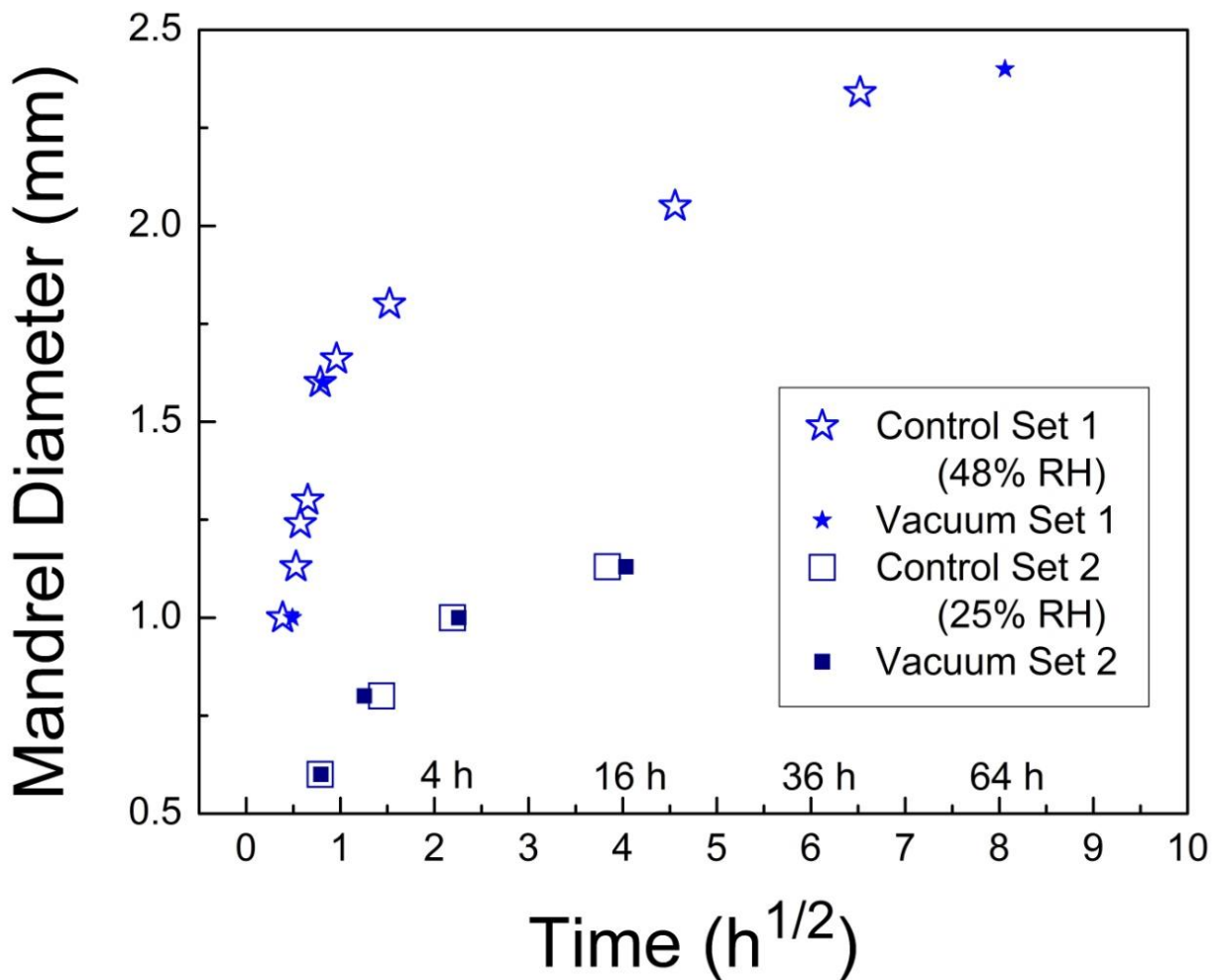
Figure 5.2. Two separate mandrel failure thermal relaxation tests conducted in different initial ambient lab humidity conditions. The vacuum test is for thermal relaxation since the control set and the vacuum set will both experience the same thermal conditions. The control set 2 and vacuum test set 2 data taken with initial lab humidity at 25% RH are replotted from Figure 4.5b with added sets of a control and vacuum test set taken prior at a higher initial lab humidity of 48% RH.

The results of the bend-over-mandrel tests show that upon removal from the controlled humidity chamber the ribbons fail the first two mandrel sizes immediately, Figure 4.8. This was not the case for ribbons placed in other gases or those tested for thermal relaxation. The test sets follow failure rates similar to control sets, except for the humidity test condition. This indicates that humidity is the likely source of the embrittlement. A paired test and control set compared to other paired set have different rates of failure due to their initial humidity they experience when the batch is divvied in ambient lab conditions. From known interactions discussed in Section

1.7.5, it is seen that calcium interacting with water vapor can produce $Ca(OH)_2$. This $Ca(OH)_2$ layer creation is a source for elemental hydrogen. The free H is absorbed by the calcium alloy. The absorbed H penetrates the ribbons forming ionic salts. These ionic bonds result in embrittlement of the calcium glasses. The compounds created though interaction with water vapor, their bond energies, and their depth of interaction are shown in the next section. The following sections demonstrate all the mechanisms and compounds associated with embrittlement.

5.2 SIMS and XPS Concurring Results

5.2.1 HRXPS Data

The XPS data in Figure 5.5 show how deep, in units of etch time, the layers of the calcium compounds are and their quantitative percent. After the location of the Ca 2p peaks of Ca, CaH_2, $Ca(OH)_2$, CaO, and $CaCO_3$ were determined, these values are plotted with values extracted from the literature in Figure 5.3. The values are found in Table 4.4 and Table 4.5. The literature has a range in values over a short energy range. Normally this difference would be tolerable, but for the Ca 2p peaks, these values need to be accurate. There is little room for error when measuring these compounds since they are all close to one another and the resolution on the XPS has the peaks all overlapping.
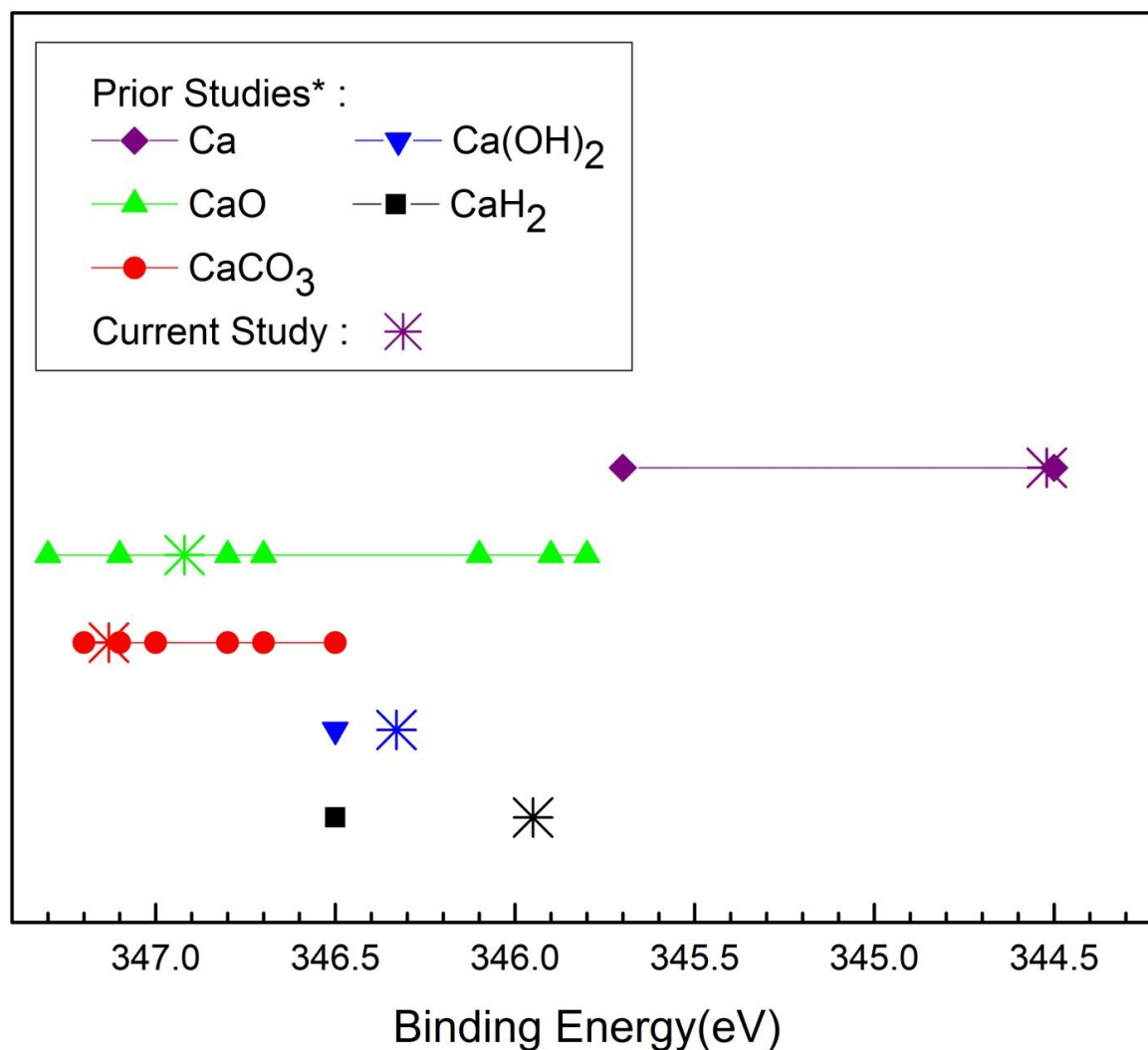
Figure 5.3. *Plot of the binding energies of various calcium compounds determined in this work and listed in Table 4.5 compared with the values that have been extracted from published literature listed in Table 4.4. The values of Ca (purple diamonds), CaO (green upward triangles), $CaCO_3$ (red dots), CaH_2 (black squares), and $Ca(OH)_2$ (blue downward triangles) were determined by HRXPS measurements.*

The different values in the literature are due to the use of different setups, analysis techniques, and measuring only one or two compounds on the same setup to determine the Ca 2p peaks. Also, only one study has a value for CaH_2 [220] and another one only has a value for $Ca(OH)_2$ [223]. The current values determined here align with what is expected for metallic as compared to insulating systems. A chemical shift in the Ca 2p doublet means that there is a change in its binding energy due to a change in the electrons surrounding the Ca atom. Hydroxides and other compounds have a higher binding energy since the electron density around

the Ca atom is lower. The most metallic behavior is characterized by lower binding energy with binding energy increasing as materials become more insulating in nature.

Next, to show where the formation of CaH_2 is occurring, a ribbon of $Ca_{75}Mg_{15}Al_{10}$ was milled. The milling proceeded until the bulk stoichiometry was reached. The concentration of Ca to Mg to Al is found as a function of etch time by sampling the full spectrum XPS survey spectra. A plot for the relative concentration of Ca to Mg to Al as a function of this etch depth is Figure 4.20. This plots show the bulk composition is reached around 125 minutes of etch time. With these Ca 2p peak locations, the HRXPS spectra are able to reveal where the five calcium compounds are located within the ribbon.
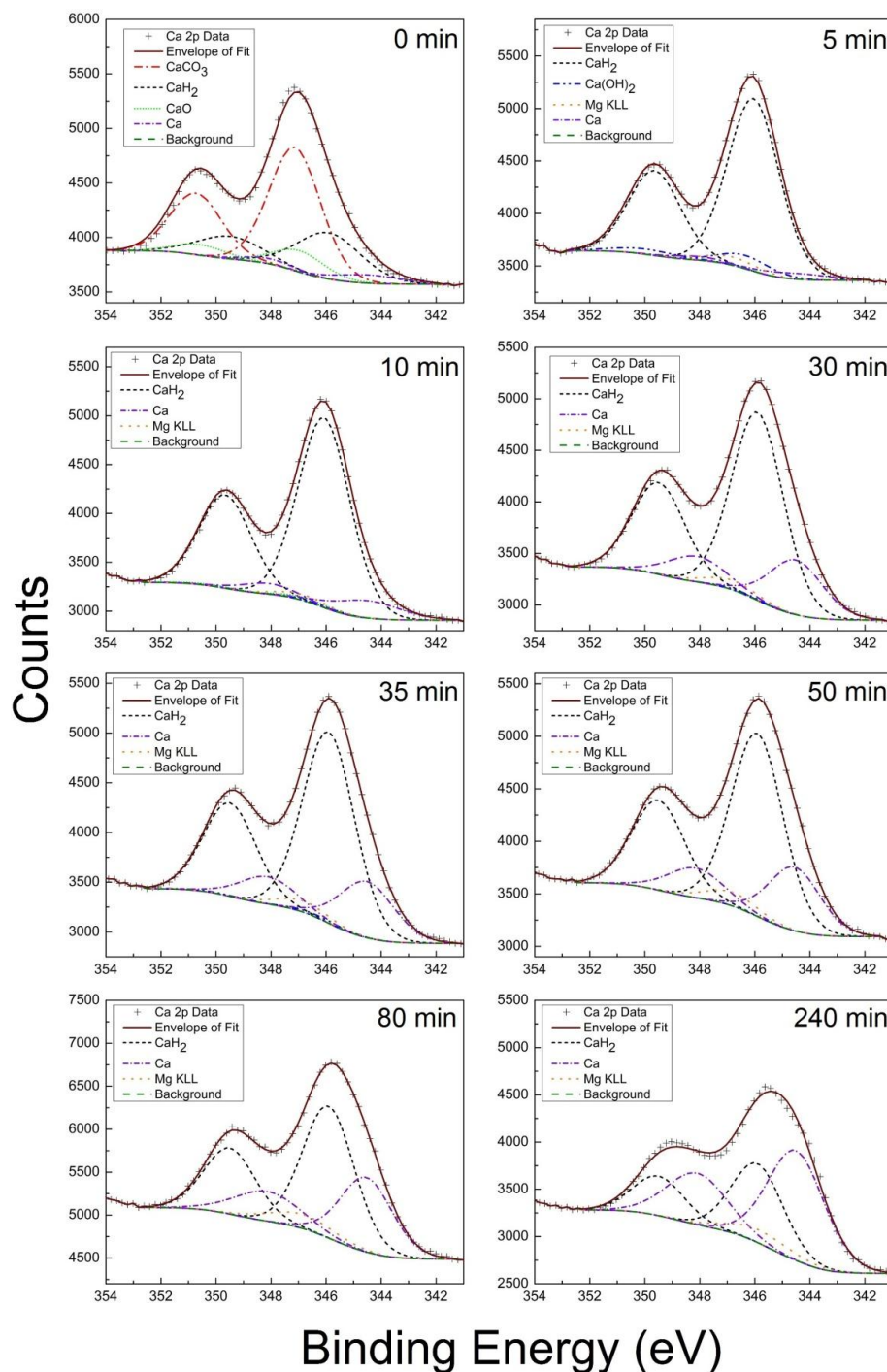
Figure 5.4. *Fitted HRXPS scans of the Ca 2p doublet line from a ribbon of $Ca_{75}Mg_{15}Al_{10}$, exposed to ambient lab conditions (23% RH, 21.5 °C) for 25 minutes, at various etch depths denoted in the figure as etch times. The eight times of Ar etching are 0, 5, 10, 30, 35, 50, 80 and 240 minutes. The unprocessed Ca 2p HRXPS data are plotted with black '+' signs. The background is plotted with dark green dashes. The envelope which is the summed fit of all the peaks is plotted with a solid maroon line. The doublet peaks are fitted with peaks of CaO (green short dots), $CaCO_3$ (red dash dots), CaH_2 (black short dashes), $Ca(OH)_2$ (blue dash dot dots), Ca (purple short dash dots), and Mg KLL (orange dots). The legend is ordered in decreasing values with respect to the total area under the fitted curves.*

Figure 5.4 shows that the surface is mainly $CaCO_3$ with a trace of CaO and metallic Ca. After 5 minutes of Ar ion etching, the $CaCO_3$ is gone and there are trace amounts of CaO present. The trace amounts are list in Table 4.6. This layer is mainly CaH_2 and $Ca(OH)_2$. After a total of 10 minutes of etching, the $Ca(OH)_2$ layer is only left in trace amounts and the metallic Ca amount is starting to increase. At 30 minutes etch time this layer is three parts CaH_2 to one part Ca. While $Ca(OH)_2$ remains in trace amounts for further mill times, the ratio of Ca to CaH_2 changes. At a point between 80 minutes of etch time and 240 minutes, the amount of metallic Ca becomes greater than CaH_2. This point is estimated to be around 170 minutes of etching. This inversion point is estimated from the HRXPS Ca compound data summarized by Figure 5.5.
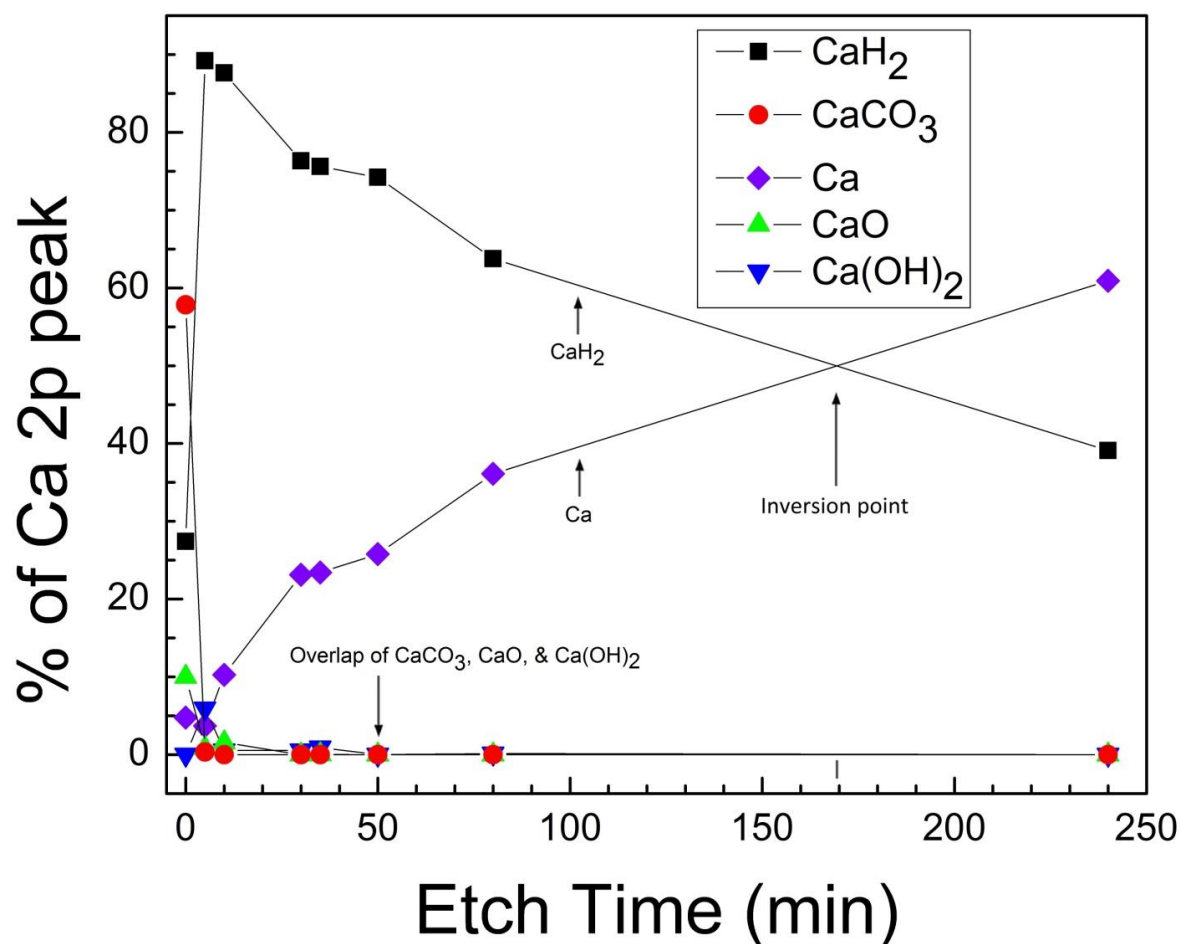
Figure 5.5. *Plot of the percent area of the HRXPS scanned Ca 2p doublet that Ca (purple diamonds), CaO (green upward triangles), $CaCO_3$ (red dots), CaH_2 (black squares), and $Ca(OH)_2$ (blue downward triangles) has as a function of depth of etching from a ribbon of $Ca_{75}Mg_{15}Al_{10}$ exposed to ambient lab conditions (23% RH, 21.5 °C) for 25 minutes. A trace line is added for each compound to be able to distinguish trends.*

These data show that CaH_2 is present in large quantities, peaking near the surface. XPS and SIMS are both surface measurement techniques. XPS measures the first several nanometers of the composition. Relative to SIMS, which samples the atoms of the surface layer; XPS is more of a bulk technique. The surface sensitivity of SIMS is crucial to process and interpret the etching results.

5.2.2 SIMS UHV Growth Data

The SIMS data in Figure 5.6 shows the relative ratio of CaH to CaOH. For the first 80 minutes of etching there are initial downward pointing tails to the data (see figure caption for definition). There is then a transition period for roughly 40 minutes. For the last 120 minutes there are upward tails. These tails are new growth that is forming on the sample surfaces during XPS measurements. The cause of these tails is once again the interaction of water vapor with the calcium metallic glass ribbon, even at a vacuum of 10^{-9} Torr.
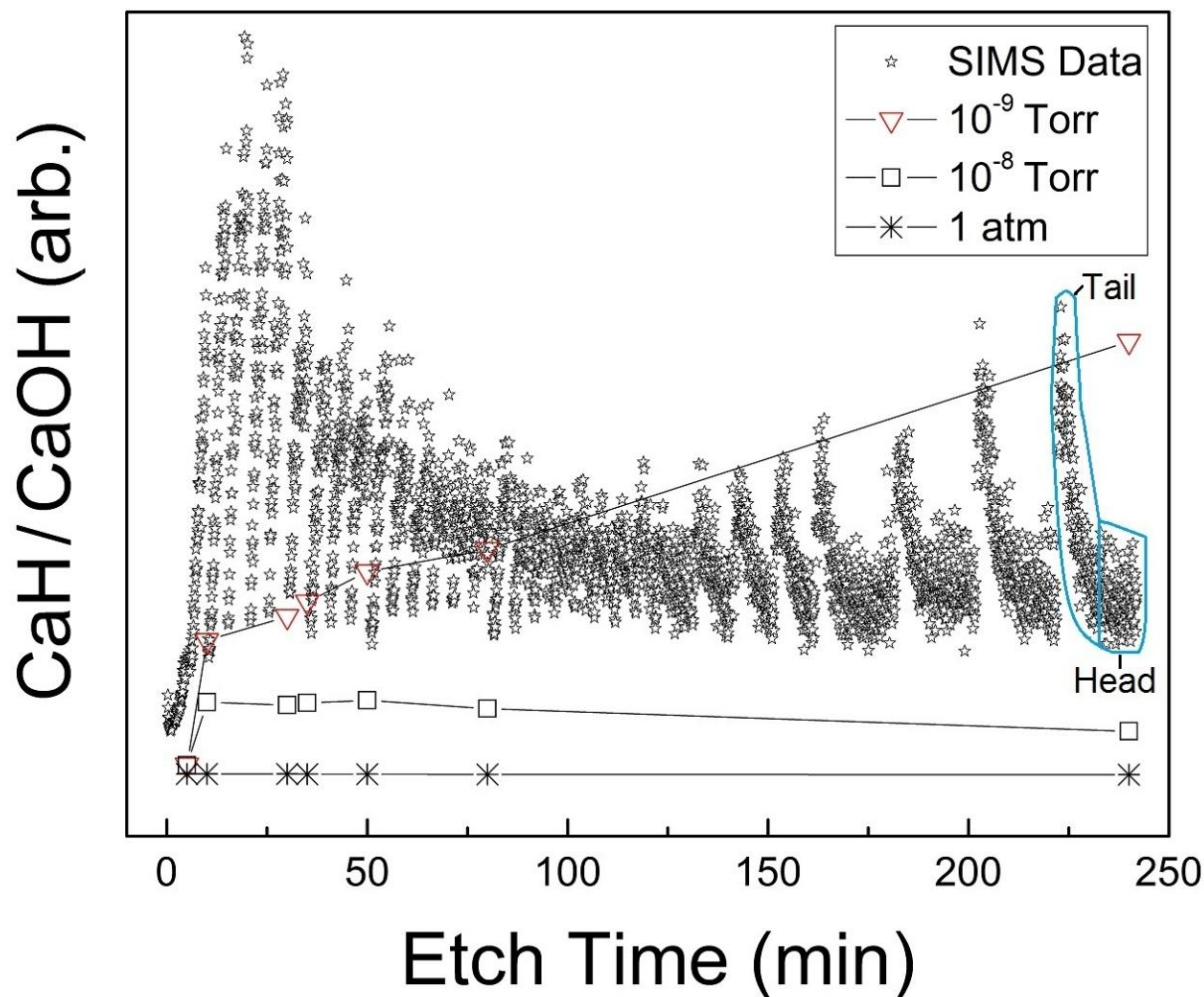
Figure 5.6. *Plot of the SIMS ion ratio of CaH to CaOH from the etching of a ribbon, of*
$Ca_{75}Mg_{15}Al_{10}$ *exposed to ambient lab conditions (23% RH, 21.5 °C) for 25 minutes, with the*
initial tails of the SIMS data fitted with data from a model using water vapor concentrations at
different pressures. Each star ☆ represents the ion ratio concentration at a given etch time. Each
of the three traces represents a different vacuum condition. The symbols: downward red
triangles ∇ are for 10^{-9} Torr, black squares □ are for 10^{-8} Torr, and the eight point stars ✷ are
for 1 atm and are meant to track the top of each growth tail of the CaH ions for the various
vacuum conditions. The definition of head and tail for a single SIMS data session is identified in
the plot. The scale is arbitrary. By taking a ratio, the systematic errors of the experimental setup
have been removed, but the quantitative amount of each ion cannot be determined, only the
relative amount between the two.
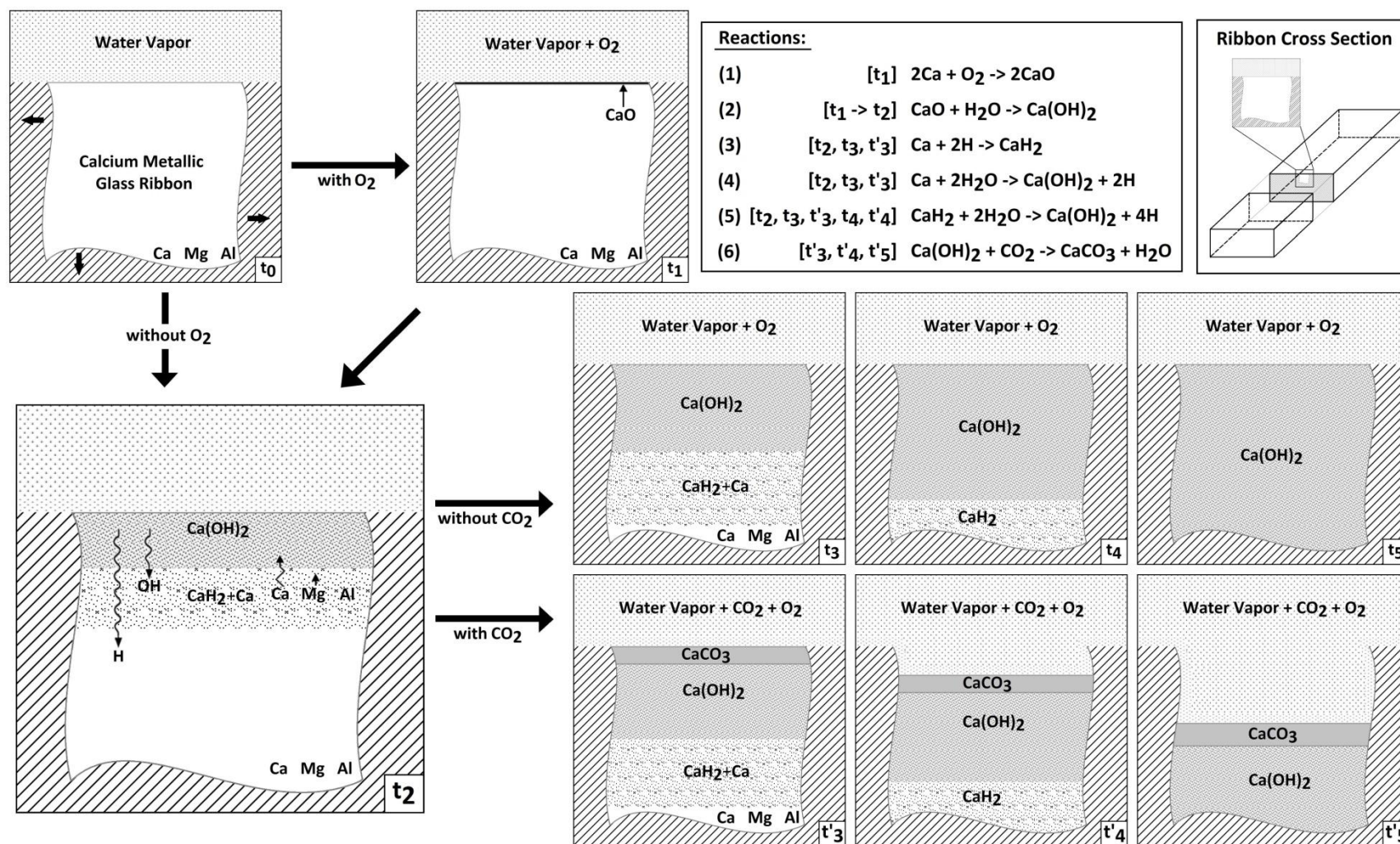
Figure 5.7. *Sketch of the ribbon cross section, not drawn to scale,* of *a ribbon of $Ca_{75}Mg_{15}Al_{10}$ as it experience exposure to water vapor; water vapor ;and O_2; and water vapor, O_2 and CO_2. The ribbon cross section box demonstrates where the hypothetical sample is taken, from the middle of the ribbon. Different snapshots of how the layers of calcium compounds through the ribbon layers will appear are shown. The different time slices 't_i' are numerically indexed with increase in time. The different possible path ways are path 1: $t_0 \rightarrow t_1 \rightarrow t_2 \rightarrow t_3 \rightarrow t_4 \rightarrow t_5$, path 2: $t_0 \rightarrow t_1 \rightarrow t_2 \rightarrow t'_3 \rightarrow t'_4 \rightarrow t'_5$, and the same two without t_1. Path 1 had an interaction with O_2 that creates CaO which is converted into $Ca(OH)_2$ by time t_2. Path 2 in the CO_2 containing path. In this path $CaCO_3$ is formed and spallation occurs as seen in Figure 4.4. Path 1 is the route for the humidity experiment. The snapshot at t_2 includes information about the movement of the various ions derived from SIMS and XPS results. The reaction square lists the possible reactions and in which path or snapshot they occur.*

These data can be roughly fitted with a simple model, described below. This model is based on the four common reactions Equations [2]-[5] in Figure 5.7 that Ca and Ca compounds have with water vapor at room temperature. Figure 5.7 is a sketch of the reactions that are and could occur in ambient lab conditions between Ca glass ribbons, O_2, CO_2, and water vapor. Of the pathways described in the figure caption, pathway 1 is the closest to the process occurring in a controlled humidity chamber. This model fits approximately the tip of new growth tails. The size of these layers can be estimated by the rate of surface growth in a ultra-high vacuum (UHV). For every hour of XPS scan, there is a 1 nm of growth on the sample at the 10^{-9} Torr [231].

The model employed is described as follows. It is based on data of the Ca compounds and metal Ca present from HRXPS data. It extrapolates the future surface growth based on the four known reactions, Equations [2]-[5] in Figure 5.7, of Ca and Ca compounds when water vapor is present. It also takes into account the relative amount of water that is present. It can be varied from the known concentration of water vapor as percentage of atmosphere given a relative humidity at 1 atm to the concentration of water at UHV. The amount of water present at the UHV condition combined with the four Ca reactions, assuming uniform duration of growth, and the concentration of each compound as a percent of total surface, yields an estimate of the amount of each Ca compound in the growth layer. The amount of the composition's growth on the surface combined with the HRXPS measured results, gives the total of each composition on the new growth monolayers.

Here the ratio of CaH to CaOH is obtained from the SIMS data and then scaled to that of the measured SIMS CaH to CaOH ratio. This fit is seen in Figure 5.6. Then juxtaposition fits at 10^{-8} Torr and 1 atm are plotted. As expected from prior measurement, when calcium is exposed to water vapor at 1 atm the growth layer is dominated by $Ca(OH)_2$ formation. It is noted that the rates cannot be quantitatively accessed. Figure 5.6, is the qualitative ratio of CaH to CaOH ions. While the tails appear large for later (150+ minutes) or earlier (5-75 minutes) etch times, it is only the relative difference of the two ions formed that is large. The physical quantities of newly grown compounds containing CaH or CaOH ions maybe low.

At UHV the rapid growth of CaH_2 is dependent on two factors. One, the greater the amount of $Ca(OH)_2$ present on the surface, the more it acts as an inhibitor of CaH_2 to form in UHV. Hence, when the last trace of $Ca(OH)_2$ is gone from the bulk HRXPS data after 80 minutes, there is an inversion in tail direction, from downward $Ca(OH)_2$ tails to upward CaH_2

tails. Factor two is the very small concentration of water in the UHV. If there were more water, the reaction would be dominated by the formation of $Ca(OH)_2$.
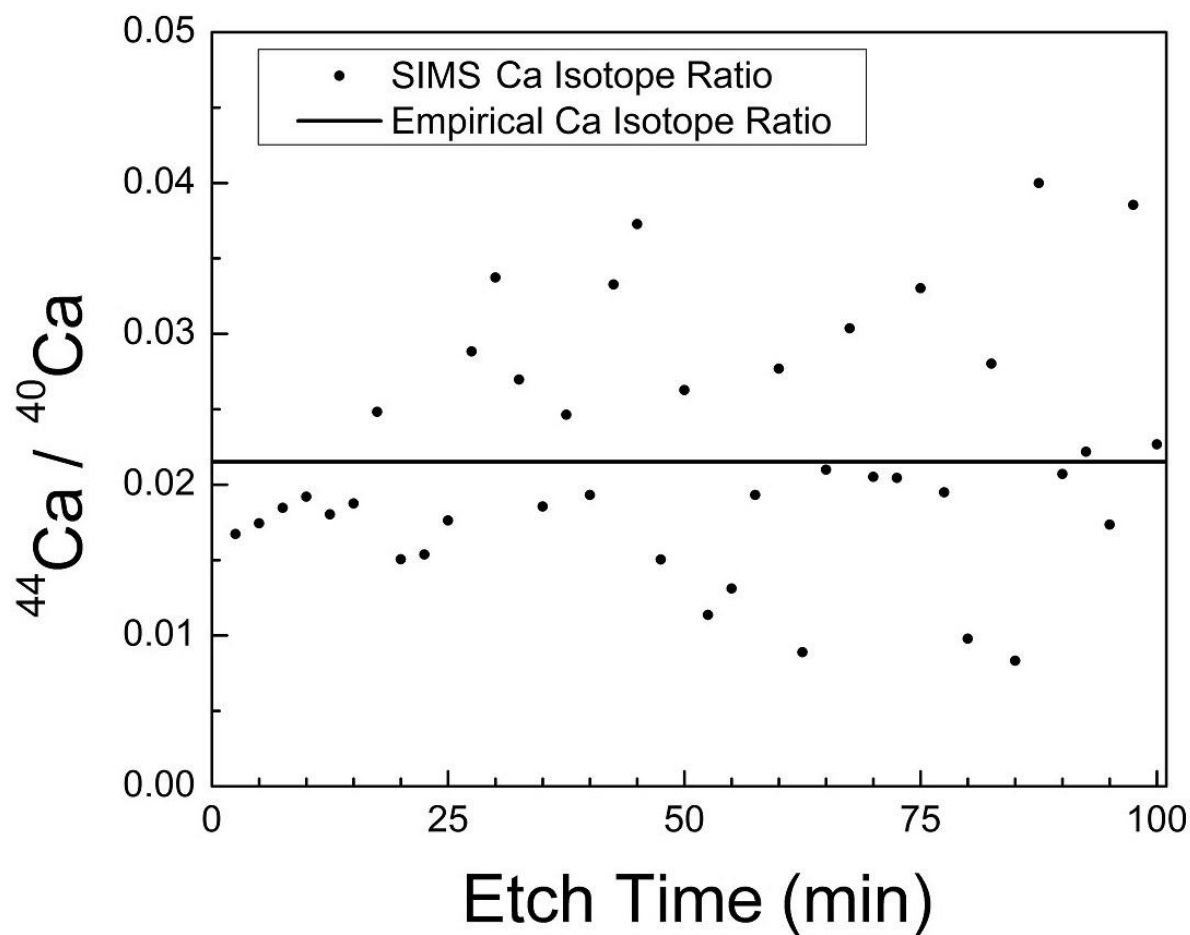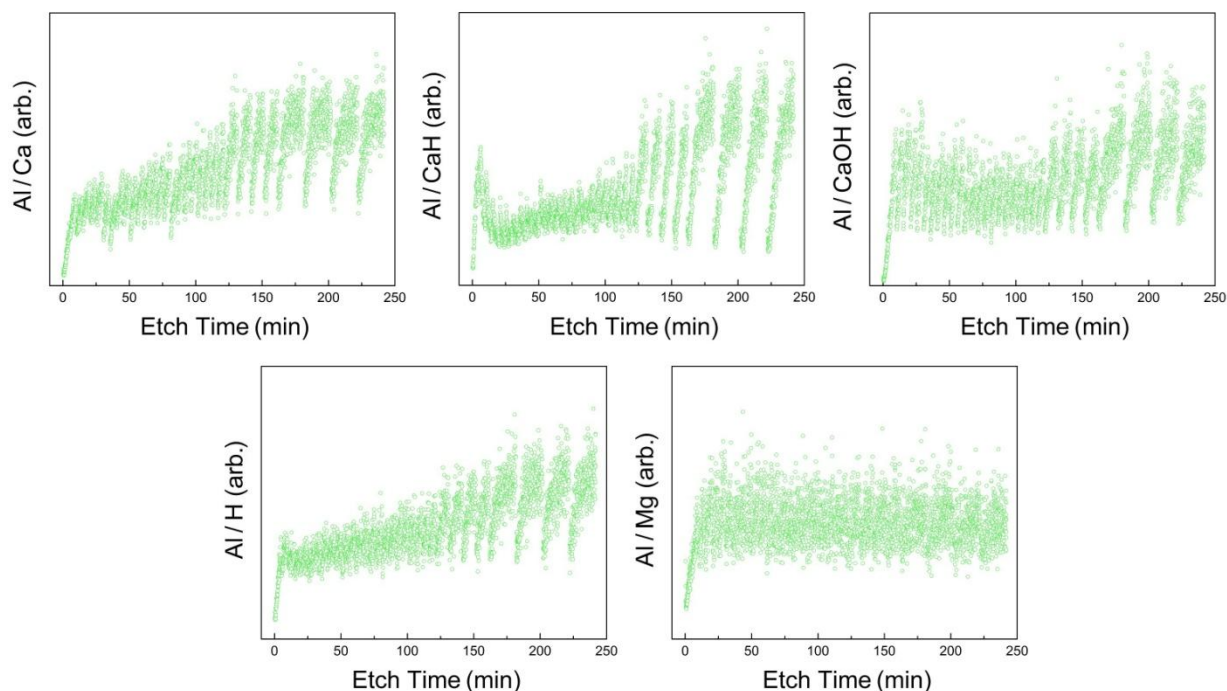

Figure 5.8. *Full SIMS data, from a ribbon of $Ca_{75}Mg_{15}Al_{10}$ exposed to ambient lab conditions (23% RH, 21.5 °C) for 25 minutes, for the ratios Al to Ca, CaH, CaOH, H, and Mg ions. These plots demonstrate the heads and tails as highlighted in Figure 5.6. The direction of the tail indicates which compound is present in a higher relative amount. If pointed downward the denominator is present in greater amounts. If pointed upward the numerator of the ratio is present in greater quantities. If no discernible tails are present then the ions are present in a fixed ratio through the SIMS sampling session of interest. Each green circle ○ represents the ion ratio concentration at a given etch time. The scale is arbitrary. By taking a ratio the systematic errors of the experimental set up have been removed, but the quantitative amount of each ion cannot be determined, only the relative amount between the two is determined.*

Additionally, looking at the SIMS ratio plots, Figure 5.8 of Al to Ca, CaH, CaOH, H or Mg it is seen that all but the Al to Mg ratio have tails pointing downward. This indicates an increase in either calcium or hydrogen compounds depending on which ratio is being examined. The ratios of Al to Ca and Al to CaOH have downward tails for the whole duration of the etch. The ratios of Al to CaH and Al to CaH have prominent downward tails from 125 minutes etch on. These four ratios imply that there are Ca compounds forming during the whole SIMS experiment during each pause for XPS data collection. In particular, the first 125 minutes are

dominated by CaOH ion containing compounds and after that it is dominated by CaH ion containing compounds. Supporting the data seen in Figure 5.6. Additionally, the ratios of Al to Mg and Al to Ca ratios in the first 10 minutes of etch indicate a depleted concentration of Al relative to the bulk. Furthermore, as expected, there are no obvious tails in the Mg-Al ratio since the amount of Al to Mg remains constant, except on the initial milled surface.
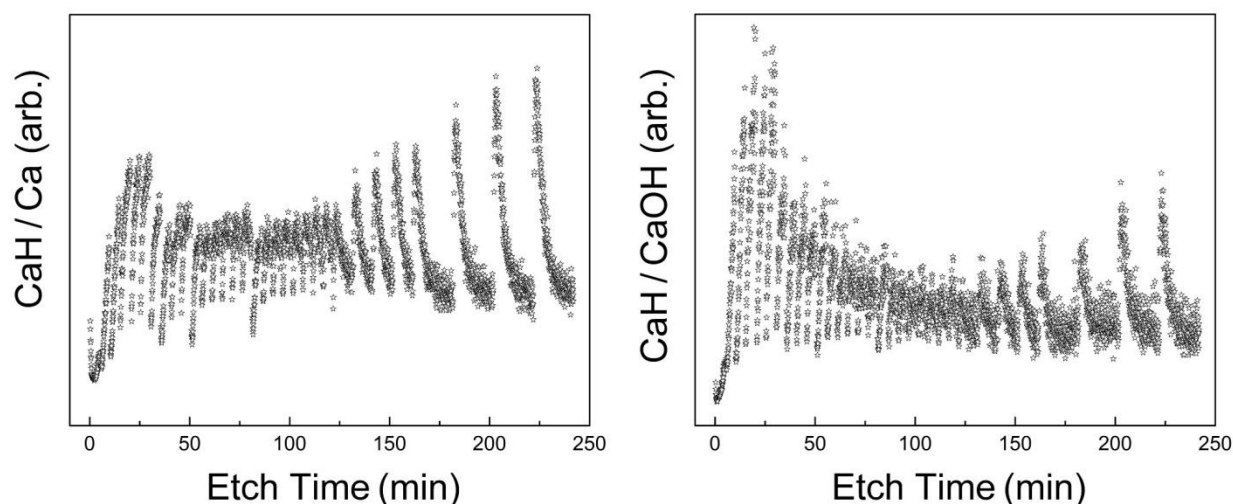
Figure 5.9. Complete raw SIMS data sets of the ratios of CaH to CaOH and CaH to Ca, from a ribbon of $Ca_{75}Mg_{15}Al_{10}$ exposed to ambient lab conditions (23% RH, 21.5 °C) for 25 minutes. These plots demonstrate the heads and tails as highlighted in Figure 5.6. The direction of the tail indicates which compound is present in a higher relative amount. If pointed downward the denominator is present in greater relative amounts. If pointed upward the numerator of the ratio is present in greater relative quantities. If no discernible tails are present then the ions are present in a fixed ratio through the SIMS sampling session of interest. Each star ☆ represents the ion ratio concentration at a given etch time. The scale is arbitrary. By taking a ratio the systematic errors of the experimental set up have been removed, but the quantitative amount of each ion cannot be determined only the relative amount between the two is determined.

Other self consistent checks are the CaH to CaOH and CaH to Ca ratios, in Figure 5.9. For the CaH to CaOH ratio, the tails are noted to be downward for the first 80 minutes with CaOH formation dominant. After 120 minutes the tails are all upward with CaH_2 formation dominant. Even though the Ca signal is a convolution of Ca from metallic Ca, CaH_2, and $Ca(OH)_2$, the tails still show that for the first 125 minutes of etch time there are calcium compounds that are not CaH_2 that are forming, but, after that point, CaH_2 tails are a majority.

The assumption that the tails can be removed from the data in Sec. 4.6.3, which will then

leave only the data of the bulk sample is demonstrated to be valid by the evidence seen in Figures 5.6, 5.8, & 5.9. The remaining data traces reveal what is occurring in the bulk of the sample and not from the in situ creation of new surface data.

5.2.3 Positive SIMS Ion Ratio Data

Based on analysis given in Section 4.6.1 positive ions are selected for analysis here. After removing each of the new growth surface contributions occurring during XPS measurements from the SIMS ratio data, the bulk data that is left tells the story of how the calcium glass ribbon looked at its initial state when loaded into the UHV. For the trimmed SIMS bulk, each ion ratio is presented in separate plots relative to the other five ions collected. The order of presentation is from most independent to dependent of the ions, where independence is based on the interactions between ions. For example, Ca, Mg, Al and H are independent from each other, while CaH and CaOH are not independent from Ca. From order of most independent to least are first Mg and Al, followed by CaH, CaOH, H and then Ca.
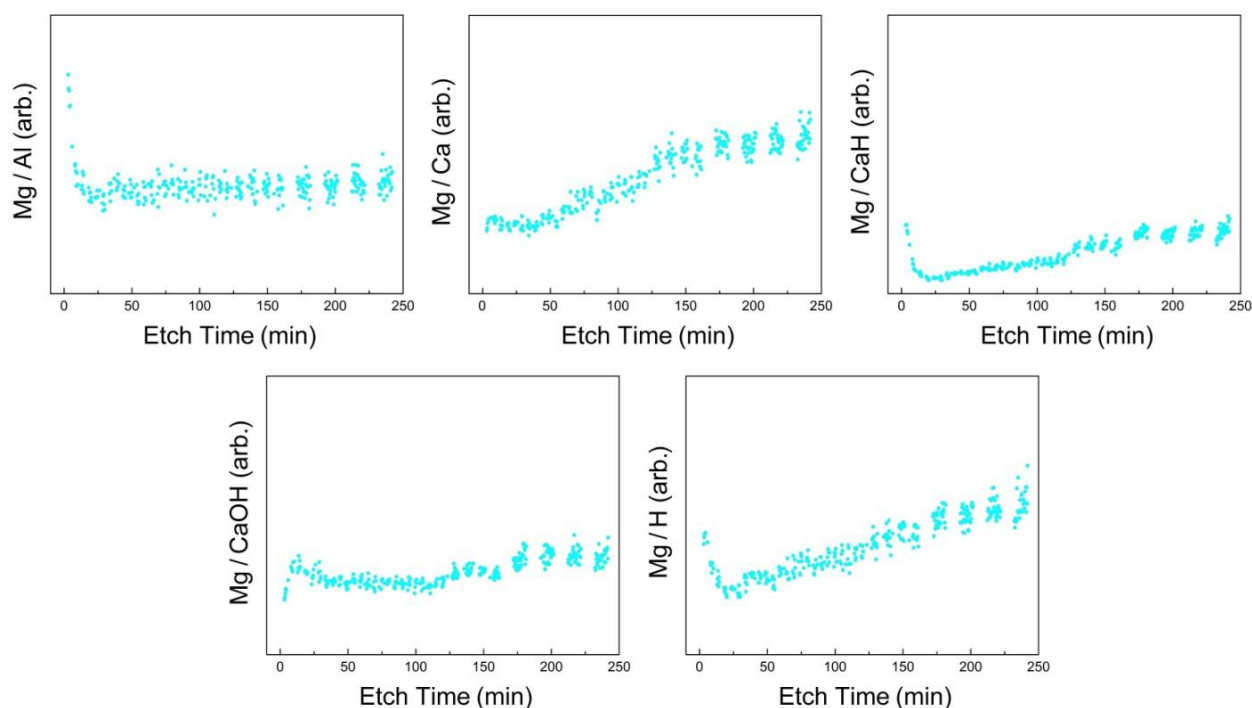
Figure 5.10. *Plot of the last half of each SIMS data scan, from a ribbon of Ca$_{75}$Mg$_{15}$Al$_{10}$ exposed to ambient lab conditions (23% RH, 21.5 °C) for 25 minutes, for the ratios Mg to Al, Ca, CaH, CaOH, and H ions. Each data point (solid light blue circle ●) represents the ion ratio concentration at a given etch time. The scale is arbitrary. By taking a ratio the systematic errors of the experimental set up have been removed, but the quantitative amount of each ion cannot be determined, only the relative amount between the two is determined.*

       Figure 5.10 contains the five Mg SIMS ratios. Initially there is more Mg than Al present on the surface. After 20 minutes of Ar ion etching the ratio of Mg to Al is constant and does not change as the sample is further etched. From the XPS full spectrum Figure 4.20 it is noted that the quantitative values of Al and Mg increase going into the bulk. From this ratio it appears that the two are increasing at roughly the same rate. Comparing the Mg to Ca ratio, initially the amount of Ca is greater at the surface and the ratio to Mg remains constant for roughly the first 25 minutes etch. This corresponds with most calcium compounds of CaO, CaCO$_3$, Ca(OH)$_2$ and CaH$_2$ from XPS. The Ca is being extracted from the bulk to form the calcium compounds. The amount of Mg relative to Ca increases with time before leveling off at 150 minutes and beyond. This also corresponded with the survey XPS scans leveling off in Ca around 150 minutes.

For the ratio of Mg to CaH, the surface has less CaH_2 than the bulk, hence the initial high ratio of Mg to CaH. The surface, known from HRXPS, is a layer of mainly $CaCO_3$. There is a decrease in the ratio due to increase in CaH. The minimum occurs near the 25 minutes of etch time. From there the amount of Mg increases and the amount of CaH_2 decreases. This yields an increasing slope of the relative ratio for the rest of the etch time. For the Mg to CaOH plot in Figure 5.10 there is more $Ca(OH)_2$ near the surface than Mg. The XPS data show there is a $Ca(OH)_2$ maximum occurring in the first few minutes of etch. Then it decreases to trace amounts. Hence, the maximum in the plot is near 10 minutes. The ratio of Mg to H is similar to CaH_2, except there is H containing compounds that are not CaH_2 near the surface, hence the lower starting Mg to CaH ratio.
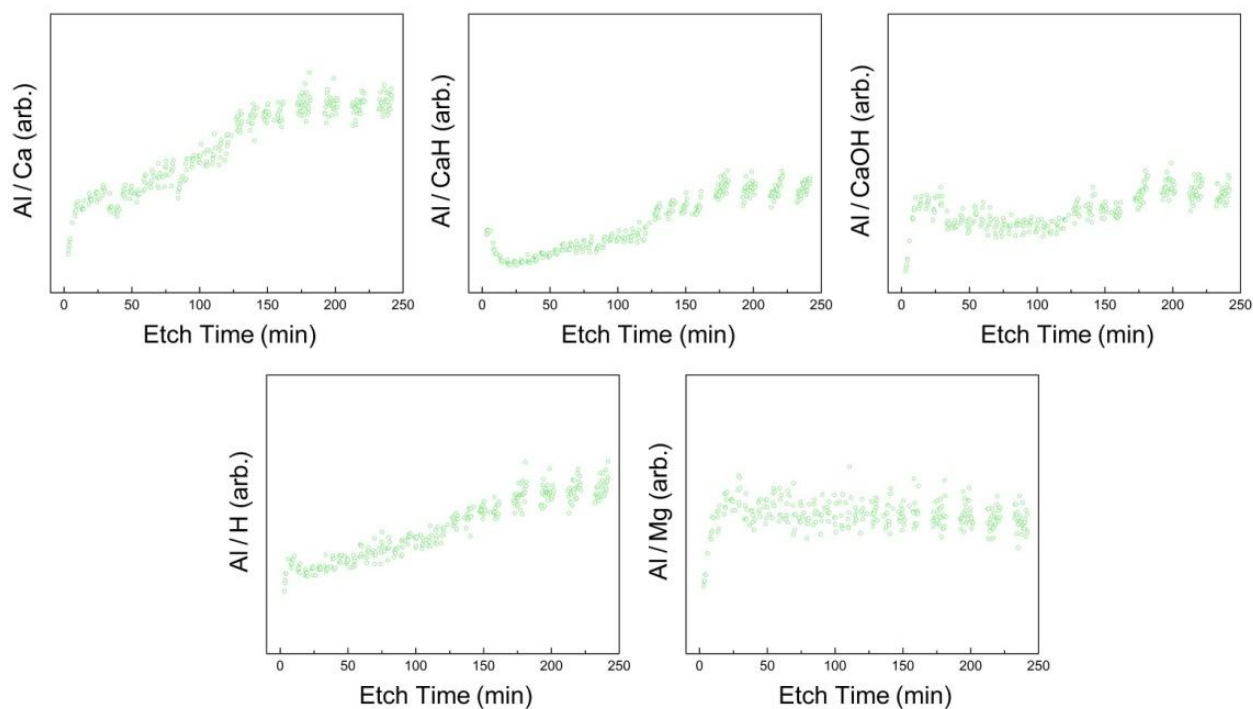
Figure 5.11. *Plot of the last half of each SIMS data scan, from a ribbon of $Ca_{75}Mg_{15}Al_{10}$ exposed to ambient lab conditions (23% RH, 21.5 °C) for 25 minutes, for the ratios Al to Ca, CaH, CaOH, H, and Mg ions. Each data point (green open circle ○) represents the ion ratio concentration at a given etch time. The scale is arbitrary. By taking a ratio the systematic errors of the experimental set up have been removed, but the quantitative amount of each ion cannot be determined, only the relative amount between the two is determined.*

The SIMS ratio plots of Al are similar to those of the Mg. Figure 5.11 contains the five plots of Al relative to the other positive ions collected. The trends are similar to the Mg plots, with the exception being that Al-Mg is inverted. The Al to Ca ratio is similar to the Mg to Ca ratio, except in the first few minutes of etching. For this ratio, since the Al content is lower than Mg at the surface, the shape of the ratio is initially lower; however, then it has the same trend as for Mg. For the Al to CaH ratio and Al to CaOH, as with the Al to Ca ratio, both these ratios follow the same trends as Mg, except once again their starting points are both lower due to less Al on the surface. For Mg-CaH, the 25-240 minute range shows an increase in Mg to CaH ions. The trend of the ratio of Al to H is the same as Mg to H after the first 20 minutes of etching. The initial difference in the ratio is due to the lack of Al on the surface. This causes the Al to H ratio to start lower in H as opposed to Mg which starts higher relative to H.
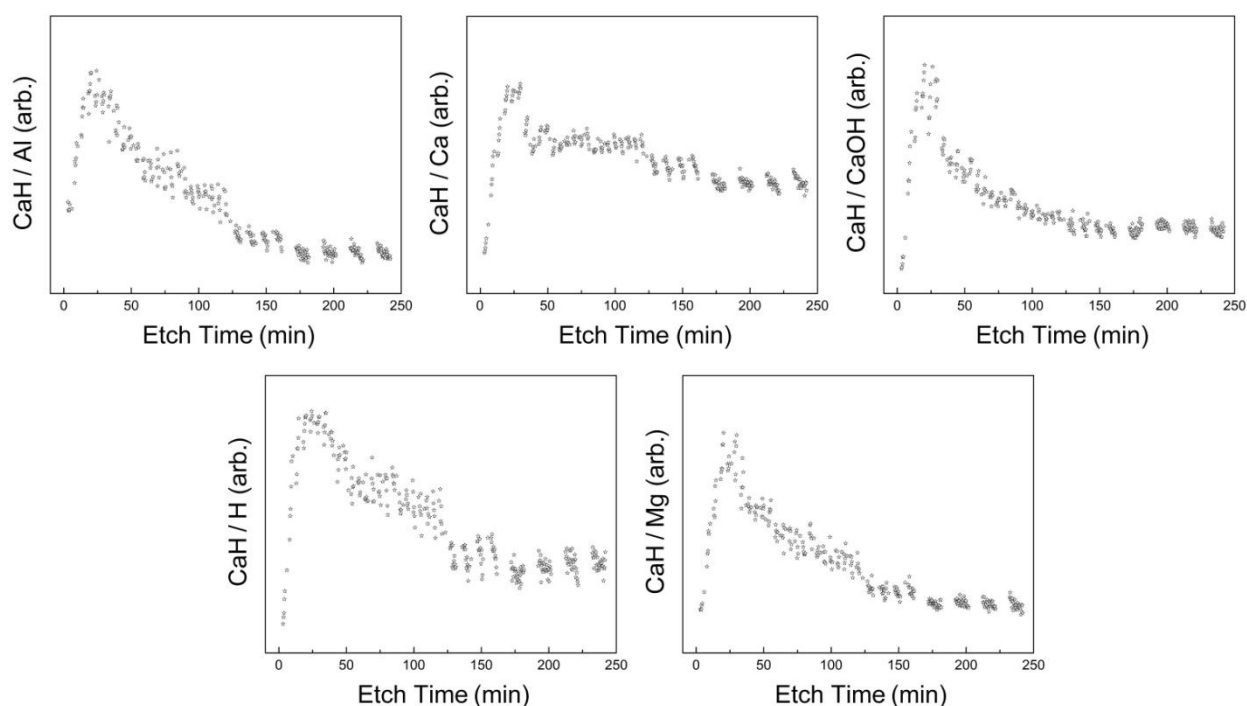
Figure 5.12. *Plot of the last half of each SIMS data scan, from a ribbon of $Ca_{75}Mg_{15}Al_{10}$ exposed to ambient lab conditions (23% RH, 21.5 °C) for 25 minutes, for the ratios CaH to Al, Ca, CaOH, H, and Mg ions. Each data point (black open star ☆) represents the ion ratio concentration at a given etch time. The scale is arbitrary. By taking a ratio the systematic errors of the experimental set up have been removed, but the quantitative amount of each ion cannot be determined only the relative amount between the two is determined.*

The ratios of CaH that have not been addressed already are CaH to Ca, CaOH and H. Figure 5.12 is a plot of these and the CaH to Al and Mg. These plots show there is less CaH_2 on surface followed by a maximum starting near 10 minutes of etching. This is followed by a decrease in the amount of CaH and this corresponded with the results from XPS. For the CaH to Ca ratio, there is little to no CaH on the surface within 5 minutes or less of etch time. Then there is a maximum of CaH between 10-20 minutes with a decrease in CaH as compared to an increase in Ca to the end of the etch time. The decreasing of the CaH to Ca ratio is less than the other ion ratios since the amount of metallic Ca is increasing further into the sample. These SIMS ratios are concomitant with locations of the HRXPS data. The CaH to CaOH and the CaH to H ratios have initial peaks in CaH around the 10 minute etch time. This is due to the large presence of CaH_2 also seen in the HRXPS data. Then, the relative amount of CaH falls until it reaches a constant relative amount to H or CaOH around 150 minutes etch time.
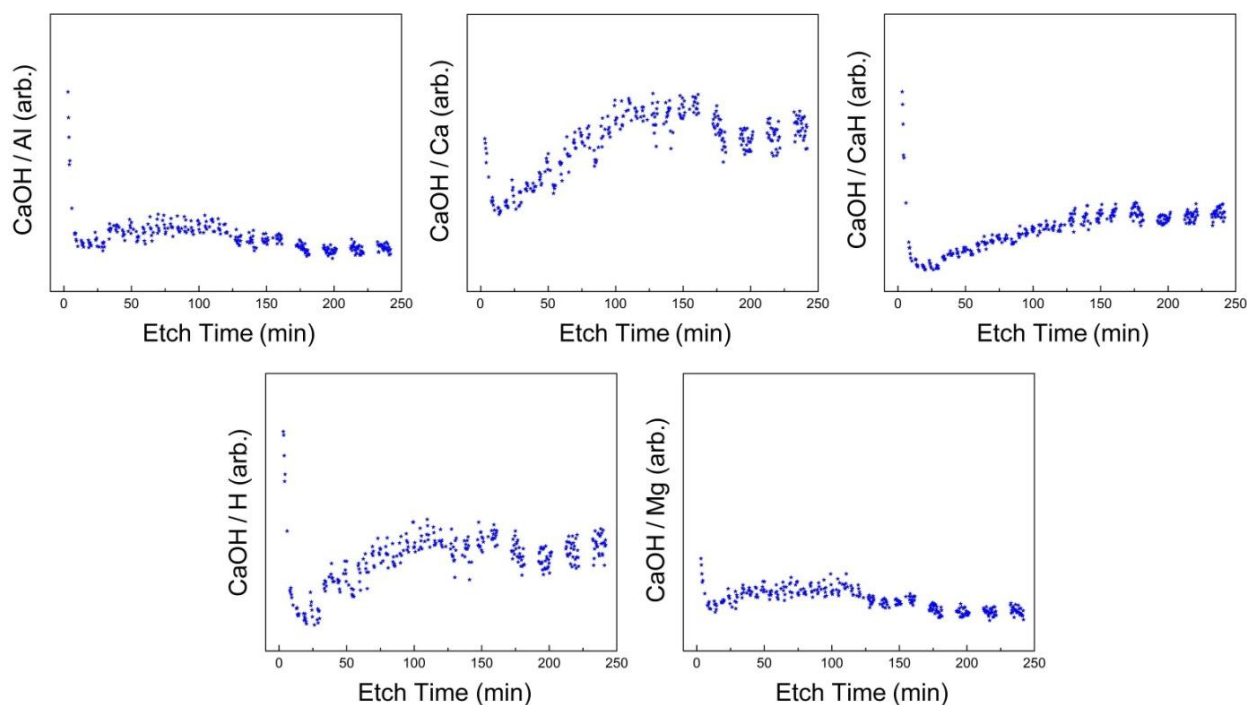
Figure 5.13. Plot of the last half of each SIMS data scan, from a ribbon of Ca$_{75}$Mg$_{15}$Al$_{10}$ exposed to ambient lab conditions (23% RH, 21.5 °C) for 25 minutes, for the ratios CaOH to Al, Ca, CaH, H, and Mg ions. Each data point (solid blue star ★) represents the ion ratio concentration at a given etch time. The scale is arbitrary. By taking a ratio the systematic errors of the experimental set up have been removed, but the quantitative amount of each ion cannot be determined, only the relative amount between the two is determined.

The unique SIMS ratio plots of CaOH to H and Ca are left to be discussed. Figure 5.13 has these in addition to the ratios of CaOH to Al, Mg and CaH. These ratios of CaOH ions show an initial high amount of CaOH relative to the ratio ion. This is followed by a decrease of the other ions implying that there is a layer of $Ca(OH)_2$ near the surface. The difference in the CaOH ratio plots after the initial 5 minutes of etching is associated with the features of the other ions. For the CaOH to H ratio, after the initial amounts of CaOH, the increase in CaOH from 25 minutes of etch time onwards is due to a decrease in hydrogen containing compounds. From XPS and other SIMS data it is seen that the decreasing H containing compound is CaH_2. For the CaOH to Ca ratio, the initial amount of CaOH is lower compared with the other ion ratios. This indicates there are Ca compounds other than CaOH on the surface. This is verified by HRXPS showing there is a layer of $CaCO_3$ on the surface.
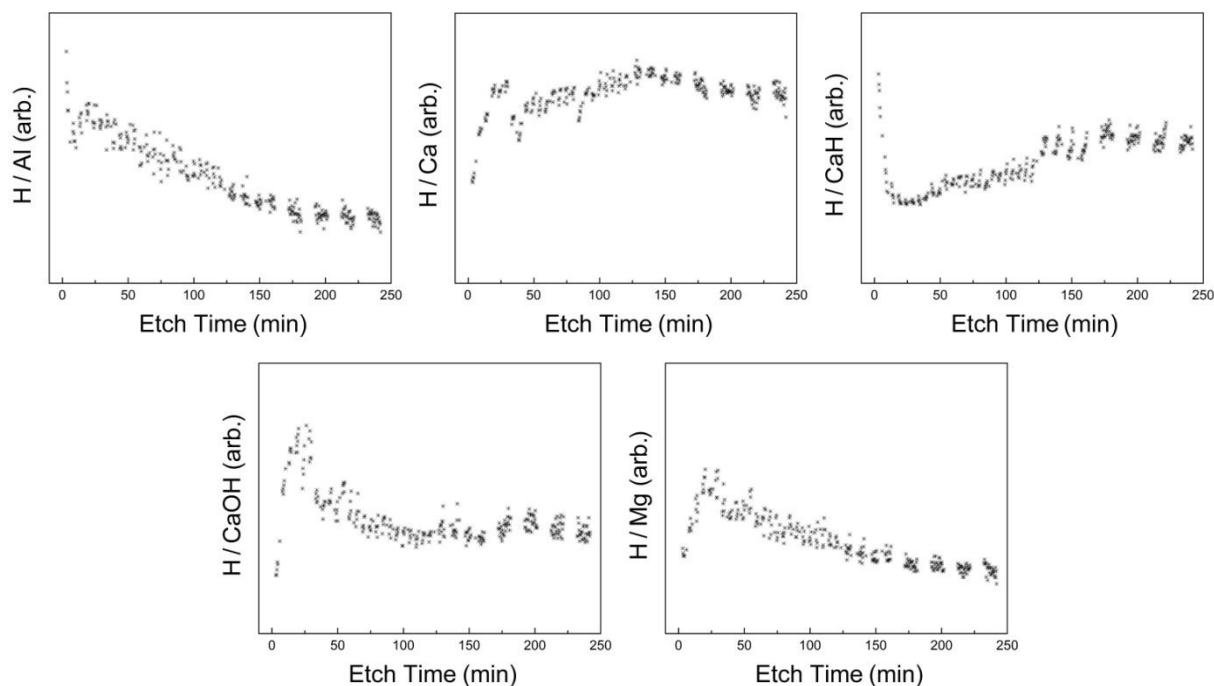
Figure 5.14. *Plot of the last half of each SIMS data scan, from a ribbon of $Ca_{75}Mg_{15}Al_{10}$ exposed to ambient lab conditions (23% RH, 21.5 °C) for 25 minutes, for the ratios H to Al, Ca, CaH, CaOH, H, and Mg ions. Each data point (black ✴) represents the ion ratio concentration at a given etch time. The scale is arbitrary. By taking a ratio the systematic errors of the experimental set up have been removed, but the quantitative amount of each ion cannot be determined, only the relative amount between the two is determined.*

The last ratio is the H to Ca ion ratio. The H to Ca ratio is convoluted. The Ca contribution is a combination of multiple compounds; $CaCO_3$, CaH_2, $Ca(OH)_2$ and CaO. The first part of the H to Ca ratio has the relative amount of Ca to be more than H. This is due to the presence of $CaCO_3$, CaO and $Ca(OH)_2$ in the first 0-10 minutes of etch time. The H to Ca ratio along with the other H ion ratios is presented in Figure 5.14. These ratios show that there is less H on the initial surface layers compared with Mg, Ca and CaOH. The first layer has little Al, so the H to Al ratio starts out high. These plots show that there is a peak in the H compounds from 10-25 minutes etching followed by a decrease. This peak is from CaH_2 as seen from HRXPS data. From 150 minutes of etch time onward there is a decrease in the H to Ca ratio, as seen from HRXPS. This result corresponds to an increase in metallic Ca to other Ca compounds.
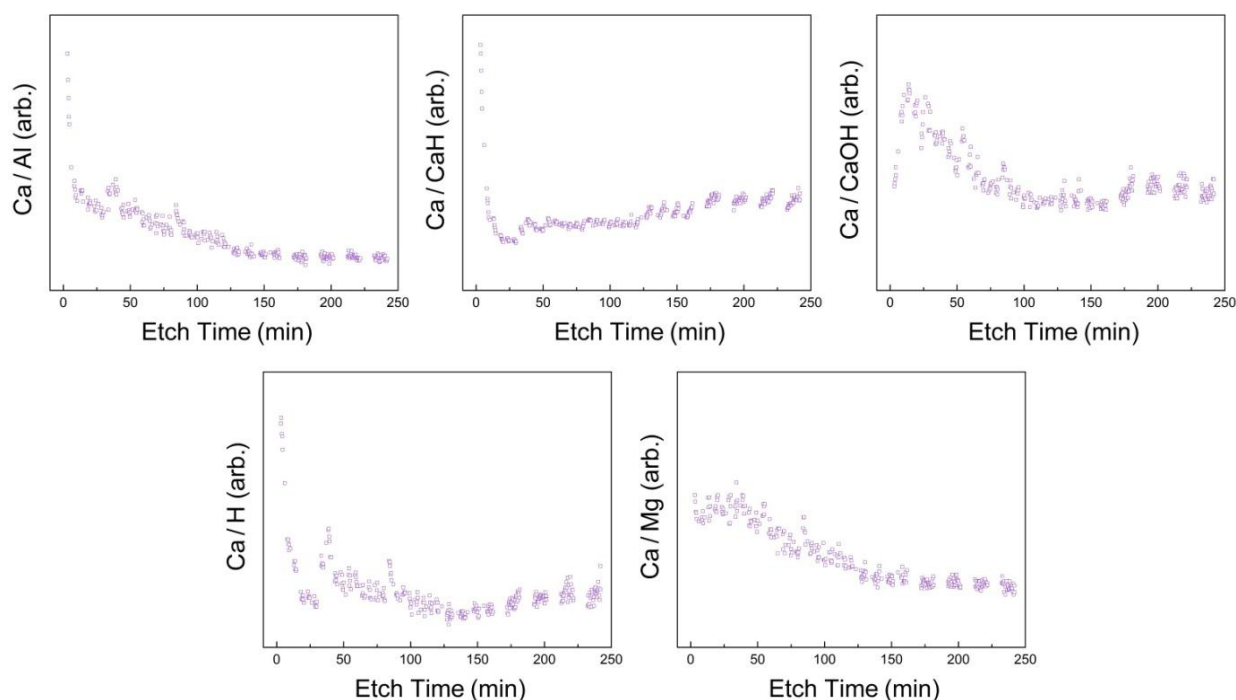
Figure 5.15. *Plot of the last half of each SIMS data scan, from a ribbon of $Ca_{75}Mg_{15}Al_{10}$ exposed to ambient lab conditions (23% RH, 21.5 °C) for 25 minutes, for the ratios Ca to Al, CaH, CaOH, H, and Mg ions. Each data point (purple open squares □) represents the ion ratio concentration at a given etch time. The scale is arbitrary. By taking a ratio the systematic errors of the experimental set up have been removed, but the quantitative amount of each ion cannot be determined, only the relative amount between the two is determined.*

Ca to other ions ratios have been previously covered, but for a direct comparison, they are present in Figure 5.15. These plots show several things. First, there is a Ca compound on the surface not containing CaH, H or Al. From HRXPS this is known to be $CaCO_3$ and CaO. Second, there is a CaOH containing compound in the first 10 minutes of etch. From HRXPS, this is seen to be $Ca(OH)_2$. Third, the ratio of Ca to Mg is constant for the first 50 minutes of etch, then decreases to another lower constant value at 150 minutes etch time. The same trend is observed in XPS survey spectra, Figure 4.20. And fourth, the amount of Al, CaH and H present at the surface is small compared to Ca.

The XPS and SIMS data provide internally consistent results. The XPS shows where the chemical compounds of Ca are, while the SIMS data reveals the relative ratios of Mg, Al, CaOH, CaH, H, and Ca ions. SIMS also adds what is occurring on the initial monolayers of the surface and, further, directly shows the presence of hydrogen. Additionally, SIMS data explains the growth layers of $Ca(OH)_2$ and CaH_2. All of these data (Figures 5.4-6 & 5.8-15), together, formulate a three dimensional picture of the reactions and relative product amounts. These results will assist kinetic analysis later in this chapter.

5.3 PPZ Connection to Brittleness

As calcium compounds form and grow in the ribbons, these ribbons become more brittle. This process can be divided into three regions. The three distinct regions are (1) 0-3 hours, (2) 3-600 hours (0.5-25 days), and (3) 600-2000+ hours (3.6-12+ weeks). The origins of these regions will be discussed further in the next Section 5.4. To track the embrittlement, ribbon samples are exposed to 75% RH environment for various periods of time. The plastic processing zones (PPZ) size, defined as the zones created on the fracture surface by the intersections of vein and river failure patterns on a tensile pulled ribbon sample, are listed in Table 4.2 are plotted here in Figure 5.16.

The plot has several lines traced to highlight certain groups of data. While the error bars are large enough that the PPZ could be fitted with only two traces, these four traces are plotted with the forethought of the regions as defined in Figure 5.17. There a correlation is seen between

a change in PPZ and the hydroxide growth. Accounting for that, the following analysis of the regions of decreasing PPZ is presented. The measurements of the decrease in PPZ show three main regions. The first region can be traced with one line and has a rapid decrease in size of 0.13 µm between the points in the group. Then there is a slower decrease in PPZ size over approximately the next 2 weeks by 0.060 µm. This second region can be traced with two lines. A sharper slope between 3 hours and 1.2 days and then a less steep gradually declining one past the 2 weeks point in the Region 2 group. This is followed by a third region traced with one line where the rate of PPZ decrease is higher than Region 2. Over the 4 weeks in Region 3 the PPZ decrease by 0.150 µm.
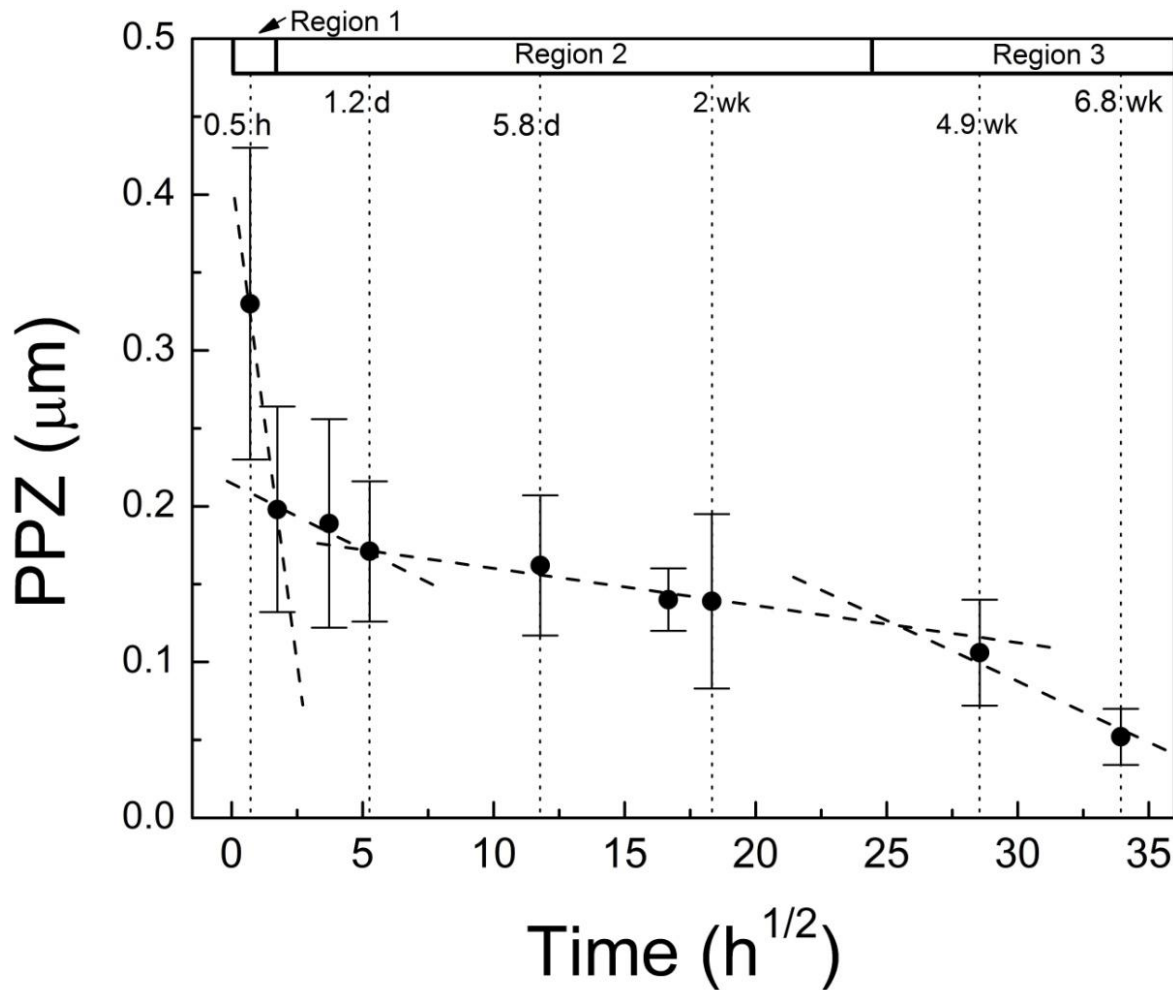
Figure 5.16. *A plot of the average measured size of PPZ from the fracture surface of a tensile tested ribbon of $Ca_{75}Mg_{15}Al_{10}$ as a function of the square root of exposure time in 75% RH environment. The error bars are a function of the sampling of the PPZ. The less exposed ribbons had a higher standard deviation from the average in sizes. The traced lines drawn are not fits but are drawn to highlight certain groups of data. The top of the plot has three different failure regions identified.*

As the sample became more brittle with longer exposures to humidity, the size of the PPZ decreases. There is an initial rapid decrease in PPZ size during the first 3 hours. This corresponds to a decrease in ductility rating. After 3hr, the ribbons did not survive the pinch portion of the pinch test. They have a ductility rating of brittle. After half a day in controlled humidity, the size of the PPZ decreases further and they do not survive the initial bend portion of the pinch test. At this point the ribbons have exceeded the brittle end of the ductility rating scale. The PPZ of the ribbons were further tracked and continued to decrease in size. The PPZ decreases at a steady rate for 2 weeks. Between 2 weeks and 4 weeks there is an uptick in the rate of decrease in PPZ size. The explanations for the selection of regions and individual lines marking PPZ slopes are given in conjunction with the following section.

5.4 Hydroxide Layer Growth Rates

As the PPZ decreased in size, a surface layer of $Ca(OH)_2$ was observed growing. This section is an explanation of models employed to fit the hydroxide growth data. Section 5.5 will describe further the changing mechanisms associated with the different slopes of growth. When humidity, which is water vapor, interacts with the calcium ribbons there is a growth of a hydroxide layer. The thicknesses listed in Table 4.1 are plotted here in Figure 5.17 against the time the ribbons were exposed to water vapor. Additionally, the PPZ from Section 5.3 are also plotted on the same plot. Many of the data points are taken at the same time, but there are thickness measurements that do not have corresponding PPZ points. For instance, 8.7 weeks and 12 weeks thickness measurements have no corresponding PPZ data. And for PPZ there is a datum point at 0.5 hours but no thickness measurement. This is due to the limitations of the measuring techniques used. The initial hydroxide at 0.5 hours is too small to measure and the PPZ after 6.8 weeks are too small to measure. Similar to the rapid decrease in PPZ size, there was a rapid change in the first day for the hydroxide thickness. This was followed by a steady layer growth for the first 2 weeks. Also, corresponding with the decrease in PPZ between 2 weeks and 4 weeks, there is an increase in the growth rate of the hydroxide. There appears to be a correlation in behavior of the PPZ and the hydroxide thickness. There is a rapid change in both

during the first 3 hours, then a slower process for the next two weeks and then a slightly more rapid process from 4 weeks on.
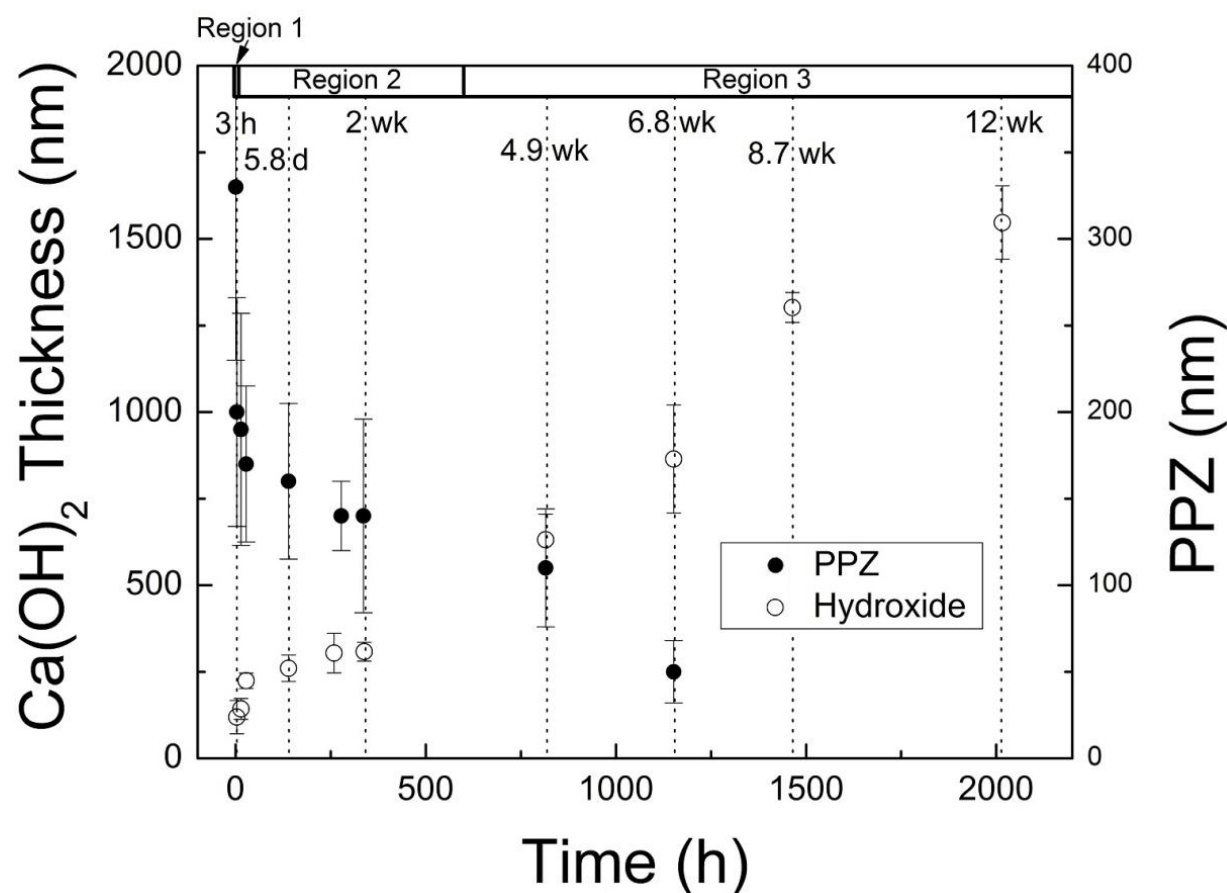
Figure 5.17. Plot of calcium hydroxide thickness (left y-axis) and PPZ diameter (right y-axis) plotted against time held in a controlled humidity environment. The plot is of the growth of Ca(OH)$_2$ thickness measured from ribbons of Ca$_{75}$Mg$_{15}$Al$_{10}$ as a function of exposure times to 75% RH before measuring. The PPZ are measured from the same material exposed to similar humidity exposure times. The top of the plot has three different regions of growth and failure identified.

The three regions of the hydroxide thickness are fitted by two models, each associated with a different mechanisms as seen in Figure 5.18. The equations used for fitting are displayed on the plot. The first region is due to chemisorption formation of hydroxides in a low temperature environment. The initial rapid film growth in Region 1 is concluded to be a result of the chemisorption process [232]. Chemisorption, the dissociation of H$_2$O, absorption of H and OH, and the reaction of OH with Ca fit this region. Logarithmic equations that fit thin hydroxide

growth were theorized by Landsberg [233] and Halsey [234] based on the assumption that the chemisorption is determining the rate. A concise summary of low temperature growth mechanisms is provided by Kofstad [235] that justifies these assumptions and conclusions. The first 0.10 µm of growth can be fit with the following direct logarithmic equation of the form $x = a \times \ln(t) + b$ where x is thickness, t is time, and a and b are constants for different conditions is given [236].
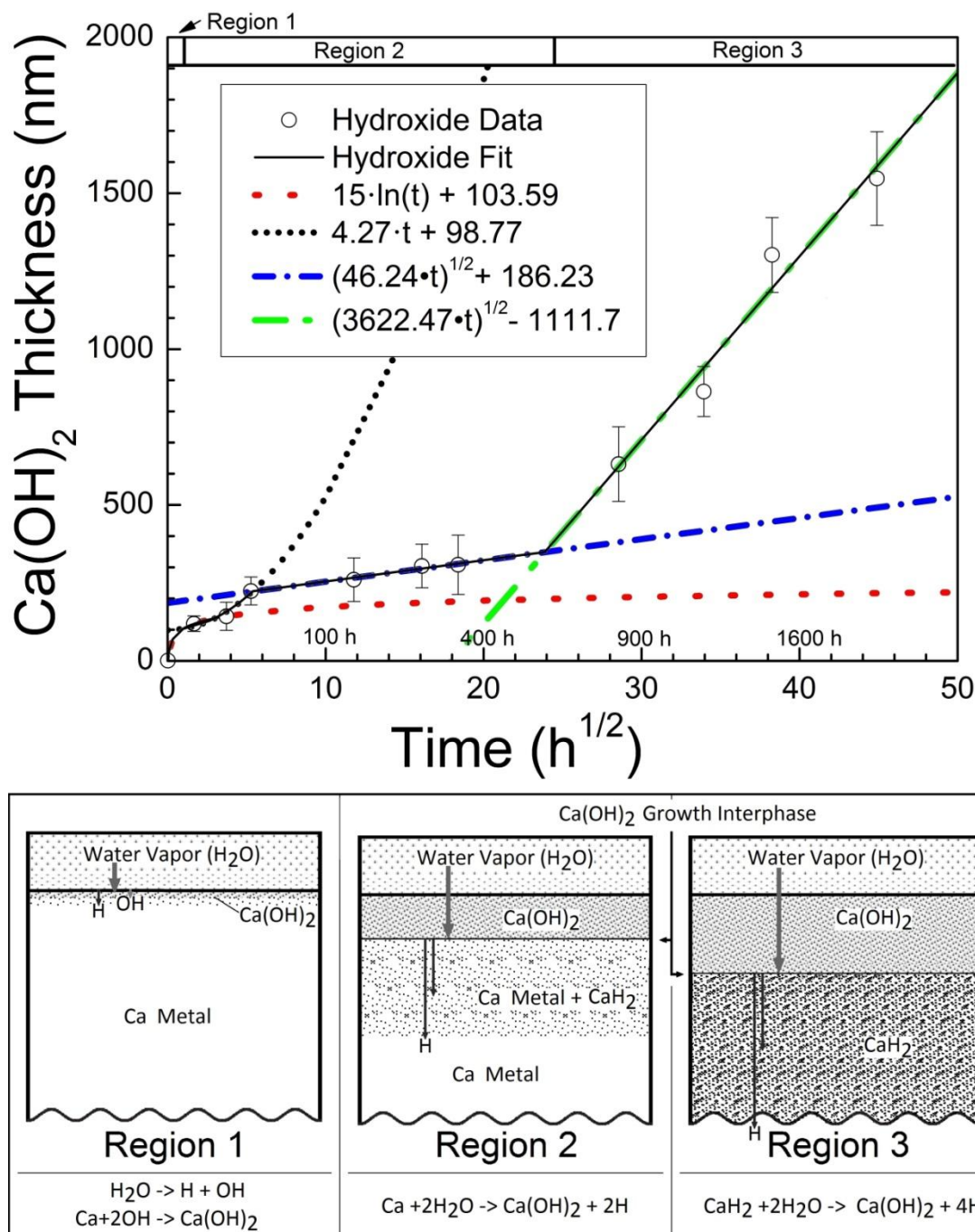
Figure 5.18. *Fitted plot of the $Ca(OH)_2$ thickness measurements from ribbons of $Ca_{75}Mg_{15}Al_{10}$ as a function of exposure times to 75% RH before measuring. The fits are (1) a direct logarithmic rate law fit (red dot), (2) a Deal-Grove linear fit (black dot), (3) a Deal-Grove square root fit (short dash dot), (4) a Deal-Grove square root fit (green long dash dot), and (5) a piecewise function fit (solid black line) of the other four fits tracing the whole hydroxide data set. The top of the plot has three different growth regions identified. The accompanying sketch, at the bottom, is of the primary reactions in each region. Listed in the bottom of the sketch, not drawn to scale, are these reactions. Region 1 is chemisorption. Region 2 is $Ca(OH)_2$ formation from Ca and water. Region 3 is $Ca(OH)_2$ formation from only CaH_2 and water.*

The second model used to fit the regions is the Deal-Grove model [237] for oxide thickness growth. This model is applied to oxide films grown on plane substrates. Here the oxide model will be applied to a hydroxide and the term will be used interchangeably with oxide. This model was originally developed for oxide growth in silicon. We will present it and fit the parameters to the current data, however, from SEM, SIMS, and XPS the current situation is shown to be more complicated. These complications are elucidated in the following text and Figure 5.18. This model is used for fitting the data from Regions 2 and 3. The Deal-Grove model is the solution to the differential equation : $\frac{dx}{dt} = Growth = \frac{B}{A+2x}$, where x is the hydroxide thickness, t is time, B is the parabolic rate constant, and $\frac{B}{A}$ is the linear rate constant. The two parameters A and B are defined as $A = \frac{2D}{k_S}$ and $B = \frac{2DN_S}{M}$. k_S is the reaction-rate coefficient at the advancing hydroxide interphase boundary. N_S is the concentration of water molecules at the advancing hydroxide interphase boundary. M is the number of hydroxidant molecules interacted per unit volume of hydroxide grown. $D = D_0 \cdot e^{-\frac{E_A}{RT}}$ is the diffusion coefficient of the water vapor molecules through the hydroxide. D is related to E_A the activation energy, R the gas constant, and T the temperature.

There are three rates that are important to defining the parameters A and B; (1) the rate water molecules are arriving at the advancing hydroxide interphase boundary that is it has with either Ca metal of calcium hydride, (2) the diffusion rate of molecules through already-formed hydroxide, and (3) the reaction rate at the calcium hydroxide interface boundary. The slowest of the three is the limiting factor for the reaction at steady state. For this experiment, as with the Deal-Grove model, the external gas (water vapor) is assumed to not be a limiting factor. The growth rate of the hydroxide is directly related to the flux of molecules reacting at the hydroxide interface boundary. The rate goes inversely with thickness. As the hydroxide increases in thickness, the rate slows. This remains true if the medium that the hydroxidant is reacting with remains the same. If there is a change in the growth rate of the hydroxide, this implies that one of the three prior rates has changed.

For thin hydroxides, if $x \ll \frac{A}{2}$, then $x = \frac{B}{A} \cdot t$. Initially the hydroxide layer is 0 nm in thickness. This zero point does not align with the linear fit of the Deal-Grove model. This is seen in Figure 5.18; the black short dots are this linear fit. When this zero point is added to Figure

5.18, a linear fit cannot fit within the error bars of the next three points. The linear fit crosses the y-axis near 100 nm. Region 1, defined as the first 100 nm of the $Ca(OH)_2$ growth, can be fitted with a chemisorption growth fit, as stated earlier. This is in agreement with the expected growth of a thin film of hydroxide due to chemisorption at low temperatures [236].

In Region 2, the first 24 hours of growth can be fit with the linear portion of the Deal-Groves model. The linear curve fits these data points from 3 hours to 1.2 d and lies within the error bars of the data. This linear part of the Deal-Grove model is due to contributions from the interface reaction, i.e., the flux of the hydroxidant reacting at the $Ca : Ca(OH)_2$ interface boundary.

For the later part of Region 2, the data lying between 25 and 600 hours, the hydroxide growth is best fit with a square root fit. This type of fit is indicative of volume diffusion-controlled growth. The region is fitted with the Deal-Grove model limit for thick hydroxide growth. For thick hydroxides, the Deal-Grove model limit is; if $x \gg \frac{A}{2}$, then $x = \sqrt{2Bt}$.

Region 3 is also fitted with the thick limit of the Deal-Grove model. From the fit in Figure 5.18, it is noted that the parabolic growth rate constant must change between Region 2 and Region 3. In Region 2, the parabolic rate constant from the fit is $B_2 = 23.12$ nm^2/h. Based on Figure 5.18, the linear fit region has a linear constant of $A_2 = 5.41$ nm. For Region 3, the parabolic rate constant from the fit is $B_3 = 1811.24$ nm^2/h. The difference in parabolic rate constants implies that B_2 and B_3 yield a relation between in different mechanism controlling the in these two regions. $B_3 = 266B_2$, this highlights that the mechanisms for growth in Region 3 is much greater than that of Region 2. This change will be discussed in Sections 5.5.3 and 5.5.4 along with three-dimensional data.

5.5 Discussions on the Correlations of Results

5.5.1 Mandrel Failure and $Ca(OH)_2$ Growth

The bend-over mandrel control sets and test condition sets results appear to show two rates of failure over the mandrels, as in Figures 5.1, 4.9, & 5.2.

The first rate is quicker over the initial 1-2 hours. This is seen across all tests. The tests which are carried out longer than 3 hours show a transition from the quick rate of failure to a second, slower rate of failure. From the combined plot of all the control sets mandrel failure data plotted versus the square of time in Figure 5.19, it can be seen that each control set l with added tracer lines reveals that each can be fitted with a combination of two rates. A quick rate followed by a slower rate. This indicates a change in mechanism. These failures on the mandrels correspond with similar times scales as Region 1 of the $Ca(OH)_2$ thickness measurement and the initial part of the Region 2. When comparing with the regions from PPZ and the growth kinetics of the hydroxide layer, this implies that the first rate is due to chemisorption while the latter rates are growth interface related.
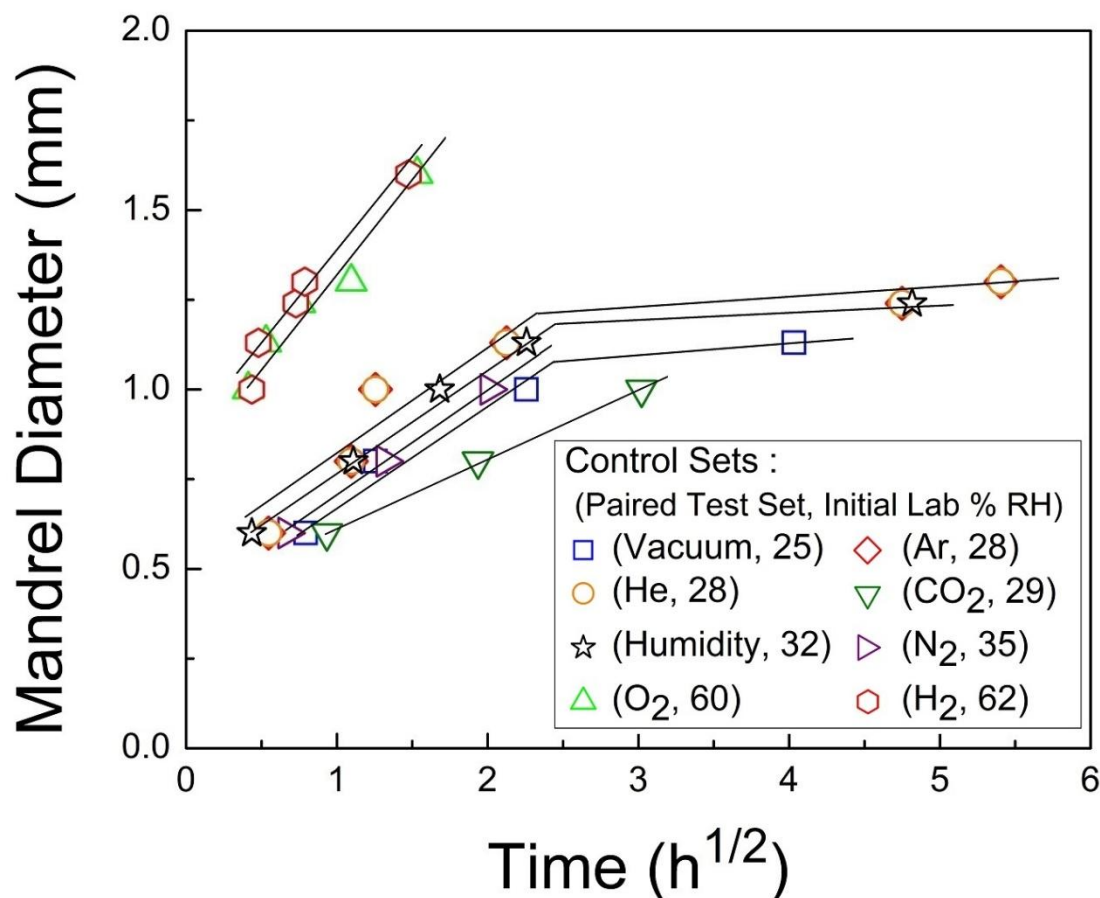
Figure 5.19. Tracer lines are added to all the control sets (i.e., the set immediately tested in ambient lab conditions) in Figure 4.9a. The plot is the combined control sets for all the ambient lab condition tests and the RH test. The plot is of square root of time plotted versus mandrel diameter failure as when exposed to individual ambient lab conditions during control sets. Note the gases listed in the legend are not the environment used, they only note the paired set tested in lab conditions.

5.5.2 PPZ Growth Compared to Ca(OH)$_2$ Growth

The decrease in PPZ size show similar points of inflection as the increase in Ca(OH)$_2$ thickness measurements, Figure 5.16 & 5.17. The samples used for the PPZ measurements and the ones used for the hydroxide thickness measurements were both exposed to the same relative humidity experiment. The boundaries of the measurements of the PPZ extend to no more than 6.8 weeks and the hydroxide thickness measurements being around 3 hours. These boundaries are due to the limitation of measuring features on calcium ribbons below 100 nm.

There is a rapid decrease in PPZ size from 0.5 to 3 hours of humidity exposure. There is then a slower decrease from 3 hours to 1.2 day. This is similar to the change from the chemisorption fit of the thickness to the linear Deal-Grove fit of the hydroxide. Then the decrease in PPZ size slows further, but at a steady rate from 1.2 day to a longer than 2 weeks but less than 5.9 weeks. This corresponds with the first Deal-Grove square root fit of hydroxide thickness for the same duration. This, finally, followed with an uptick in the rate of decreasing size of the PPZ from a point between the second and fourth week until the last measured PPZ at 6.8 weeks. This is also when the change to the second Deal-Grove square root fit of hydroxide thickness occurs.

5.5.3 Change in Growth Mechanisms During Ca(OH)$_2$ Growth

The following analysis explains the transitions in growth from Region 1 to Region 3, Figure 5.18, focusing particularly on the mechanism change between Region 2 to Region 3.

In Region 1, O$_2$ and water vapor are first chemisorbed on the surface. This is shown in the time slices t1 and t2 in Figure 5.7. The primary chemisorption is of water vapor that reacts with Ca to form Ca(OH)$_2$. While not the primary chemisorption event, O$_2$ is chemisorbed to form CaO. The formation CaO is observed on the surface in the HRXPS data in Figure 5.5. It is known that CaO formation from Ca and O$_2$ when water vapor is present is not a favored reaction at room temperature [194], but it can form on the surface of Ca due to chemisorption [185]. The trace CaO that forms will be readily converted into Ca(OH)$_2$ in the presence of water vapor. After chemisorption ceases to fit the data, the initial surface layer of metallic Ca layer has transformed in to a layer of Ca(OH)$_2$ thicker than 100nm. With the increase in thickness of the

$Ca(OH)_2$ layer, the formation of CaO by chemisorption of O_2 terminates. Additionally, the dissociation of H_2O into OH and H stops, since it becomes energetically unfavored due to the change in the surface to $Ca(OH)_2$.

The next region, Region 2, grows following a Deal-Grove model fit. In this region, see the associated sketch for the region in Figure 5.18, the molecular water vapor diffuses through the $Ca(OH)_2$ to the growth interphase boundary and reacts there with metallic Ca to produce the $Ca(OH)_2$ [238]. During the formation of this layer, elemental hydrogen is released which is then absorbed further in the bulk of the ribbon to form CaH_2. This same reaction of water vapor with Ca forming products of $Ca(OH)_2$ and CaH_2 was observed in the SIMS data collected in UHV, plotted in Figure 5.6.

Region 2 is fit with the linear-parabolic Deal-Grove model. If the formation of $Ca(OH)_2$ were only dependent on the Ca and water interactions, then the Deal-Grove fit would only have one square root fit that would be limited by the volume diffusion of water vapor. Then Region 3 would be only a continuation of Region 2. But in Figure 5.18, the thickness data changes and a second square root fit is needed. This implies that there is a change in the parabolic growth rate constant. For this to occur, there would need to be a change in either diffusivity of water or the reaction mechanism due to the structure of the phase adjacent to the advancing calcium hydroxide interphase boundary. It is the later because calcium hydroxide remains the medium for water vapor to penetrate from the surface, therefore its diffusivity does not change.

A change in the medium that the hydroxide is growing into occurs. The formation of CaH_2, verified present from HRXPS spectra in Figure 5.4, is the source of these differences in growth rates. The change from Region 2 to Region 3 is the result of the remaining ribbon transforming from metallic Ca to CaH_2. The reaction of CaH_2 with H_2O has an end product of $Ca(OH)_2$. It is known that when comparing CaH_2 and Ca reactivities, the reaction of Ca with H_2O is less reactive than the reaction of CaH_2 with H_2O [239].

In the next section, it is shown that the calcium glass ribbons can be converted to ribbons that are saturated with CaH_2 in the time frame needed to correlate with the hydroxide thickness growth results.

5.5.4 CaH$_2$ Saturation Growth Time Estimate

The amount of time it takes to saturate the ribbons with CaH$_2$ can be approximated by an order of magnitude estimate. To do this first an assumption from new growth in the UHV is used to set a distance scale to the SIMS and XPS data.

The twenty-four SIMS measurements had a collection time of 5 minutes each. There is approximately an hour of time between each SIMS collection of this 5 minutes. The first 2.5 minutes of each SIMS etching removes the new growth layer that appeared during the 1 hour between collections. This is the time for the set up and collection of XPS data. In a vacuum of 10^{-9} Torr it takes roughly an hour to grow a 1nm [231]. The second 2.5 minutes of the SIMS etching is of the alloy in the state it was in when loaded in to the UHV chamber. Based on this, for every 5 minutes of SIMS etching approximately 1 nm of the alloy material is removed. For the first 120 minutes of etching or first 24 SIMS collections a total of 24 nm of the alloy is etched away and 24 nm of inside the UHV growth is removed. Between 120 to 160 minutes of etching the SIMS collection was increased to 10 min durations, for a total of 12 SIMS collections or 12 nm of alloy material to remove and 4 nm of hydroxide growth removed. The running total to 160 minutes is 36 nm alloy and 28 nm internal to UHV new growth. Between 160 and 240 minutes of etching there were four 20 min SIMS collection periods for a total of 4 nm of new growth to remove and a total of 28 nm of alloy material removed. For the whole 240 minute period of SIMS etching the totals are 64 nm of the base alloy removed and 32 nm of internal to the UHV growth removed.

Second, from the HRXPS plot from Figure 5.5, the saturation of CaH$_2$ occurs in the first 10 minutes of etch time. Using the prior SIMS depth estimates, this saturation point occurs in the first 2 nm of the ribbon which has been exposed to 23% RH during the preparation for loading into the UHV chamber. The Ca(OH)$_2$ thickness for this sample is near the 10 minutes etch time and has then a thickness of approximately 2 nm.

Using the fit of Ca(OH)$_2$ thickness of the humidity exposed ribbons, Figure 5.18, at 2 nm of hydroxide growth is equivalent to 3 minutes of exposure to 75% RH. The thickness of the calcium ribbons used here, like that of the SEM line scan measured in Figure 4.11, are around 20 μm. Using a linear estimate of the growth of CaH$_2$ saturation to the 10 μm half way point of the ribbons and taking a rate of 3 minutes per 2 nm of saturation gives a total time to saturate the

ribbons of 1.5 weeks. Assumptions made here are that (1) as the layers grow the growth rate slows and (2) that the diffusion medium is not a finite bound material. Since the ribbons here are thin and the diffusion of hydrogen is rapid, the diffusion from one side will interact with that from the other half before the middle of the ribbon is saturated with CaH_2. Hence this estimate sets a limit on how rapidly the ribbons can saturate with calcium hydride.

The estimate here of 1.5 weeks is less than the second Deal-Grove square root fit of the thickness growth. But for an order of magnitude estimate it sets the upper limit for the minimum time in which the reaction can occur. It is near the 2 to 4 weeks data point range where the second Deal-Grove square root fit occurs. Based on this saturation time frame combined with the HRXPS results for compounds present, it can be concluded that the second Deal-Grove square root fit is the transformation of CaH_2 to $Ca(OH)_2$ and the first square root fit is the conversion of Ca to $Ca(OH)_2$ and CaH_2.

5.5.5 SIMS, XPS, and Charge Transfer

From the data of the ribbon exposed to ambient lab conditions for less than 30 minutes before being place in UHV, the comparison of the XPS and SIMS data show several results. First from XPS, the 0 min plot in Figure 5.4, at the surface there is a thin layer of $CaCO_3$ and CaO. CaO exist from the chemisorption of O_2. $CaCO_3$ exist from the interaction of $Ca(OH)_2$ with CO_2.

Second, a significant finding from the SIMS data is that there is almost no Al present within the first few nanometers of the surface. There is also less Mg near the surface than present in the bulk. The calcium ribbons are uniform in composition when as spun. The exposure to water vapor causes difference concentrations at the surface of Mg, Al, and Ca. This suggests that the reaction in the Ca glass with the water vapor is preferentially binding to Ca as opposed to Al and Mg. Thus it is creating a Ca rich layer on the surface. The slight signal of Mg as opposed to no signal for Al on the surface indicates that there is preference for interacting with Mg over Al when the water vapor interacts with the Ca-based glass. Time slice t_2, in Figure 5.7, illustrates this process.

Below the majority $CaCO_3$ initial surface layer is a layer of $Ca(OH)_2$ from HRXPS, 5 min plot Figure 5.4 and in Figure 5.5. Additionally, from SIMS ratio of Al to Mg, in Figure 5.11, the

levels of Al and Mg present are lower than levels in the bulk. From HRXPS, the amount of CaH_2 present is at a maximum, but is being consumed to form $Ca(OH)_2$, as expected by the known reactions of calcium listed in Figure 5.7.

Moving further into the sample the SIMS data show that the amounts of CaH ions and H ions decrease, Figure 5.12. The amounts of Al and Mg increase until they level off at values of the original alloy composition seen from both the full spectrum XPS scans (Figure 4.20) and SIMS ion ratios, Figures 5.10 & 5.11. From XPS, the amount of metallic calcium increases, Figures 5.4 & 5.5. At the same time, the amount of calcium over all decreases into the bulk until the value of the original alloy composition is reached, Figure 4.20.

The most important observation is that the ribbon contains large amounts of hydrogen bonded to calcium. This is verified by the large concentrations of CaH_2 present in the XPS data (Figures 5.4 & 5.5) and the observed presence of hydrogen in SIMS (Figure 5.14). This sample which was prepared in a relatively low 23% RH day and loaded in the short time of 25 minutes to the UHV chamber has significant amounts of hydrogen present near the surface.

The XPS and SIMS data confirm that hydrogen is penetrating the sample and readily binding with the calcium to form CaH_2. The CaH_2 is a strong ionic salt. When Ca forms a strong ionic bond it is transferring electrons away, in this case to the hydrogen atom. It was shown, in Section 3.2, that ionic bonds will result in embrittling the calcium metallic glass.

This quick absorption of hydrogen from an interaction with water vapor in low humidity shows that it is possible for ribbons with high ductility ratings to embrittle within a matter of minutes in high humidity environments.

Chapter 6 – Conclusions & Future Work

6.1 Conclusions

The initial motivation for this research was to design a metallic glass that could be used for satellite applications. It was required to have a low density and possess ductility. A calcium glass, $Ca_{60}Mg_{15}Zn_{15}Al_5Cu_5$, was designed that had good GFA, possessed good mechanical properties, had a metallic luster, and a low density. Unfortunately, it was brittle and the useful properties were short lived. This thesis was a study to design a ductile calcium glass and to unravel why there is dramatic deterioration of properties of these glasses.

The first part of the thesis focuses on the factors that make a calcium metallic glass alloy ductile. There have been close to 80 papers on calcium metallic glasses published in the past 40 years. Many only focused on the causes of the amorphous nature of these calcium glasses. Only four have examined their mechanical properties. No work focused on calcium glass ductility. From prior studies on ductility and metallic glasses, a correlation between a Poisson's ratios greater than 0.3 and ductile glasses has been observed.

Based on high Poisson's ratio and on estimates of the elastic moduli calculated from first principles, the set of calcium glass alloys studied here should have been ductile. A pinch test which assigned a ductility rating was conducted on the calcium ribbons made. Additionally, measurements of PPZs structures on the fracture surface of tensile pulled ribbons showed a decrease in size with an increase in brittleness. The results of the PPZ and ductility rating of the ribbons revealed that moduli estimates alone were lacking and require additional inputs for accurate ductility predictions.

Better estimates were gleaned from molecular dynamic simulations by Widom. The elastic moduli values from the model, aiding in predicting ductility, were closer to the experimentally measured values. With feedback from binary calcium glasses the model was refined and resulted in predictions of ductile ternary systems which could be validated experimentally.

From these simulations charge transfer, enthalpy of formation, and radial distribution profiles were derived. The comparison of charge transfer to Poisson's ratio showed a correlation

between an increase in the charge transfer and a decrease in Poisson's ratio. For the calcium glasses, the decrease in Poisson's ratio correlated with a decrease in measured bend ductility ratings. This model is the first to predict which calcium alloy compositions are ductile glasses.

It was found that a ductile calcium glass can be designed if the elements used would decrease the amount of charge transferred away from calcium. When calcium retained a crucial amount of charge, it would maintain its metallic nature and the calcium glass would be ductile. When enough charge was transferred away from calcium it would exhibit a covalent or ionic bond nature and the calcium glass would be brittle. Mg and Zn had less charge transferred to them from Ca and made ductile glasses. Al and Cu took more charge from calcium and created stronger bonds with Ca, resulting in brittle glasses. The glasses that were ductile did not remain ductile for long. Glasses like Ca_3Mg and Ca_3Zn would remain ductile for a few minutes up to 30 minutes depending on the day.

An initial effort to identify the mechanism for the rapid decay in the system by substituting various elements showed that Al and Mg extended the duration of the ductile nature of the alloys. Zn and Cu did not help to prevent the decay. No element addition was discovered that could passivate the system to prevent the decay. Only with knowledge of the factors that are responsible for degradation would it be possible to attempt the mitigation of the embrittlement.

The majority of this thesis focuses on the factors that make ductile calcium metallic glass alloys become brittle. The decay occurs in the ambient lab environment. It was hypothesized that the cause of embrittlement resulted from electronic transfer associated with the solvent metal creating brittle glasses. A bonding event occurs where strong bonds nonmetallic bond are being formed. Calcium is transferring charge associated with losing its metallic bond character in ambient lab conditions.

For this study, the alloy $Ca_{75}Mg_{15}Al_{10}$ was selected. While it is not the most ductile alloy of the calcium based glasses examined, it does have ductility duration for at least 30 minutes. This is an order of magnitude longer than $Ca_{72}Mg_{28}$, the most ductile calcium glass alloy discovered. This duration length would allow for adequate time for ductile decay experiments to be performed.

The ductile decay was found not to be related to thermal relaxation or the most common gases present in the atmosphere like Ar, CO_2, H_2, He, N_2, and O_2. These gases were all tested by placing the ribbons in a pressure chamber with each individual gas. It was found that none of

these gases embrittled the Ca-based glasses. H_2 is known to penetrate Ca quickly, but it does not interact with Ca at room temperature. When it is dissociated, it can interact with Ca at room temperature. It was found, however, that humidity correlated with the embrittlement of the calcium glass ribbons. Water vapor is the key to understanding calcium glass embrittlement. Water vapor with calcium is needed to form dissociated hydrogen.

The reaction of water vapor and calcium to form $Ca(OH)_2$ in the ribbons is the source of dissociated hydrogen. The dissociated hydrogen penetrates rapidly below the initial surface $Ca(OH)_2$ layer. Being in an ionic form, H interacts with Ca forming an ionic salt, CaH_2. Calcium hydride formation is the calcium-hydrogen bonding event occurring which is causing embrittlement. After the initial layer of $Ca(OH)_2$ formation, the subsequent $Ca(OH)_2$ growth front contributes to the further creation of dissociated hydrogen.

To verify the presence of these layers several techniques were employed. The first technique was powder XRD. The ribbons required about 3 weeks of exposure in ambient lab conditions to show a slight peak in the XRD pattern. The first peak was the main peak of $Ca(OH)_2$ crystal XRD pattern. While the surface is covered with $Ca(OH)_2$, the crystals growing were nanometers in scale. It took 3 weeks for their size to be large enough to be resolved in XRD.

SEM images and EDS, taken of cross sections of 6 year old ribbon pieces, showed a layer of spalling $CaCO_3$ with a layer of $Ca(OH)_2$ below. A series of EDS maps and line scans were taken of ribbons that had been exposed to fixed duration relative humidity of 75% at room temperature. These scans showed the growth dynamics of the $Ca(OH)_2$ layer. Four different stages of growth were fitted. The first 3 hours of growth are dominated by chemisorption growth. The next 23 hours is a linear fit of a Deal-Grove model which is rate controlled by the interface reaction. The next 24 days are fitted by a square root fit of the Deal-Grove model controlled by volume diffusion of water vapor to the interphase boundary. The $Ca(OH)_2$ interphase boundary growth is the reaction of Ca to $Ca(OH)_2$. After the first 25 days, a second Deal-Grove model square root fit needs to be applied to fit the $Ca(OH)_2$ growth. The parabolic rate constant of the fit changed. There is a change in the reaction mechanism due to the structure of the phase adjacent to the advancing calcium hydroxide interphase boundary changing. The $Ca(OH)_2$ interphase boundary growth is no longer controlled by the reaction of Ca to $Ca(OH)_2$ but instead it is the reaction of CaH_2 to $Ca(OH)_2$ controlling the growth.

Having determined the mechanism for embrittlement, the ductile decay was also studied using BSE imaging on the SEM of PPZ size changes. The PPZ measured were formed on the fracture surface of tensile pulled calcium glass ribbons exposed to various durations of 75% RH. The PPZ became smaller as the ribbons embrittled. The changes in decreasing ductility correlate with the changes in hydroxide thickness growths.

To verify hydrogen was present and forming CaH_2, XPS and SIMS were employed. XPS identified local chemical compounds, while SIMS identified which ions were present at each etch layer. Both were needed to present a complete picture of the interactions occurring. The XPS and SIMS data were collected for $Ca(OH)_2$ powder, CaH_2 powder, and samples of $Ca_{75}Mg_{15}Al_{10}$. The $Ca(OH)_2$ and CaH_2 powder samples were used as standards for XPS and SIMS to fit the $Ca_{75}Mg_{15}Al_{10}$ alloy results. Additionally, the powder samples demonstrated that positive ions detection in SIMS would provide the hydrogen information sought.

The ribbon $Ca_{75}Mg_{15}Al_{10}$ spent minimum time in ambient lab conditions before loading into UHV test chamber. The ambient relative humidity level was 23%. XPS and SIMS revealed that there was a thin layer of $CaCO_3$ and CaO on the surface that was removed with initial Ar ion etching. This was followed by a small surface layer of $Ca(OH)_2$ that took 10 minutes of etching to remove. SIMS also showed that there was amount no Al on the surface, that there was hydrogen present throughout the sample and that CaH and H ions decreased in amounts going into the bulk, and that after the $Ca(OH)_2$ layer, the Al and Mg are present in amounts that do not change relative to each other.

XPS showed that the CaH_2 concentration peaked right below the surface of the ribbon. The XPS data also showed that there was a thin layer of $CaCO_3$ and CaO followed by a layer of $Ca(OH)_2$. As the ribbon was etched further into the bulk, the composition became dominated by metallic calcium instead of other calcium compounds. Both SIMS and XPS showed that the surface and several layers below the surface were calcium rich and depleted in Al and Mg. This demonstrates that calcium is the main constituent, the most reactive, and relevant for the embrittlement process.

The SIMS data had an unexpected, but explainable, feature. In even an ultra-high vacuum system, there was evidence of minute traces of water vapor. The UHV was not enough to prevent monolayers of $Ca(OH)_2$ and CaH_2 from forming on the sample surface during XPS collection. This did not drastically affect the XPS signal since XPS is a technique that is over 3-5 nm in

depth. It does affect the SIMS data since SIMS collects every ion. The monolayer contributes to an initial increase in signal until it has been milled away. The signal was normalized by removing the first 2.5 minutes of data to remove the added monolayer affect in the SIMS spectra.

Knowing the amount of time it took to remove a monolayer, gave a rough depth estimate to the etch times of the SIMS Ar ion etching. This combined with estimates of hydroxide thickness, hydroxide fit, hydride penetration depth, and width of ribbons gave an approximation of the time it took to saturate the ribbons with CaH_2. The approximation was on the same order of magnitude as the starting time of the second Deal-Grove square root fit for the hydroxide thickness. That combined with the fact that CaH_2 rapidly converts to $Ca(OH)_2$ in the presence of water vapor, quicker than metallic Ca does, this lends credence to the conclusion that the second square root fit is due to the conversion of CaH_2 to $Ca(OH)_2$ in the CaH_2 saturated ribbons.

These combined results demonstrate that the environment is embrittling calcium metallic glasses. Specifically, hydrogen is dissociating from water vapor and is bonding with calcium. The charge transferred from calcium results in a decrease in metallic bonds and an increase in the ionic bonds which embrittle an initially ductile calcium glass.

6.2 Future Work

Overall, in this thesis, it is shown that when calcium does not form tight bonds, it is ductile. When the charge transferred from calcium is high enough, the glasses are brittle. Ductile glass become brittle in ambient lab conditions. Dissociated hydrogen was shown to be the source of this embrittlement. Dissociated hydrogen is a byproduct of the $Ca(OH)_2$ layer formation on the surface of calcium glasses. A comprehensive literature review shows that this failure mechanism has not been observed in calcium metallic glasses before.

From the results there are several avenues of research that can be perused. First, failure rate results can be applied to biomedical applications to understand corrosion rates. Research groups currently studying biodegradable calcium glasses do not account for this hydride decay mechanism. It would improve their understanding of decay in biodegradable skeletal applications, in controlling bioresorbable rates, and in controlling passivity improvements. Certain improvements made to this research would aid these future studies. The focus here was

on a single alloy system $Ca_{75}Mg_{15}Al_{10}$ studied primarily at 75% RH. In these biomedical applications different calcium glass alloys, humidity levels, and the liquid vapor conditions would need to be tested.

Second, improvements to the rough estimate of the time it takes for calcium ribbons to be saturated with CaH_2 could be refined. One way would be finding the activation energies of water vapor with Ca compared to that of water with CaH_2. Incorporating results of multiple humidity level tests would expand the hydroxide growth and the PPZ size measurements. An additional experiment could be an in situ exposure to a controlled amount of heavy water vapor. The experimental setup used would need to be able to do a depth profile etching of the calcium glass ribbon used. The measurement of the deuterium atoms would reveal the diffusion rates of OH and H in a calcium metallic glass. Additionally for PPZ, as noted in Section 4.4, there is a gradient in the form of increasing PPZ size from outer surface of the ribbon starting at the hydroxide layer to the inner core. This could correspond with the penetration depth of CaH_2 formation. The prior mentioned needed kinetic studies in conjunction with these ductility gradients could be used as support for the hydroxide and hydride formation rates observed.

Third, based on the control set of the bend-over-mandrel calcium metallic glass ribbons tested in ambient lab conditions, the sets that experienced a lower initial relative humidity took longer to fail. A study testing different initial humilities that examined initial hydroxide growths would explore this temporary passivation effect. And this could further work to find ways to mitigate the embrittlement. One way would be to block the formation of $Ca(OH)_2$ thus reducing the dissociated H that forms the CaH_2. This could be done by creating and processing the metallic glass to final structural stage in a water vapor free environment. Another way would be to hinder the penetration of the dissociated hydrogen.

Finally, an improvement to the Deal-Grove model relating to the thin layer linear fit of the initial oxide formation and for the fit of the second parabolic rate constant could be made. For the second parabolic rate constant it is proposed that a change from Ca to $Ca(OH)_2$ to the CaH_2 to $Ca(OH)_2$ reaction is responsible for the increase. The question still exist as to what the change in mechanism is that allows for the limit of diffusion of water vapor though the hydroxide to be bypassed and the second reaction to occur. It is possible that once the CaH_2 has saturated the ribbon, that the excess free hydrogen that no longer has Ca to bond with could be altering the dynamics of the system. Further test need to be conducted. Additionally, for the

Deal-Grove model, the physics behind the linear fit part of the model is explained by a blanket statement stating that the fit is due to multiple undifferentiated physics phenomena embedded in the surface rate constant term, k_s. In this work, the chemisorption is observed for the first 3 hours of 75% RH exposure; if the humidity of control chamber were set to a lower humidity the growth process of the hydroxide would be elongated. This prolonged growth at low temperatures would lead to more data in a regime that study of has been limited in by lack of data for high temperature oxide studies. This increase in data points could lead to a determination of the physics involved in surface rate constant or an adjustment to the model for the thin layer regime.

References

1   Davies, H. A., Aucote, J., & Hull, J. B. (1973). Amorphous nickel produced by splat quenching. *Nature Physical Science*, 246(149), 13.

2   Zhong, L., Wang, J., Sheng, H., Zhang, Z., & Mao, S. X. (2014). Formation of monatomic metallic glasses through ultrafast liquid quenching. *Nature*, 512(7513), 177.

3   Brill, R. (1930). X-ray Determination of the Form and Boundary Surfaces of Submicroscopic Crystals. *Z. Krist.*, 75, 217

4   Kramer, J. (1934). Über nichtleitende metallmodifikationen. *Annalen der Physik*, 411(1), 37-64.

5   Kramer, J. (1937). Der amorphe Zustand der Metalle. *Zeitschrift für Physik*, 106(11-12), 675-691.

6   Brenner, A., Couch, D. E., & Williams, E. K. (1950). Electrodeposition of alloys of phosphorus with nickel or cobalt. *J. Res. Nat. Bur. Stand*, 44(1), 109.

7   Buckel, W., & Hilsch, R. (1954). Einfluß der Kondensation bei tiefen Temperaturen auf den elektrischen Widerstand und die Supraleitung für verschiedene Metalle. *Zeitschrift für Physik*, 138(2), 109-120.

8   Jun, W. K., Willens, R. H., & Duwez, P. O. L. (1960). Non-crystalline structure in solidified gold–silicon alloys. *Nature*, 187(4740), 869.

9   Duwez, P. (1981). Metallic glasses-historical background. In *Glassy Metals I* (pp. 19-23). Springer, Berlin, Heidelberg.

10   Duwez, P., Willens, R. H., & Klement Jr, W. (1960). Continuous series of metastable solid solutions in silver-copper alloys. *Journal of Applied Physics*, 31(6), 1136-1137.

11   Chen, H. S., & Turnbull, D. (1969). Formation, stability and structure of palladium-silicon based alloy glasses. *Acta Metallurgica*, 17(8), 1021-1031.

12   Liebermann, H., & Graham, C. (1976). Production of amorphous alloy ribbons and effects of apparatus parameters on ribbon dimensions. *IEEE Transactions on Magnetics*, 12(6), 921-923.

13   Inoue, A., Zhang, T., & Masumoto, T. (1989). Al–La–Ni amorphous alloys with a wide supercooled liquid region. *Materials Transactions, JIM*, 30(12), 965-972.

14   Inoue, A., Zhang, T., & Masumoto, T. (1990). Zr–Al–Ni amorphous alloys with high glass transition temperature and significant supercooled liquid region. *Materials Transactions, JIM*, 31(3), 177-183.

References

15   Inoue, A., Zhang, T., & Masumoto, T. (1990). Production of amorphous cylinder and sheet of $La_{55}Al_{25}Ni_{20}$ alloy by a metallic mold casting method. *Materials Transactions, JIM*,31(5), 425-428.

16   Inoue, A., Kato, A., Zhang, T., Kim, S. G., & Masumoto, T. (1991). Mg–Cu–Y amorphous alloys with high mechanical strengths produced by a metallic mold casting method. *Materials Transactions, JIM*, 32(7), 609-616.

17   Zhang, T., Inoue, A., & Masumoto, T. (1991). Amorphous Zr–Al–TM (TM= Co, Ni, Cu) alloys with significant supercooled liquid region of over 100 K. *Materials Transactions, JIM*, 32(11), 1005-1010.

18   Inoue, A., Zhang, T., Nishiyama, N., Ohba, K., & Masumoto, T. (1993). Preparation of 16 mm diameter rod of amorphous $Zr_{65}Al_{7.5}Ni_{10}Cu_{17.5}$ alloy. *Materials Transactions, JIM*, 34(12), 1234-1237.

19   Peker, A., & Johnson, W. L. (1993). A highly processable metallic glass: $Zr_{41.2}Ti_{13.8}Cu_{12.5}Ni_{10.0}Be_{22.5}$. *Applied Physics Letters*, 63(17), 2342-2344.

20   Inoue, A., Nishiyama, N., & Kimura, H. (1997). Preparation and thermal stability of bulk amorphous $Pd_{40}Cu_{30}Ni_{10}P_{20}$ alloy cylinder of 72 mm in diameter. *Materials Transactions, JIM*, 38(2), 179-183.

21   Kündig, A.A., Löffler, J.F., Johnson, W.L., Uggowitzer, P.J., Thiyagarajan, P.,(2001). Influence of decomposition on the thermal stability of undercooled Zr-Ti-Cu-Ni-Al alloys. *Scripta Materialia*, 44(8–9), 1269-1273.

22   Kauzmann, W. (1948). The nature of the glassy state and the behavior of liquids at low temperatures. *Chemical Reviews*, 43(2), 219-256.

23   Turnbull, D., & Fisher, J. C. (1949). Rate of nucleation in condensed systems. *The Journal of Chemical Physics*, 17(1), 71-73.

24   Turnbull, D., & Cohen, M. H. (1958). Concerning reconstructive transformation and formation of glass. *The Journal of Chemical Physics*, 29(5), 1049-1054.

25   Turnbull, D., & Cohen, M. H. (1961). Free-volume model of the amorphous phase: glass transition. *The Journal of Chemical Physics*, 34(1), 120-125.

26   Turnbull, D. (1969). Under what conditions can a glass be formed?. *Contemporary Physics*, 10(5), 473-488.

27   Uhlmann, D. R. (1969). Crystallization and melting in glass-forming systems. In *Kinetics of Reactions in Ionic Systems* (pp. 172-197). Springer, Boston, MA.

References

28   Uhlmann, D. R. (1972). A kinetic treatment of glass formation. *Journal of Non-Crystalline Solids*, 7(4), 337-348.

29   Laws, K. J., Miracle, D. B., & Ferry, M. (2015). A predictive structural model for bulk metallic glasses. *Nature Communications*, 6, 8123.

30   Polk, D. E. (1970). Structural model for amorphous metallic alloys. *Scripta Metallurgica*, 4(2), 117-122.

31   Nagel, S. R., & Tauc, J. (1975). Nearly-free-electron approach to the theory of metallic glass alloys. *Physical Review Letters*, 35(6), 380.

32   Senkov, O. N., & Miracle, D. B. (2003). A topological model for metallic glass formation. *Journal of Non-Crystalline Solids*, 317(1-2), 34-39.

33   Miracle, D. B. (2004). A structural model for metallic glasses. *Nature Materials*, 3(10), 697.

34   Egami, T., & Waseda, Y. (1984). Atomic size effect on the formability of metallic glasses. *Journal of Non-Crystalline Solids,* 64(1-2), 113-134.

35   Pang, S. J., Zhang, T., Asami, K., & Inoue, A. (2002). Synthesis of Fe–Cr–Mo–C–B–P bulk metallic glasses with high corrosion resistance. *Acta Materialia*, 50(3), 489-497.

36   Chen, W., Wang, Y., Qiang, J., & Dong, C. (2003). Bulk metallic glasses in the Zr-Al-Ni-Cu system. *Acta Materialia*, 51(7), 1899-1907.

37   Johnson, W. L. (1999). Bulk glass-forming metallic alloys: Science and technology. *MRS Bulletin*, 24(10), 42-56.

38   Takeuchi, A., & Inoue, A. (2005). Classification of bulk metallic glasses by atomic size difference, heat of mixing and period of constituent elements and its application to characterization of the main alloying element. *Materials Transactions*, 46(12), 2817-2829.

39   Chen, N., Feng, P., & Pu, G. (1984). Pattern Recognition Applied to the Formability Criteria of Metallic Glasses. *Rapidly Quenched Metals*., 1, 195-196.

40   Hasegawa, R., & Tanaka, K. (1985). Electronic Structure and Glass Formability in Metallic Glasses. *MRS Online Proceedings Library Archive*, 58.

41   Bormann, R., Gärtner, F., & Zöltzer, K. (1988). Application of the CALPHAD method for the prediction of amorphous phase formation. *Journal of the Less Common Metals*, 145, 19-29.

References

42   Yan, X. Y., Chang, Y. A., Yang, Y., Xie, F. Y., Chen, S. L., Zhang, F., ... & He, M. H. (2001). A thermodynamic approach for predicting the tendency of multicomponent metallic alloys for glass formation. *Intermetallics*, 9(6), 535-538.

43   Kim, D., Lee, B. J., & Kim, N. J. (2004). Thermodynamic approach for predicting the glass forming ability of amorphous alloys. *Intermetallics*, 12(10-11), 1103-1107.

44   Dong, B. S., Zhou, S. X., Li, D. R., Lu, C. W., Feng, G. U. O., Ni, X. J., & Lu, Z. C. (2011). A new criterion for predicting glass forming ability of bulk metallic glasses and some critical discussions. *Progress in Natural Science: Materials International*, 21(2), 164-172.

45   Neite, G., Kubota, K., Higashi, K., Hehmann, F., & Matucha, K. H. (1996). Structure and properties of nonferrous alloys. *Materials Science and Technologie*, 8.

46   Ashby, M. F., & Greer, A. L. (2006). Metallic glasses as structural materials. *Scripta Materialia*, 54(3), 321-326.

47   Widom, M., Sauerwine, B., Cheung, A. M., Poon, S. J., Tong, P., Louca, D., & Shiflet, G. J. (2011). Elastic properties of Ca-based metallic glasses predicted by first-principles simulations. *Physical Review B*, 84(5), 054206.

48   Lutgens, F. K., & Tarbuck, E. J. (2000). *Essentials of Geology* (7th ed.). Upper Saddle River, NJ: Prentice Hall.

49   Loomis, C. C. (1946). The Production of Metallic Calcium by Thermal Reduction. *Transactions of the Electrochemical Society*, 89(1), 207-216.

50   Amand, R. S., & Giessen, B. C. (1978). Easy glass formation in simple metal alloys: amorphous metals containing calcium and strontium. *Scripta Metallurgica*, 12(11), 1021-1026.

51   Giessen, B. C., Hong, J., Kabacoff, L., Polk, D. E., & Raman, R. (1979). *Compositional Dependence of the Thermal Stability and Related Properties. of Metallic Glasses I: T_g for $Ca_{.65}M_{.35}$ and $Zr_{.4750}Cu_{.475}M_{.05}$ Glasses*. Ft. Belvoir: Defense Technical Information Center.

52   Suck, J. B., Guntherodt, H. J., & Beck, H. (1981). Dynamical structure factor of the metallic glass $Ca_{70}Mg_{30}$ at room temperature. *Journal of Physics F: Metal Physics*, 11(7), 1375.

53   Love, D. P., Wang, F. C., Naugle, D. G., Tsai, C. L., Giessen, B. C., & Callaway, T. O. (1982). Electrical properties of $Ca_{1-x}Al_x$ metallic glasses. *Physics Letters A*, 90(6), 303-308.

54   Nagel, S. R., Gubler, U. M., Hague, C. F., Krieg, J., Lapka, R., Oelhafen, P., ... & Williams, A. R. (1982). Electronic structure studies of Ca_xAl_{1-x} metallic glasses. *Physical Review Letters*, 49(8), 575.

References

55   Mizutani, U., & Matsuda, T. (1983). Electronic properties of $Ca_{1-x}Al_x$ metallic glasses. *Journal of Physics F: Metal Physics*, 13(10), 2115.

56   Erwin, J., Delgado, R., Armbrüster, H., Naugle, D. G., Love, D. P., Wang, F. C., ... & Callaway, T. O. (1984). Thermopower of $Ca_{1-x}Al_x$ metallic glasses. *Physics Letters A*, 100(2), 97-100.

57   Hafner, J., & Philipp, A. (1984). Low-temperature electrical resistivity of amorphous Ca-Mg alloys. *Journal of Physics F: Metal Physics*, 14(7), 1685.

58   Hines, W. A., Paoluzi, A., Budnick, J. I., Clark, W. G., & Tsai, C. L. (1984). Atomic and electronic structures of the Ca-Al metallic glass system: A pulse NMR study. *Journal of Non-Crystalline Solids*, 61, 1255-1260.

59   Tsai, C. L., & Lu, F. C. (1984). Electronic transport properties of La-Al metallic glasses. *Journal of Applied Physics*, 55(6), 1945-1947.

60   Naugle, D. G., Delgado, R., Armbrüster, H., Tsai, C. L., Callaway, T. O., Reynolds, D., & Moruzzi, V. L. (1986). Electron transport in calcium-based metallic glasses. *Physical Review B*, 34(12), 8279.

61   Laakkonen, J., & Nieminen, R. M. (1986). Resistivity of Ca-Al metallic glasses. *Physical Review B*, 34(2), 567.

62   Hafner, J., Egami, T., Aur, S., & Giessen, B. C. (1987). The structure of calcium-aluminium glasses: X-ray diffraction and computer simulation studies. *Journal of Physics F: Metal Physics*, 17(9), 1807.

63   Hafner, J., & Jaswal, S. S. (1988). Atomic and electronic structure of crystalline and amorphous alloys. II. Strong electronic bonding effects in Ca-Al compounds. *Physical Review B*, 38(11), 7320.

64   Jaswal, S. S., & Hafner, J. (1988). Atomic and electronic structure of crystalline and amorphous alloys. I. Calcium-magnesium compounds. *Physical Review B*, 38(11), 7311.

65   Bose, S. K., Jaswal, S. S., Andersen, O. K., & Hafner, J. (1988). Linear-muffin-tin-orbital (LMTO) supercell and LMTO recursion calculations for the electronic structure of metallic glasses: Ca7Al3. *Physical Review B*, 37(17), 9955.

66   Lançon, F., Billard, L., & Pasturel, A. (1989). A computer simulation of local order in metallic glasses. *Europhysics Letters*, 8(2), 147.

67   Hafner, J., & Tegze, M. (1989). Structural and electronic properties of crystalline and glassy calcium-zinc compounds. I. Trigonal prismatic ordering or tetrahedral close packing. *Journal of Physics: Condensed Matter*, 1(44), 8277.

References

68   Tegze, M., & Hafner, J. (1989). Structural and electronic properties of crystalline and glassy calcium-zinc compounds. II. Electronic density of states. *Journal of Physics: Condensed Matter*, 1(44), 8293.

69   Mizutani, U., Shimizu, T., Fukunaga, T., Koyano, T., Tanaka, K., Yamada, M., & Matsuda, T. (1990). Electronic structure and electron transport properties of calcium-zinc amorphous alloys and several intermetallic compounds. *Journal of Physics: Condensed Matter*, 2(38), 7825.

70   Naugle, D. G., Delgado, R., Armbruster, H., Tsai, C. L., Johnson, W. L., & Williams, A. R. (1985). Low-temperature enhancement of the thermopower of La-Al, Ca-Al and Ca-Al-Ga glassy metal alloys. *Journal of Physics F: Metal Physics*, 15(10), 2189.

71   Mizutani, U., Sasaura, M., Yamada, Y., & Matsuda, T. (1987). Electronic structure and electron transport of Ca-Mg-Al metallic glasses. *Journal of Physics F: Metal Physics*, 17(3), 667.

72   Mizutani, U., Sasaura, M., Moruzzi, V. L., & Matsuda, T. (1988). Electronic structure and electron transport in Ca- Mg-Cu metallic glasses. *Materials Science and Engineering*, 99(1-2), 295-299.

73   Sommer, F., Krull, H. G., & Lee, J. J. (1991). Calorimetric studies of liquid Ca-Cu-Mg alloys. *Journal of the Less Common Metals*, 169(2), 361-368.

74   Bose, S. K. (1998). Electronic structure and related properties of metallic glasses: Linear muffin-tin orbital approach. *Metallurgical and Materials Transactions A*, 29(7), 1853.

75   Amiya, K., & Inoue, A. (2002). Formation and thermal stability of Ca-Mg-Ag-Cu bulk glassy alloys. *Materials Transactions*, 43(10), 2578-2581.

76   Senkov, O. N., & Scott, J. M. (2004). Formation and thermal stability of Ca–Mg–Zn and Ca–Mg–Zn–Cu bulk metallic glasses. *Materials Letters*, 58(7-8), 1375-1378.

77   Senkov, O. N., & Scott, J. M. (2004). Specific criteria for selection of alloy compositions for bulk metallic glasses. *Scripta Materialia*, 50(4), 449-452.

78   Park, E. S., & Kim, D. H. (2004). Formation of Ca–Mg–Zn bulk glassy alloy by casting into cone-shaped copper mold. *Journal of Materials Research*, 19(3), 685-688.

79   Park, E. S., & Kim, D. H. (2005). Effect of atomic configuration and liquid stability on the glass-forming ability of Ca-based metallic glasses. *Applied Physics Letters*, 86(20), 201912.

80   Park, E. S., Kim, W. T., & Kim, D. H. (2005). Effect of alloy composition on the glass forming ability in Ca-Mg-Zn alloy system. In *Materials Science Forum* (Vol. 475, pp. 3415-3418). Trans Tech Publications.

References

81   Senkov, O. N., & Scott, J. M. (2005). Glass forming ability and thermal stability of ternary Ca–Mg–Zn bulk metallic glasses. *Journal of Non-Crystalline Solids*, 351(37-39), 3087-3094.

82   Senkov, O. N., Scott, J. M., & Miracle, D. B. (2006). Composition range and glass forming ability of ternary Ca–Mg–Cu bulk metallic glasses. *Journal of Alloys and Compounds*, 424(1-2), 394-399.

83   Senkov, O. N., Miracle, D. B., & Scott, J. M. (2006). Development and characterization of Ca–Mg–Zn–Cu bulk metallic glasses. *Intermetallics*, 14(8-9), 1055-1060.

84   Senkov, O. N., Miracle, D. B., Keppens, V., & Liaw, P. K. (2008). Development and characterization of low-density Ca-based bulk metallic glasses: an overview. *Metallurgical and Materials Transactions A*, 39(8), 1888-1900.

85   Senkov, O. N., Scott, J. M., Miracle, D., & Miracle, B. (2007). Development of Low Density Ca-Mg-Al-Based Bulk Metallic Glasses". *Materials Transactions*, 48(8), 2258.

86   Senkov, O., Scott, J., & Miracle, D. (2007). Effect of Al Addition on Glass Forming Ability and Glass Stability of Ca-Mg-Zn-Cu Based Bulk Metallic Glasses. *Metallurgical and Materials Transactions A*, 39(8), 1901-1907.

87   Li, J. F., Zhao, D. Q., Zhang, M. L., & Wang, W. H. (2008). CaLi-based bulk metallic glasses with multiple superior properties. *Applied Physics Letters*, 93(17), 171907.

88   Wang, J. Q., Qin, J. Y., Gu, X. N., Zheng, Y. F., & Bai, H. Y. (2011). Bulk metallic glasses based on ytterbium and calcium. *Journal of Non-Crystalline Solids*, 357(3), 1232-1234.

89   Amiya, K., & Inoue, A. (2002). Formation, thermal stability and mechanical properties of Ca-based bulk glassy alloys. *Materials Transactions*, 43(1), 81-84.

90   Senkov, O. N., & Scott, J. M. (2003). New calcium based bulk metallic glasses. *MRS Online Proceedings Library Archive*, 806.

91   Guo, F. Q., Poon, S. J., & Shiflet, G. J. (2004). CaAl-based bulk metallic glasses with high thermal stability. *Applied Physics Letters*, 84(1), 37-39.

92   Morrison, M. L., Buchanan, R. A., Liaw, P. K., Senkov, O. N., & Miracle, D. B. (2006). Electrochemical behavior of Ca-based bulk metallic glasses. *Metallurgical and Materials Transactions A*, 37(4), 1239-1245.

References

93   Babilas, R., Cesarz-Andraczke, K., Babilas, D., & Simka, W. (2015). Structure and corrosion resistance of $Ca_{50}Mg_{20}Cu_{30}$ bulk metallic glasses. *Journal of Materials Engineering and Performance*, 24(1), 167-174.

94   Dahlman, J., Senkov, O. N., Scott, J. M., & Miracle, D. B. (2007). Corrosion properties of Ca based bulk metallic glasses. *Materials Transactions*, 48(7), 1850-1854.

95   Wang, Y. B., Xie, X. H., Li, H. F., Wang, X. L., Zhao, M. Z., Zhang, E. W., ... & Qin, L. (2011). Biodegradable CaMgZn bulk metallic glass for potential skeletal application. *Acta Biomaterialia*, 7(8), 3196-3208.

96   Li, J. L., Zhao, D. Q., Pan, M. X., & Wang, W. H. (2011). Dissoluble and degradable CaLi-based metallic glasses. *Journal of Non-Crystalline Solids*, 357(1), 236-239.

97   Cao, J. D., Kirkland, N. T., Laws, K. J., Birbilis, N., & Ferry, M. (2012). Ca–Mg–Zn bulk metallic glasses as bioresorbable metals. *Acta Biomaterialia*, 8(6), 2375-2383.

98   Cao, J. D., Laws, K. J., Liu, C., & Ferry, M. (2013). Thermoplastic formability of CaMgZn bulk metallic glasses for biomedical applications. *International Journal of Materials and Product Technology*, 47(1-4), 233-240.

99   Li, H. F., Xie, X. H., Zhao, K., Wang, Y. B., Zheng, Y. F., Wang, W. H., & Qin, L. (2013). In vitro and in vivo studies on biodegradable CaMgZnSrYb high-entropy bulk metallic glass. *Acta Biomaterialia*, 9(10), 8561-8573.

100   Nowosielski, R., Bajorek, A., & Babilas, R. (2016). Corrosion behavior of bioresorbable Ca-Mg-Zn bulk metallic glasses. *Journal of Non-Crystalline Solids*, 447, 126-133.

101   Babilas, R., Bajorek, A., Radoń, A., & Nowosielski, R. (2017). Corrosion study of resorbable $Ca_{60}Mg_{15}Zn_{25}$ bulk metallic glasses in physiological fluids. *Progress in Natural Science: Materials International*, 27(5), 627-634.

102   Babilas, R., Szyba, D., Kania, A., Pilarczyk, W., & Nowosielski, R. (2018). Electrochemical Characterization of $Ca_{65}Mg_{15}Zn_{20}$ Amorphous Alloy in Selected Physiological Fluids. *Acta Physica Polonica, A.*, 133(2).

103   Neuville, D. R., Cormier, L., Flank, A. M., Briois, V., & Massiot, D. (2004). Al speciation and Ca environment in calcium aluminosilicate glasses and crystals by Al and Ca K-edge X-ray absorption spectroscopy. *Chemical Geology*, 213(1-3), 153-163.

104   Zhang, Z., Keppens, V., Senkov, O. N., & Miracle, D. B. (2007). Elastic properties of Ca-based bulk metallic glasses studied by resonant ultrasound spectroscopy. *Materials Science and Engineering: A*, 471(1-2), 151-154.

References

105   Zhang, Z. (2008). *Elastic Properties of Bulk-Metallic Glasses Studied by Resonant Ultrasound Spectroscopy* (Unpublished master's thesis).

106   Raphael, J., Wang, G. Y., Liaw, P. K., Senkov, O. N., & Miracle, D. B. (2010). Fatigue and Fracture Behavior of a Ca-Based Bulk-Metallic Glass. *Metallurgical and Materials Transactions A*, 41(7), 1775-1779.

107   Senkov, O. N., Miracle, D. B., Barney, E. R., Hannon, A. C., Cheng, Y. Q., & Ma, E. (2010). Local atomic structure of Ca-Mg-Zn metallic glasses. *Physical Review B*, 82(10), 104206.

108   Senkov, O. N., & Miracle, D. B. (2010). Relaxation behavior of Ca-based bulk metallic glasses. *Metallurgical and Materials Transactions A*, 41(7), 1677-1684.

109   Wang, G., Liaw, P. K., Senkov, O. N., & Miracle, D. B. (2011). The Duality of Fracture Behavior in a Ca-based Bulk-Metallic Glass. *Metallurgical and Materials Transactions A*, 42(6), 1499-1503.

110   Barney, E. R., Hannon, A. C., Senkov, O. N., Scott, J. M., Miracle, D. B., & Moss, R. M. (2011). A neutron and X-ray diffraction study of Ca–Mg–Cu metallic glasses. *Intermetallics*, 19(7), 860-870.

111   Senkov, O. N., Cheng, Y. Q., Miracle, D. B., Barney, E. R., Hannon, A. C., & Woodward, C. F. (2012). Atomic structure of $Ca_{40}+ XMg_{25}Cu_{35}- X$ metallic glasses. *Journal of Applied Physics*, 111(12), 123515.

112   Laws, K. J., Gun, B., & Ferry, M. (2008). Mechanical stability of $Ca_{65}Mg_{15}Zn_{20}$ bulk metallic glass during deformation in the supercooled liquid region. *Materials Science and Engineering: A*, 480(1-2), 198-204.

113   Lou, H. B., Fang, Y. K., Zeng, Q. S., Lu, Y. H., Wang, X. D., Cao, Q. P., ... & Chu, W. S. (2012). Pressure-induced amorphous-to-amorphous configuration change in Ca-Al metallic glasses. *Scientific Reports*, 2, 376.

114   Michalik, Š., Ďurišin, J., Balga, D., Saksl, K., Ďurišin, M., & Drakopoulos, M. (2016). In situ HEXRD study of a $Ca_{61}Al_{39}$ metallic glass. *Journal of Alloys and Compounds*, 687, 188-196.

115   Saksl, K., Ďurišin, J., Balga, D., Milkovič, O., Brestovič, T., Jasminská, N., ... & Šuliková, M. (2017). Devitrification and hydrogen storage capacity of the eutectic $Ca_{72}Mg_{28}$ metallic glass. *Journal of Alloys and Compounds*, 725, 916-922.

116   Laws, K. J., Gun, B., & Ferry, M. (2007). The Production and Elevated Temperature Properties of $Ca_{65}Mg_{15}Zn_{20}$ Bulk Metallic Glass. In *Materials Science Forum* (Vol. 561, pp. 1263-1266). Trans Tech Publications.

References

117   Laws, K. J., Gun, B., & Ferry, M. (2008). Large-scale production of $Ca_{65}Mg_{15}Zn_{20}$ bulk metallic glass samples by low-pressure die-casting. *Materials Science and Engineering: A*, 475(1-2), 348-354.

118   Nowosielski, R., Borowski, A., Guwer, A., & Babilas, R. (2013). Fabrication of ternary Ca-Mg-Zn bulk metallic glasses. *Journal of Achievements in Materials and Manufacturing Engineering*, 56(2), 67-74.

119   Guthrie, R. I., Isac, M., Li, D., & Calzado, L. (2014). Horizontal Single Belt Casting (HSBC) of Ca-Based Bulk Metallic Glass (BMG) Strips. In *Celebrating the Megascale* (pp. 105-117). Springer, Cham.

120   Zhao, K., Liu, K. S., Li, J. F., Wang, W. H., & Jiang, L. (2009). Superamphiphobic CaLi-based bulk metallic glasses. *Scripta Materialia*, 60(4), 225-227.

121   Jin, Y., Li, R., & Zhang, T. (2015). Formation of nanoporous silver by dealloying Ca–Ag metallic glasses in water. *Intermetallics*, 67, 166-170.

122   Gu, X., Shiflet, G. J., Guo, F. Q., & Poon, S. J. (2005). Mg–Ca–Zn bulk metallic glasses with high strength and significant ductility. *Journal of Materials Research*, 20(8), 1935-1938.

123   Li, H. F., Wang, Y. B., Cheng, Y., & Zheng, Y. F. (2010). Surface modification of $Ca_{60}Mg_{15}Zn_{25}$ bulk metallic glass for slowing down its biodegradation rate in water solution. *Materials Letters*, 64(13), 1462-1464.

124   Marshall, E. R., & Shaw, M. C. (1952). The determination of flow stress from a tensile specimen. *ASM TRANS Q*, 44, 705-720.

125   Taplin, D. M. (1978). *Physical Metallurgy of Fracture*. Oxford: Pergamon Press.

126   Rufe, P. D. (2005). *Fundamentals of Manufacturing Supplement*. Society of Manufacturing Engineers.

127   Davis, L. A. (1977). Metallic Glasses. In R. Jaffee (Eds.), *Fundamental Aspects of Structural Alloy Design* (pp. 431-450). New York, NY: Plenum Press.

128   Chen, H. S., Leamy, H. J., & O'brien, M. J. (1973). Bending deformation in metallic glasses. *Scripta Metallurgica*, 7(4), 415-419.

129   Suto, S., Matsuno, K., Sano, T., & Matsui, K. (1992). Bending of amorphous alloys. *Journal of Materials Processing Technology*, 33(3), 215-227.

References

130   Takayama, S., & Maddin, R. (1975). Rolling and bending deformation of Ni-Pd-P metal glasses. *Acta Metallurgica*, 23(8), 943-952.

131   Spaepen, F. (1982). *Defects in Amorphous Metals* (No. TR-16). Harvard University Cambridge MA Division of Applied Sciences.

132   Kim, K. B., Das, J., Venkataraman, S., Yi, S., & Eckert, J. (2006). Work hardening ability of ductile $Ti_{45}Cu_{40}Ni_{7.5}Zr_5Sn_{2.5}$ and $Cu_{47.5}Zr_{47.5}Al_5$ bulk metallic glasses. *Applied Physics Letters*, 89(7), 071908.

133   Chen, M., Inoue, A., Zhang, W., & Sakurai, T. (2006). Extraordinary plasticity of ductile bulk metallic glasses. *Physical Review Letters*, 96(24), 245502.

134   Davis, L. A., Ray, R., Chou, C. P., & O'handley, R. C. (1976). Mechanical and thermal properties of $Fe_{80}B_{20}$ glass. *Scripta Metallurgica*, 10(6), 541-546.

135   Lewandowski, J. J., & Greer, A. L. (2006). Temperature rise at shear bands in metallic glasses. *Nature Materials*, 5(1), 15.

136   Sergueeva, A. V., Mara, N. A., Kuntz, J. D., Branagan, D. J., & Mukherjee, A. K. (2004). Shear band formation and ductility of metallic glasses. *Materials Science and Engineering: A*, 383(2), 219-223.

137   Zhang, Y., Wang, W. H., & Greer, A. L. (2006). Making metallic glasses plastic by control of residual stress. *Nature Materials*, 5(11), 857.

138   Chen, M. (2008). Mechanical behavior of metallic glasses: microscopic understanding of strength and ductility. *Annu. Rev. Mater. Res*., 38, 445-469.

139   Liu, Y., Wu, H., Liu, C. T., Zhang, Z., & Keppens, V. (2008). Physical factors controlling the ductility of bulk metallic glasses. *Applied Physics Letters*, 93(15), 151915.

140   Yao, K. F., Ruan, F., Yang, Y. Q., & Chen, N. (2006). Superductile bulk metallic glass. *Applied Physics Letters*, 88(12), 122106.

141   Wu, F. F., Zhang, Z. F., Jiang, F., Sun, J., Shen, J., & Mao, S. X. (2007). Multiplication of shear bands and ductility of metallic glass. *Applied Physics Letters*, 90(19), 191909.

142   Schroers, J., & Johnson, W. L. (2004). Ductile bulk metallic glass. *Physical Review Letters*, 93(25), 255506.

143   Staudinger, A., & Nakahara, S. (1977). The structure of the crack network in amorphous films. *Thin Solid Films*, 45(1), 125-133.

References

144   Sarac, B., & Schroers, J. (2013). Designing tensile ductility in metallic glasses. *Nature Communications*, 4, 2158.

145   Lewandowski, J. J., Wang, W. H., & Greer, A. L. (2005). Intrinsic plasticity or brittleness of metallic glasses. *Philosophical Magazine Letters*, 85(2), 77-87.

146   Jang, D., & Greer, J. R. (2010). Transition from a strong-yet-brittle to a stronger-and-ductile state by size reduction of metallic glasses. *Nature Materials*, 9(3), 215.

147   Chi, G. C., Chen, H. S., & Miller, C. E. (1978). The influence of quenching procedures on the kinetics of embrittlement in a $Fe_{40}Ni_{40}B_{20}$ metallic glass. *Journal of Applied Physics*, 49(3), 1715-1717.

148   Ast, D. G., & Krenitsky, D. (1976). Fracture toughness and yield strength of annealed Ni-Fe base metallic glasses. *Materials Science and Engineering*, 23(2-3), 241-246.

149   Chen, H. S. (1977). Thermal and mechanical stability of metallic glass ferromagnets. *Scripta Metallurgica*, 11(5), 367-370.

150   Murali, P., & Ramamurty, U. (2005). Embrittlement of a bulk metallic glass due to sub-T_g annealing. *Acta Materialia*, 53(5), 1467-1478.

151   Barth, E. P., Spaepen, F., Bye, R., & Das, S. K. (1997). Influence of processing on the ductile-to-brittle transition temperature of an Fe-B-Si metallic glass. *Acta Materialia*, 45(1), 423-428.

152   Dasa, S. K., Bye, R. L., Barth, E. P., Spaepen, F., Ramanan, V. R. V., & Vu, T. (1997). Processing of thick ductile metallic glass. *Materials Science and Engineering: A*, 226, 1-7.

153   Bengus, V. Z., Tabachnikova, E. D., Miškuf, J., Csach, K., Ocelik, V., Johnson, W. L., & Molokanov, V. V. (2000). New features of the low temperature ductile shear failure observed in bulk amorphous alloys. *Journal of Materials Science*, 35(17), 4449-4457.

154   Raghavan, R., Murali, P., & Ramamurty, U. (2006). Ductile to brittle transition in the $Zr_{41.2}Ti_{13.75}Cu_{12.5}Ni_{10}Be_{22.5}$ bulk metallic glass. *Intermetallics*, 14(8-9), 1051-1054.

155   Chen, H. S. (1976). Ductile-brittle transition in metallic glasses. *Materials Science and Engineering*, 26(1), 79-82.

156   Ramamurty, U., Lee, M. L., Basu, J., & Li, Y. (2002). Embrittlement of a bulk metallic glass due to low-temperature annealing. *Scripta Materialia*, 47(2), 107-111.

157   Gu, X. J., Poon, S. J., Shiflet, G. J., & Lewandowski, J. J. (2009). Ductile-to-brittle transition in a Ti-based bulk metallic glass. *Scripta Materialia*, 60(11), 1027-1030.

References

158 Raghavan, R., Murali, P., & Ramamurty, U. (2009). On factors influencing the ductile-to-brittle transition in a bulk metallic glass. *Acta Materialia*, 57(11), 3332-3340.

159 Magagnosc, D. J., Ehrbar, R., Kumar, G., He, M. R., Schroers, J., & Gianola, D. S. (2013). Tunable tensile ductility in metallic glasses. *Scientific Reports*, 3, 1096.

160 Wang, W. H. (2007). Roles of minor additions in formation and properties of bulk metallic glasses. *Progress in Materials Science*, 52(4), 540-596.

161 Liu, Y. H., Wang, G., Wang, R. J., Pan, M. X., & Wang, W. H. (2007). Super plastic bulk metallic glasses at room temperature. *Science*, 315(5817), 1385-1388.

162 Zheng, Q., Ma, H., Ma, E., & Xu, J. (2006). Mg–Cu–(Y, Nd) pseudo-ternary bulk metallic glasses: The effects of Nd on glass-forming ability and plasticity. *Scripta Materialia*, 55(6), 541-544.

163 Gu, X. J., Poon, S. J., Shiflet, G. J., & Widom, M. (2008). Ductility improvement of amorphous steels: roles of shear modulus and electronic structure. *Acta Materialia*, 56(1), 88-94.

164 Lewandowski, J. J., Gu, X. J., Shamimi Nouri, A., Poon, S. J., & Shiflet, G. J. (2008). Tough Fe-based bulk metallic glasses. *Applied Physics Letters*, 92(9), 091918.

165 Gu, X. J., McDermott, A. G., Poon, S. J., & Shiflet, G. J. (2006). Critical Poisson's ratio for plasticity in Fe–Mo–C–B–Ln bulk amorphous steel. *Applied Physics Letters*, 88(21), 211905.

166 Poon, S. J., Zhu, A., & Shiflet, G. J. (2008). Poisson's ratio and intrinsic plasticity of metallic glasses. *Applied Physics Letters*, 92(26), 261902.

167 Guo, F., Poon, S. J., Gu, X., & Shiflet, G. J. (2007). Low-density Mg-rich metallic glasses with bending ductility. *Scripta Materialia*, 56(8), 689-692.

168 Huang, Y. J., Shen, J., & Sun, J. F. (2007). Bulk metallic glasses: Smaller is softer. *Applied Physics Letters*, 90(8), 081919.

169 Xi, X. K., Zhao, D. Q., Pan, M. X., Wang, W. H., Wu, Y., & Lewandowski, J. J. (2005). Fracture of brittle metallic glasses: Brittleness or plasticity. *Physical Review Letters*, 94(12), 125510.

170 Sun, B. A., Yu, H. B., Jiao, W., Bai, H. Y., Zhao, D. Q., & Wang, W. H. (2010). Plasticity of ductile metallic glasses: A self-organized critical state. *Physical Review Letters*, 105(3), 035501.

References

171   Wang, X. D., Yang, L., Jiang, J. Z., Saksl, K., Franz, H., Fecht, H. J., ... & Xian, H. S. (2007). Enhancement of plasticity in Zr-based bulk metallic glasses. *Journal of Materials Research*, 22(9), 2454-2459.

172   Conner, R. D., Johnson, W. L., Paton, N. E., & Nix, W. D. (2003). Shear bands and cracking of metallic glass plates in bending. *Journal of Applied Physics*, 94(2), 904-911.

173   Matsumoto, R., & Miyazaki, N. (2008). The critical length of shear bands in metallic glass. *Scripta Materialia*, 59(1), 107-110.

174   Hays, C. C., Kim, C. P., & Johnson, W. L. (2000). Microstructure controlled shear band pattern formation and enhanced plasticity of bulk metallic glasses containing in situ formed ductile phase dendrite dispersions. *Physical Review Letters*, 84(13), 2901.

175   Das, J., Tang, M. B., Kim, K. B., Theissmann, R., Baier, F., Wang, W. H., & Eckert, J. (2005). "Work-hardenable" ductile bulk metallic glass. *Physical Review Letters*, 94(20), 205501.

176   Inoue, A., Zhang*, W., Tsurui, T., Yavari, A. R., & Greer, A. L. (2005). Unusual room-temperature compressive plasticity in nanocrystal-toughened bulk copper-zirconium glass. *Philosophical Magazine Letters*, 85(5), 221-237.

177   Hofmann, D. C., Suh, J. Y., Wiest, A., & Johnson, W. (2008). New processing possibilities for highly toughened metallic glass matrix composites with tensile ductility. *Scripta Materialia*, 59(7), 684-687.

178   Hofmann, D. C., Suh, J. Y., Wiest, A., Duan, G., Lind, M. L., Demetriou, M. D., & Johnson, W. L. (2008). Designing metallic glass matrix composites with high toughness and tensile ductility. *Nature*, 451(7182), 1085.

179   Pauly, S., Gorantla, S., Wang, G., Kühn, U., & Eckert, J. (2010). Transformation-mediated ductility in CuZr-based bulk metallic glasses. *Nature Materials*, 9(6), 473.

180   Chen, H. S. (1980). Glassy metals. *Reports on Progress in Physics*, 43(4), 353.

181   Owens, J. C. (1967). Optical refractive index of air: dependence on pressure, temperature and composition. *Applied Optics*, 6(1), 51-59.

182   Mueller, W. M., Blackledge, J. P., & Libowitz, G. G. (1968). *Metal Hydrides*. New York: Academic Press.

183   Lennard-Jones, J. E. (1932). Processes of adsorption and diffusion on solid surfaces. *Transactions of the Faraday Society*, 28, 333-359.

References

184   Trapnell, B. M., & Hayward, D. O. (1964). *Chemisorption*. Washington: Butterworths.

185   Trapnell, B. M. W. (1953). The activities of evaporated metal films in gas chemisorption. *Proc. R. Soc. Lond. A*, 218(1135), 566-577.

186   Switendick, A. C. (1978). The change in electronic properties on hydrogen alloying and hydride formation. In *Hydrogen in Metals I* (pp. 101-129). Springer, Berlin, Heidelberg.

187   Völkl, J., & Alefeld, G. (1978). Diffusion of hydrogen in metals. In *Hydrogen in Metals I* (pp. 321-348). Springer, Berlin, Heidelberg

188   Nørskov, J. K., Houmøller, A., Johansson, P. K., & Lundqvist, B. I. (1981). Adsorption and dissociation of H2 on Mg surfaces. *Physical Review Letters*, 46(4), 257.

189   Eichenauer, W., & Pebler, A. (1957). Messung des Diffusionskoeffizienten und der Loslichkeit von Wasserstoff in Aluminium und Kupfer. *Zeitschrift fur Metallkunde*, 48(7), 373-378.

190   McLellan, R. B., & Oates, W. A. (1973). The solubility of hydrogen in rhodium, ruthenium, iridium and nickel. *Acta Metallurgica*, 21(3), 181-185.

191   Bulanov, A. D., Troshin, O. Y., & Balabanov, V. V. (2004). Synthesis of high-purity calcium hydride. *Russian Journal of Applied Chemistry*, 77(6), 875-877.

192   Lide, D. R. (Ed.). (2004). *CRC Handbook of Chemistry and Physics* (Vol. 85). Boca Raton, FL: CRC Press.

193   Johnson, W. C., Stubbs, M. F., Sidwell, A. E., & Pechukas, A. (1939). The rate of formation and the dissociation of calcium hydride. *Journal of the American Chemical Society*, 61(2), 318-329.

194   Cros, S., Firon, M., Lenfant, S., Trouslard, P., & Beck, L. (2006). Study of thin calcium electrode degradation by ion beam analysis. *Nuclear Instruments and Methods in Physics Research Section B: Beam Interactions with Materials and Atoms*, 251(1), 257-260.

195   Nishiyama, H., Sawada, T., Takana, H., Tanaka, M., & Ushio, M. (2006). Computational simulation of arc melting process with complex interactions. *ISIJ international*, 46(5), 705-711.

196   American Society for Testing and Materials. (2003). *Standard Test Method for Assignment of the Glass Transition Temperatures by Differential Scanning Calorimetry (E1356-03)*. West Conshohocken, PA / USA: ASTM International.

References

197   American Society for Testing and Materials. (2012). *Standard Practice for Maintaining Constant Relative Humidity by Means of Aqueous Solutions (E104-02)*. West Conshohocken, PA / USA: ASTM International.

198   Hofmann, S. (2012). *Auger-and X-ray Photoelectron Spectroscopy in Materials Science: A User-Oriented Guide* (Vol. 49). Springer Science & Business Media.

199   Thompson, A., & Taylor, B. N. (2008). *Guide for the Use of the International System of Units* (SI) (No. Special Publication (NIST SP)-811).

200   Voigt, W. (1889). Ueber die Beziehung zwischen den beiden Elasticitätsconstanten isotroper Körper. *Annalen Der Physik*, 274(12), 573-587.

201   Reuss, A. (1929). Berechnung der Fließgrenze von Mischkristallen auf Grund der Plastizitätsbedingung für Einkristalle. *ZAMM - Zeitschrift Für Angewandte Mathematik Und Mechanik*, 9(1), 49-58.

202   Chung, D. H. (1963). Elastic moduli of single crystal and polycrystalline MgO. *Philosophical Magazine*, 8(89), 833-841.

203   Kresse, G., & Furthmüller, J. (1996). Efficient iterative schemes for ab initio total-energy calculations using a plane-wave basis set. *Physical Review B*, 54(16), 11169.

204   Kohn, W., & Sham, L. J. (1965). Self-consistent equations including exchange and correlation effects. *Physical Review*, 140(4A), A1133.

205   Kresse, G., & Joubert, D. (1999). From ultrasoft pseudopotentials to the projector augmented-wave method. *Physical Review B*, 59(3), 1758.

206   Perdew, J. P., Chevary, J. A., Vosko, S. H., Jackson, K. A., Pederson, M. R., Singh, D. J., & Fiolhais, C. (1992). Atoms, molecules, solids, and surfaces: Applications of the generalized gradient approximation for exchange and correlation. *Physical Review B*, 46(11), 6671.

207   Gu, X. J., Poon, S. J., Shiflet, G. J., & Widom, M. (2008). Mechanical properties, glass transition temperature, and bond enthalpy trends of high metalloid Fe-based bulk metallic glasses. *Applied Physics Letters*, 92(16), 161910.

208   Mihalkovic, M., & Widom, M. (2004). Ab initio calculations of cohesive energies of Fe-based glass-forming alloys. *Physical Review B*, 70(14), 144107.

209   Argon, A. S., & Salama, M. (1976). The mechanism of fracture in glassy materials capable of some inelastic deformation. *Materials Science and Engineering*, 23(2-3), 219-230.

References

210   Shamimi Nouri, A., Gu, X. J., Poon, S. J., Shiflet, G. J., & Lewandowski, J. J. (2008). Chemistry (intrinsic) and inclusion (extrinsic) effects on the toughness and Weibull modulus of Fe-based bulk metallic glasses. *Philosophical Magazine Letters*, 88(11), 853-861.

211   Gregg, S. J., & Jepson, W. B. (1961). 186. The oxidation of calcium in moist oxygen. *Journal of the Chemical Society (Resumed)*, 884-888.

212   Nissen, D. A. (1977). The low-temperature oxidation of calcium by water vapor. *Oxidation of Metals*, *11*(5), 241-261.

213   Moulder, J. F., Chastain, J., & King, R. C. (1992). *Handbook of X-ray Photoelectron Spectroscopy: A Reference Book of Standard Spectra for Identification and Interpretation of XPS Data*. Eden Prairie, Minnesota: Physical Electronics Division, Perkin-Elmer Corporation.

214   Sosulnikov, M. I., & Teterin, Y. A. (1992). X-ray photoelectron studies of Ca, Sr and Ba and their oxides and carbonates. *Journal of Electron Spectroscopy and Related Phenomena*, 59(2), 111-126.

215   Doveren, H. V., & Verhoeven, J. T. (1980). XPS spectra of Ca, Sr, Ba and their oxides. *Journal of Electron Spectroscopy and Related Phenomena*, 21(3), 265-273.

216   Christie, A. B., Lee, J., Sutherland, I., & Walls, J. M. (1983). An XPS study of ion-induced compositional changes with group II and group IV compounds. *Applications of Surface Science*, 15(1-4), 224-237.

217   Demri, B., & Muster, D. (1995). XPS study of some calcium compounds. *Journal of Materials Processing Technology*, 55(3-4), 311-314.

218   Briggs, D. (1977). *Handbook of X-ray and Ultraviolet Photoelectron Spectroscopy*. London/UK: Heyden & Son

219   Barr, T. L. (1991). Recent advances in x-ray photoelectron spectroscopy studies of oxides. *Journal of Vacuum Science & Technology A: Vacuum, Surfaces, and Films*, 9(3), 1793-1805.

220   Franzen, H., Merrick, J., Umaña, M., Khan, A., Peterson, D., Mccreary, J., & Thorn, R. (1977). XPS spectra and crystalline potentials in alkaline-earth chalcogenides and hydrides. *Journal of Electron Spectroscopy and Related Phenomena*, 11(4), 439-443.

221   Seyama, H., & Soma, M. (1984). X-ray photoelectron spectroscopic study of montmorillonite containing exchangeable divalent cations. *Journal of the Chemical Society, Faraday Transactions 1: Physical Chemistry in Condensed Phases*, 80(1), 237-248.

References

222   Inoue, Y., & Yasumori, I. (1981). Catalysis by alkaline earth metal oxides. III. X-ray photoelectron spectroscopic study of catalytically active MgO, CaO, and BaO surfaces. *Bulletin of the Chemical Society of Japan*, 54(5), 1505-1510.

223   Sugama, T., Kukacka, L. E., Carciello, N., & Hocker, N. J. (1989). Study of interactions at water-soluble polymer/Ca (OH)$_2$ or gibbsite interfaces by XPS. *Cement and Concrete Research*, 19(6), 857-867.

224   Fairley, N. (2009). CasaXPS v 2.3. 15. *Casa Software Ltd*.

225   Shirley, D. A. (1972). High-resolution X-ray photoemission spectrum of the valence bands of gold. *Physical Review B*, 5(12), 4709.

226   Barr, T. L. (1994). *Modern ESCA The Principles and Practice of X-Ray Photoelectron Spectroscopy*. CRC press. Chicago

227   Levenberg, K. (1944). A method for the solution of certain non-linear problems in least squares. *Quarterly of Applied Mathematics*, 2(2), 164-168.

228   Marquardt, D. W. (1963). An algorithm for least-squares estimation of nonlinear parameters. *Journal of the Society for Industrial and Applied Mathematics*, 11(2), 431-441.

229   Perkin-Elmer. (1995). *The PHI Model 560 ESCA/SAM: PHI Analytical Lab Manual*. Waltham, MA: Author.

230   Morris, M. D. (1993). *Microscopic and Spectroscopic Imaging of the Chemical State*. CRC Press. Chicago

231   Woodruff, D. P., and Delchar, T.A.(1994) *Modern Techniques of Surface Science*. Cambridge(England): Cambridge University Press.

232   Fehlner, F. P., & Mott, N. F. (1970). Low-temperature oxidation. *Oxidation of Metals*, 2(1), 59-99.

233   Landsberg, P. T. (1955). On the logarithmic rate law in chemisorption and oxidation. *The Journal of Chemical Physics*, 23(6), 1079-1087.

234   Halsey Jr, G. D. (1951). The rate of adsorption on a nonuniform surface. *The Journal of Physical Chemistry*, 55(1), 21-26.

235   Kofstad, P. (1988). *High temperature Corrosion*. Elsevier Applied Science Publishers, Crown House, Linton Road, Barking, Essex IG 11 8 JU, UK, 1988.

References

236   Birks, N., Meier, G. H., & Pettit, F. S. (2006). *Introduction to the High Temperature Oxidation of Metals*. Cambridge University Press.

237   Deal, B. E., & Grove, A. S. (1965). General relationship for the thermal oxidation of silicon. *Journal of Applied Physics*, 36(12), 3770-3778.

238   Svec, H. J., & Apel, C. (1957). Metal-Water Reactions IV. Kinetics of the Reaction between Calcium and Water Vapor. *Journal of The Electrochemical Society*, 104(6), 346-349
.
239   Budavari, S., & E. Merck (Firma). (1996). *The Merck index: An Encyclopedia of Chemicals, Drugs, and Biologicals*. Whitehouse Station (N.J.): Merck.